The Influence of Strain on Shock-Induced Turbulent Mixing

Bradley Pascoe

A thesis submitted in fulfilment
of the requirements of the degree of
Doctor of Philosophy

Faculty of Engineering
The University of Sydney

December 2024

This research reported in this thesis was supported
by the award of a Research Training Program scholarship
to the Ph.D. Candidate.

Statement of Originality

This is to certify that to the best of my knowledge, the content of this thesis is my own work. This thesis has not been submitted for any degree or other purposes.

I certify that the intellectual content of this thesis is the product of my own work and that all the assistance received in preparing this thesis and sources have been acknowledged.

Bradley Pascoe

31 December 2024

Authorship Attribution Statement

The material in Chapter 4 of this thesis contains previously published research (Pascoe et al.*, 2024):*

- ***Pascoe, B.**, Groom, M., Youngs, D.L., Thornber, B. (2024). Impact of axial strain on linear, transitional, and self-similar turbulent mixing layers. Journal of Fluid Mechanics, 999:A5.*

The contents of Chapter 5 of this thesis contains research that has been submitted and is currently under review:

- ***Pascoe, B.**, Groom, M., Youngs, D.L., Thornber, B. Impact of transverse strain on linear, transitional, and self-similar turbulent mixing layers. (Submitted)*

The material in Chapter 6 of this thesis contains previously published research (Pascoe et al.*, 2025*a*):*

- ***Pascoe, B**, Groom, M., Thornber, B. (2025). Turbulence modeling of mixing layers under anisotropic strain. Physical Review Fluids, 10:064609.*

For the aforementioned publications, I am responsible for the implementation of the novel numerical methods into the code that enable the simulations to be conducted, as well as responsible for conducting the simulations, analysis, and writing of the manuscripts.

Bradley Pascoe
31 December 2024

As supervisor for the candidature upon which this thesis is based, I can confirm that the authorship attribution statements above are correct.

Professor Ben Thornber
31 December 2024

Abstract

Hydrodynamic instabilities, such as the Rayleigh-Taylor (RTI) and Richtmyer-Meshkov instability (RMI), are responsible for the generation of turbulent mixing layers between fluids separated by an interface. The ability to quantitatively describe and predict these mixing layers is vital for the development of inertial confinement fusion and supersonic combustion, and will improve the understanding of mixing within supernova. Obtaining experimental data for these configurations can be difficult, driving the necessity for accurate simulations and models to capture the flow physics.

The analysis of these instabilities has previously been focused largely towards the planar, Cartesian regime. However, in inertial confinement fusion and supernova collapse the configuration is spherical, which alters the development of the mixing layer. The movement of mixing layers due to a radial velocity causes the mixing layer to be affected by strain rates, which for a spherically symmetric flow can be separated into the radial and circumferential directions. Previously, simulations in spherical geometry have not focused on the effects of these strain rates on the mixing layer development, meaning the effect of the strain rate on the turbulent mixing layer is not well understood.

The influence of the strain rates on RMI and the RMI-induced mixing layer is investigated by applying spatially uniform strain rates in planar geometry and simulating the flow with high-order numerical methods. By advecting the mesh and boundaries in a Lagrangian method with the strain, the uniform velocity gradients can be preserved in the domain. The planar application of the strain rates allows for a decoupling between the strain rates, which is hard to achieve in spherical geometry. The radial strain rate is represented by the axial strain rate (normal to the interface), and the circumferential is represented by the transverse strain rate (in the plane of the interface).

The influence of axial strain in the linear regime of RMI is found to be the superposition of the instability growth rate and the velocity difference across the perturbation, where the strain causes the mixing layer to stretch or compress depending upon the sign. The turbulent RMI-induced mixing layer is investigated by implicit large eddy simulations and shows similar behaviour, but the stretching/compression effect of the strain is counteracted by shear production of turbulent kinetic energy. The shear production changes the mixedness and turbulent kinetic energy anisotropy of the mixing layer, deviating from the self-similar

behaviour observed at late-time. Corrections to the buoyancy-drag model to describe the mixing layer width under axial strain are found, which correspond to the terms for shear production.

The influence of transverse strain on RMI depends upon the regime of the flow. The linear regime model shows amplification of the amplitude growth under compression, which is verified by simulations. The turbulent mixing layer observes reduced growth under compression. This difference is the result of the modification of the turbulent length scale of the flow compressing as well, increasing the dissipation of turbulent kinetic energy. An analysis of the effective drag length scale for the buoyancy-drag model shows that the model for the unstrained case can be used for transverse compression when the drag length scale is scaled relative to the transverse expansion factor. Likewise, a Reynolds stress model for the domain-integrated quantities is able to predict the effects of the transverse strain rate when adjusted to use a length scale based on the integral width and transverse expansion factor.

The modelling of the turbulent mixing layers under strain is investigated with the K-L turbulence model. The typical bulk compression closure of the model assumes isotropy of the strain rates, which is invalid for the simulation cases with only axial or transverse strain, as well as invalid for many realistic flow conditions. Two alternate closures are investigated, achieving closure using the axial strain rate or transverse strain rate, specifically. The transverse model is the most accurate closure under the application of axial and transverse strain rates, as measured by the integral width and domain-integrated turbulent kinetic energy. Given the transverse closure is equivalent to the isotropic closure under isotropic strain, the transverse closure is recommended for future modelling of inhomogeneous flows with bulk compression.

Acknowledgements

My gratitude is extended to my technical supervisors, Professor Ben Thornber and Dr. Michael Groom. I appreciate the efforts both of you have gone through for the past few years, especially as you continued to be involved and supervise from your new institutions. I appreciate your mentorship and time invested, and despite the inconvenient meeting times, I will miss having meetings with you both. I would also like to thank David Youngs for his contributions to the project, and wonderful insights and discussions regarding turbulent mixing and RANS modelling.

I had the fortune to share an office with some wonderful individuals during my studies. Whilst I initially had an entire office to myself due to COVID-19, the experience was lacking as compared to the community that existed in S346. I would like to thank Brendan Waters, Shaka Chu, Clara Morris, and Jack Park for their company, no matter how brief their presence may have been.

I would like to thank the Sydney University Judo Club for being a wonderful source of fitness and entertainment — there are many days where getting thrown and grappled is more enjoyable and far less painful than debugging code.

My parents have been a source of support throughout all of my studies, which I am grateful for. To Ebony, I appreciate you staying in Sydney to be with me the past few years, and I apologise for not finishing three years earlier.

Contents

Abstract *v*
Acknowledgements *vii*
Contents *ix*
List of Figures *xiii*
List of Tables *xxi*
Nomenclature *xxiii*

1 Introduction **1**

1.1 Background and motivation 1
1.2 Objectives and approach 7
1.3 Thesis structure 8
1.4 Publications 9

2 Literature Review **11**

2.1 Fundamental instabilities 11
2.1.1 Linear Regime 12
2.1.2 Non-linear regime 16
2.1.3 Transition to turbulence 19
2.2 Spherical geometry 22
2.3 Turbulent mixing 25
2.3.1 Direct numerical simulation 25
2.3.2 Large eddy simulation 28
2.3.3 Reynolds-averaged Navier–Stokes 31
2.3.4 Buoyancy-drag model 34
2.4 Compression and strain 37
2.4.1 Compressed inhomogeneous turbulence 39

3 Governing Equations & Numerical Methods **43**

3.1 Governing Equations . . . 43
3.1.1 Four-equation model . . . 43
3.1.2 Five-equation model . . . 46
3.1.3 K-L model . . . 47
3.1.4 Equation of state . . . 50
3.2 Numerical Methods . . . 52
3.2.1 Godunov's method . . . 52
3.2.2 High resolution schemes . . . 56
3.2.3 Moving mesh . . . 59
3.2.4 Time integration . . . 61
3.2.5 Low Mach correction . . . 62
3.2.6 Strain rates . . . 62

4 Influence of Axial Strain 69

4.1 Introduction . . . 69
4.2 Problem formulation . . . 70
4.2.1 Axial strain rate . . . 70
4.2.2 Governing equations . . . 71
4.2.3 Numerical methods . . . 71
4.3 Two-dimensional single mode . . . 71
4.3.1 Potential Flow . . . 71
4.3.2 Initial conditions . . . 74
4.3.3 Results . . . 76
4.4 Self-similar mixing layer . . . 79
4.4.1 Models . . . 80
4.4.2 Initial conditions . . . 82
4.4.3 Convergence . . . 86
4.4.4 Results . . . 86
4.5 Conclusion . . . 106

5 Influence of Transverse Strain 109

5.1 Introduction . . . 109
5.2 Problem formulation . . . 111
5.2.1 Transverse strain rate . . . 111

5.2.2 Governing equations . . . 113
5.2.3 Numerical methods . . . 113
5.3 Two-dimensional linear regime . . . 114
5.3.1 Linear potential flow . . . 114
5.3.2 Initial conditions . . . 118
5.3.3 Results . . . 118
5.4 Self-similar mixing layer . . . 121
5.4.1 Initial conditions . . . 122
5.4.2 Convergence . . . 124
5.4.3 Results . . . 126
5.5 Conclusion . . . 151

6 Turbulence modelling of anisotropic strain **155**

6.1 Introduction . . . 155
6.2 Computational Approach . . . 156
6.2.1 Strain rates . . . 156
6.2.2 Governing Equations . . . 157
6.2.3 Numerical Implementation . . . 157
6.2.4 Problem Description . . . 157
6.2.5 Bulk compression closure . . . 161
6.3 Results and Discussion . . . 163
6.3.1 Integral Width . . . 163
6.3.2 Turbulent kinetic energy . . . 166
6.3.3 Turbulent mass flux velocity . . . 170
6.3.4 Reynolds Stress . . . 171
6.3.5 Self-similar analysis of the K-L model . . . 173
6.3.6 Equivalence of two-equation models . . . 178
6.4 Conclusion . . . 183

7 Conclusions and Further Research **185**

7.1 Summary of current research . . . 185
7.2 Recommendations for future research . . . 189

References **193**

A K-L model verification and validation **217**

A.1 Verification 217
A.1.1 Advection 218
A.1.2 Diffusion 218
A.1.3 Reynolds stress 222
A.1.4 Source terms 225
A.2 Instability validation 226
A.2.1 Rayleigh–Taylor 227
A.2.2 Richtmyer–Meshkov 227
A.2.3 Kelvin–Helmholtz 227

B Strain rate verification **231**

B.1 One-dimensional strain 232
B.2 Two-dimensional strain 232
B.3 Three-dimensional strain 232

List of Figures

1.1 Planar laser-induced fluorescence photographs of a turbulent jet for increasing Reynolds number, coloured by scalar concentration of the jet fluid. (*a*) $Re = 1500$, (*b*) $Re = 5000$, (*c*) $Re = 20\,000$. Source: Figure 1 of Dahm & Dimotakis (1990). . 2

1.2 Clouds formations showing natural occurrences of hydrodynamic instabilities. (*a*) Kelvin–Helmholtz instability. Source: Rejmanek (2017) ; (*b*) Cirrus clouds with the Rayleigh-Taylor instability visible at the bottom of the clouds. Source: Prof. David Jewitt, University of California at Los Angeles. 3

1.3 Indirect and direct drive inertial confinement fusion. The ablator absorbs the radiation and drives the implosion of the inner material, generating a hotspot at the centre which is susceptible to instabilities arising at the perturbations between layers. Source: Figure 1 of Betti & Hurricane (2016). 4

1.4 Supernova remnants. (*a*) SN1006, suspected type Ia supernova (NASA *et al.*, 2013); (*b*) Crab Nebula, type II supernova (NASA *et al.*, 2024). 5

1.5 Experiment 110 of the tilted-rig at times: (*a*) $t_{\text{exp}} = 45.2\,\text{ms}$; (*b*) $t_{\text{exp}} = 59.8\,\text{ms}$; (*c*) $t_{\text{exp}} = 71.1\,\text{ms}$. Source: Figure 7 of Andrews *et al.* (2014). 6

2.1 Vorticity generation due to the baroclinic term for the Rayleigh-Taylor instability. (*a*) Unstable RTI with $\rho_2 > \rho_1$, where vorticity production will increase the perturbation amplitude; (*b*) Stable RTI with $\rho_2 < \rho_1$, where vorticity production will reduce and invert the perturbation amplitude. The initial interface is depicted with solid lines, and the evolved interface at the time Δt is depicted with dashed lines. 12

2.2 Evolution of Richtmyer–Meshkov instability in a heavy-to-light configuration ($\rho_2 > \rho_1$) in the interface frame-of-reference. (*a*) Initial interface set-up; (*b*) Compression and vorticity generation as shock transits the interface; (*c*) Amplitude growth following amplitude inversion. 13

2.3 Slice at $z = 0$ for the multimode, narrowband, quarter-scale θ-group RMI case (Thornber *et al.*, 2017) at $t = 0.03\,\text{s}$. Heavy fluid ($f_1 = 1$) is red, light fluid ($f_1 = 0$) is blue. 16

2.4 Slice at $z = 0$ for the multimode, narrowband, quarter-scale θ-group RMI case (Thornber *et al.*, 2017) at $t = 0.01$ s. Heavy fluid ($f_1 = 1$) is red, light fluid ($f_1 = 0$) is blue. 17

2.5 Slice at $z = 0$ for the multimode, narrowband, quarter-scale θ-group RMI case (Thornber *et al.*, 2017) at $t = 0.42$ s. Heavy fluid ($f_1 = 1$) is red, light fluid ($f_1 = 0$) is blue. 20

2.6 Energy spectrum as a function of wave number and the range of scales that are calculated and modelled through different numerical approaches. 26

2.7 Modification of a cubic cell from the given strain profile. 38

2.8 Self similar profiles as a function of relative radius, $\zeta = r/R(t)$, for the Taylor-von Neumann-Sedov blast wave. (*a*) Velocity, density, and pressure normalised to values immediately behind the shock front; (*b*) Strain rate anisotropy. 40

2.9 Characteristics of idealised implosion simulation (El Rafei & Thornber, 2024). (*a*) Implosion profile, (*b*) mean radial velocity profile at several time-steps, (*c*) strain rate anisotropy across the mixing layer. 41

3.1 Characteristic wave-speeds for the Riemann problem with the Euler equations. . . . 53

3.2 Discretisation of a continuous and discontinuous solution into cell averages. 54

3.3 One-dimensional Riemann problem at the boundaries of cell i, with labelled HLLC wave-speeds and intermediate states for the left interface. 56

3.4 Linear advection of a passive scalar with a sharp discontinuity in one-dimension. . 57

3.5 Linear reconstruction of the piece-wise constant flow field using a slope limiter. . . 58

3.6 Change in time-step size as a function of the expansion factor (Λ), the specific heat ratio (γ), and the number of dimensions under strain (n). 65

4.1 Change of domain size and amplitude for systems compressed with axial strain by a factor of two in the x-direction. (*a*) Two-dimensional system with a single mode perturbation; (*b*) Three-dimensional system with a multimode perturbation, bound by the $f_1 = 0.01$ iso-surface. 70

4.2 Visualisation of the volume fraction at $\tau = 0.1$ for the 2D single-mode simulations. Heavy fluid ($f_1 = 1$) is red, light fluid ($f_1 = 0$) is blue. Major ticks indicate a distance of $\lambda/4$; (*a*) Constant boundary velocity, $\hat{S}_0 = -7.5$, (*b*) Unstrained case, (*c*) Constant boundary velocity, $\hat{S}_0 = 30$, (*d*) Constant strain rate, $\hat{S} = -14$; (*e*) Constant strain rate, $\hat{S} = 14$. 77

4.3 Amplitude of the single-mode linear regime for (a) constant boundary velocity and (b) constant strain rate. Solid lines indicate numerical results, dashed lines indicate linear model. 78
4.4 Error in the amplitude for the linear regime under (a) constant velocity and (b) constant strain rate. 79
4.5 Amplitude of the single-mode linear regime for (a) constant velocity and (b) constant strain rate. Solid lines indicate numerical results, dashed lines indicate linear model. 79
4.6 (a) Isosurface for volume fraction $f_1 = 0.5$ for the initial interface (b) Isosurfaces for $f_1 = 0.01$ (blue) and 0.99 (red) for the mixing layer at $\tau = 1$. 84
4.7 Effect of axial interpolation for (a) integral width, and (b) molecular mixing fraction. Solid lines indicate original mesh, dashed lines indicate refined mesh with interpolated solution. 86
4.8 Contours of the volume fraction for the constant velocity ILES cases at $z = 0$. Heavy fluid ($f_1 = 1$) is red, light fluid ($f_1 = 0$) is blue. Major ticks on the axes correspond to $\Delta x = \Delta y = 1$m; (*a,b,d,f,h*) $\tau = 9.843$, (*c,e,g*) $\tau = 34.451$. (*a*) $\hat{S}_0 = -0.051$; (*b,c*) $\hat{S}_0 = -0.013$; (*d,e*) $\hat{S}_0 = 0$, (*f,g*) $\hat{S}_0 = 0.025$, (*h*) $\hat{S}_0 = 0.102$ 88
4.9 Contour of volume fraction f_1 for the expansion mixing layers at $\Lambda \approx 1.866$, bounded by $f_1 = 0.999$ (red) and $f_1 = 0.001$ (blue). (*a*) $\hat{S}_0 = 0.102$, $\tau = 9.55$, (*b*) $\hat{S} = 0.081$, $\tau = 8.66$, (*c*) $\hat{S}_0 = 0.025$, $\tau = 35.0$, (*d*) $\hat{S}_0 = 0.020$, $\tau = 31.7$. 89
4.10 Contour of volume fraction f_1 for the expansion mixing layers at $\Lambda \approx 0.567$, bounded by $f_1 = 0.999$ (red) and $f_1 = 0.001$ (blue). (*a*) $\hat{S}_0 = -0.051$, $\tau = 9.55$, (*b*) $\hat{S} = -0.081$, $\tau = 7.97$, (*c*) $\hat{S}_0 = -0.013$, $\tau = 35.0$, (*d*) $\hat{S}_0 = -0.020$, $\tau = 28.9$. 90
4.11 Integral width for (a) constant velocity, and (b) constant strain rate. Solid lines indicate ILES, dashed lines indicate buoyancy-drag. 90
4.12 Alternate non-dimensionalisation for integral width for (a) constant velocity, and (b) constant strain rate. Solid lines indicate ILES, dashed lines indicate buoyancy-drag. 91
4.13 Bubble heights for (a) constant velocity, and (b) constant strain rate. Solid lines indicate ILES, dashed lines indicate buoyancy-drag. 91
4.14 Spike heights for (a) constant velocity, and (b) constant strain rate. Solid lines indicate ILES, dashed lines indicate buoyancy-drag. 92
4.15 Ratio of spike-to-bubble height for (a) constant velocity, and (b) constant strain rate. 92
4.16 Integral mixing measures for the (a) constant velocity, and (b) constant strain rate. Solid lines indicate ILES results, dashed line is FLAMENCO's final value from Thornber *et al.* (2017). 93

4.17 Planar averaged volume-fraction profiles for the constant velocity cases. (*a,b*) $\tau = 9.843$, (*c,d*) $\tau = 34.451$. 94

4.18 Planar averaged volume-fraction profiles for the constant strain rate cases. (*a,b*) $\tau = 9.843$, (*c,d*) $\tau = 34.451$. 95

4.19 Total turbulent kinetic energy for (a) constant velocity, and (b) constant strain rate. . 96

4.20 Turbulent kinetic energy in the x-direction for (a) constant velocity, and (b) constant strain rate. 96

4.21 Turbulent kinetic energy in the y-direction for (a) constant velocity, and (b) constant strain rate. 97

4.22 Anisotropy of the turbulent kinetic energy for (a) constant velocity, and (b) constant strain rate. 98

4.23 Total enstrophy for (a) constant velocity and (b) constant strain rate. 99

4.24 Enstrophy in the $y - z$ plane for (a) constant velocity and (b) constant strain rate. . 100

4.25 Enstrophy in the $x - z$ plane for (a) constant velocity and (b) constant strain rate. Solid lines indicate ILES results, dashed lines indicate enstrophy model. 100

4.26 Axial turbulent mass flux for (*a,c*) constant velocity cases, and (*b,d*) constant strain rate cases. (*a,b*) $\tau = 9.843$, (*c,d*) $\tau = 34.451$. 102

4.27 Corrected buoyancy-drag model for the integral width. (a) Constant velocity, and (b) constant strain rate. Solid lines indicate ILES results, dashed lines indicate buoyancy-drag model. 104

4.28 Corrected buoyancy-drag model for bubbles. (a) Constant velocity, and (b) constant strain rate. Solid lines indicate ILES results, dashed lines indicate buoyancy-drag model. 104

4.29 Corrected buoyancy-drag model for spikes. (a) Constant velocity, and (b) constant strain rate. Solid lines indicate ILES results, dashed lines indicate buoyancy-drag model. 105

5.1 Change of domain size and wavelength for systems compressed with transverse strain by a factor of two. (a) Two-dimensional system with a single mode perturbation and compressed in y; (b) Three-dimensional system with a multimode perturbation, compressed in y- and z-directions, and bound by the $f_1 = 0.01$ iso-surface. 112

5.2 Interface at $\tau = 0.1$ for the 2-D single-mode simulations. Heavy fluid ($f_1 = 1$) is red, light fluid ($f_1 = 0$) is blue. Major ticks indicate a distance of $\lambda(t)/4$, with the final wavelength marked below the plot. (*a*) Constant velocity, $\hat{S}_0 = -7.5$; (*b*) Unstrained case; (*c*) Constant velocity, $\hat{S}_0 = 30$; (*d*) Constant strain rate, $\hat{S} = -14$; (*e*) Constant strain rate, $\hat{S} = 14$. 120

5.3 Amplitude growth as a function of the transverse expansion for the specified non-dimensionalised constant strain rates. Solid lines indicate numerical results, black dashed lines indicate linearised potential theory. 121

5.4 Amplitude of the single mode linear regime, non-dimensionalised for the initial wavelength for (*a*) constant velocity and (*b*) constant strain rate. Solid lines indicate numerical results, dashed lines indicate the linearised potential model. 122

5.5 Amplitude of the single mode linear regime, non-dimensionalised by the time-varying wavelength for (*a*) constant velocity and (*b*) constant strain rate. Solid lines indicate numerical results, dashed lines indicate the linearised potential model. . . 122

5.6 Error in the amplitude for the linear regime under (*a*) constant velocity and (*b*) constant strain rate. 123

5.7 Convergence of constant strain rate simulations under transverse compression for (a) integral width and (b) molecular mixing fraction. Solid lines indicate results for 512 cells across, dashed lines for 768 cells, dotted lines for 1024 cells. 126

5.8 Contours of the volume fraction for the constant velocity ILES cases at the centre x-y plane ($z = \mathcal{L}(t)/2$): (*a,b,d,f,h*) $\tau = 9.843$; (*c,e,g*) $\tau = 34.451$; (*a*) $\hat{S}_0 = -0.051$; (*b,c*) $\hat{S}_0 = -0.013$; (*d,e*) $\hat{S}_0 = 0$; (*f,g*) $\hat{S}_0 = 0.025$; (*h*) $\hat{S}_0 = 0.102$. Heavy fluid ($f_1 = 1$) is red, light fluid ($f_1 = 0$) is blue. Major ticks on the axes correspond to $\mathcal{L}(t)/8$; 127

5.9 Contour of volume fraction f_1 for the expansion mixing layers at $\Lambda \approx 1.82$, bounded by $f_1 = 0.99$ (red) and $f_1 = 0.01$ (blue). (*a*) $\hat{S}_0 = 0.102$, $\tau = 9.05$, (*b*) $\hat{S} = 0.081$, $\tau = 8.37$, (*c*) $\hat{S}_0 = 0.025$, $\tau = 33.5$, (*d*) $\hat{S}_0 = 0.020$, $\tau = 30.5$ 128

5.10 Contour of volume fraction f_1 for the expansion mixing layers at $\Lambda \approx 0.57$, bounded by $f_1 = 0.99$ (red) and $f_1 = 0.01$ (blue). (*a*) $\hat{S}_0 = -0.051$, $\tau = 9.45$, (*b*) $\hat{S} = -0.081$, $\tau = 7.88$, (*c*) $\hat{S}_0 = -0.013$, $\tau = 34.9$, (*d*) $\hat{S}_0 = -0.020$, $\tau = 28.5$ . . 128

5.11 Integral width for (*a*) constant velocity, and (*b*) constant strain rate. 129

5.12 Mixed mass for (*a*) constant velocity and (*b*) constant strain rate. 130

5.13 Bubble and spike heights for (*a*) constant velocity and (*b*) constant strain rate. Solid lines indicate bubble height, dashed lines indicate spike height. 131

5.14 Ratio of spike-to-bubble height for (*a*) constant velocity and (*b*) constant strain rate. 132

5.15 Mixing measures for the (*a*) constant velocity and (*b*) constant strain rate. Solid lines indicate Θ, dashed lines indicate Ψ, dotted line is FLAMENCO's final Θ value at $\tau = 246$ (Thornber *et al.*, 2017). 133

5.16 Planar-averaged volume-fraction profiles for the constant velocity cases: (*a,b*) $\tau = 9.843$; (*c,d*) $\tau = 34.451$ 134

5.17 Planar-averaged volume-fraction profiles for the constant strain rate cases: (*a,b*) $\tau = 9.843$; (*c,d*) $\tau = 34.451$ 135

5.18 Total turbulent kinetic energy for (*a*) constant velocity and (*b*) constant strain rate. Solid lines indicate ILES, gray dashed lines indicate the turbulent kinetic energy model, and black dotted lines indicate the corrected turbulent kinetic energy model. 137

5.19 Turbulent kinetic energy in the y-direction for (*a*) constant velocity and (*b*) constant strain rate. Solid lines indicate ILES, gray dashed lines indicate the turbulent kinetic energy model, and black dotted lines indicate the corrected turbulent kinetic energy model. 138

5.20 Turbulent kinetic energy in the x-direction for (*a*) constant velocity and (*b*) constant strain rate. Solid lines indicate ILES, and black dotted lines indicate the corrected turbulent kinetic energy model. 139

5.21 Anisotropy of the turbulent kinetic energy for (*a*) constant velocity and (*b*) constant strain rate. Solid lines indicate ILES, black dotted lines indicate the corrected turbulent kinetic energy model, and grey dot-dash lines indicate the turbulent kinetic energy model with the original LRR-IP coefficients. 140

5.22 Spectrum for the transverse fluctuating turbulent kinetic energy component at the mixing layer centre for (a,c) constant velocity, and (b,d) constant strain-rate. (*a,b*) $\tau = 9.84$, (*c,d*) $\tau = 34.45$. 143

5.23 Turbulent mass flux for (*a*) constant velocity, and (*b*) constant strain rate. Solid lines indicate results at $\tau = 9.843$, dashed lines indicate results at $\tau = 34.451$. 144

5.24 Enstrophy in the $y - z$ plane for (*a*) constant velocity and (*b*) constant strain rate. Solid lines indicate ILES, dashed lines indicate the enstrophy model. 147

5.25 Enstrophy in the $x - z$ plane for (*a*) constant velocity and (*b*) constant strain rate. Solid lines indicate ILES, dashed lines indicate the enstrophy model. 147

5.26 Effective drag length scale as a function of non-dimensionalised integral width for (*a*) constant velocity and (*b*) constant strain rate. Solid lines indicate integral width non-dimensionalised by $\bar{\lambda}_0$, dotted lines indicate integral width non-dimensionalised by $\bar{\lambda}(t)$, and dashed lines indicate planar narrowband effective length scale model. . 150

5.27 Buoyancy-drag model for integral width: (*a*) constant velocity and (*b*) constant strain rate. Solid lines indicate ILES results, dashed lines indicate the buoyancy-drag model. 151

5.28 Buoyancy-drag model for bubble height: (*a*) constant velocity and (*b*) constant strain rate. Solid lines indicate ILES results, dashed lines indicate the buoyancy-drag model. 152

5.29 Buoyancy-drag model for spike height. (*a*) constant velocity and (*b*) constant strain rate. Solid lines indicate ILES results, dashed lines indicate the buoyancy-drag model. 152

6.1 Contours of the mass fraction of species 1 at $\tau = 34.5$ along the centre-plane from the ILES constant strain rate cases. Major ticks indicate a distance of 1 m. 159

6.2 Integral width for simulations under the applied axial strain rate with (left) constant velocity profile and (right) constant strain rate profile. Solid lines indicate ILES, dashed lines indicate K-L model with (top) axial closure, (middle) isotropic closure, and (bottom) transverse closure for bulk compression. 165

6.3 Integral width for simulations under the applied transverse strain rate with (left) constant velocity profile and (right) constant strain rate profile. Solid lines indicate ILES, dashed lines indicate K-L model with (top) axial closure, (middle) isotropic closure, and (bottom) transverse closure for bulk compression. 167

6.4 Turbulent kinetic energy for simulations under the applied axial strain rate with (left) constant velocity profile and (right) constant strain rate profile. Solid lines indicate ILES, dashed lines indicate K-L model with (top) axial closure, (middle) isotropic closure, and (bottom) transverse closure for bulk compression. 168

6.5 Turbulent kinetic energy for simulations under the applied transverse strain rate with (left) constant velocity profile and (right) constant strain rate profile. Solid lines indicate ILES, dashed lines indicate K-L model with (top) axial closure, (middle) isotropic closure, and (bottom) transverse closure for bulk compression. 169

6.6 Mean turbulent kinetic energy profile at $\tau = 34.45$ for constant strain rate cases under (*a*) axial strain, and (*b*) transverse strain. Cases are displayed with a vertical offset of $\Delta\tilde{K} = 0.50$. Solid coloured lines represent ILES, solid black lines represent transverse closure, dotted black lines represent isotropic closure, and dashed black lines represent axial closure. 170

6.7 Turbulent mass flux velocity profile at $\tau = 34.45$ for cases under (a) axial strain, and (b) transverse strain. Cases are displayed with a vertical offset of $\Delta a_1 = 0.20$. Solid coloured lines represent ILES, solid black lines represent transverse closure, dotted black lines represent isotropic closure, and dashed black lines represent axial closure. 171

6.8 Reynolds stress components at $\tau = 34.45$ for cases with constant axial strain rates. (a) $\widetilde{u_1'' u_1''}$, and (b) $\widetilde{u_2'' u_2''}$. Cases are displayed with a vertical offset of $\Delta\widetilde{u'' u''} = 0.50$. Solid coloured lines represent ILES, solid black lines represent transverse closure, dotted black lines represent isotropic closure, and dashed black lines represent axial closure. 172

6.9 Reynolds stress components at $\tau = 34.45$ for cases with constant transverse strain rates. (a) $\widetilde{u_1'' u_1''}$, and (b) $\widetilde{u_2'' u_2''}$. Cases are displayed with a vertical offset of $\Delta\widetilde{u'' u''} = 0.50$. Solid coloured lines represent ILES, solid black lines represent transverse closure, dotted black lines represent isotropic closure, and dashed black lines represent axial closure. 173

6.10 β_W for simulations under the applied axial strain rate with (left) constant velocity profile and (right) constant strain rate profile for the K-L model with (top) axial closure, (middle) isotropic closure, and (bottom) transverse closure for bulk compression. . 175

6.11 β_W for simulations under the applied transverse strain rate with (left) constant velocity profile and (right) constant strain rate profile for the K-L model with (top) axial closure, (middle) isotropic closure, and (bottom) transverse closure for bulk compression. 176

6.12 Buoyancy-drag model for simulations under the applied axial strain rate with (left) constant velocity profile and (right) constant strain rate. Sold line indicates ILES, dashed line indicates buoyancy-drag model from Eq. 6.26. 179

6.13 Buoyancy-drag model for simulations under the applied transverse strain rate with (left) constant velocity profile and (right) constant strain rate. Solid line indicates ILES, dashed line indicates buoyancy-drag model from Eq. 6.26. 179

A.1 Results for the linear advection of $\tilde{K}$ and L at the final time. (a) $\tilde{K}$ profile; (b) L profile; (c) Convergence of $\tilde{K}$ and L; (d) Pressure error. 219

A.2 Results for the diffusion of $\tilde{K}$ and L at the final time. (a) $\tilde{K}$ profile; (b) L profile; (c) Convergence of $\tilde{K}$ and L; (d) Pressure error. 221

A.3 Species and enthalpy diffusion for equal γ; (a) density profile; (b) density and temperature error. 221

A.4 Species and enthalpy diffusion for differing γ; (a) density profile; (b) density and temperature error. 222
A.5 Convergence of the test case with uniform total pressure: (a) evolution of the integral width and the maximum turbulent kinetic energy; (b) profiles of the volume fraction and turbulent kinetic energy at the final time. 224
A.6 Comparison of evolution of $\tilde{K}$ for the shear stress test. 225
A.7 Isotropic decay test case, showing the decay of the turbulent kinetic energy and growth of the turbulent length scale. 226
A.8 Bulk compression of L test case, showing the reduction of L with bulk compression according to the constant velocity (CV) and constant strain rate (CS) profiles. . . . 227
A.9 One-dimensional Rayleigh-Taylor simulation: (a) evolution of the integral width and the maximum turbulent kinetic energy; (b) Profiles of the volume fraction and turbulent kinetic energy at the final time. 228
A.10 Cut-off width of one-dimensional RMI case 228
A.11 Quasi-one- dimensional Kelvin–Helmholtz; (a) evolution of the mixing width and maximum integral length scale L_{max}; (b) evolution of the maximum value of turbulent kinetic energy $\tilde{K}_{\text{max}}$. 229

B.1 Errors at the final time of $t = 0.1$s for applied strain in one direction; (a) absolute mass error; (b) absolute volume error; (c) pressure NRMSD; (d) velocity NRMSD. 233
B.2 Errors at the final time of $t = 0.1$s for applied strain in two directions; (a) absolute mass error; (b) absolute volume error; (c) pressure NRMSD; (d) velocity NRMSD. 234
B.3 Errors at the final time of $t = 0.1$s for applied strain in three directions; (a) absolute mass error; (b) absolute volume error; (c) pressure NRMSD; (d) velocity NRMSD. 235

List of Tables

4.1 Fluid properties for the linear regime cases. 75
4.2 The strain rates, total simulation time, initial domain size, grid resolution, and final expansion factor for each of the linear regime cases. 76
4.3 Buoyancy-drag coefficients for $At = 0.5$, narrowband RMI (Youngs & Thornber, 2020*a*,*b*) 81

4.4 The strain cases, total simulation time, domain size, grid resolution, and final expansion factor for each of the ILES cases. 85
4.5 Optimised coefficients for the buoyancy-drag model. 103

5.1 Fluid properties for the linear regime cases. 119
5.2 The strain rates, total simulation time, domain size, grid resolution, and final expansion factor for each of the linear regime cases. 119
5.3 The strain cases, total simulation time, domain size, grid resolution, and final expansion factor for each of the ILES cases. 125
5.4 Test cases employed for the convergence study. Check-marks indicate the mesh used for results in the chapter, circles indicate meshes used for convergence study. 125
5.5 Power law scaling for the transverse turbulent kinetic energy spectra at $\tau = 34.45$. 143
5.6 Buoyancy-drag coefficients for $At = 0.5$, narrowband RMI (Youngs & Thornber, 2020*a*,*b*) 149

6.1 Properties of the implicit large eddy simulation cases. Simulations cases exist for *D*=A for the axial strain cases, and *D*=T for the transverse cases. 158
6.2 Coefficients for the K-L turbulence model. Previous coefficients come from Xiao *et al.* (2020*a*); Zhang *et al.* (2020) 161
6.3 The $\hat{C}_C$ coefficients for the different bulk compression closures under different applied strain rates, representing the equivalent C_C coefficient/scaling of the velocity divergence for the specified applied strain rates. 162
6.4 Values of L used for simulation initialisation 163
6.5 Mean absolute percentage error (MAPE) at the final simulation time for the low-magnitude strain cases. Closure model with lowest MAPE for each strain application are highlighted in bold text. 165

B.1 Strain rates applied for the specified simulation test cases. 231

Nomenclature

Acronyms

ALE	Arbitrary Lagrangian–Eulerian
CFL	Courant–Friedrichs–Lewy
DNS	Direct Numerical Simulation
DT	Deuterium-Tritium
ICF	Inertial Confinement Fusion
ILES	Implicit Large Eddy Simulation
KHI	Kelvin–Helmholtz Instability
LES	Large Eddy Simulation
MUSCL	Monotone Upstream-centred Scheme for Conservation Laws
RANS	Reynolds-Averaged Navier–Stokes
RMI	Richtmyer–Meshkov Instability
RTI	Rayleigh–Taylor Instability
TKE	Turbulent Kinetic Energy
TVD	Total Variation Diminishing

Constants

$\mathcal{R}$	Universal gas constant	$8.1314\,\mathrm{kg\,m^{-3}}$
k_B	Boltzmann constant	$1.381 \times 10^{-23}\,\mathrm{J\,K^{-1}}$

Symbols

$\bar{\mathcal{R}}$	Specific gas constant	$(\mathrm{J\,kg\,K^{-1}})$
γ	Ratio of specific heats	
$\hat{S}$	Non-dimensionalised strain rate	
κ	Wavenumber	$(\mathrm{m^{-1}})$
λ	Perturbation wavelength	(m)
$\mathcal{L}$	Domain length	(m)
$\mathcal{M}$	Mixed mass	(kg)
μ	Dynamic viscosity	$(\mathrm{kg\,m^{-1}\,s^{-1}})$
ν	Kinematic viscosity	$(\mathrm{m^2\,s^{-1}})$

Ψ	Non-dimensionalised mixed mass	
ρ	Density	($\mathrm{kg\,m^{-3}}$)
τ	Non-dimensional time	
Θ	Molecular mixing fraction	
θ	Power-law growth rate parameter	
$\tilde{L}$	Turbulent kinetic energy	($\mathrm{m^2\,s^{-2}}$)
a	Perturbation amplitude	(m)
At	Atwood number	
c_p	Specific heat capacity at constant pressure	($\mathrm{J\,kg^{-1}\,K^{-1}}$)
c_v	Specific heat capacity at constant volume	($\mathrm{J\,kg^{-1}\,K^{-1}}$)
E	Total energy	($\mathrm{J\,kg^{-1}}$)
e	Internal energy	($\mathrm{J\,kg^{-1}}$)
f_a	Volume fraction of species a	
L	Turbulent length scale	(m)
Le	Lewis number	
m_a	Molecular mass of species a hfill($\mathrm{g\,mol^{-1}}$)	
p	Pressure	(Pa)
Pr	Prandtl number	
Re	Reynolds number	
S	Strain rate	($\mathrm{s^{-1}}$)
Sc	Schmidt number	
t	Time	(s)
u	x component of velocity	($\mathrm{m\,s^{-1}}$)
u_r	Radial velocity	($\mathrm{m\,s^{-1}}$)
u_ϕ	Azimuthal velocity	($\mathrm{m\,s^{-1}}$)
u_θ	Polar velocity	($\mathrm{m\,s^{-1}}$)
v	y component of velocity	($\mathrm{m\,s^{-1}}$)
W	Integral width	(m)
X_a	Mole fraction of species a	
Y_a	Mass fraction of species a	

Modifiers

$\bar{\phi}$	Reynolds-average of quantity ϕ
Δ	Increment
$\dot{\phi}$	Time derivative of quantity ϕ

∂	Partial derivative	
ϕ'	Reynolds-averaged fluctuation of quantity ϕ	
ϕ''	Favre-averaged fluctuation of quantity ϕ	
D	Substantial derivative	
d	Total derivative	
$\tilde{\phi}$	Favre-average of quantity ϕ	
$\tilde{\mathrm{D}}$	Substantial derivative with Favre-averaged flow field	

Units

g	Grams	
J	Joules	
K	Kelvin	
kg	Kilograms	
m	Metres	
mol	Moles	
N	Newtons	
Pa	Pascals	
s	Seconds	

Vectors and Tensors

ω_i	Vorticity vector	(s^{-1})
τ_{ij}	Viscous stress tensor	(Pa)
a_i	Turbulent mass flux vector	($\mathrm{m\,s}^{-1}$)
u_i	Velocity vector	($\mathrm{m\,s}^{-1}$)
x_i	Position vector	(m)

CHAPTER 1

Introduction

1.1 Background and motivation

Fluid dynamics has shaped the world that we live in. It occurs across a diverse range of applications and a large range of orders of magnitude. On the length scale of up to millions of kilometres, plasma is advected throughout the Sun, helping to achieve fusion in the core to produce energy, which in turn provides the heat and visible light that life depends upon. The climate of the Earth is contingent upon atmospheric and ocean currents which moves rain clouds and regulates temperatures, with length scales up to thousands of kilometres. The movement of air in lungs and the blood in veins are also governed by fluid dynamics, transporting the necessary components to our cells to ensure survival, going down to a scale of micrometres. In of all these cases, fluid dynamics serves an important role of mixing the fluid, moving and introducing fluid from one area into another.

In most applications, mixing is driven by the non-linear advection of the fluid, as opposed to diffusive forces, which allows for greater efficiency of mixing. The ratio of the advection forces to the viscous diffusion forces is governed by the Reynolds number (Re). At low Reynolds numbers, where the viscous forces inhibit motion, the fluid flow is laminar and can be described as smooth, stable, and predictable. For sufficiently large Reynolds numbers the flow can become turbulent, causing the flow to become a three-dimensional, complex, and seemingly chaotic velocity field with large eddies generating smaller eddies, which in turn create smaller eddies and so on. The eddies allow the fluid to mix down to the smallest scales until the viscous forces oppose the motion, as determined by the Reynolds number. This can be observed in figure 1.1 – as the Reynolds number increases, the smallest scales of the eddies in the jet flow decreases, and greater homogeneity in the mixture is achieved by increased mixing efficiency. However, understanding turbulence is not an easy task, as noted by Richard Feynman: "*turbulence is the*

last, great unsolved problem of classical physics". The governing equations for fluid dynamics have no general solution, which drives the necessity for models and approximations to understand turbulence for the wide variety of flow conditions it applies to.

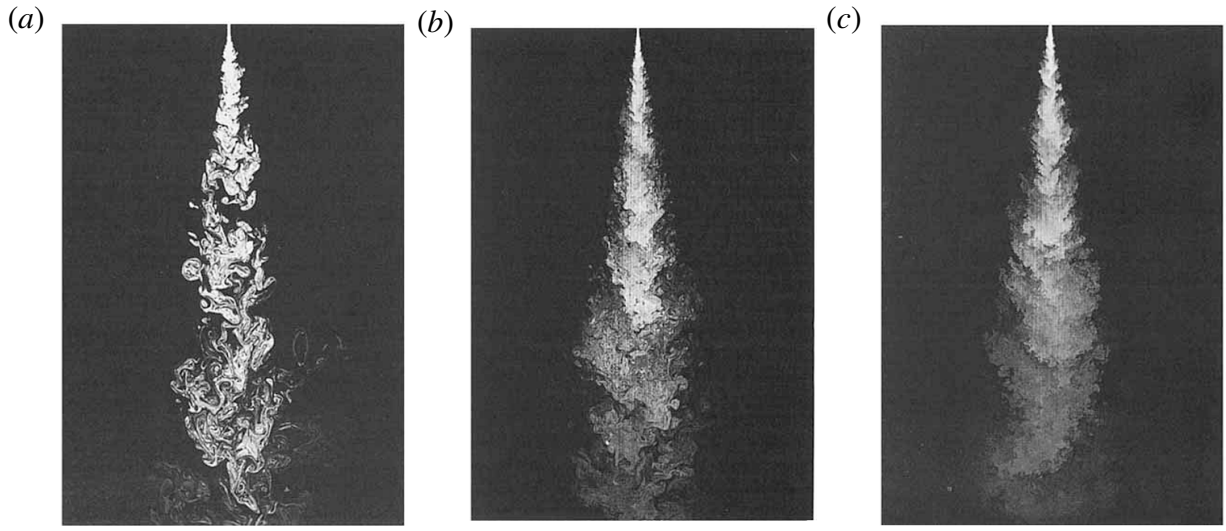

Figure 1.1: Planar laser-induced fluorescence photographs of a turbulent jet for increasing Reynolds number, coloured by scalar concentration of the jet fluid. (*a*) $Re = 1500$, (*b*) $Re = 5000$, (*c*) $Re = 20\,000$. Source: Figure 1 of Dahm & Dimotakis (1990).

The triggering of turbulence from an initially laminar state can occur from many mechanisms. There are three canonical hydrodynamic instabilities, which describe the transition from an initially smooth but perturbed interface between two fluids into a turbulent mixing layer. These instabilities are the Kelvin–Helmholtz (KHI), Rayleigh–Taylor (RTI), and Richtmyer–Meshkov (RMI) instability. The instabilities will be described in greater detail in Chapter 2, and a more in-depth description is provided by Zhou (2017*a*,*b*); Zhou *et al.* (2021). A brief description is provided here for completeness. KHI describes the case of an interface between two fluids with a shear velocity difference. RTI occurs for the continual acceleration of a heavier fluid into a lighter fluid, such as water on top of oil under the influence of gravity. RMI is the impulsive limit of RTI, with only a short acceleration, such as experienced from a shock wave. The analysis of these instabilities is crucial for understanding a variety of physical phenomena. A visual example of KHI and RTI naturally occurring is provided in figure 1.2.

One prominent source of research into hydrodynamic instabilities is centred on the development of inertial confinement fusion (ICF), a potential form of clean energy production. Nuclear fusion is achieved by compressing ionised atoms close enough together to allow the atoms to fuse into heavier elements, which can release large amounts of energy in the process. Where stars use their immense mass and gravity to compress the atoms together, inertial confinement fusion instead relies on the inertia of an ablative capsule of fuel for compression. These capsules

(*a*)

(*b*)

Figure 1.2: Clouds formations showing natural occurrences of hydrodynamic instabilities. (*a*) Kelvin–Helmholtz instability. Source: Rejmanek (2017) ; (*b*) Cirrus clouds with the Rayleigh-Taylor instability visible at the bottom of the clouds. Source: Prof. David Jewitt, University of California at Los Angeles.

are in the order of a millimetre in radius, consisting of several layers of material, with fusion fuel of deuterium-tritium (DT) in the centre layer and an ablative outer layer, commonly made of plastic or a high-density carbon. ICF can be driven in two methods as shown in figure 1.3, either directly through lasers impacting the surface of the capsule or indirectly where the lasers instead are reflected off a hohlraum to produce X-ray radiation (Nuckolls *et al.*, 1972; Betti & Hurricane, 2016). The radiation is designed to compress the fuel at the centre of the capsule to a high enough temperature and pressure to form a hotspot which will undergo fusion. Depending upon the implosion profile used, the inner radius of the outer shell can be reduced by a factor between 12 and 40 (Lindl *et al.*, 2014; Olson *et al.*, 2016), which corresponds to an increase in density of between 1728 and 64000. In the past it has been identified that hydrodynamic instabilities between the different layers within the capsule can cause mixing of cold outer fluid into the hot spot of the capsule, preventing or inhibiting the fusion of the fuel (Lindl *et al.*, 2014). For these hydrodynamic instabilities to form there must be perturbations in the interfaces or surface of the capsule, with causes such as imperfections in the machined surface on the inside of the capsule shell or asymmetries in the radiation impacting on the outer surface. As the radiation compresses the capsule, shock waves are created, which can help compress the fluid. However, these shock waves will also cause RMI to occur, amplifying the amplitudes of any perturbations in the interface. As the capsule continues to implode it will start to decelerate which makes it unstable to RTI, further exacerbating the hydrodynamic instabilities and increasing the mixing within the capsule. Whilst ICF has recently achieved ignition at the National Ignition Facility at the Lawrence Livermore National Laboratory (Collaboration, 2024), resulting in a fusion reaction that achieved a greater amount of energy production than the energy deposited into the capsule, there is still a long way go before ICF can be considered a viable energy source. This requires ICF to achieve much larger yields (as ICF has not yet achieved ignition relative

to the total energy used in the process) and also requires more rapid operation. Improving our understanding of these hydrodynamic instabilities, particularly in this highly compressive regime, is crucial for improving capsule design and operation.

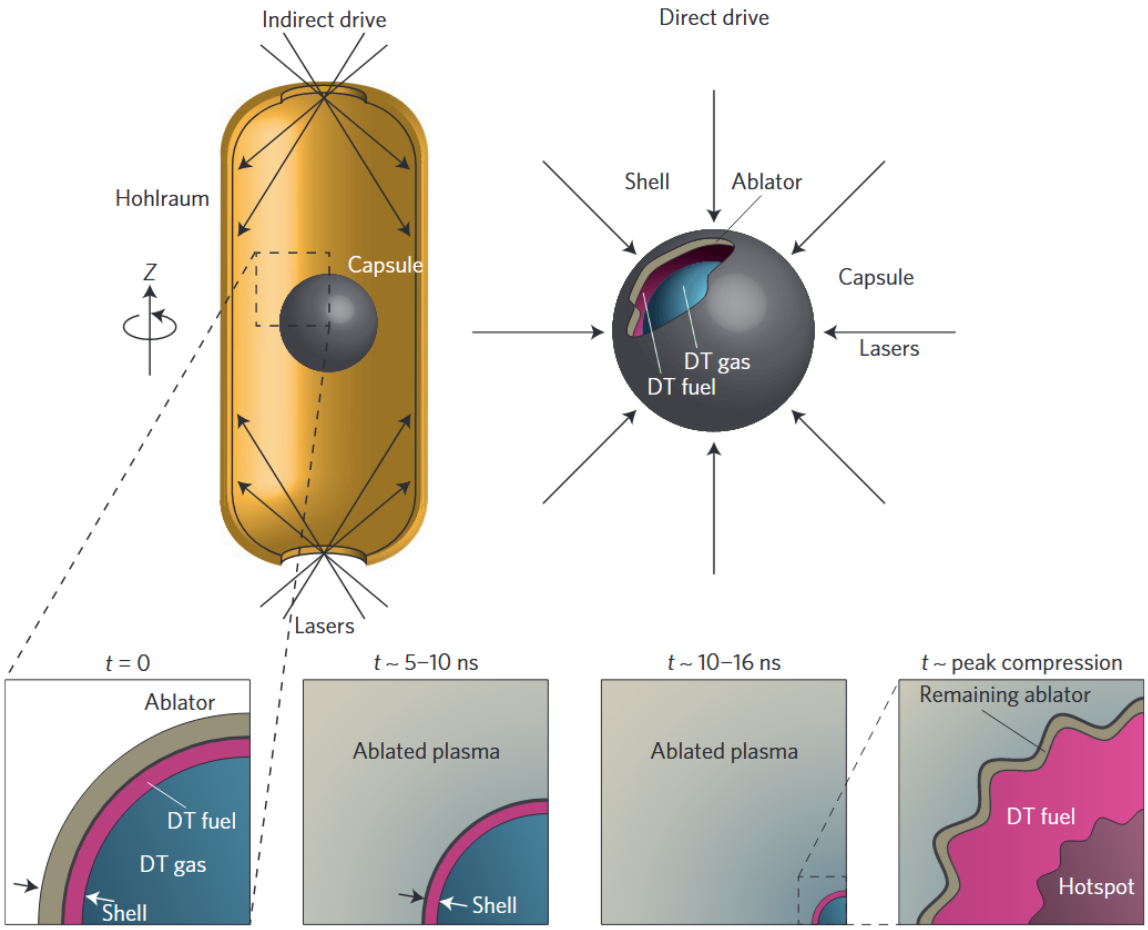

Figure 1.3: Indirect and direct drive inertial confinement fusion. The ablator absorbs the radiation and drives the implosion of the inner material, generating a hotspot at the centre which is susceptible to instabilities arising at the perturbations between layers. Source: Figure 1 of Betti & Hurricane (2016).

The internal behaviour of stars is governed by a variety of physics, such as magnetohydrodynamics and radiation transport, and with a huge range of scales to be considered. The role of hydrodynamic instabilities is crucial for understanding the behaviour of the stars which undergo supernova explosions at the end of their life. Stars can go supernova in two primary manners. The first approach, which corresponds to type Ia supernovae, begins with a binary star system with a white dwarf star stripping the atmosphere of the neighbouring star (Woosley & Weaver, 1986). Upon reaching a sufficient mass, the white dwarf will explode due to rapid nuclear fusion at the core, generating an RT unstable flame-front which may transition to a detonation wave which will additionally cause RMI (Drake, 1999). Core collapse supernovae, such as type II

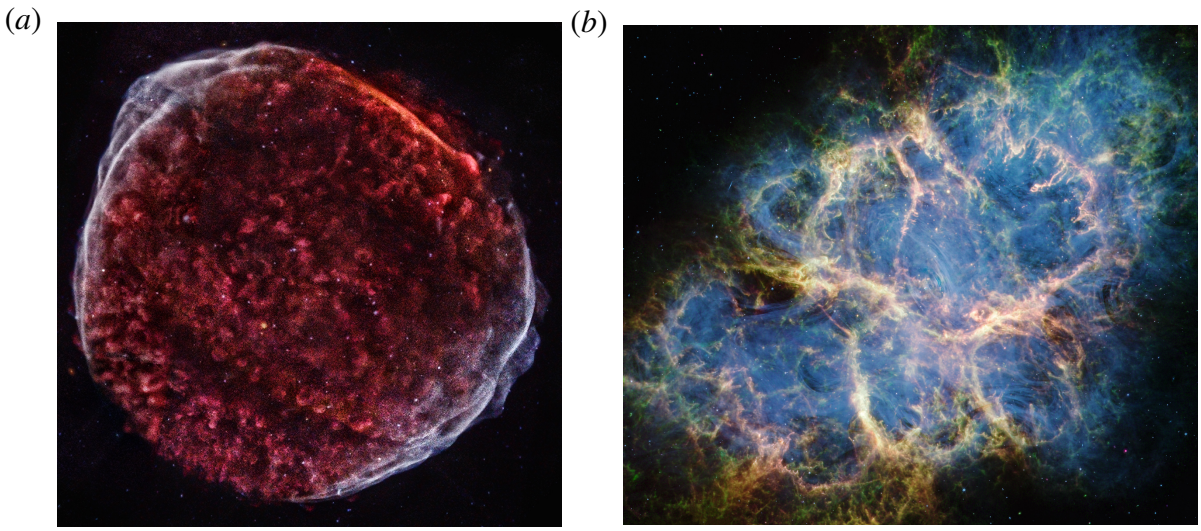

Figure 1.4: Supernova remnants. (*a*) SN1006, suspected type Ia supernova (NASA *et al.*, 2013); (*b*) Crab Nebula, type II supernova (NASA *et al.*, 2024).

supernova, instead occurs because the weight of the star is greater than the pressure generated from fusion reactions and the pressure from electron degeneracy. This occurs once the star has formed an iron core which will not fuse further and causes the star to collapse, with the core collapsing faster than the outer layers. The collapsed core rebounds and collides with the collapsing outer layers, resulting in the generation of a large blast-wave, causing ejection of the outer layers of the star (Woosley & Weaver, 1986). The blast-waves are able to instigate both RMI and RTI – examples of the remnant products for both supernova types are shown in figure 1.4, with asymmetric features due to the amplification of pre-existing asymmetries by the instabilities. Unmixed and stratified predictions for the spectral behaviour of supernova do not align with observations, demonstrating the hydrodynamic instabilities play a crucial role in mixing and shaping the configuration of stellar remnants (Arnett *et al.*, 1989; Arnett, 2000). The induced mixing from the hydrodynamic instabilities allows for the heavier metals that are concentrated closer towards the core to mix outward, achieving a higher level of dispersion from ejecta. Supernovae are the primary creation and distribution method for a variety of metals, without which life could not exist.

In both ICF and supernova, the instabilities occur in a spherical context. The fluids move with a radial velocity, such that the radial interface of the mixing varies as the instabilities evolves. As the fluid compresses or expands, and as the interface converges or diverges, additional mechanisms modify the development of the instabilities as compared to the planar configuration. One approach to quantifying the effects of compression and expansion is to describe the flow in terms of the strain rates. The strain rates, which are the rate at which the fluid is deformed, can measure how much the fluid flow expands or compresses in a given direction. This is because

the rate of change of density or volume is a function of the normal strain rates (and not shear strain rates, which deform the flow but do not cause compression or expansion). For spherically symmetric problems, flow can be categorised by two distinct strain rates: the radial strain rate and the circumferential strain rate. It is important to note that strain rates do not just occur in spherical geometry but can occur in any configuration. Additionally, the strain rates do not have to be isotropic. The most simple case is for the passage of a shock wave or expansion wave, for which there will be a single strain rate aligned with the direction of the wave traversal. Nozzle flows will experience strain rates as the flow compresses or expands, with the sign of the strain rate in the direction of mean flow depending upon the regime of the flow (subsonic or supersonic). Incompressible flows are inherently limited to zero divergence, requiring the sum of the strain rates to be zero. In the case of the tilted-rig experiment (Smeeton & Youngs, 1987; Youngs, 1989; Andrews *et al.*, 2014), as shown in figure 1.5 the interface tilts as the two fluid penetrate from the Rayleigh-Taylor instability. This causes the interface to get stretched along the interface, and compressed normal to the interface.

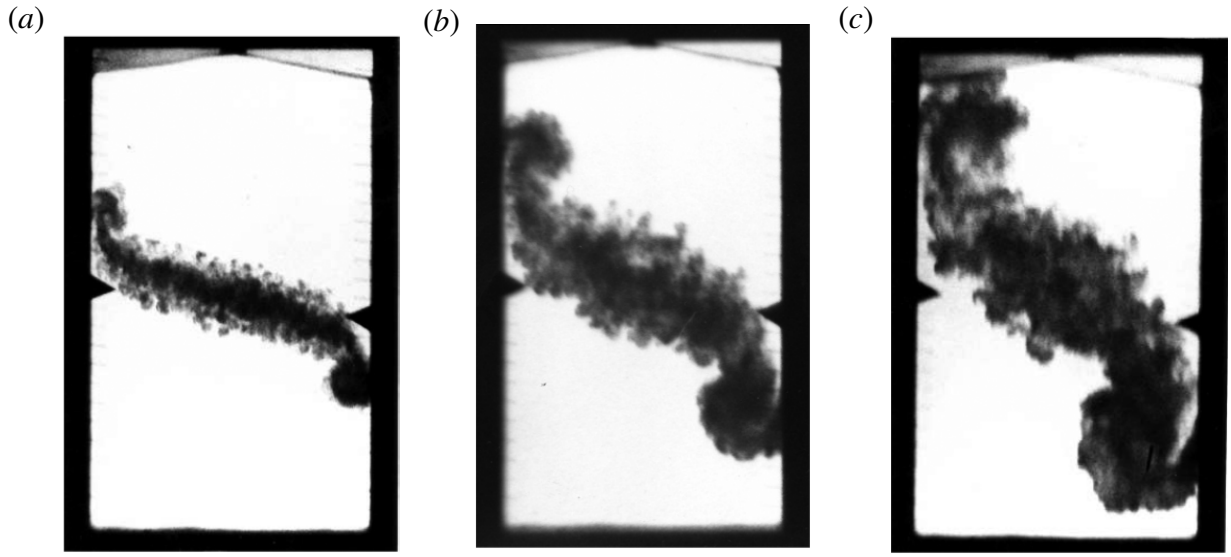

Figure 1.5: Experiment 110 of the tilted-rig at times: (*a*) $t_{\text{exp}} = 45.2\,\text{ms}$; (*b*) $t_{\text{exp}} = 59.8\,\text{ms}$; (*c*) $t_{\text{exp}} = 71.1\,\text{ms}$. Source: Figure 7 of Andrews *et al.* (2014).

Trying to achieve detailed measurements of internal dynamics and physics of ICF and supernova is not easily possible due to the scales involved. Likewise, isolating the effects of the individual strain rates on the development of turbulent mixing layers for a clear analysis of the impacts of the strain rates is not easily attainable. Maintaining a controlled and spatially uniform strain rate across a mixing layer requires a linear velocity profile, which can be difficult to sustain. Where experimental measurements are not possible, numerical simulations provide an alternative avenue for investigation of the behaviour of the fluid flows in these complicated

regimes and configurations. These simulations are an important tool to be utilised – the results of these simulations serve to improve the understanding of the underlying physics, and allows for the development of models which may be used for prediction of future experimental observations.

1.2 Objectives and approach

The role of compression or expansion on the evolution of the turbulent mixing layer is not well understood in practical applications. The role of this thesis is to investigate the role of compression or expansion on the development of the turbulent mixing layer. Simulations are performed for mixing layers under isentropic compression or expansion by applying a linear velocity profile to the domain and moving the mesh in a Lagrangian fashion. By controlling and preserving the spatially-uniform strain rates, the compression or expansion of the domain can be controlled. Focusing of the anisotropy of strain rates, the strain rates in the simulations can be applied individually in each dimension. This methodology allows for the influence of individual strain rate terms, i.e. different methods of compression or expansion, to be investigated. The results obtained are further justified through the construction of simplified models for different quantities of the flow, helping to elucidate the physical mechanisms that occur.

The investigation of the influence of strain rates is conducted for two main stages: linear and transitional-to-turbulent. Firstly, in the linear regime limit the theory is described by Bell-Plesset effects, further described in §2.2. Based in linearised potential flow theory, the models neglect the non-linear contributions to the unsteady Bernoulli equation to achieve a model for the amplitude growth (Epstein, 2004). The same approach is used in chapters 4 and 5 to modify the model to include strain rates, which are validated by resolved two-dimensional, single-mode simulations similarly to Walchli & Thornber (2017).

To evaluate the turbulent regime, a test case from the θ-group collaboration (Thornber *et al.*, 2017) is employed. This collaboration involved a cross-code comparison of eight different numerical solvers for the modelling of RMI in the high-Reynolds number limit. The investigations conducted use the quarter-scale θ-group case, This three-dimensional, narrowband, multimode configuration is initialised with scales a quarter of the size of the standard case from the θ-group. Using implicit large eddy simulations to represent the high-Reynolds number limit, the original results represent the unstrained case. The application of strain to this test case allows for the impact of the strain on the turbulent mixing layer to be easily studied. The strained simulations are conducted in chapter 4 and 5, and further modelled in chapter 6.

1.3 Thesis structure

In chapter 2, an overview of the literature relevant to the research in the thesis is provided. This review covers fundamentals of the Rayleigh–Taylor and Richtmyer–Meshkov instability from the linear to turbulent regime, followed by information regarding the theory, experiments, and modelling of these instabilities for convergent geometry. Details of the different methods available for modelling turbulent mixing layers are provided, followed by an introduction to the physics of compression and strain.

Chapter 3 focuses on the technical details for performing the simulations conducted. Firstly, the governing equations for the four-equation, five-equation, and K-L turbulence model are described, along with the equations of state used to achieve closure for multi-species mixtures. The second part of the chapter consists of the numerical methods used to discretise the governing equations in time and space. In particular, details are provided regarding the modelling of the applied strain rates.

Chapter 4 focuses on the role of the axial strain rate on the development of the RMI-induced mixing layer. The linear regime may be modelled by the linearised potential flow model with axial strain, which is validated using two-dimensional simulations. Implicit large eddy simulation (ILES) of the RMI-induced mixing layer with axial strain rates in the transitional-to-turbulent stage are conducted. To explain the changes between the unstrained and strained cases, several models are proposed to explain the alteration in the turbulent mixing layer's development.

Chapter 5 investigates the impact of transverse strain rate on the mixing layer. A reformulation of the Bell-Plesset model into the strain rate framework is presented, and validated for the linear regime with simulations. The turbulent mixing layer is again investigated with ILES. Due to the deviation from both the unstrained results and linear regime theory, alternate models are proposed to describe the obtained integral results.

In chapter 6, the previous ILES cases are used for the calibration of the bulk compression closure for the K-L turbulence model. Simulations are conducted for three different closures, with the efficacy of each closure investigated using the alignment between the ILES and K-L model results for the integral width and turbulent kinetic energy. A comparison of closure models for bulk compression in two-equation models is also presented, highlighting similarities and differences between the models.

Chapter 7 summarises the findings of chapters 4, 5 & 6. It also includes recommendations for potential avenues for further research regarding the influence of strain rates on turbulent mixing layers. Finally, appendices A and B include a sample of test cases used for the verification and validation of the K-L model and applied strain rates, respectively. The K-L model verification

consists of a series of test cases, verifying each term individually, as well as several test cases for instability validation. The strain rate verification focuses on the ability of the applied strain rate methods to maintain the desired velocity profile and uniform pressure whilst conserving mass.

1.4 Publications

At the time of submission, the work in this thesis has been accepted into the following research publications:

- **Pascoe, B.**, Groom, M., Youngs, D.L., Thornber, B. 2024 Impact of transverse strain on linear, transitional, and self-similar turbulent mixing layers. *Journal of Fluid Mechanics*, 99:A5.
- **Pascoe, B.**, Groom, M., Thornber, B. 2025, Turbulence modeling of mixing layers under anisotropic strain. *Physical Review Fluids*, 10:064609.

Additionally, the following manuscripts are submitted to journals and are currently under review:

- **Pascoe, B.**, Groom, M., Youngs, D.L., Thornber, B., Impact of transverse strain on linear, transitional, and self-similar turbulent mixing layers.

In addition to journal papers, the following conference papers have been presented:

- **Pascoe, B.**, Groom, M., Thornber, B. 2022 Richtmyer–Meshkov Instability under Axial Strain. *23rd Australasian Fluid Mechanics Conference*, 419
- **Pascoe, B.**, Groom, M., Thornber, B. 2024 Turbulence modelling of the Richtmyer–Meshkov instability under anisotropic strain. *24th Australasian Fluid Mechanics Conference*, 372

CHAPTER 2

Literature Review

2.1 Fundamental instabilities

The Rayleigh–Taylor and Richtmyer–Meshkov instabilities are two fundamental instabilities which describe the growth of amplitude perturbations at the interface between two fluids. The Rayleigh-Taylor instability (RTI), first looked at by Rayleigh (1882) and Taylor (1950*c*), analyses the case of continual acceleration normal to the perturbed interface. The acceleration creates buoyancy effects such that the stability of the system depends on the direction of the acceleration acting on the system. The system is unstable if acceleration points from the light to the heavy fluid. This criterion for the RTI growth is defined mathematically by

$$\nabla\rho \cdot \nabla p < 0. \tag{2.1}$$

When this dot product is positive, such as the case for a lighter fluid sitting on top of a heavier fluid under the influence of gravity, the system is instead oscillatory with viscous effects damping out the motion. The vorticity paradigm helps provide insight into the development of the instability (Hawley & Zabusky, 1989). The vorticity equation is given by

$$\frac{D\boldsymbol{\omega}}{Dt} = \underbrace{(\omega \cdot \nabla)u}_{\text{vortex tilting}} - \underbrace{\omega(\nabla \cdot u)}_{\text{vortex stretching}} + \underbrace{\frac{1}{\rho^2}\nabla\rho \times \nabla p}_{\text{baroclinic}} + \underbrace{\nabla \times \left(\frac{\nabla \cdot \tau}{\rho}\right)}_{\text{diffusion}} + \underbrace{\nabla \times \left(\frac{B}{\rho}\right)}_{\text{body force}}. \tag{2.2}$$

The baroclinic term occurs when the density and pressure gradients do not align. For a perturbed interface under acceleration, the buoyancy effects create a pressure differential which will create vorticity, as shown in figure 2.1. The vortices generated for the unstable configuration will cause the amplitude to grow, whilst for the stable configuration the amplitude will be inverted. After inversion, vorticity will be generated with the opposite sign, causing the amplitude to oscillate.

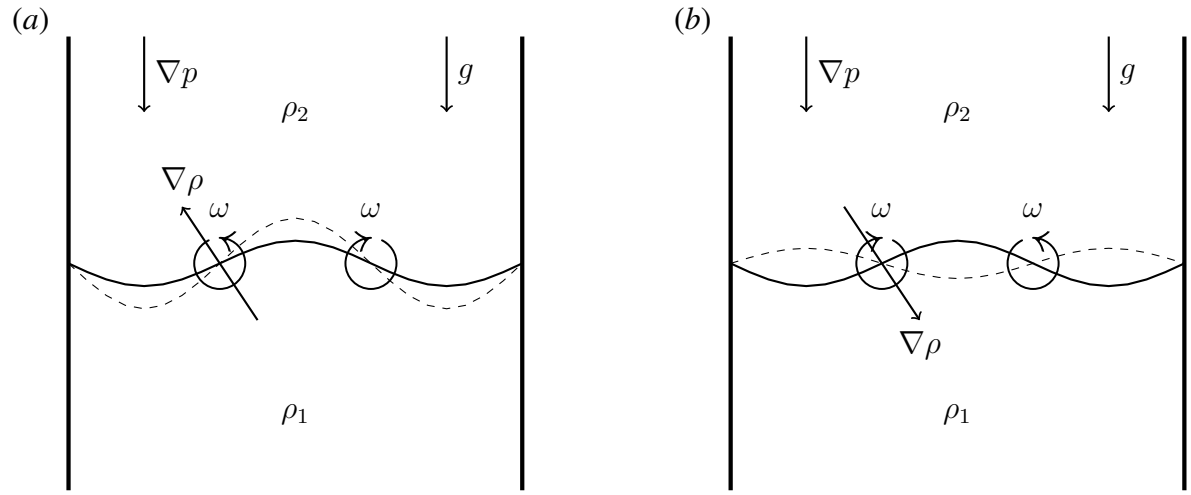

Figure 2.1: Vorticity generation due to the baroclinic term for the Rayleigh-Taylor instability. (*a*) Unstable RTI with $\rho_2 > \rho_1$, where vorticity production will increase the perturbation amplitude; (*b*) Stable RTI with $\rho_2 < \rho_1$, where vorticity production will reduce and invert the perturbation amplitude. The initial interface is depicted with solid lines, and the evolved interface at the time Δt is depicted with dashed lines.

The Richtmyer–Meshkov instability (RMI) is the impulsive variation of RTI resulting from an instantaneous acceleration of the interface, such as that from a shock-wave. Unlike RTI, RMI is unstable regardless of the direction of the impulsive acceleration. Again looking at the vorticity, it can be seen for RMI that as the shock-wave passes through the already perturbed interface, there is a misalignment between the pressure and the density gradients. As the shock passes creating a sudden pressure differential, vorticity will deposit at the interface, causing the amplitude to either directly grow or invert depending upon the density gradient. Unlike the stable configuration of RTI, the inverted amplitude (commonly referred to as a phase inversion for RMI) does not create any new vorticity such that the amplitude will continue to grow in the inverted form. An example of the heavy-to-light RMI is shown in figure 2.2, showing the inversion of the interface.

2.1.1 Linear Regime

The first analysis of RTI done by Rayleigh (1882) was performed by analysing the incompressible, inviscid Navier–Stokes equations and linearising them about an unperturbed state. Solving for the perturbed variables results in a differential equation for the interface amplitude,

$$\ddot{a}_k = At\, gka_k. \tag{2.3}$$

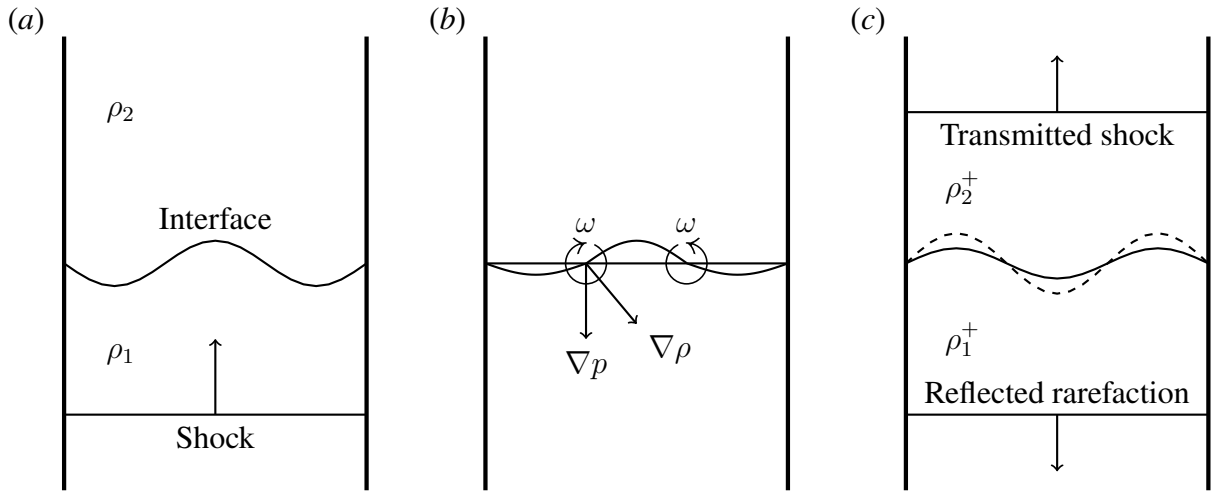

Figure 2.2: Evolution of Richtmyer–Meshkov instability in a heavy-to-light configuration ($\rho_2 > \rho_1$) in the interface frame-of-reference. (a) Initial interface set-up; (b) Compression and vorticity generation as shock transits the interface; (c) Amplitude growth following amplitude inversion.

Here a_k is the amplitude corresponding to wave-number k, g is the gravity force pointing downwards, and At is the Atwood number defined by,

$$At = \frac{\rho_2 - \rho_1}{\rho_2 + \rho_1}, \tag{2.4}$$

where ρ_2 is the fluid sitting on top. The differential equation provides exponential solutions in time, with exponent coefficients of the form $n = \pm\sqrt{At\, gk}$. For negative Atwood numbers, the system has imaginary exponent coefficients and is therefore oscillatory, whilst for positive Atwood numbers the system has a positive exponent coefficient. These equations are only valid for small perturbations, with the common assumption that $ak < 1$. A slightly more conservative estimate for the linear regime is that $a < 0.1\lambda$, where $\lambda = 2\pi/k$ is the perturbation wavelength (Brouillette, 2002).

This formulation assumes a discontinuous interface, which is often impractical in experiments and simulations. Duff *et al.* (1962) derived a solution to RTI for a diffuse interface,

$$n = \sqrt{\frac{At\, gk}{\varphi}}, \tag{2.5}$$

where φ is the growth reduction factor, a complicated function of the density gradient and the Atwood number. A simple model that incorporates viscosity is given by,

$$n = \sqrt{At\, gk + (\nu k^2)^2} - \upsilon k^2, \tag{2.6}$$

where ν is the mean kinematic viscosity of the fluids, calculated using the average dynamic viscosity coefficient and average density (Bellman & Pennington, 1954; Hide, 1955).

The first model for RMI was formulated by Richtmyer (1960) using an impulsive treatment to the solution of RTI. Under this limit it is assumed that instead of a constant acceleration, the acceleration of the system is defined by an impulse that creates a change in velocity, $g = \delta(t)\Delta V$, where $\delta(t)$ is the Dirac delta function. This assumption gives a constant amplitude growth rate,

$$\dot{a}_k = At\Delta V k a_{k,0}, \tag{2.7}$$

where $a_{k,0}$ is the initial amplitude of the perturbation with wave number k, and At is again the Atwood number for a shock originating in fluid 1. This impulsive model does not attempt to model the shock traversal through the interface or the compressibility effects, and instead can be assumed to be valid only once the shock-wave has moved a sufficient distance away from the interface.

Some values change during the shock passage, such as the amplitude and the Atwood number, causing ambiguity in the model for which values to use. As Richtmyer focused on light-to-heavy shocks, it was found that the optimum values to match the simulations were the post-shock Atwood number and amplitude,

$$\dot{a}_k^+ = At^+\Delta V k a_{k,0}^+, \tag{2.8}$$

using the notation of a superscript $+$ denotes post-shock, and a superscript $-$ denotes pre-shock. The post-shock amplitude is related to the pre-shock amplitude by the expression,

$$a_0^+ = a_0^- \left(1 - \frac{\Delta V}{W_i}\right), \tag{2.9}$$

where W_i is the velocity of the incoming shock responsible for compressing the interface. It should be noted that ΔV, as well as At^+ and a_0^+, are implicit terms and cannot be explicitly solved for.

Further analysis by Meyer & Blewett (1972) show that for the alternate configuration, heavy-to-light, a better choice of values is to again use the post-shock Atwood number, but to use the average of the pre- and post-shock amplitude values. Vandenboomgaerde *et al.* (1998) proposed a model that would be valid for both configurations,

$$\dot{a}_k = k\Delta V \left\{ \frac{1}{2}\left(At^+ a_{k,0}^+ + At^- a_{k,0}^-\right) - \frac{1}{6}\left(At^+ - At^-\right)\left(a^+ - a^-\right) \right\}, \tag{2.10}$$

These impulsive models can be compared to the solutions obtained by actually looking at the linearised compressible perturbation equations. Fraley (1986) solved these equations using Laplace transforms and found the asymptotic amplitude growth rate for a shock passing from

fluid 1 to fluid 2 is described by,

$$\dot{a}_k = At^- + \epsilon F/\gamma_1, \tag{2.11}$$

where

$$F = 2\left[1 - R + \frac{2R(R-y^2)}{y(R+1)}\right](R+1)^{-1}(y+1)^{-1},$$
$$\epsilon = 1 - p_1^-/\tilde{p}_1^+,$$
$$R = \rho_2^-/\rho_1^-,$$
$$y = (R\gamma_2/\gamma_1)^{1/2},$$

Here R is the initial density ratio, and ϵ is a measure of the incoming shock strength. The intermediate pressure $\tilde{p}_1$ is the pressure in fluid 1 after the incoming shock but before the reflected wave. The nature of the reflected wave depends upon the fluid properties. For fluids that have the same specific heat ratios, γ, and are in pressure equilibrium, then a shock passing from light to heavy creates a reflected shock whilst a shock passing from heavy to light creates a reflected rarefaction wave (Hurricane & Miller, 1998). For fluids that do not fit this condition, it instead depends upon the acoustic impedance, ρc, where c is the speed of sound. For low to high acoustic impedance, there is a reflected shock and for high to low acoustic impedance there is a reflected shock (Yang *et al.*, 1994).

The solution by Fraley was compared to Richtmyer's impulsive model by Mikaelian (1994). The formulations showed agreement for some RMI configurations, however Fraley's work was more accurate and more capable of predicting single-shock freeze-out, where the interface amplitude does not grow due to the combination of initial density ratio and specific heat ratios (i.e. compressibility of the fluids).

Just like for RTI, there are several stabilising mechanisms that reduce the growth rate of the perturbation amplitude in RMI. For the continuous interface, Brouillette & Sturtevant (1994) adapted the method of Duff to find the growth reduction factor, φ, for RMI with a finite interface thickness, however it does not have a closed form. Mikaelian (1993) adapted the method for RTI with viscosity but used the impulse assumption to derive the growth rate,

$$a(t)/a_0 = 1 + \frac{\Delta V At}{2k\nu}\left(1 - e^{-2k^2\nu t}\right), \tag{2.12}$$

as well as a formulation that incorporates surface tension.

Within the linear regime, it is possible to apply the principle of superposition to determine the amplitude growth rate of multi-modal perturbations. Each wave-number should grow independently within the linear regime, allowing the total interface perturbation to be calculated

by the summation of the independent wave-number perturbations (Drazin & Reid, 2004). When $a_k > 0.1\lambda$, the perturbation mode begins to saturate and the amplitude growth rate will decrease.

2.1.2 Non-linear regime

In the non-linear regime, the growth rate of the perturbation amplitudes decreases, and an asymmetry in the growth rate forms between the species depending upon the Atwood number. The interface growth rate is better defined by bubbles and spikes, which are protrusion of the light fluid into the heavy fluid and protrusions of the heavy fluid into the light fluid, respectively. Whilst in the early non-linear regime the mean interface is smooth and connected, as the instability continues to develop these qualities do not hold. Figure 2.3 shows a narrowband mixing layer in the non-linear stage with an interface that is becoming less smooth. At late non-linear time, the perturbations will begin to roll-up due to the shearing motion between the penetrating structure and the bulk fluid, which instigates the Kelvin–Helmholtz instability. An example of this behaviour is shown in figure 2.4 for the late non-linear or early transitional stage of mixing layer development. The light fluid (blue) tends to form large bulbous structures at the interface, hence the label of bubbles. The denser fluid (red) structures are sharper, hence the label of spikes.

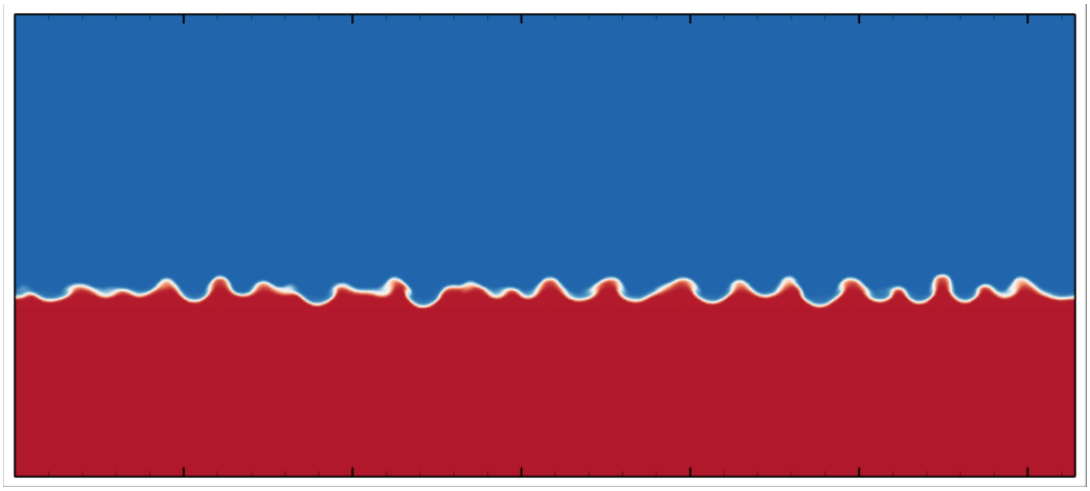

Figure 2.3: Slice at $z = 0$ for the multimode, narrowband, quarter-scale θ-group RMI case (Thornber *et al.*, 2017) at $t = 0.03\,\text{s}$. Heavy fluid ($f_1 = 1$) is red, light fluid ($f_1 = 0$) is blue.

There are several approaches to non-linear models, all of which cannot be covered here. For a more in-depth discussion, refer to works by Zhou (2017*a*,*b*). Layzer (1955) proposed a single-mode RTI model for the limiting case of $At = 1$ for the velocity of the bubble tip in 2D and 3D. Classified as a potential flow model, this approach has been adapted by several authors in an attempt to generalise to arbitrary Atwood numbers (Goncharov, 2002; Sohn, 2003).

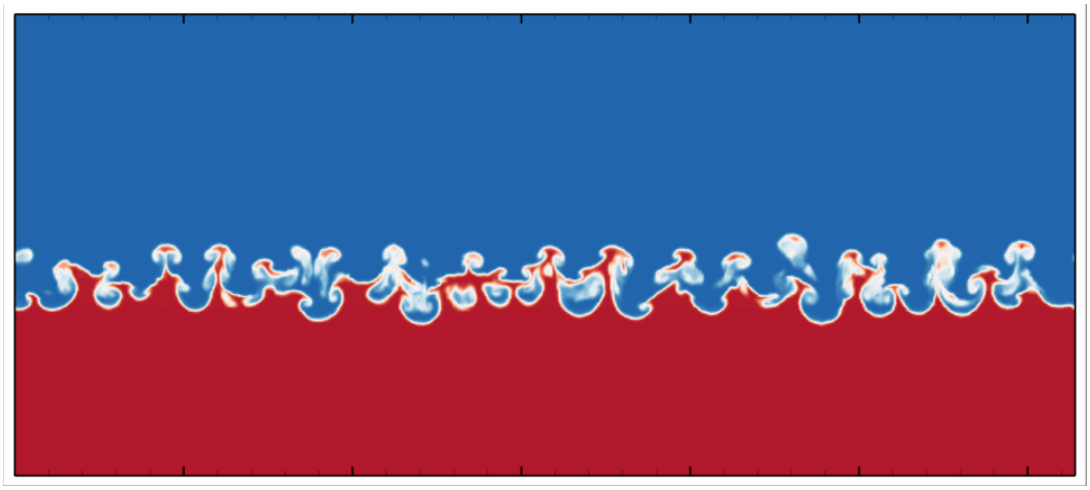

Figure 2.4: Slice at $z = 0$ for the multimode, narrowband, quarter-scale θ-group RMI case (Thornber *et al.*, 2017) at $t = 0.01$ s. Heavy fluid ($f_1 = 1$) is red, light fluid ($f_1 = 0$) is blue.

For RMI, Brouillette (2002) provides a second order solution to the perturbation equations at the interface to obtain the bubble and spike velocities,

$$\dot{h}_b(t) = k\Delta V A t^+ a_0^+ (1 - k\Delta V A t^+ a_0^+ t) \tag{2.13}$$

$$\dot{h}_s(t) = k\Delta V A t^+ a_0^+ (1 + k\Delta V A t^+ a_0^+ t) \tag{2.14}$$

Whilst this clearly demonstrates that spikes grow faster than bubbles (when $At^+ \neq 0$), it is insufficient to be accurate, instead a much higher order expansion is required for later times. To achieve this, Zhang & Sohn (1996, 1997) took higher-order terms and then utilised Pade approximations to develop a model for the bubbles and spikes. The model does not use the impulse assumption, but assumes the perturbation is initially linear and compressible, and then non-linear and incompressible at late times. The equation for total amplitude growth rate is dependent upon whether the system is 2D or 3D, and whether there is a phase inversion (Li & Zhang, 1997).

$$\dot{a}(t) = \frac{\dot{a}_{Lin}}{1 + \zeta\xi_1 \dot{a}_{Lin} a_0^+ k^2 t + max[0, (a_0^+ k\xi_1)^2 - \xi_2]\dot{a}_{Lin}^2 k^2 t^2} \tag{2.15}$$

Here $\dot{a}_{Lin}$ represents the linear growth rate, and ζ depends on whether there is a phase inversion, and ξ_1 & ξ_2 are geometric parameters that are determined by whether it is a 2D or 3D perturbation.

Jacobs & Sheeley (1996) proposed a vortex model for RMI, which models the induced vorticity by placing vortices on the interface at the mean interface line intersections. The induced velocity field can be used to describe the amplitude growth. This model was originally only valid for vanishing Atwood numbers, however it was generalised by Likhachev & Jacobs (2005) for finite Atwood numbers.

There are several approaches which can be used to define the extents of the mixing layer. In the linear regime, the amplitude can be measured using the maximum and minimum position

of an isocontour, such as the line or surface of even volume fraction distribution between the two fluids, $f_1 = 0.5$ (Walchli & Thornber, 2017). The same approach is still possible in the non-linear regime, however it becomes biased towards penetrating structures such as vortex rings which do not represent the mean qualities of the mixing layer. Likewise, the cut-off width can be used, defining the mixing layer width as the distance between the planar averages of 1% and 99% volume fraction concentration:

$$h = x_{99} - x_{01} \tag{2.16}$$

where

$$\bar{f_1}(x = x_{99}) \quad = 0.99, \tag{2.17a}$$

$$\bar{f_1}(x = x_{01}) \quad = 0.01. \tag{2.17b}$$

Again, the mixing layer measurement is sensitive to statistical fluctuations. A more robust approach is to use integral measurements for the mixing layer width. There are several metrics which may be used. One of the most common is the integral width (Andrews & Spalding, 1990; Youngs, 1994), which is dependent upon the mean volume fraction profile,

$$W = \int_{-\infty}^{\infty} \bar{f}_1 \bar{f}_2 \, \mathrm{d}x. \tag{2.18}$$

The mean volume fraction profile is calculated using planar averages according to

$$\bar{\phi}(x) = \frac{1}{L_y L_z} \int_0^{L_z} \int_0^{L_y} \phi \, \mathrm{d}y \, \mathrm{d}z, \tag{2.19}$$

which does not necessitate planes of statistical homogeneity, as the original application was toward the measurement of the width of the tilted rig mixing layer. Outside the mixing layer, in the regions of the pure fluids, either $\bar{f_1}$ or $\bar{f_2}$ will be zero for the plane and will therefore not contribute to the integral width. Isolated features propagating away from the mixing layer will have negligible contributions to the integral width. For a mixing layer with a linear volume fraction profile between 0 and 1 in the mixing layer of some width, the integral width will be equal to a sixth of the width.

For the evaluation of bubbles and spike heights, the cut-off heights using the distance between the mixing layer extents outlined in equation (2.17) and the mixing layer centre is an easy choice, but is susceptible to statistical fluctuations. The total cut-off width is then the sum of the two heights,

$$h = h_b + h_s. \tag{2.20}$$

The choice of the mixing layer centre is also to be considered. In RTI, where there may be no bulk fluid velocity, the mixing layer centre can be attributed to the mean position of the original interface. A similar approach is viable for RMI in using the mean position of the original interface. Due to the movement of the mixing layer from the velocity impulse, a separate realisation with an unperturbed interface is required to determine how the mixing layer centre moves with time. An alternative approach is to define the mixing layer centre by the position where there are equal volumes of penetrating species on each side (Walchli & Thornber, 2017; Krivets *et al.*, 2017). For the configuration where the species for f_1 is initially at lower values of x, the mixing layer centre x_c is calculated given the constraint

$$\int_{-\infty}^{x_c} \bar{f}_2 \, \mathrm{d}x = \int_{x_c}^{\infty} \bar{f}_1 \, \mathrm{d}x. \tag{2.21}$$

The two approaches for the mixing layer centre are not equivalent, and possess different properties – the unperturbed interface position is theoretically calculable but not identifiable from the realised experiment, whilst the equal volume position is identifiable from the realised experiment but is not theoretically calculable without detailed knowledge of the mixing (Mikaelian & Olson, 2020).

Krivets *et al.* (2017) uses bubble and spike heights calculated in the same manner as the integral width. Youngs & Thornber (2020*a*) defined integral measures for the bubble and spike heights which are normalised to reproduce the heights for a bi-linear mean volume fraction profile:

$$\bar{h}_b^{(m)} = \left[\frac{(m+1)(m+2)}{2} \frac{\int_{-\infty}^{0} |x|^m (1-\bar{f}_1) \mathrm{d}x}{\int_{-\infty}^{0} (1-\bar{f}_1) \mathrm{d}x} \right]^{1/m}, \tag{2.22}$$

$$\bar{h}_s^{(m)} = \left[\frac{(m+1)(m+2)}{2} \frac{\int_{0}^{\infty} x^m \bar{f}_1 \mathrm{d}x}{\int_{0}^{\infty} \bar{f}_1 \mathrm{d}x} \right]^{1/m} \tag{2.23}$$

for some exponent m, originally considered for the cases of m =1, 2, and 3.

2.1.3 Transition to turbulence

As the development of the mixing layer enters the late-time, the viscous forces within the mixing layer will cause structures to break down, transitioning the mixing layer to a turbulent state. An example of the turbulent mixing layer is shown in figure 2.5 for RMI, showing a range of scales of mixing as compared to the initial interface, which was dominated by the large bubble and spike structures.

The mixing layer growth for the RTI was proposed by Youngs (1984) to follow the formula,

$$h_i = \alpha_i \, At \, g \, t^2, \tag{2.24}$$

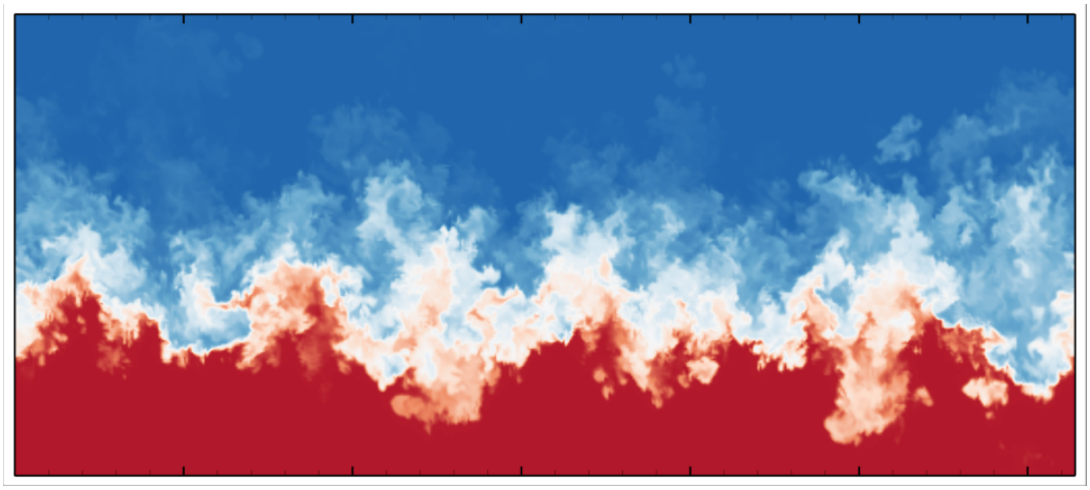

Figure 2.5: Slice at $z = 0$ for the multimode, narrowband, quarter-scale θ-group RMI case (Thornber *et al.*, 2017) at $t = 0.42$ s. Heavy fluid ($f_1 = 1$) is red, light fluid ($f_1 = 0$) is blue.

where i represents either the bubble or the spike. The total mixed width is given as the summation of the two. The bubble velocity is considered to be roughly constant across Atwood numbers, whilst the spike height and asymmetry depend on the Atwood number. The α-group collaboration (Dimonte *et al.*, 2004) provides an overview of simulated and experimental values for the bubble velocity, showing a disparity of $\alpha_b = 0.025 \pm 0.003$ for simulation as compared to $\alpha_b = 0.057 \pm 0.008$ for experiments. The simulated estimate is considered to be a lower bound, as the simulations were composed of short wavelengths perturbations. The addition of longer wavelengths, which may be present in experiments, would cause greater amplitude growth rates at later time as the larger wavelengths take longer to saturate.

Late time RMI is also believed to be governed by a power law formula,

$$h_i \propto t^{\theta_i}, \tag{2.25}$$

for some sublinear value of θ_i for the bubble, spike, and mixing layer width, respectively. An effective upper-bound of θ for the mixing layer is 2/3, which corresponds to the case of conserved turbulent kinetic energy in the mixing layer (Ramshaw, 1998). However, the dissipation of turbulent kinetic energy further reduces the observed values of θ. The value of θ is dependent upon the initial conditions and Atwood number, which is evident as the kinetic energy available in the system depends upon the shock interaction with the initial interface (Saffman & Meiron, 1989). The Linear Electric Motor (LEM) experiments by Dimonte & Schneider (2000) found that θ_b was constant for all Atwood numbers, but θ_s deviated from θ_b for $At > 0.8$. If the bubble and spike heights are modelled by different exponents ($\theta_s \neq \theta_b$), then it is not possible to express the mixing layer width as a function of a single value of θ (Mikaelian & Olson, 2020). The results of Dimonte & Schneider (2000) are believed to have not run for a long enough amount of time

to achieve the self-similar growth to properly demonstrate the late-time power-law growth rate, which requires several generations of mode coupling (Elbaz & Shvarts, 2018). Self-similarity of the turbulent mixing layer suggests the mean volume fraction profile should become invariant when non-dimensionalised by the outer length scale. This is only possible for bubble and spikes which grow with the same θ, and does not depend upon which of the two methods is used for the mixing layer centre (Li *et al.*, 2024).

The θ-group collaboration (Thornber *et al.*, 2017) performed a cross-code comparison for modelling late-time RMI with $At = 0.5$ and narrowband initial conditions. Two cases were considered: the standard case with initial perturbation with wave-numbers of $\kappa \in [4, 8]$, and the quarter-scale case with wave-numbers of $\kappa \in [16, 32]$. The power law growth rate between codes was well converged but differed for the two cases. For the standard case, which was conducted to shorter non-dimensional time, the exponent was calculated to be $\theta = 0.219 \pm 0.009$, whilst the quarter-scale case achieved $\theta = 0.292 \pm 0.009$, calculated using a non-linear regression fit. Instantaneous measurements of θ suggest that the growth rate varies with time and is decreasing in the late-time. Whilst Youngs & Thornber (2020*a*,*b*) are able to model the growth using the theoretical value of $\theta = 1/3$, even longer simulations may converge towards the growth rate of $\theta = 1/4$ as posited by Soulard & Griffond (2022). The same value of $\theta = 1/3$ was used to model the bubble and spike heights for the moderate Atwood number of $At = 0.5$, as well as for $At = 0.9$, which is in the disharmonious regime of Dimonte & Schneider (2000).

To achieve a fully turbulent mixing layer, it is necessary for the outer scale Reynolds number to achieve a certain threshold. Dimotakis (2000) analysed several turbulent flow phenomena and identified a Reynolds number of 10^4 as the threshold for a mixing transition, below which the mixing layer is quantitatively different. In the scales of the energy spectrum, the length scale of the eddies (λ) in the inertial region should be greater than the inner viscous scale (λ_v), which is proportional to the Kolmogorov scale (η). Further, the size of the eddies should be smaller than the scales directly generated from the outer length scale, taken as the Liepmann-Taylor scale (λ_L). Estimates for the size of these scales give the equality:

$$\lambda_v \approx 50\, Re^{-3/4} L < \lambda < \lambda_L \approx 5\, Re^{-1/2} L \tag{2.26}$$

for some outer scale length L, which requires

$$Re > 10^4 \tag{2.27}$$

to establish the necessary range for the inertial scales. The upper range is modified for time-varying flows, where the consideration of the laminar viscous scale introduces an additional constraint (Zhou *et al.*, 2003). Further analysis by Zhou (2007) suggests that the lower bound

of the inertial range should not directly interact with the energy scales as the time-dependent flow evolves, now requiring $\lambda_L/2 > \lambda_v$, which raises the threshold outer Reynolds number to $Re = 1.6 \times 10^5$. The hypothesis of this scaling is that reaching the threshold outer Reynolds number will achieve the *minimum state* and the energy containing scales will be resolved and not affected by the dissipation scales.

2.2 Spherical geometry

Whilst most commonly analysed in planar or non-convergent geometry, it is noticeable that in applications such as ICF and supernova the geometry is spherical. It is of interest then to analyse these instabilities in convergent geometry, a term used to encompass both cylindrical and spherical geometries. Some of the first research into the effects of the convergent geometry in the linear regime was conducted by Bell (1951) and Plesset (1954), as well as by Penney & Price (1942) in a confidential paper. The model of Bell (1951) allowed for uniform compressibility, but was limited to $At = 1$, whilst the model of Plesset (1954) was incompressible but valid for all Atwood numbers. Epstein (2004) combined and recast the equations to derive model equations for convergent geometry which is suitable for all Atwood numbers and uniform compression between the two fluids. The equations by Epstein (2004) for planar, cylindrical, and spherical geometry for the amplitude a_l of mode l are given by

$$\left(-\gamma_\rho + \frac{\mathrm{d}}{\mathrm{d}t}\right)\frac{\mathrm{d}}{\mathrm{d}t}\left(a_l\rho\right) = \gamma_0^2 a_l\rho, \tag{2.28a}$$

$$\left(-\gamma_\rho + \frac{\mathrm{d}}{\mathrm{d}t}\right)\frac{\mathrm{d}}{\mathrm{d}t}\left(a_l\rho R\right) = \gamma_0^2 a_l\rho R, \tag{2.28b}$$

$$\left(-\gamma_\rho - \gamma_R + \frac{\mathrm{d}}{\mathrm{d}t}\right)\frac{\mathrm{d}}{\mathrm{d}t}\left(a_l\rho R^2\right) = \gamma_0^2 a_l\rho R^2. \tag{2.28c}$$

The model introduces dependence upon two fluid parameters, the compression rate of the fluid $\gamma_\rho = \dot{\rho}/\rho$, and the convergence rate of the mean interface radius $\gamma_R = \dot{R}/R$. Labelled Bell-Plesset effects, the additional dependence upon these parameters modifies the growth rate of RMI and RTI in convergent geometry as compared to planar geometry. The right-hand-side of equation (2.28) represents the driving term for RTI which depends on the local pressure gradient ($g_p = -(1/\rho)[\partial p(R,t])/\partial x$), where

$$\gamma_0^2 = k\frac{\rho_2 - \rho_1}{\rho_2 + \rho_1}g_p, \tag{2.29a}$$

$$\gamma_0^2 = \frac{l}{R}\frac{\rho_2 - \rho_1}{\rho_2 + \rho_1}g_p, \tag{2.29b}$$

$$\gamma_0^2 = \frac{l(l+1)}{R}\frac{\rho_2 - \rho_1}{l\rho_2 + (l+1)\rho_1}g_p, \tag{2.29c}$$

for planar, cylindrical, and spherical geometry, respectively. Whilst the driving term is expressed differently for the different geometries, which may be interpreted as a modification of the Atwood number. In the high mode limit ($l = kR >> 1$) the driving expressions converge (Mikaelian, 1987).

There have been many experimental set-ups that have been able to create RMI in either a converging or diverging geometry. Cylindrically converging shocks have been produced in annular vertical coaxial shock tubes to analyse RMI (Hosseini *et al.*, 2000), for both single-mode perturbations (Lei *et al.*, 2017) and polygonal shapes (Si *et al.*, 2015). Dimotakis & Samtaney (2006) used a gas lens technique to convert a planar shock to a converging cylindrical shock, which has been applied to investigating single-mode RMI (Biamino *et al.*, 2015). This method has been extended to create a converging spherical shock wave (Brasseur *et al.*, 2021). An alternate approach has been to design the curvature of the shock tube to create a convergent shock wave (Zhai *et al.*, 2010), which has been used to study single-mode interfaces (Luo *et al.*, 2018). Luo *et al.* (2019) modified the design so that the transmitted shock exits through the tube as a planar wave, preventing re-shock and interface deceleration. Divergent cylindrical shock wave are also possible with this approach and have been applied to single-mode interfaces (Li *et al.*, 2020), as well as a two interface system with a single-mode perturbation of the inner interface (Zhang *et al.*, 2023). Musci *et al.* (2020) utilised detonations to create repeatable blast waves and investigated the blast driven-instability, a mixture of RMI and RTI, on a multimode interface in cylindrical geometry.

Simulations have been the prominent method to examine multimode convergent geometries, as well as to analyse to a later non-dimensional time. Many simulations utilise a Cartesian mesh to simulate the spherical or cylindrical geometries, however the mesh topology can affect the numerics of the simulation. Investigations into the impacts of using Cartesian geometry have been conducted by Joggerst *et al.* (2014) and Woodward *et al.* (2013), showing that increasing the Cartesian mesh resolution can reduce the symmetry breaking in implicit large eddy simulations, however these cases still observe a mesh imprint on the small scale mixing. A common approach to modelling implosions is to simulate a system with an external time-varying high-pressure region to help drive the implosion (Youngs & Williams, 2008), and this has been applied to spherical 2D single-mode (Flaig *et al.*, 2018), as well as 3D multimode simulations (El Rafei & Thornber, 2020). Bell-Plesset models are able to describe the initial growth, with accuracy decreasing once the modes begin to saturate (El Rafei *et al.*, 2019). Lombardini *et al.* (2014) used a Bell-Plesset model for a 3D spherical implosion with a Cartesian mesh, and separates the effects into three terms: RT/RM-like, convergence, and compression contributions. Of

these contributions for simulated implosion, convergence was found to have had the smallest contribution to the mixing layer growth, whilst the RT/RM-like contribution was the largest.

Spherical simulations of ICF capsules have been used to identify potential issues and predict future performance. Simulations by Thomas & Kares (2012) focused on the effects of an asymmetric drive on the capsule, using a driving energy source that was perturbed by a Legendre polynomial of order 30 to create the asymmetry. The simulations were conducted with adaptive mesh refinement and achieved a convergence ratio of 8, which is lower than the realistic cases. The simulations showed that turbulence with an established inertial range is able to develop in the interior under these conditions, mixing the outer fluid into the hotspot. In contrast, the simulations by Weber *et al.* (2014) find that the inclusion of viscous effects greatly dampen the out the turbulent motion in the core. The Reynolds number in the core is around 10 for the majority of the simulation, reaching a maximum of around 170 at the final time. The method used to improve resolution as the mesh converges in this case was different from the cases previously mentioned. Instead of using adaptive mesh refinement or a moving mesh algorithm that moves the mesh in radially with the implosion, the simulations improved the resolution by repeatedly discarding the outer 6% of the simulation and interpolating the remaining solution onto a mesh of the original size.

Inclusion of viscous effects make the simulations more computationally expensive. To avoid this cost, many simulations do not include these effects. This is partially justified by the low mixture viscosity for high-density-carbon and deuterium-tritium mixing (Grinstein *et al.*, 2024). Examples of simulations that do include viscous effects are the post-shot simulations of experiments from the National Ignition Facility. Labelling of the ICF shots/experiments is done with an identifier of the form N*YYMMDD*, where *YYMMDD* refers to the date the shot was conducted. Clark *et al.* (2015) analyses the shot N120321 for simulations in two- and three-dimensions, and for inviscid and viscous fluids. The greatest improvements in the simulated-to-measured yield ratio are obtained by conducting higher dimensional simulations. Where 1-D estimates expect $125\times$ larger yields, the 2-D estimate is reduced to 15, and the 3-D simulated-to-measured yield ratio is reduced to 1.5, showing that the three-dimensional nature of the problem is important to capture for the implosion. Clark *et al.* (2019) analyse the shots N170601, N170821, and N170827 with improved neutron yield estimates to within 10%. These simulations resolve up to a Legendre mode of $l \sim 100$, however ideally this would be extended to $l \sim 1000$ to fully resolve the features of the capsule. Such a resolution increase requires a 10^4 increase in compute power, which is not easily attainable.

2.3 Turbulent mixing

Turbulence is the result of the competition between the non-linear advection and the viscous dissipation terms in the Navier–Stokes equations. Most easily quantified by the Reynolds number (Reynolds, 1883),

$$Re = \frac{\rho U L}{\mu}, \tag{2.30}$$

which compares the advection scales to the diffusion scales. For laminar flows with low-Reynolds numbers, the flow may remain smooth and easy to describe through analytical means. For high-Reynolds numbers, the flow becomes chaotic, with eddies forming over a range of length scales. The large, eddy containing eddies that may be caused by boundary conditions or initial conditions of the flow will create smaller eddies, which in turn create smaller eddies. This cascade of energy from the low wave-numbers to the high wave-numbers results in an energy spectrum such as shown in figure 2.6, where the majority of the energy is at the low wave-numbers but continues on to the higher wave-numbers. The theory of Kolmogorov (1991) proposes that the turbulent cascade ends at the scale of η, the Kolmogorov scale, where the Reynolds number is unity. The range of length scales that fluid flow occupies is a function of the Reynolds number, making simulating turbulence difficult. There are several methodologies that can be used to model turbulent mixing, depending upon the scales that are sought to be resolved. The three main simulation methods used for turbulence modelling are direct numerical simulation (DNS), large eddy simulation (LES), and Reynolds-averaged Navier–Stokes (RANS).

2.3.1 Direct numerical simulation

Direct numerical simulations (DNS) involve solving the Navier-Stokes equations, resolving all the spatial and temporal scales with accurate numerical methods. Given the vast range of scales involved in many applications, such simulations are computationally impossible to perform with modern technology. The first DNS by Orszag & Patterson (1972) was simulating homogenous isotropic turbulence with a mesh of 32^3 and a Taylor Reynolds number of 35. In comparison, Yeung *et al.* (2025) performed a DNS of forced isotropic turbulence with a mesh of $32\,768^3$ to achieve a Taylor Reynolds number of 2500. The utilisation of the world's largest supercomputer and 35 trillion grid points represents the pinnacle of modern computational efforts, and even then this is not enough to resolve many realistic flow conditions. The application of DNS is expensive and limited, however it provides detailed insights into the fluid dynamics that are used to help shape other computational methods that are more accessible.

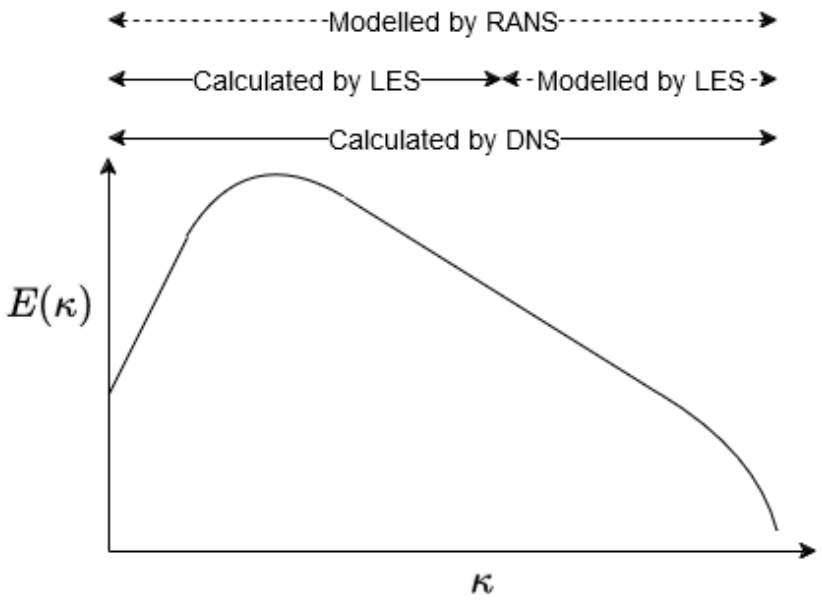

Figure 2.6: Energy spectrum as a function of wave number and the range of scales that are calculated and modelled through different numerical approaches.

In order to obtain converged and consistent first and second order statistics of the flow field, a majority of the dissipation needs to be captured (Moin & Mahesh, 1998). To achieve this, the mesh must capture length scales on the order of the Kolmogorov length scale,

$$\eta = \left(\frac{v^3}{\epsilon}\right)^{1/4}. \tag{2.31}$$

In many DNS cases, the required resolution is a multiple larger than the Kolmogorov scale, however this will depend upon the numerical scheme employed. The numerical errors of a scheme need to be sufficiently small such that properties like the numerical dissipation are not significant compared to the physical properties. Spectral methods have a very small differentiation error and are the preferred numerical method for flows with homogeneity and periodicity in a given direction. Low accuracy schemes will require greater resolution, where Moin & Mahesh (1998) provides a rule of thumb that a mesh requires twice the spatial resolution for a central difference scheme compared to a spectral scheme. On the other end of the domain sizing constraints, with periodic boundary conditions the domain needs to be at least twice as large as the integral length scale so that it still achieves a zero two-point correlation (Reynolds, 1990).

The Kolmogorov scale can be related to the outer length scale by using the outer Reynolds number:

$$\frac{L}{\eta} = Re^{3/4}. \tag{2.32}$$

The ratio of L/η represents the bandwidth of modes that will need to be resolved for the given outer Reynolds number. For RTI and RMI, it is common to use the mixing layer width as the

measure of the outer length scale,

$$Re = \frac{\bar{\rho} h \dot{h}}{\bar{\mu}}. \tag{2.33}$$

At late-time, RTI will grow according to $h \propto t^2$, which will give a Reynolds number $Re \propto t^3$, showing an increasing range of length scales that will need to be captured as the simulation progresses. In contrast, RMI's Reynolds number will scale according to $Re \propto t^{2\theta-1}$. For $\theta < 1/2$ the Reynolds number will decrease with time, and this is the case for many configurations of RMI, however broadband configurations can attain $\theta > 1/2$ resulting in a Reynolds number that increases with time. This expression can also be rearranged to expresses the Kolmogorov scale as a function of the mixing layer width or time. Ristorcelli & Clark (2004) give the relation for RTI that $\eta \propto h^{-1/8} t^{-1/4}$, which was evident in the DNS at late-time by Cabot & Cook (2006). For RMI, the same maths implies that $\eta \propto h^{-1/2+3/4\theta} \propto t^{-\theta/2+3/4}$, which requires $\theta > 3/2$ to achieve a Kolmogorov scale that decreases with time.

The necessity to resolve all time-scales of the system and achieve good temporal accuracy requires reasonably short time-steps, as the error will increase with the time-step size. Higher-order Runge-Kutta schemes provide a way to minimise this error, and as they are explicit schemes and depend upon the CFL condition they should resolve the smallest timescales. Implicit schemes may be advantageous when the physical timescales are greater than the time-step restriction and solving the implicit system is computationally economical (Moin & Mahesh, 1998).

The computational cost of performing DNS at a given outer Reynolds number can be estimated from the above relations. The number of cells necessary will scale according to

$$N \sim \left(\frac{L}{\eta}\right) = Re^{3/4}, \tag{2.34}$$

and assuming the number of iterations is limited by the CFL time-step which in turn depends on the cell size and number of cells, the computational cost will scale according to (Pope, 2000),

$$\text{Cost} \propto Re^3. \tag{2.35}$$

According to Moore's Law, computational power should double every two years, requiring eight years to develop the available computing resource to run a simulation with double the Reynolds number. Using computational fluid dynamics for design and testing purposes, where many configurations need to be investigated within a reasonable time-frame, is clearly beyond the scope of practicality, driving the necessity of simple methodologies for capturing dynamics of the fluid flow.

2.3.2 Large eddy simulation

Large eddy simulations (LES) are a less computationally expensive option compared to direct numerical simulation. Rather than resolve all length scales, LES instead aim to resolve the large, energy-containing eddies of the flow. The smallest scales, which contain a fraction of the energy and are responsible for the majority of the dissipation, are instead modelled. There are two approaches to modelling the dissipation, either explicitly with a specified sub-grid-scale model, or implicitly using the inherent properties of numerical schemes to dissipate the flow. The aim of LES is to resolve around 80% of the energy, such that large-scale features of the flow should be converged (Pope, 2000).

One of the first tenets of explicit large eddy simulations is to apply a low pass filter to the domain, thereby removing the smaller scales of motion. There are several choices of filter that may be used such as Gaussian, box, or a spectral filter, and they all must satisfy the condition

$$\int G(\boldsymbol{r})\mathrm{d}\boldsymbol{r} = 1. \tag{2.36}$$

where $G(\boldsymbol{r})$ is a filter that is uniform in space and time (although it need not be uniform in either). The filtering operation applied to a variable is denoted with an over-bar,

$$\bar{\phi}(\boldsymbol{x}, t) = \int G(\boldsymbol{r})\phi(\boldsymbol{x} + \boldsymbol{r}, t)\mathrm{d}\boldsymbol{r} \tag{2.37}$$

where $\boldsymbol{r} = \boldsymbol{x}' - \boldsymbol{x}$ represents the vector between two spatial coordinates. Applying the filtering equation to the non-dimensionalised, incompressible Navier-Stokes equations will create a new partial differential equation (PDE),

$$\frac{\partial \bar{u}_i}{\partial t} + \frac{\partial}{\partial x_j}\left(\bar{u}_i\bar{u}_j\right) = -\frac{\partial \bar{p}}{\partial x_j} - \frac{\partial \tau_{ij}}{\partial x_j} + \frac{1}{Re}\frac{\partial^2 \bar{u}_i}{\partial x_j \partial x_j}. \tag{2.38}$$

The objective is to solve this new PDE which only resolves the scales about some filter width Δ determined by the filter operator $G(\boldsymbol{r})$. All the variables denoted with an overbar in equation 2.38 are functions of the resolved flow field; the subgrid-scale effects manifest in the shear stress term

$$\tau_{ij} = \overline{u_i u_j} - \bar{u}_i\bar{u}_j. \tag{2.39}$$

The scales below the filter width still affect the flow and must be modelled in the stress term. For accurate LES, the resolved scales should capture the scales and motions that are responsible for energy production (Kosović, 1997). The subgrid-scale contribution primarily acts to dissipate the energy that would normally be performed on the order of the Kolmogorov scale. A common assumption in closure models is that the filter width is within the inertial subrange, and that

the subgrid-scale behaviour is invariant between different parts of the flow (Mason, 1994). In applications of wall bounded or transitional flows, these assumptions are not valid and LES can perform poorly (Pope, 2000).

There are many models to choose from to achieve closure of the derived PDEs. One of the most simple is the Smagorinsky model, which models the stress using an eddy viscosity assumption, where

$$\tau_{ij} = 2\nu_e \bar{S}_{ij}, \tag{2.40}$$

and ν_e is the eddy viscosity,

$$\nu_e = (C_s \Delta)^2 \left(2\bar{S}_{ij}\bar{S}_{ij}\right)^{1/2} \tag{2.41}$$

with the Smagorinsky constant C_s and the filtered, local strain rate, $\bar{S}_{ij} = \frac{1}{2}(\partial u_i/\partial x_j + \partial u_j/\partial x_i)$. Through the divergence of the tensor, the model diffuses the velocity, and dissipates the kinetic energy ($\propto u_i u_i$). In contrast to incompressible models, compressible models which need to close the filtered energy equation may have closures for the turbulent stress, pressure-velocity, pressure-dilatation, and turbulent dissipation rate (Vreman *et al.*, 1994).

For a given filter width Δ, it is desirable to obtain solutions that are converged and grid-independent by analysing the accuracy of solutions for different meshes with spacing Δx. Realistically, LES is applied when the limitation of computational resources prohibits DNS. It is potentially more worthwhile to consider what filter width Δ is most accurate for a fixed given mesh with spacing Δx. Pope (2004) outlines that a large ratio $\Delta/\Delta x$ should converge and have no numerical error, at the risk of resolving less of the flow field features due to the large Δ. A small $\Delta/\Delta x$ ratio instead will resolve more scales of motion, better representing the true solution, however the numerical errors are increased as it will not be converged. The optimum solution therefore is somewhere in between. Many closure models are designed assuming that $\Delta = \Delta x$, however Chow & Moin (2003) recommends for reliable results that $\Delta/\Delta x > 2$ for sixth-order Pade schemes, and > 4 for second order finite difference. Achieving a balance is also beneficial, as the errors from the modelling and discretisation may cancel out (Meyers *et al.*, 2003).

An alternative to the conventional LES modelling approach is the implicit large eddy simulation (ILES). ILES differs in the approach of modelling the subgrid stress tensor, or more precisely it is the lack of modelling of the subgrid stress tensor. ILES rely on the numerical scheme to provide the dissipation and stabilise the flow. Just like LES, the dissipation that should occur at the unresolved dissipation length scales is replaced. The numerical diffusion and dissipation for a solver is dependent upon the numerical scheme and the grid resolution.

For ILES, the scales at which the numerical dissipation acts needs to be sufficiently distant from the large scales of the flow, in order to not impact the evolution of the largest eddies and the development of the turbulent cascade. ILES will therefore require sufficient resolution to converge for the largest scales. By virtue of the diminishing turbulent kinetic energy for increasing wave number, ILES are able to reasonably predict the behaviour of turbulence in the high-Reynolds number limit by capturing the largest scales of the flow.

There are a variety of different numerical schemes that are capable of being used for ILES, with the numerics of many non-oscillatory finite volume schemes being well suited for acting as an implicit subgrid model. The first scheme identified was the monotonic scheme known as the flux-corrected transport method Boris & Book (1973). This method preserves monotonicity of the flow field by using an initially numerically diffusive convection step, followed by an anti-diffusion stage, filtering out the high-frequency components of the flow (Fureby & Grinstein, 2002). The numerical scheme's preservation of monotonicity acts as an integrated LES model, hence the name of Monotonically Integrated Large Eddy Simulation (MILES) (Boris *et al.*, 1992). Through Modified Equation Analysis (MEA), it can be shown that different numerical methods, not just monotone methods, operate with an implicit sub-grid model, hence the more common name of ILES. The simplicity of not applying a specific filter and not having to explicitly model the sub-grid scales make ILES an attractive option over traditional LES.

Another numerical method for ILES is the Lagrange-Remap scheme (Van Leer, 1977; Youngs, 1982, 1991). This scheme is separated into two stages, as given by the name: the Lagrangian phase and the remap phase. The Lagrangian phase calculates the new values of the density, velocity and internal energy according to a scheme of choice, whether finite difference or a finite volume method. The remap phase does not evolve the solution, but considers the movement of the mesh from the calculated values, and remaps the solution back onto the original mesh. Using monotonic advection methods for the remap, the total energy is conserved, however kinetic energy is dissipated. The application of this method has been used for many investigations into the development of hydrodynamic instabilities (Youngs, 1984, 1991, 1994, 2013, 2017).

Another broad category of ILES scheme is the usage of finite-volume methods with high-resolution reconstruction with limiters. The Godunov method Godunov & Bohachevsky (1959) is a versatile upwind scheme that has been improved upon for second order scheme through the MUSCL scheme (van Leer, 1979), and for third order scheme through the Piecewise-Parabolic Method (Colella & Woodward, 1984). The use of reconstructed interface values for flux calculations improves the order of accuracy of the scheme in smooth areas of the flow, as well as improves the order of convergence for the numerical dissipation. However, it is necessary for

these schemes to reduce to first order around discontinuity to prevent unphysical oscillations.

Whilst many methods are capable of being used for ILES, this does not mean they perform the same for a given problem. A comparison of methods is shown in the RMI cross-code comparison of the θ-group (Thornber *et al.*, 2017). Despite most of the different numerical methods converging towards the same solution for the large scale properties of the flow, the turbulent kinetic energy spectra differs by a much more significant extent. As ILES of relies on the numerical dissipation which is scheme dependent, the smallest scales resolved will vary with scheme, depending upon the nature of the numerics. Not all numerical methods will give quality results. A fifth-order Weighted Essentially Non-Oscillatory scheme can give poor results when applied to the fluxes rather than variable reconstruction (Garnier *et al.*, 1999; Grinstein *et al.*, 2007).

2.3.3 Reynolds-averaged Navier–Stokes

The objective of Reynolds-averaged Navier–Stokes (RANS) is to compute only the mean flow, leaving the majority of the scales to be modelled. First proposed by Reynolds (1895), the process involved performing an average over some small region of space or duration of time. Generally, the mean may quantify the average across time, space, or ensembles. For stationary turbulence, it is common to average over time with the averaged quantity denoted with an overbar:

$$\bar{\phi} = \lim_{T\to\infty} \frac{1}{T} \int_{t}^{t+T} \phi(x_i, t)\, \mathrm{d}t. \tag{2.42}$$

Analysing over an infinite period is not physically feasible, but as long as the averaging period is sufficiently greater than the timescales of the turbulent fluctuations then the temporal correlations of the flow will not pollute the measured average. An alternative to time averaging is the averaging over an ensemble of samples. Through the principle of ergodicity, the same average should be achieved as the statistics of the flow are time invariant for the steady state solution.

Hydrodynamic instabilities are unsteady, requiring a different averaging process to stationary turbulence. There is some debate regarding the exact physical basis to justify the usage of Unsteady Reynolds-Averaged Navier–Stokes (URANS) (Israel, 2023). In some cases, this involves a localised time-averaging to remove the smaller turbulent fluctuations of the flow. This can cause issues for problems with both turbulent fluctuations and deterministic unsteadiness, which each correspond to some timescale. The averaging process needs to resolve the deterministic unsteadiness and model the turbulent fluctuations. This is not possible if there is no separation, or spectral gap, between the associated timescales of the flow (Wilcox, 2006; Sandberg & Zhao, 2022). An alternative interpretation of URANS is that the computed flow field is the average of

an ensemble of equivalent realisations. Here, equivalence means that the macroscopic features of the flow are identical, but the microscopic scales differ between realisations of the flow. Averaging over these realisations removes the differing fluctuations, and represents the mean macroscopic flow as desired of the RANS models.

For many canonical flows that are two- or three-dimensional, homogeneity along a direction or plane allows for the flow features to be statistically averaged and reduced to a one-dimensional mean profile. This reduction down from two or three dimensions to modelling in just one-dimension can provide an incredible speed-up of simulations, providing the turbulence that is now modelled is accurately captured. In other cases the flow may only be reduced to two-dimensions, or a coarser mesh is viable as the same mesh resolution is not required to converge the simulation. RANS modelling of hydrodynamic instabilities is a key tool for applications where the range of scales are not computationally possible to resolve. Examples include modelling ICF capsule designs (Amendt *et al.*, 2002; Bradley, 2014; Bradley *et al.*, 2012; Casey *et al.*, 2014; Smalyuk *et al.*, 2014), high-energy density mixing (Hurricane *et al.*, 2012), and astrophysics (Scannapieco & Brüggen, 2008).

The Reynolds-average of the flow is denoted by an over-bar, which allows the field variables to be decomposed into the mean and fluctuating components,

$$\phi = \bar{\phi} + \phi'. \tag{2.43}$$

The average of the mean variable is itself, whilst the average of the fluctuating quantity is zero. For compressible and variable-density flows, the Favre average is used, where the average is density weighted:

$$\tilde{\phi} = \frac{\overline{\rho\phi}}{\bar{\rho}} \tag{2.44}$$

which permits the decomposition

$$\phi = \tilde{\phi} + \phi'', \tag{2.45}$$

where the fluctuating component has a density weighted average of zero, $\overline{\rho\phi''} = 0$. Decomposing the compressible, multi-species Navier-Stokes equations gives rise to higher order correlations like the stress tensor for LES shown in equation (2.38). There are an assortment of models which can be used to achieve closure for the high-order correlations. Given the necessity to model the Reynolds stress, $\widetilde{u_i''u_j''}$, there are two main approaches to doing this. The most accurate method is to use a transport equation to calculate the Reynolds stress. The work by Besnard *et al.* (1992) derives the Favre-averaged transport equations for the Reynolds stresses $R_{ij} = \overline{u_i''u_j''}$. However,

the number of equations required makes this approach expensive, leading to the simpler approach of using a transport equation for the turbulent kinetic energy, $\tilde{K} = \widetilde{u_i'' u_i''}/2$. In the absence of velocity gradients, this method assumes isotropy for the distribution of the turbulent kinetic energy. This assumption is not accurate for RTI and RMI, which possess anisotropic energy distributions in the absence of velocity gradients.

In addition to the Reynolds stress or turbulent kinetic energy, it is necessary to transport another variable with different dimensionality that allows for the construction of a turbulent viscosity and a turbulent dissipation rate of the turbulent kinetic energy. A common approach is to transport the turbulent dissipation rate, leading to the common K-ϵ model Speziale (1987). The K-ϵ has found some use in modelling interfacial instabilities (Gauthier & Bonnet, 1990; Morán-López & Schilling, 2013, 2014), and the early Reynolds stress models use the turbulent dissipation rate Besnard *et al.* (1992); Grégoire *et al.* (2005). It is more common to use the turbulent length scale L (or S in the BHR models), instead of the turbulent dissipation rate, for two main reasons. Firstly, the turbulent length scale has a more physical meaning for initialisation of non-turbulent interfaces, where it may be initialised in relation to the perturbation amplitude or surface roughness, as compared to the dissipation rate. Secondly, using the length scale allows for easier comparison and analysis of the late time, when the length scale is expected to grow self-similarly with the mixing layer width. The turbulent dissipation rate is then calculated as a function of $\tilde{K}$ and L,

$$\epsilon = C_D \frac{\tilde{K}^{3/2}}{L}. \tag{2.46}$$

Youngs (1989, 1994) uses a two-equation two-fluid model, transporting K and a turbulent length scale. As a two-fluid model it is capable of describing de-mixing whilst other models cannot. The turbulent length scale is also used in this model to act as a drag length scale between the two fluids, providing energy to the turbulent kinetic energy. The K-L model by Dimonte & Tipton (2006) uses a phenomenologically derived transport equation for L, based off the buoyancy-drag equations. The K-L model has seen many evolutions, just like the neighbouring BHR model, which is based off the work in Besnard *et al.* (1992). The BHR-1 model (Banerjee *et al.*, 2010) is a three-equation model, which also transports the turbulent mass flux ($a_i = -\overline{u_i''}$). The benefit of transporting the turbulent mass flux is it simplifies the buoyancy-production in the transport equation for turbulent kinetic energy, which otherwise requires a shock-detection system to ensure that RTI is treated correctly for the different acceleration directions (Dimonte & Tipton, 2006; Kokkinakis *et al.*, 2019). Despite this, K-L remains a popular model for investigation and calibration (Campos & Morgan, 2019; Chiravalle, 2006; Kokkinakis *et al.*, 2015, 2020; Morgan & Greenough, 2016; Xiao *et al.*, 2020*a*, 2021; Zhang *et al.*, 2020). The

addition of the turbulent mass-flux also allows for closure approaches besides gradient diffusion for the turbulent transport of the species mass fraction, as the turbulent mass-flux can be better aligned with the turbulent transport at early times (Morgan & Greenough, 2016; Kokkinakis *et al.*, 2019).

The K-L and BHR models have continued to evolve, introducing additional equations to transport quantities that may have previously been algebraically closed. In the transport equation for a_i in the K-L-a model (Morgan & Wickett, 2015) and the BHR-1 model (Banerjee *et al.*, 2010), an algebraic closure is used for the specific density-volume covariance, $b = \overline{\rho'(1/\rho)'}$ which is used for the production of a_i. The BHR-2 model (Denissen *et al.*, 2012, 2014) introduces a transport equation for b, whilst the K-L-a-V model Morgan *et al.* (2018*a*) introduces the scalar variance for species mass fraction $V = \widetilde{Y_a'' Y_a''}$, as it behaves better in the low-Atwood number limit and is more useful for calculating reaction rates of the flow. The addition of a second length scale has been found to be beneficial, separating the dissipation and turbulence length scales, allowing the models to more accurately capture the difference between homogenous and inhomogeneous flows (Schwarzkopf *et al.*, 2016) and capture the correct turbulence intensity and growth rate for shear flows (Morgan *et al.*, 2018*b*).

The return of Reynolds stress models in BHR-3 models (Schwarzkopf *et al.*, 2011, 2016), BHR-4 (Braun & Gore, 2021), and for several K-L models (Morgan *et al.*, 2023) demonstrate that the computational cost of the more expensive models is no longer an inhibition, and the improved capability of capturing anisotropy of the turbulent kinetic energy is worthwhile. With the improvement of computational power over the decades and the increased demand for fast and accurate results for modelling purposes, the RANS models have become more complicated than ever. Whilst the early two-equation models might involve solving eight equations for two species, BHR-4 requires 26 equations and the R-ϕ-$2L$-a-$\mathcal{C}$ model requires 19 equations. These simulations can still be far cheaper than performing the far more highly resolved DNS or LES. The utility of these models is only in their ability to approximate the results of experimental results, DNS, and LES. The closure and modelling of higher-order correlations in turbulence will always leave room for improvement, hence the development of turbulence models will continue.

2.3.4 Buoyancy-drag model

The buoyancy-drag model is an approximation to the growth of a turbulent mixing layer through ordinary differential equations (ODEs) that aims to connect the initial growth rate of the mixing layer in the linear regime to the late time growth rates of the mixing layer. Layzer (1955) used a potential flow model to analyse the growth of a bubble for $At = 1$ RTI, reproducing an

exponential growth rate and a quadratic growth rate (constant acceleration) expected for free-fall in the late time. The heuristic model of Baker & Freeman (1981) in contrast modelled the forces on simplified bubble and spike structures with large density ratios. Through Newton's law, the resulting ODE was able to satisfy the linear and late-time growth rates for a single mode. Defining the growth velocity of the mixing length, V_i, the second-order ODE may be expressed as two first-order ODEs. The evolution of the mixing length h_i is evolved according to,

$$\frac{\mathrm{d}h_i}{\mathrm{d}t} = V_i + \Delta U_h \tag{2.47}$$

where commonly h_S is the spike height, h_b is the bubble height. Linden *et al.* (1994) adjusts the model by Layzer (1955) for all Atwood numbers with the evolution equation

$$(2+E)\frac{\mathrm{d}V_b}{\mathrm{d}t} = At\, g(1-E) - C_{d,b}\frac{V_b^2}{\lambda}, \tag{2.48}$$

where $E = \exp[-6\pi h_b/\lambda]$ acts to transition the solution between the linear regime ($h_b << \lambda$) and the late-time, self-similar regime ($h_b > \lambda$). An alternate but similar general form for the evolution of the mixing velocity is specified by

$$(\rho_1 + C_A\rho_2)\frac{\mathrm{d}V_b}{\mathrm{d}t} = \beta(\rho_1 - \rho_2)g - C_{d,b}\frac{V_b^2}{h_b}. \tag{2.49}$$

The left-hand side represents the volume-normalised inertial term of the form mass multiplied by acceleration (rate of change of velocity). For the bubble, the density is ρ_1 plus the added mass $C_A\rho_2$. The first term on the right-hand side is the buoyancy term that depends upon the difference in the fluids densities and the gravitational acceleration. The β term acts to further decrease the buoyancy within the mixing layer due to the mixing of the fluids causing a smaller density contrast (Dimonte & Schneider, 1996). The last term is the drag term, which is reminiscent of Newtonian drag. Simplifying the model by assuming $C_A = 1$ the equation now uses the Atwood number,

$$\frac{\mathrm{d}V_b}{\mathrm{d}t} = \beta At\, g - C_{d,b}\frac{V_b^2}{h_b}, \tag{2.50}$$

and $C_{d,b}$ has been modified to incorporate the density factor. The coefficients of this model can be calibrated for the late-time behaviour. For RTI with constant g, the solution $h_b = \alpha_B\, At\, gt^2$ provides the constraint that $\beta = 2(1 + 2C_{d,b})$. Likewise for RMI, where following the impulsive acceleration the gravity is zero, the expected solution is of the form $h_B = A(t - t_0)^\theta$, which requires $C_{d,b} = (1-\theta)/\theta$.

In the late-time this term depends upon the bubble height as represented here, however this can be overly dissipative in the early time when the height is very small. Ramshaw (1998) uses a

model which used the minimum of the perturbation wavelength and an adjusted bubble height for the drag length scale. Srebro *et al.* (2003) likewise uses the initial wavelength, and then at an Atwood number dependent bubble height threshold the length scale evolves with the scaled bubble velocity.

Youngs & Thornber (2020*a*,*b*) likewise use a piecewise function for the effective drag length scale, however this approach is further justified by the physics of the problem. The evolution of the mixing layer is described in four stages, with different expected evolution equations for the mixing layer growth rate. Firstly, the impulsive acceleration regime expects an almost constant growth rate ($\dot{V} = 0$). In the weakly non-linear stage ($h \propto \lambda$) the mixing layer will conserve the turbulent kinetic energy, creating a drag term. In the non-linear stage, the addition of viscous dissipation causes the net drag to increase. This is similar to the approach taken by Ramshaw (1998) using Lagrange equations for conservation of turbulent kinetic energy in the mixing layer to obtain the inviscid solution, and with the introduction of viscosity the RMI growth rate is restricted to $\theta \leq 2/3$. At late-time, the mixing layer drag should scale dominantly by the mixing width. The functional form of the calibrated effective drag length scale varies depending upon the Atwood number. For $At = 0.5$, the effective drag length scale takes the form,

$$l^{\text{eff}} = \bar{\lambda} \max \left[a - b\left(1 - e^{-cW/\bar{\lambda}}\right), \frac{\theta}{1-\theta}\left(\frac{W}{\bar{\lambda}} - d\right)\right], \tag{2.51}$$

whilst for $At = 0.9$ it is

$$l^{\text{eff}} = \bar{\lambda} \max \left[a + b\frac{W}{\bar{\lambda}}, \frac{\theta}{1-\theta}\left(\frac{W}{\bar{\lambda}} - d\right)\right]. \tag{2.52}$$

It is interesting to note the moderate Atwood number case has resemblance to the Layzer model with the exponential term scaling the drag length scale.

For estimating the spike profile, several approaches have been used. The models that assume the same power-law growth applies for bubbles and spikes often use the bubble height for the spike drag, but often scaled by an Atwood number dependent factor (Hansom *et al.*, 1990; Youngs & Thornber, 2020*a*). Oron *et al.* (2001) instead preferred to use a single Atwood number-independent drag length scale for both the bubble and spike.

Strain rates in fluid flow are a key driver of turbulence, responsible for the shear production of turbulent kinetic energy and the vortex stretching of eddies. Large scale mean strain rates are observed under a variety of scenarios, with shear strain occurring in boundary layers and normal strain occurring at geometric deformations such as nozzles. Shear driven mixing layers, such as those induced by the Kelvin-Helmholtz instability, are more well studied than the evolution of turbulent mixing layers under mean normal strain. In the high strain rate limit, where the

strain timescale is much smaller than the turbulence timescale, the evolution of turbulence is described by rapid-distortion theory (Hunt & Carruthers, 1990; Durbin & Zeman, 1992; Cambon *et al.*, 1993; Blaisdell *et al.*, 1996). These studies provide useful tools for understanding the pressure-dilatation tensor, however many are limited by the assumption of homogenous turbulence. This is in contrast to realistic applications where turbulence is inhomogeneous and may not satisfy the high strain limit. Likewise, the analysis of incompressible fluid flow is simpler than the analysis of compressible flow, with many compressible flow models relying upon incompressible flow closures.

2.4 Compression and strain

The effects of strain rates are present in both compressible and incompressible flows. A distinction between the two regimes is clearly the compressibility, for which the incompressible cases enforce zero divergence. This is quantified by looking at the velocity gradient tensor,

$$A_{ij} = \frac{\partial u_i}{\partial x_j}. \tag{2.53}$$

For incompressible flow, the trace of the velocity gradient tensor must be zero,

$$A_{ii} = \frac{\partial u_i}{\partial x_j} = 0. \tag{2.54}$$

however this does not preclude the individual components from being non-zero. The off-diagonal components, which correspond to shear strain, do not affect the bulk compression of the flow. There are four base arrangements observed for incompressible flows with mean velocity gradients (Pope, 2000). These four arrangements correspond to axisymmetric contraction, axisymmetric expansion, plane strain, and shear, with visualisations of the deformations shown in figure 2.7. All cells have the same volume, however they have been distorted due to the different combinations of the strain rates in each direction.

Compressible flows also permit isotropic compression or expansion, which will uniformly contract or expand the fluid and will change the volume of a fluid packet, affecting the density. With strain rates, the position of a particle in the flow field $x_i(X_j, t)$ is given by,

$$\mathrm{d}x_i = \frac{\partial x_i}{\partial t}\mathrm{d}t + \frac{\partial x_i}{\partial X_j}\mathrm{d}X_j = U_i\mathrm{d}t + F_{ij}\mathrm{d}X_j, \tag{2.55}$$

where X_i is the particle's position at the initial time $t = 0$, and F_{ij} is the Lagrangian displacement tensor (Cambon *et al.*, 1993). The evolution of the Lagrangian displacement tensor is calculated from the velocity gradient,

$$\dot{F}_{ij} = A_{ik}F_{kj} \tag{2.56}$$

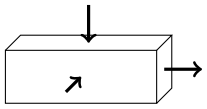

(a) Axisymmetric contraction

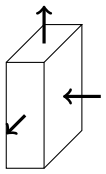

(b) Axisymmetric expansion

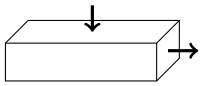

(c) Planar strain

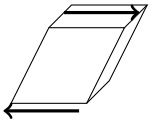

(d) Shear

Figure 2.7: Modification of a cubic cell from the given strain profile.

with the initial conditions of $F_{ij}(t=0) = \delta_{ij}$. Using the Lagrangian displacement vector for the mean strain rates can allow for simulating using an alternate coordinate basis, which deforms with the mean flow (Rogallo, 1981; Blaisdell *et al.*, 1996). If considering only the mean flow with normal strain rates, thereby removing the spatial variance of F_{ij} and the off-diagonal terms, the mean deformation tensor evolution takes the form

$$\begin{pmatrix} \dot{F}_{11} & 0 & 0 \\ 0 & \dot{F}_{22} & 0 \\ 0 & 0 & \dot{F}_{33} \end{pmatrix} = \begin{pmatrix} \partial U_1/\partial x_1 & 0 & 0 \\ 0 & \partial U_2/\partial x_2 & 0 \\ 0 & 0 & \partial U_3/\partial x_3 \end{pmatrix} \begin{pmatrix} F_{11} & 0 & 0 \\ 0 & F_{22} & 0 \\ 0 & 0 & F_{33} \end{pmatrix} \tag{2.57}$$

In this configuration, the terms are decoupled and evolve independently, with solutions taking the form

$$F_{11} = \exp\left[\int_0^t \partial U_1/\partial x_1 \, \mathrm{d}t\right]. \tag{2.58}$$

For the case of only normal strain rates, each component describes the expansion factor in the given direction. More generally, the determinant of F_{ij} is equal to the total expansion ratio, or volumetric ratio, of the domain.

It is also common to describe flows using the strain rate tensor, which corresponds to the symmetric component of the velocity gradient tensor,

$$S_{ij} = \frac{1}{2}\left(A_{ij} + A_{ji}\right). \tag{2.59}$$

The main diagonal is unchanged by this transformation, whilst the shear components are modified. Therefore, when discussing only the effects of the normal strain rates, the two tensors are functionally equivalent. It is common to define the total strain rate magnitude for the domain as,

$$\mathcal{S}^2 = S_{ij}S_{ij}. \tag{2.60}$$

The strain rate magnitude has units of s^{-1} and can be used to quantify the strain timescale,

$$\tau_S = 1/\mathcal{S}. \tag{2.61}$$

For cases where the strain rate timescale is much shorter than the turbulence timescale, resulting in the strain rate affects dominating and driving the development of the flow, the flow is considered to be in the rapid distortion regime (Hunt & Carruthers, 1990; Coleman & Mansour, 1993; Pope, 2000). The turbulence timescale is given by k/ϵ, such that the rapid distortion regime requires

$$1/\mathcal{S} \ll k/\epsilon, \tag{2.62}$$

$$1 \ll \mathcal{S}k/\epsilon. \tag{2.63}$$

Rapid distortion theory is a useful tool for studying turbulence, however the analysis is limited to homogenous flow fields. By nature of homogeneity, the statistics of the flow are greatly simplified as they are invariant of space and direction. Further, many regimes of interest do not achieve the rapid distortion limit. Instead, the flow is not strained fast enough for the other effects, such as dissipation, to be negligible compared to the strain effects, like shear production.

2.4.1 Compressed inhomogeneous turbulence

In spherical configurations, implosions and explosions are examples of bulk fluid moving to inner and outer radii, respectively. A turbulent mixing layer in an implosion or explosion will experience mean strain rates due to the radial velocity profile. The mean radial strain rate ($\bar{S}_{rr}$) and circumferential strain rate ($\bar{S}_{\theta\theta}$) for a spherically symmetric flow are given by,

$$\bar{S}_{rr} = \frac{\partial \bar{u}_r}{\partial r}, \tag{2.64}$$

$$\bar{S}_{\theta\theta} = \frac{\bar{u}_r}{r}. \tag{2.65}$$

These strain rates depend upon the mean radial velocity ($\bar{u}_r$) and the radius (r).

Hydrodynamic instabilities and the advection of fluids play an important role in the evolution of stellar bodies (Arnett, 2000). For example, core-collapse supernovae are some of the largest explosions in the universe, with mixing occurring due to an expansive blast-wave from the core that induces both RMI and RTI (Miles, 2009). An idealised version of this problem is given by the Taylor-von Neumann-Sedov blast-wave, which provides a self-similar analytical solution for a spherically expanding blast-wave (Sedov, 1946; Taylor, 1950*b*,*a*; Goldstine & Neumann, 1955). The self-similar profiles are functions of the radius relative to the time-varying radial position of the shock front of the blast-wave, $\zeta = r/R(t)$. The velocity profile scales proportionally to the

self-similar function $V(\zeta)$, which is typically solved for numerically. The velocity profile,

$$v(r,t) = \frac{2rV(\zeta)}{5t} \tag{2.66}$$

describes a self-similar profile as shown in figure 2.8, where the velocity is normalised by the velocity of the fluid immediately behind the shock-wave, v_1. The velocity profile can be used to obtain the radial and circumferential strain rates. The anisotropy of the strain rates is also self-similar as a function of ζ:

$$\bar{S}_{rr}/\bar{S}_{\theta\theta} = 1 + \frac{\zeta}{V(\zeta)}\frac{dV(\zeta)}{d\zeta}. \tag{2.67}$$

This equation is plotted in figure 2.8 and shows a profile that deviates away from the isotropic value of unity. Immediately behind the shock-front, the strain rates are anisotropic, with the radial strain rate up to twice as large as the circumferential strain rate. Whilst this model does not explicitly consider the interaction of the blast-wave with an interface and the resulting wave transmission and reflection, inferences can still be obtained about the evolution of the mixing layer. The interaction between the blast-wave and an interface between different density fluids will induce RMI due to the blast-wave's impulsive acceleration. Following the blast-wave interaction, the mixing layer's relative radius (ζ) will decrease from $\zeta = 1$, and experience anisotropic strain rates, stretching more in the radial direction than the circumferential direction. As time continues, the strain rates experienced by the mixing layer will tend toward isotropy.

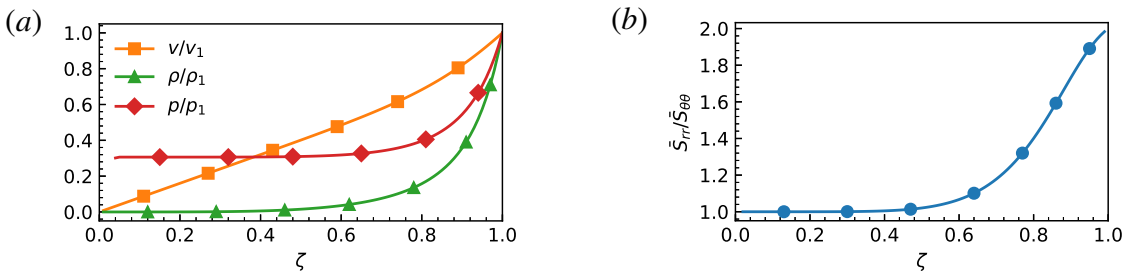

Figure 2.8: Self similar profiles as a function of relative radius, $\zeta = r/R(t)$, for the Taylor-von Neumann-Sedov blast wave. (*a*) Velocity, density, and pressure normalised to values immediately behind the shock front; (*b*) Strain rate anisotropy.

Inertial confinement fusion is an example of an implosion profile, where small capsules containing fuel for nuclear fusion are compressed (Nuckolls *et al.*, 1972), driven directly by lasers, or indirectly by X-rays (Betti & Hurricane, 2016). To achieve the pressures and temperatures necessary for fusion to occur, a series of pulses are used to launch shock waves into the capsule, causing the capsule to compress. Perturbations in the interfaces between the capsule's layers can arise from limitations in machining, or from asymmetries in the driving on the capsule

surface. These perturbations make the system susceptible to hydrodynamic instabilities, either from shock interaction (RMI) or interface accelerations (RTI). The instabilities are responsible for mixing the cold, outer fuel with the hot fuel at the centre hot-spot, degrading performance and preventing ignition (Lindl *et al.*, 2004, 2014). A simplified, idealised implosion profile used for modelling the hydrodynamics of inertial confinement fusion was presented in Youngs & Williams (2008) and used as a template for many further investigations for both single-mode (Flaig *et al.*, 2018; Heidt *et al.*, 2021) and multimode interface perturbations (Joggerst *et al.*, 2014; Boureima *et al.*, 2018; El Rafei *et al.*, 2019; El Rafei & Thornber, 2020, 2024). The mixing layer position and the mean radial velocity profile at several time instants are shown in figure 2.9 for the implosion profile, using the data from El Rafei & Thornber (2024). Evaluating the displayed mean radial velocity profiles, the radial velocity gradient across the mixing layer shows a positive trend, indicating expansive radial strain rates. The radial velocity is negative, as expected for an implosion, which correlates to a compressive circumferential strain rate. These profiles are taken during the intervals between shock interactions, and suggest that when the mixing layer is evolving between shocks, it experiences anisotropic strain rates. The anisotropy of the strain rates across the mixing layer is also plotted in figure 2.9, and shows that the ratio of the strain rates tends towards -1 rather than unity. There are times at which the anisotropy ratio goes above unity, aligning with the times the shock wave is compressing the turbulent mixing layer, such that the radial strain rate is more compressive than the circumferential strain rate. However, for the majority of the simulation the circumferential strain rate is negative (compression), whilst the radial strain rate is positive (expansive).

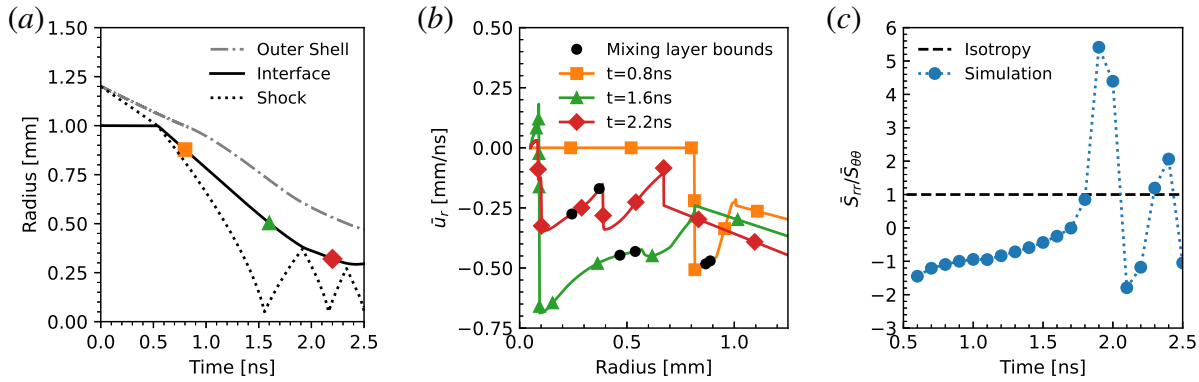

Figure 2.9: Characteristics of idealised implosion simulation (El Rafei & Thornber, 2024). (*a*) Implosion profile, (*b*) mean radial velocity profile at several time-steps, (*c*) strain rate anisotropy across the mixing layer.

In these examples, the inhomogeneous mixing layers develop under the influence of strain rates. However, there are also the effects from other physics that are often the focus of the

research. Such effects include buoyancy production due to the pressure gradients, and shock and/or re-shock interactions, which rapidly compress the mixing layer and deposit vorticity. Analysing the role that continuous strain rates play on the mixing layer is important for better understanding and modelling the hydrodynamic instabilities in these scenarios. This is further complicated by the presence of anisotropic strain rates, which vary in time. Depending upon the scenario, different anisotropy ratios for strain will be observed for the mixing layer. It is therefore necessary to analyse how the different directions of strain affect the mixing layer development.

Given the different regimes of hydrodynamic instabilities and the anisotropic strain rates experienced, the investigation into the influence of the strain rates on the mixing layer development is broken down into the following research questions:

1. How does axial strain affect the growth of RMI in the linear regime, and how can it be modelled?

2. How does axial strain affect the growth of RMI in the turbulent regime, and how can it be modelled?

3. How does transverse strain affect the growth of RMI in the linear regime, and how can it be modelled?

4. How does transverse strain affect the growth of RMI in the turbulent regime, and how can it be modelled?

5. Are the assumptions used for closure in two-equation turbulence models valid in the anisotropic strain regimes, and/or can the models be improved?

Chapter 4 investigates questions 1 & 2, focusing on the axial strain effects, whilst chapter 5 focuses on transverse strain for questions 3 & 4. Both chapters use simulations to validate and/or derive models for the influence of strain of the mixing layers. Chapter 6 targets point 5 by comparing the efficacy of different RANS closures in simulating the cases performed in the aforementioned chapters.

CHAPTER 3

Governing Equations & Numerical Methods

The work conducted within this thesis employs numerical simulations to analyse the evolution of fluid flows under the application of strain rates. In section 3.1, the governing equations for the different models employed are described. Section 3.2 describes the computational approach taken to solve these models.

3.1 Governing Equations

3.1.1 Four-equation model

The four-equation model is the standard approach to computing the evolution of compressible, multi-species flows. The compressible Navier-Stokes equations (density ρ, velocity u_i, and total energy E) are augmented with a transport equation for species mass fraction Y_a, resulting in a total of four unique transport equations. The mass fraction represents the ratio of the species' mass to the total mass in a given cell,

$$Y_a = M_a/M \tag{3.1}$$

where M_a is the species mass and M is the total mass. Each Y_a is limited to the range of zero to one, with the sum of all species' mass fractions required to add to one for conservation of mass:

$$\rho = \sum_a \rho Y_a \tag{3.2}$$

$$1 = \sum_a Y_a \tag{3.3}$$

The four-equation model is given by the governing equations (Williams, 1985; Echekki &

Mastorakos, 2011; Poinsot & Veynante, 2012),

$$\frac{\partial \rho}{\partial t} + \frac{\partial}{\partial x_j}\left(\rho u_j\right) = 0 \tag{3.4a}$$

$$\frac{\partial \rho Y_a}{\partial t} + \frac{\partial}{\partial x_j}\left(\rho Y_a u_j\right) = \frac{\partial}{\partial x_j}\left(-\rho Y_a V_j^a\right) \tag{3.4b}$$

$$\frac{\partial \rho u_i}{\partial t} + \frac{\partial}{\partial x_j}\left(\rho u_j u_i + p\delta_{ij}\right) = \frac{\partial \tau_{ij}}{\partial x_j} + \rho g_i \tag{3.4c}$$

$$\frac{\partial \rho E}{\partial t} + \frac{\partial}{\partial x_j}\left(\left(\rho E + p\right)\tilde{u}_j\right) = \frac{\partial}{\partial x_j}\left(\tau_{ij}u_i - q_j - q_{d,j}\right) + \rho g_i u_i \tag{3.4d}$$

where the subscript a denotes species and is not used for tensor notation. The transport equation for mass is unchanged from single-species flows, as mass is still conserved. The transport equation for mass fraction takes a similar form as density, but includes a diffusion term on the right-hand-side, which diffuses species a in direction j with the species diffusion velocity $V_{a,j}$. The true velocity of each species is therefore a combination of the mass-weighted velocity u_i and the diffusive velocity $V_{a,i}$. There are several approximations to the calculation of $V_{a,i}$, the simplest of which is Fick's law of diffusion, which is valid for either a two-species system or a multi-species system with identical binary diffusion coefficients (D) between all species. These systems allow the computation of the diffusion velocity as

$$V_{a,i} = -\frac{D}{Y_a}\frac{\partial Y_a}{\partial x_i}. \tag{3.5}$$

With the single diffusivity then, the sum of the mass fraction diffusion fluxes will be zero,

$$\sum_a \rho Y_a V_{a,i} = \sum_a \rho D \frac{\partial Y_a}{\partial x_i} = \rho D \frac{\partial}{\partial x_i}\left(\sum_a Y_a\right) = 0, \tag{3.6}$$

consistent with the original density transport equation. All the simulations conducted within this work fulfil the requirements to use Fick's law of diffusion. As FLAMENCO, the in-house code used for simulations, uses the approximation of Hirschfelder *et al.* (1969) it is worthwhile describing the method. In this method, the diffusion velocity is calculated from the mole fraction X_a,

$$V_{a,i} = -\frac{D_a}{X_a}\frac{\partial X_a}{\partial x_i} \tag{3.7}$$

where the effective diffusivity has been calculated from the binary diffusivity coefficients between species,

$$D_a = \frac{1 - Y_a}{\sum_{b,a\neq b} X_b / D_{ab}}. \tag{3.8}$$

The mole fraction of each species is calculated using the species molecular weight m_a and the mixture mean molecular weight $\bar{m}$:

$$\bar{W}^{-1} = \sum_b \frac{Y_b}{m_b}, \tag{3.9}$$

$$X_a = \frac{Y_a \bar{m}}{m_a} = \frac{Y_a/m_a}{\sum_b Y_b/m_b}. \tag{3.10}$$

Unlike Fick's law, the Hirschfelder and Curtiss approximation does not always have a net-zero diffusive flux over all species, inconsistent with the density equation. To account for this, it is common to apply a correction velocity offset to the diffusion velocity,

$$V_i^c = \sum_a D_a \frac{m_a}{m} \frac{\partial X_a}{\partial x_i}, \tag{3.11}$$

$$V_{a,i} = -\frac{D_a}{X_a} \frac{\partial X_a}{\partial x_i} + V_i^c. \tag{3.12}$$

For constant diffusivity for all species, the approximation will reduce down to Fick's law. In the case of N species, it is only necessary to have N transport equations for density and mass fraction. For N transport equations, this may be either transporting the total density and $N-1$ species mass fractions, or transporting N species mass fractions. Transporting the total density may allow numerical errors to accumulate in the uncalculated species which in some applications may not be significant where the last species is inert.

The momentum equation is also unchanged as compared to single-species flow. The viscous stress tensor is treated under the assumption of Newtonian fluids, taking the form

$$\tau_{ij} = \mu \left(\frac{\partial u_i}{\partial x_j} + \frac{\partial u_i}{\partial x_j} \right) + \left(\frac{2}{3}\mu - \mu_b \right) \frac{\partial u_k}{\partial x_k} \delta_{ij}, \tag{3.13}$$

with a mixture dynamic viscosity μ and a bulk viscosity μ_b which is often taken to be zero. The total energy consists of an internal energy component $e = e(\rho, p)$ and a kinetic energy component,

$$E = e + \frac{1}{2} u_i u_i. \tag{3.14}$$

In the energy equation there is the enthalpy diffusion term $q_{d,j}$, and the conduction term q_j. The enthalpy diffusion term is responsible for transporting the species' enthalpy with the species as it diffuses,

$$q_{d,j} = \sum_a \rho Y_a V_{a,j} h_a. \tag{3.15}$$

The enthalpy of the species is given by $h_a = e_a + p_a/\rho_a$. The conduction term is calculated using Fourier's Law of conduction,

$$q_j = -\kappa \frac{\partial T}{\partial x_j}. \tag{3.16}$$

The conductivity of species a is calculated using kinetic theory,

$$\kappa_a = \mu_a \left(\frac{5}{4} \frac{\mathcal{R}}{m_a} + c_{p,a} \right) \tag{3.17}$$

with the species viscosity μ_a, species specific heat at constant pressure $c_{p,a}$, and the universal gas constant $\mathcal{R} = 8.3145\,\mathrm{J\,K^{-1}\,mol^{-1}}$. The mixture viscosity and mixture conductivity are calculated using Wilke's rule (Wilke, 1950),

$$K = \sum_a \frac{X_a K_a}{\sum_b X_b \phi_{ab}}, \tag{3.18}$$

$$\tag{3.19}$$

where $K = \mu$ for viscosity and $K = \kappa$ for the conductivity. Wilke's rule depends upon the Wilke coefficients ϕ_{ab} which are a function of the species' molecular weights and viscosity,

$$\phi_{ab} = \begin{cases} 1 & \text{if } a = b, \\ \left[8 \left(1 + \frac{W_a}{W_b} \right) \right]^{-1/2} \left[1 + \sqrt{\frac{\mu_a}{\mu_b}} \left(\frac{W_b}{W_a} \right)^{1/4} \right]^2 & \text{otherwise.} \end{cases} \tag{3.20}$$

It is common to calculate the diffusivity of the mixture viscosity or conductivity instead of the Hirschfelder and Curtiss approximation in equation 3.8. If using the mixture viscosity, then

$$D = \frac{\mu}{\rho\, Sc}, \tag{3.21}$$

where Sc is the Schmidt number as defined by the equation above. To use the conductivity, the equation is

$$D = \frac{\kappa}{\rho c_p\, Le}, \tag{3.22}$$

where Le is the Lewis and is the ratio of the Prandtl number to the Schmidt number.

3.1.2 Five-equation model

The number fraction model of Thornber *et al.* (2018) represents an extension of the non-conservative five-equation model of Allaire *et al.* (2002) and Massoni *et al.* (2002) to include the effects of viscosity and diffusion. The inclusion of the number fraction equation allows the model to more accurately capture the multi-species flows for fluids of different thermodynamics properties. The addition of the volume fraction reduces the number of assumptions that need to be made regarding the properties of species mixtures within a cell. Assuming a binary mixture for simplicity, the governing equations are composed of five transport equations for density, momentum, total energy, species mass fraction, and volume fraction:

$$\frac{\partial \rho}{\partial t} + \frac{\partial}{\partial x_j}\left(\rho u_j\right) = 0, \tag{3.23}$$

$$\frac{\partial \rho u_i}{\partial t} + \frac{\partial}{\partial x_j}\left(\rho u_i u_j + p\delta_{ij}\right) = \frac{\partial \tau_{ij}}{\partial x_j} + \rho g_i, \tag{3.24}$$

$$\frac{\partial \rho E}{\partial t} + \frac{\partial}{\partial x_j}\left(\left(\rho E + p\right) u_j\right) = \frac{\partial}{\partial x_j}\left(\tau_{ij} u_i + q_j + q_{dj}\right) + \rho g_i u_i, \tag{3.25}$$

$$\frac{\partial \rho Y_a}{\partial t} + \frac{\partial}{\partial x_j}\left(\rho Y_a u_j\right) = \frac{\partial}{\partial x_j}\left(D_{12}\rho \frac{\partial Y_a}{\partial x_j}\right), \tag{3.26}$$

$$\frac{\partial f_a}{\partial t} + u_j \frac{\partial f_a}{\partial x_j} = \frac{\partial}{\partial x_j}\left(D_{12}\frac{\partial f_a}{\partial x_j}\right) - \underline{m} D_{12}\frac{\partial f_1}{\partial x_j}\frac{\partial f_a}{\partial x_j} + D_{12}\frac{\partial f_a}{\partial x_j}\frac{\partial N}{\partial x_j}\frac{1}{N}. \tag{3.27}$$

The number fraction introduces the total number density, $N = p/k_b T$, and the parameter $\underline{m} = (m_1 - W_2)/(m_1 f_1 + m_2 f_2)$. The viscous stress tensor, heat flux, and enthalpy flux are all defined the same way as previously specified for the four-equation model.

The five-equation models have the advantage of allowing distinct species temperatures. This differs from the four-equation model which is commonly closed with isobaric and isothermal assumptions for the sub-cell mixture. Whilst the five-equation models are most advantageous for mixtures with differing thermodynamic properties, for which it prevents the generation of spurious pressure oscillations at contact surfaces, at the same grid size the five-equation model observes reduced errors compared to the mass fraction model.

3.1.3 K-L model

The K-L turbulence model is a two-equation RANS model first proposed by Dimonte & Tipton (2006). The K-L model is derived from the inviscid four-equation model, representing the high Reynolds number limit. Designed for compressible flows, the model uses Favre averages instead of Reynolds averages where possible. The Reynolds average of some quantity ϕ is given by $\bar{\phi}$, and is calculated by taking the average of the variable either in time, space, or an ensemble average.

$$\phi = \bar{\phi} + \phi' \tag{3.28}$$

By definition, the average of the fluctuating component is zero, $\overline{\phi'} = 0$. The Favre averaged is used for flows with variable density or compressibility, where the density may not be uniform, $\rho' \neq 0$. Decomposing a density scaled variable into the mean and fluctuation components gives the result,

$$\rho\phi = \bar{\rho}\bar{\phi} + \bar{\rho}\phi' + \rho'\bar{\phi} + \rho'\phi' \tag{3.29}$$

$$\overline{\rho\phi} = \bar{\rho}\bar{\phi} + \overline{\rho'\phi'} \tag{3.30}$$

Therefore, in compressible flows the Reynolds average of a variable multiplied by density will not reduce to $\bar{\rho}\bar{\phi}$ or $\rho\bar{\phi}$ as it does for the incompressible case, but now also includes the average of the fluctuation product. The Favre average is used to avoid this inclusion, by using the density weighted average.

$$\tilde{\phi} = \overline{\rho\phi}/\bar{\rho} \tag{3.31}$$

that allows a decomposition into the form,

$$\phi = \tilde{\phi} + \phi'' \tag{3.32}$$

with a fluctuation term that does not have a zero mean, $\overline{\phi''} \neq 0$, instead it has a zero-mean when density weighted, $\overline{\rho\phi''} = 0$. The averaging process of the governing equations introduces additional higher-order terms, such as caused by the non-linear advection term. In order to close the model, it is necessary to either derive transport equations for the higher-order correlations (introducing even higher-order correlations), or model the higher-order terms. The K-L model achieves closure through the introduction of two additional variables: the turbulent length scale L and the turbulent kinetic energy $\tilde{K} = \frac{1}{2}\widetilde{u_i''u_i''}$. This model was inspired by the buoyancy-drag model, such that using a self-similar analysis can reduce the transport equations for $\tilde{K}$ and L into a buoyancy-drag model. The governing equations for the K-L model are given by

$$\frac{\partial\bar{\rho}}{\partial t} + \frac{\partial}{\partial x_j}\left(\bar{\rho}\tilde{u}_j\right) = 0 \tag{3.33a}$$

$$\frac{\partial\bar{\rho}\tilde{u}_i}{\partial t} + \frac{\partial}{\partial x_j}\left(\bar{\rho}\tilde{u}_j\tilde{u}_i + \bar{p}\delta_{ij}\right) = \frac{\partial\bar{\tau}_{ij}}{\partial x_j} + \bar{\rho}g_i \tag{3.33b}$$

$$\frac{\partial\bar{\rho}\tilde{E}}{\partial t} + \frac{\partial}{\partial x_j}\left(\left(\bar{\rho}\tilde{E} + \bar{p}\right)\tilde{u}_j\right) = \frac{\partial}{\partial x_j}\left(\frac{\mu_T}{N_H}\frac{\partial\tilde{h}}{\partial x_j} + \frac{\mu_T}{N_K}\frac{\partial\tilde{K}}{\partial x_j}\right) + \frac{\partial\bar{\tau}_{ij}\tilde{u}_i}{\partial x_j} + \bar{\rho}g_i\tilde{u}_i \tag{3.33c}$$

$$\frac{\partial\bar{\rho}\tilde{Y}_a}{\partial t} + \frac{\partial}{\partial x_j}\left(\bar{\rho}\tilde{Y}_a\tilde{u}_j\right) = \frac{\partial}{\partial x_j}\left(\frac{\mu_T}{N_Y}\frac{\partial\tilde{Y}_a}{\partial x_j}\right) \tag{3.33d}$$

$$\frac{\partial\bar{\rho}\tilde{K}}{\partial t} + \frac{\partial}{\partial x_j}\left(\bar{\rho}\tilde{u}_j\tilde{K}\right) = \frac{\partial}{\partial x_j}\left(\frac{\mu_T}{N_K}\frac{\partial\tilde{K}}{\partial x_j}\right) + \bar{\tau}_{ij}\frac{\partial\tilde{u}_i}{\partial x_j} + S_K - C_D\bar{\rho}\frac{\tilde{V}^3}{L} \tag{3.33e}$$

$$\frac{\partial\bar{\rho}L}{\partial t} + \frac{\partial}{\partial x_j}\left(\bar{\rho}\tilde{u}_jL\right) = \frac{\partial}{\partial x_j}\left(\frac{\mu_T}{N_L}\frac{\partial L}{\partial x_j}\right) + C_L\bar{\rho}V + C_C\bar{\rho}L\frac{\partial\tilde{u}_j}{\partial x_j} \tag{3.33f}$$

The turbulent velocity is defined from the turbulent kinetic energy, $\tilde{V} = \left(2\tilde{K}\right)^{1/2}$. The equations have been closed by using a turbulent viscosity for the gradient diffusion approximation,

$$\mu_t = C_\mu\bar{\rho}L\sqrt{2\tilde{K}}. \tag{3.34}$$

The gradient diffusion approximates the higher-order correlation of the turbulent scalar flux to transport the mean scalar towards areas of lower concentration,

$$-\overline{\rho\phi'' u''} = \frac{\partial}{\partial x_i}\left(\frac{\mu_T}{N_\phi}\frac{\partial \bar{\phi}}{\partial x_i}\right). \tag{3.35}$$

The turbulent diffusivity is adjusted for each variable through the N_ϕ coefficient. The Reynolds stress tensor, $\bar{\tau}_{ij} = -\bar{\rho}\widetilde{u_i'' u_j''}$, is defined with the Boussinesq eddy viscosity assumption, using the mean velocity gradients and turbulent kinetic energy. The coefficient C_P is taken to be $2/3$ to ensure the trace of the Reynolds stress tensor is equal to the turbulent kinetic energy.

$$\bar{\tau}_{ij} = \mu_t\left(\frac{\partial \tilde{u}_i}{\partial x_j} + \frac{\partial \tilde{u}_j}{\partial x_i} - \frac{2}{3}\frac{\partial \tilde{u}_k}{\partial x_k}\delta_{ij}\right) - C_P\bar{\rho}\tilde{K}\delta_{ij} \tag{3.36}$$

This model differs from the original K-L model by Dimonte & Tipton (2006), instead using the enthalpy diffusion and the equation for total energy conservation given by Kokkinakis *et al.* (2015). With the inclusion of the turbulent kinetic energy, the total energy is given by

$$\tilde{E} = \tilde{e} + \frac{1}{2}\tilde{u}_i\tilde{u}_i + \tilde{K}, \tag{3.37}$$

which is why the diffusion of $\tilde{K}$ is also present in the total energy equation. The source term for the turbulent kinetic energy, S_K, is a buoyancy production term which is required to differentiate between the different forms of acceleration in RMI and RTI. The method implemented uses the approach by Xiao *et al.* (2020*a*), which is based on the work by Kokkinakis *et al.* (2015). The source term takes the form,

$$S_K = \begin{cases} C_B\bar{\rho}\tilde{V}\ \max\left(A_{L_i}g_i, 0\right), & \Theta_{g_f} \geq \Theta_{g_m} \\ C_B\bar{\rho}\tilde{V}|A_{L_i}g_{L_i}|, & \Theta_{g_f} < \Theta_{g_m} \end{cases} \tag{3.38}$$

where $g_{L_i} = -(1/\bar{\rho})\partial\bar{p}/\partial x_i$ is the local acceleration calculated from the pressure gradient, and A_{L_i} is the local Atwood number to be calculated from the local flow field. The flow is considered RT-like if the turbulent acceleration, $\Theta_{g_f} = \sqrt{\tilde{K}}/\Delta t^*$, is greater than the mean-field acceleration, $\Theta_{g_m} = (1/\bar{\rho})|\partial p/\partial x|$. The minimum timescale, Δt^*, is calculated by,

$$\Delta t^* = \min\left(\frac{\min(\Delta x_i)CFL}{|\tilde{u} + \bar{c}|}, \frac{L}{\bar{c}}\right), \tag{3.39}$$

using the CFL number, the minimum side length of the cell, Δx_i, and the local speed of sound, $\bar{c}$. The local Atwood number is calculated from densities reconstructed at the faces using van Leer's monotonicity principle (Kokkinakis *et al.*, 2015). The second-order slope for the density within each cell is calculated according to

$$\Delta_i = \left\{ \begin{array}{ll} \text{sign}(\Delta_{i+\frac{1}{2}})\min(|\Delta_{i-\frac{1}{2}}|, |\Delta_{i+\frac{1}{2}}|), & \text{if sign}(\Delta_{i-\frac{1}{2}}) = \text{sign}(\Delta_{i+\frac{1}{2}}) \\ 0, & \text{otherwise} \end{array} \right\} \tag{3.40}$$

where $\Delta_{i-\frac{1}{2}} = \bar{\rho}_i - \bar{\rho}_{i-1}$ is the unrestricted difference between the adjacent cells. The reconstructed states at each side of the cells are:

$$\bar{\rho}_i^L = \bar{\rho}_i - \frac{1}{2}\Delta_i, \qquad \bar{\rho}_i^R = \bar{\rho}_i + \frac{1}{2}\Delta_i \tag{3.41}$$

Using the reconstructed densities at each face, the values from either side of the face are averaged to give the face density:

$$\bar{\rho}_{i+\frac{1}{2}} = \frac{1}{2}\left(\bar{\rho}_i^R + \bar{\rho}_{i+1}^L\right) \tag{3.42}$$

The local Atwood number is calculated based upon an initial estimate and a steady-state estimate,

$$A_{L_i} = (1 - w_L)A_{0_i} + w_L A_{SS_i}. \tag{3.43}$$

The local initial Atwood number is calculated from the face-averaged density values, which in one-dimension may be written as,

$$A_{0_i} = \left(\frac{\bar{\rho}_{i+\frac{1}{2}} - \bar{\rho}_{i-\frac{1}{2}}}{\bar{\rho}_{i+\frac{1}{2}} + \bar{\rho}_{i-\frac{i}{2}}}\right)_i \tag{3.44}$$

The self-similar local Atwood number uses density gradient calculated from the mean density values at the faces. The one dimensional calculation takes the form,

$$\left(\frac{\partial\bar{\rho}}{\partial x}\right)_i = \frac{\bar{\rho}_{i+\frac{1}{2}} - \bar{\rho}_{i-\frac{1}{2}}}{\Delta x}, \tag{3.45}$$

$$A_{SS_i} = C_A \frac{L}{\bar{\rho} + L|\partial\bar{\rho}/\partial x|_i}\left(\frac{\partial\bar{\rho}}{\partial x}\right)_i. \tag{3.46}$$

The transition between the two Atwood number estimates is controlled by the weighting factor $w_L = \min(L/\Delta x, 1)$.

Verification of the implemented K-L model into the in-house code FLAMENCO is provided in Appendix A.

3.1.4 Equation of state

The previously mentioned governing equations provide a way to calculate the specified conserved variables. The systems require additional closure in the form of equations of state. All cases require a caloric equation of state, which typically relates the internal energy to pressure and density. For viscous simulations with conductivity, it is necessary to have a thermal equation relating the temperature to the other state variables. The caloric ideal equation of state is

$$p_a = (\gamma_a - 1)\rho_a e_a \tag{3.47}$$

where $\gamma_a = c_{p,a}/c_{v,a}$ is the ratio of specific heat at constant pressure to the specific heat ratio at constant volume. The thermal ideal gas equation of state is

$$p_a = \rho_a \bar{\mathcal{R}} T_a, \tag{3.48}$$

where the specific gas constant is the universal gas constant scaled by the molecular weight of the gas, $\bar{\mathcal{R}} = \mathcal{R}/m_a$. These equations of state apply to the individual fluids, however the conservation variables will provide information regarding the mixture. The internal energy within a cell is calculated according to

$$\rho e = \rho E - \frac{1}{2}\rho u_i u_i \, (-\rho \tilde{K}) \tag{3.49}$$

where the turbulent kinetic energy is also subtracted from the total energy only if it is the K-L model in use. For the models with only mass fraction information, the pressure of the mixture is found by using two approximations. Firstly, an isothermal closure is used across the species. Where $e_a = c_{v,a} T_a$, this allows the mass weighted internal energy to be calculated as

$$\rho e = \sum_a \rho Y_a c_{v,a} T_a = \rho c_v T \tag{3.50}$$

where $c_v = \sum_a Y_a c_{v,a}$ for the mass weighted specific heat at constant volume. The second approximation is Dalton's law of partial pressure, relating the volume fraction to the total pressure:

$$p = \sum_a f_a p_a. \tag{3.51}$$

Using equation 3.47 for the species on the right-hand side as well as for the mixture pressure will give the specific heat ratio for the mixture:

$$\gamma = \frac{\sum_a Y_a c_{p,a}}{\sum_a Y_a c_{v,a}}. \tag{3.52}$$

To obtain further information, such as ρ_a or f_a, it is then necessary to make further approximations. This typically involves using the isobaric closure so that all species are at the same pressure. Under this assumption the mole fraction and the number fraction are equal, $X_a = f_a$. For the five-equation model, the isobaric closure leads directly to the relation

$$\frac{1}{\gamma - 1} = \sum_a \frac{f_a}{\gamma_a - 1}, \tag{3.53}$$

for the mixture specific heat ratio.

3.2 Numerical Methods

The simulations performed in the thesis are conducted with the finite-volume code Flamenco. Finite volume codes are well-suited for simulating problems with discontinuities.

The integral form of a conservative partial differential equation takes the form

$$\frac{\partial}{\partial t}\int_V \boldsymbol{U} dV + \oint_S \boldsymbol{F} dS = 0. \tag{3.54}$$

for the vector of conservative variables $\boldsymbol{U}$ and the flux vector $\boldsymbol{F}$ for a cell with volume V and surface S. In the case of the Euler equations, the vectors are given by,

$$\boldsymbol{U} = \begin{pmatrix} \rho \\ \rho u_j \\ \rho E \end{pmatrix}, \tag{3.55}$$

$$\boldsymbol{F} = \begin{pmatrix} \rho u_k n_k \\ (\rho u_j u_k + p\delta_{jk}) n_k \\ ([\rho E + p]\, u_k n_k \end{pmatrix}. \tag{3.56}$$

where n_k is the normal vector from the surface of integration. In one-dimension with an explicit time-step, the system evolves according to,

$$\boldsymbol{U}_i^{n+1} = \boldsymbol{U}_i^n + \frac{\Delta t}{\Delta x}\left[\boldsymbol{F}_{i-1/2} - \boldsymbol{F}_{i+1/2}\right]. \tag{3.57}$$

Here the subscript of the vectors refers to the position of the vector along the mesh, as opposed to an index for summation in tensor notation. $\boldsymbol{U}_i^n$ refers to the solution vector in cell i at time iteration n, and $\boldsymbol{F}_{i-1/2}$ is the flux between cells $i-1$ and i.

Section 3.2.1 details the basis of the Godunov scheme used to calculate the finite-volume flux, whilst section 3.2.2 details the methods used to increase the spatial order of accuracy, whilst section 3.2.4 details methods to improve the temporal order of accuracy. The adaptations for the flux calculations for a moving mesh are detailed in section 3.2.3. Finally, section 3.2.5 details the modifications necessary to improve Godunov schemes at low Mach numbers.

3.2.1 Godunov's method

The method introduced by Godunov *et al.* (1976) focuses on solving the Riemann problem to evaluate the fluxes of the discretised system. The Riemann problem is a method to solve

hyperbolic partial differential equations, such as the Euler equations, with a suitable equation of state. The initial conditions for the Riemann problem consist of two discontinuous states, taken about a reference origin.

$$ICs : \boldsymbol{U}(x,0) = \begin{cases} \boldsymbol{U}_L & \text{if } x < 0 \\ \boldsymbol{U}_R & \text{if } x > 0 \end{cases} \tag{3.58}$$

Solving the Riemann problem requires solving for the eigenvalues/wave-speeds of the problem, as well as any intermediate states. The Euler equations in one-dimension will produce a solution of three waves, as shown in figure 3.1.

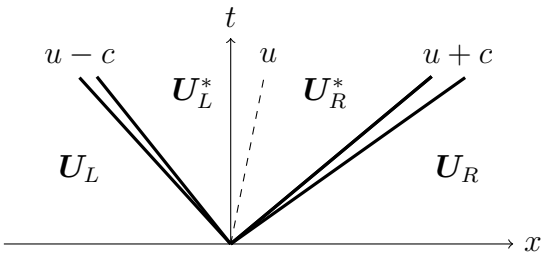

Figure 3.1: Characteristic wave-speeds for the Riemann problem with the Euler equations.

One wave is an entropy, or contact, wave which travels at velocity u, whilst the other waves are acoustic waves which may be either shock waves or rarefaction waves with some associated speed of $u \pm c$. There are four total states, consisting of the two initial condition states outside the pressure waves, and two intermediate star states within. As the waves move with a constant speed, the solution of the Riemann problem for a given time and position will only depend upon the ratio x/t.

$$\boldsymbol{U}(x,t) = \boldsymbol{U}^{RP}\left(\frac{x}{t}\right) \tag{3.59}$$

The Godunov method utilises the cell-averaged solution within each cell, creating a piece-wise constant distribution:

$$\boldsymbol{U}_i^n = \frac{1}{\Delta x}\int_{x_{i-1/2}}^{x_{i+1/2}} \boldsymbol{U}(x,t^n)dx \tag{3.60}$$

An example of the resulting distribution is shown in figure 3.2 for a quarter sine wave and discontinuity. Whilst the cell average solution at the centre of the cell is close to the corresponding true solution, the two values are not equal. As the number of cells is increased, this difference shrinks and discretisation becomes more representative of the underlying function.

Initialised with this discretisation, the face between two cells corresponds to a Riemann problem that can be used to evolve the system. Whilst the first version of the Godunov method

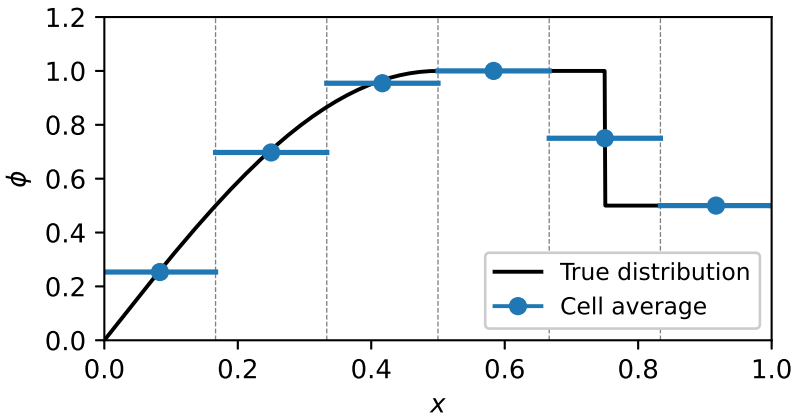

Figure 3.2: Discretisation of a continuous and discontinuous solution into cell averages.

solved the Riemann problem to integrate over the solution at time Δt to determine the solution, the second method is less computationally expensive and allows for a larger time step size. This Godunov method solves the Riemann problem centred on each interface and uses the solution state at the cell boundary to calculate the flux. For the face at location $i + 1/2$ between cells i and $i + 1$, this may be written as,

$$\boldsymbol{F}_{i+1/2} = \boldsymbol{F}\left(\boldsymbol{U}^{RP}_{i+1/2}\left(\frac{x}{t} = 0\right)\right). \tag{3.61}$$

For a one-dimensional calculation, the flux needs to be evaluated at both faces of the cell as shown in figure 3.3. The time step restriction then naturally arises from requiring the solution waves to only act within the adjacent cells and to not alter the Riemann problem solution at a neighbouring face. Ensuring the maximum wave-speed does not travel more than the cell width limits the time step size to,

$$\Delta t = CFL\frac{\Delta x}{S_{\text{max}}}, \tag{3.62}$$

where the CFL number is limited to the domain of $\in (0, 1)$.

Calculating the exact Riemann problem solution for the Euler equations is an expensive, iterative process. Instead of using the exact Riemann solver, a variety of approximate Riemann solvers have been designed to more efficiently solve the Riemann problem, with a small cost in accuracy. The approximate Riemann solver employed in the thesis is the Harten-Lax-van Leer-Contact (HLLC) Riemann solver (Toro *et al.*, 1994), which is an evolution of the HLL Riemann solver (Harten *et al.*, 1983) but with the additional capability of being able to resolve the contact wave. The first step in the HLLC Riemann solver is the estimation of the wave speeds.

A simple method to estimate the left and right wave speeds is

$$S_L = \min(u_L - a_L, u_R - a_R), \tag{3.63}$$

$$S_K = \max(u_L + a_L, u_R + a_R). \tag{3.64}$$

A more accurate method uses a pressure-based estimate (Toro *et al.*, 1994), where the intermediate pressure is estimated using the primitive-variable Riemann solver approximation,

$$p_{pvrs} = \frac{1}{2}(p_L + p_R) - \frac{1}{2}(u_R - u_L)\bar{\rho}\bar{a} \tag{3.65}$$

$$p^* = max(0, p_{pvrs}) \tag{3.66}$$

with the mean density $\bar{\rho} = (\rho_L + \rho_R)/2$ and the mean speed of sound $\bar{a} = (a_L + a_R)/2$. Depending upon the pressures, it can be beneficial to re-calculate the intermediate pressure with either the two-rarefaction estimate or the two-shock estimate for pressure, as done in the Adaptive Non-iterative Riemann Solver by Toro (2009). The wave speeds are then calculated by

$$S_L = u_L - a_L q_L, \tag{3.67}$$

$$S_R = u_R + a_R q_R, \tag{3.68}$$

where the speed of sound contribution is scaled by the correspond variable for $K = L$ and $K = R$:

$$q_K = \begin{cases} 1 & \text{if } p^* < p_K \\ \left[1 + \frac{\gamma+1}{2\gamma}\left(\frac{p^*}{p_K} - 1\right)\right]^{1/2} & \text{otherwise} \end{cases} \tag{3.69}$$

The flux to be evaluated will then depend accordingly on the wave-speeds, selecting the state that is aligned with $x/t = 0$. Figure 3.1 shows these wave-speeds for the control volume. It is only necessary to calculate the intermediate states for subsonic flow.

$$\boldsymbol{F}_{i-1/2} = \begin{cases} \boldsymbol{F}(\boldsymbol{U}_{i-1}) & \text{if } 0 \leq S_L \\ \boldsymbol{F}^*_L & \text{if } S_L \leq 0 \leq S^* \\ \boldsymbol{F}^*_R & \text{if } S^* \leq 0 \leq S_R \\ \boldsymbol{F}(\boldsymbol{U}_i) & \text{if } S_R \leq 0 \end{cases} \tag{3.70}$$

The intermediate wave solution can either be calculated from the left and right wave speeds, or from the intermediate pressure estimate for the specific estimation methodology. Estimates for

the intermediates states are then given by

$$\mathbf{U}_{*K} = \rho_K \left(\frac{S_K - u_K}{S_K - S_*} \right) \begin{bmatrix} \rho_K \\ \rho_K S_* \\ \rho_K v_K \\ \rho_K w_K \\ E_K + (S_* - u_K) \left[\rho_K S_* + \frac{p_K}{(S_K - u_K)} \right] . \end{bmatrix} \tag{3.71}$$

The HLLC Riemann solver solves for the intermediates state fluxes based upon estimates of the wave speeds by using the Rankine-Hugoniot jump condition rather than using the intermediate state variables directly to calculate the flux. The jump relations across these waves for the intermediate fluxes are given by

$$\boldsymbol{F}_L^* = \boldsymbol{F}_L + S_L \left(\boldsymbol{U}_L^* - \boldsymbol{U}_L \right), \tag{3.72}$$

$$\boldsymbol{F}_R^* = \boldsymbol{F}_R + S_R \left(\boldsymbol{U}_R^* - \boldsymbol{U}_R \right). \tag{3.73}$$

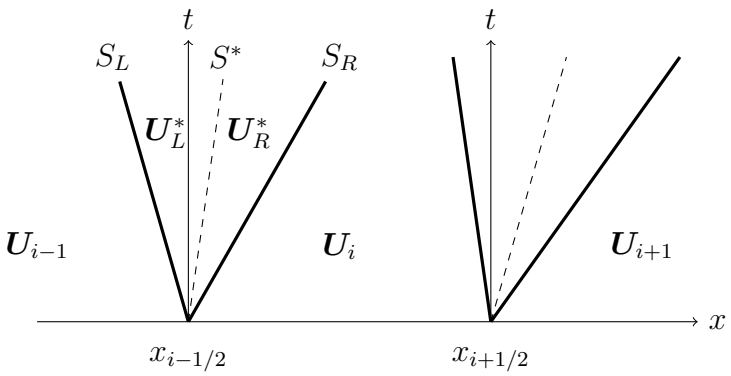

Figure 3.3: One-dimensional Riemann problem at the boundaries of cell i, with labelled HLLC wave-speeds and intermediate states for the left interface.

3.2.2 High resolution schemes

Godunov's method is a first-order upwind method, enabling it to avoid spurious oscillations in the solution. As the method is only first order, the resolution of sharp interfaces can quickly become diffuse. Higher order linear methods suffer from the problem of spurious oscillations at sharp interfaces. In figure 3.4, two schemes have been used to advect a passive scalar with a discontinuous interface in one-dimension with a constant velocity flow field. The analytical solution would maintain the sharp discontinuity, whereas the numerical results do not. The

Lax-Wendroff scheme shown is second-order in space and resolves a sharper interface compared to the first-order Godunov scheme. However, the Lax-Wendroff scheme suffers from spurious oscillations behind the sharp discontinuity. Such oscillations are disastrous in the case of the advection of density or energy, which could cause negative mass or negative pressure within a simulation. This is tied to Godunov's theorem of monotonicity (Godunov & Bohachevsky, 1959), which states that a linear method (constant coefficients) that is monotonic can only be first-order accurate. A monotone scheme for a conservative, linear equation is defined by having only positive weights in the stencil that is used to evolve the system to the next solution. This restriction forces the next solution to be bounded by the minimum and maximum values of the previous solution.

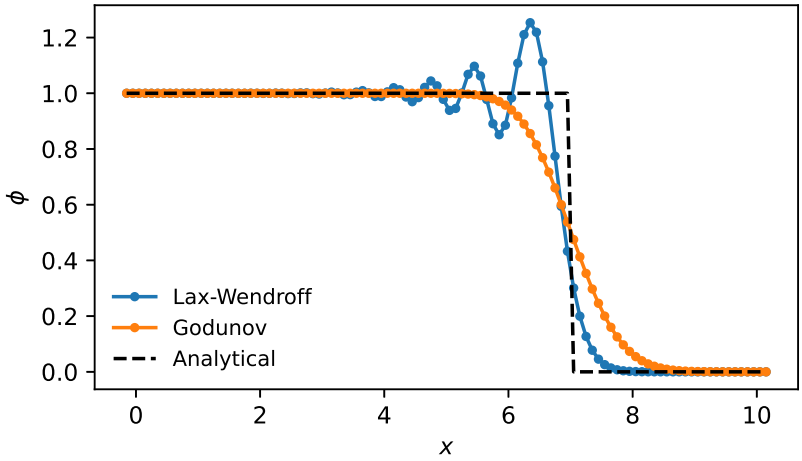

Figure 3.4: Linear advection of a passive scalar with a sharp discontinuity in one-dimension.

The oscillations in the Lax-Wendroff solution can be quantified by calculating the total variation (TV) of the solution. The total variation for a discretised solution at time step n is calculated according to

$$TV(u^n) = \sum_i |u^n_{i+1} - u^n_i|. \tag{3.74}$$

A Total Variation Diminishing (TVD) scheme is therefore a scheme which has a total variation that decreases in time, $TV(u^{n+1}) \leq TV(u^n)$. For non-linear problems, such as fluid dynamics, the goal is to attain a high-order TVD method.

To attain higher-order accuracy for the Godunov method, the Monotone Upstream-centred Scheme for Conservation Laws (MUSCL) approach introduces two key modifications to the solution process. Firstly, the MUSCL scheme achieves a higher order of accuracy by reconstructing the data within a cell to more accurately represent the spatial distribution of the cell averaged value for the cell. In the most basic form, this is done by reconstructing the cell

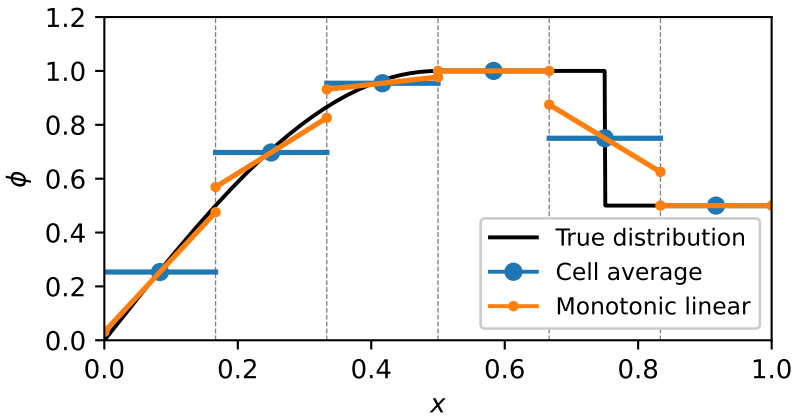

Figure 3.5: Linear reconstruction of the piece-wise constant flow field using a slope limiter.

to have a linear gradient, calculated from the neighbouring cells, that passes through the cell averaged value at the cell centre. The second aspect of the MUSCL approach is applying a limiter to the reconstructed slope. In order to achieve monotonicity for the linear reconstruction, it is necessary to ensure that the reconstructed states do not exceed the values of the neighbouring cells. A simple scheme to limit the gradient within the cell is the minmod limiter by van Leer (1979),

$$\bar{\Delta}_i = \begin{cases} \text{sign}\left(\Delta_{i-\frac{1}{2}}\right) \min\left(|\Delta_{i-\frac{1}{2}}|, |\Delta_{i+\frac{1}{2}}|\right) & \text{if sign}\left(\Delta_{i-\frac{1}{2}}\right) = \text{sign}\left(\Delta_{i+\frac{1}{2}}\right), \\ 0 & \text{otherwise.} \end{cases} \tag{3.75}$$

The MUSCL scheme allows for a high-order reconstruction in smooth, continuous parts of the flow field, and first-order, monotonic behaviour at discontinuities. An example of this reconstruction is shown in figure 3.5.

More accurate slope-limiter methods have been designed since then, such as the third-order piecewise parabolic method of Colella & Woodward (1984); Woodward & Colella (1984), and the nominally fifth-order scheme of Kim & Kim (2005). These schemes need an increasing stencil size to improve the accuracy of the method. The reconstructed states of Kim & Kim (2005) are calculated by using the equations,

$$\boldsymbol{U}^L_{i+1/2} = \boldsymbol{U}_i + \frac{1}{2}\phi(r^L_i)(\boldsymbol{U}_i - \boldsymbol{U}_{i-1}), \tag{3.76}$$

$$\boldsymbol{U}^R_{i+1/2} = \boldsymbol{U}_{i+1} - \frac{1}{2}\phi(r^R_{i+1})(\boldsymbol{U}_{i+2} - \boldsymbol{U}_{i+1}), \tag{3.77}$$

with the limiter function ϕ given by

$$\phi(r^L_i) = \max(0, \min(2, 2r^L_i, \beta^L)), \tag{3.78}$$

$$\phi(r^R_{i+1}) = \max(0, \min(2, 2r^R_{i+1}, \beta^R)). \tag{3.79}$$

The values of β^L and β^R are given by

$$\beta^L = \frac{-2/r_{L,i-1} + 11 + 24r_{L,i} - 3r_{L,i}\, r_{L,i+1}}{30}, \tag{3.80}$$

$$\beta^R = \frac{-2/r_{R,i+2} + 11 + 24r_{R,i+1} - 3r_{R,i+1}\, r_{R,i}}{30} \tag{3.81}$$

where

$$r_{L,i} = \frac{\Delta U_{i+\frac{1}{2}}}{\Delta U_{i-\frac{1}{2}}}, \tag{3.82}$$

$$r_{R,i} = \frac{\Delta U_{i-\frac{1}{2}}}{\Delta U_{i+\frac{1}{2}}}. \tag{3.83}$$

As the solution array of the conservative variables holds multiple values, it is necessary to perform the reconstruction and limiting for each variable. This process does not need to be performed with the conservative variables. Reconstructing primitive variables for multi-species flows can prevent the reconstruction of a state with unphysical species densities and prevent oscillations at contact discontinuities (Williams, 2019).

3.2.3 Moving mesh

In the analysis of the effects of strain-rate on the development of RMI in chapters 4 and 5, a moving mesh algorithm is required to effectively model the flow as the domain compresses or expands due to the applied strain-rates, whilst maintaining the theoretical linear background velocity profile for the given strain-rate. The implemented moving mesh algorithm is based upon the Arbitrary Lagrangian-Eulerian (ALE) formulation, a flexible framework which allows for customised mesh velocities (Thomas & Lombard, 1979; Mavriplis & Yang, 2006; Luo *et al.*, 2004; Trépanier *et al.*, 1991; Farhat *et al.*, 2001).

For a moving control volume, the transport equation in the ALE formulation uses a velocity relative to the control volume surface's velocity. Focusing on the compressible Euler equations, the equations for a control volume $V(t)$ with surface $S(t)$ can be written as,

$$\frac{\partial}{\partial t}\int_{V(t)} \boldsymbol{U} dV + \int_{S(t)} \boldsymbol{F} dS = 0. \tag{3.84}$$

The conserved variable vector $\boldsymbol{U}$ and flux vector $\boldsymbol{F}$ are given by,

$$\boldsymbol{U} = \begin{pmatrix} \rho \\ \rho u_j \\ \rho E \end{pmatrix} \tag{3.85}$$

$$\boldsymbol{F} = \begin{pmatrix} (u_k - \dot{x}_k) n_k \rho \\ \rho u_j (u_k - \dot{x}_k) n_k + p n_j \\ \rho E (u_k - \dot{x}_k) n_k + p v_k n_k \end{pmatrix} \tag{3.86}$$

Here $\dot{x}$ denotes the mesh velocity for a cell face, and n denotes the normal vector to the cell face. The value of $\dot{x}$ changes the underlying scheme: for $\dot{x} = 0$ the scheme is static and Eulerian, whilst for $\dot{x} = u$ the mesh advects with the flow and is Lagrangian. Values outside these two options may be specified, as is the case for the strain-rate simulations conducted.

For time-varying mesh velocities, there are a few options in how to specify the mesh motions within the sub-iterations of a time-step (Mavriplis & Yang, 2006). A reasonable method when the mesh velocity is a known function is to use the secant velocity of the time step.

$$\dot{x} = \frac{x^{n+1} - x^n}{\Delta t} \tag{3.87}$$

As the moving mesh algorithm adjusts the flux vector, the Riemann solver needs to be adjusted to account for the new behaviour. The modified HLLC approximate Riemann solver is given by Luo *et al.* (2004), which changes the frame of reference to be relative to the movement of the mesh, adjusting the face-normal velocity and the estimated signal speeds accordingly.

The inclusion of the moving mesh scheme increases the computational cost of solving the system, with the percentage increase depending upon the computational expense of the numerical methods used to solve the system. A $\sim$40% increase in cost is created if using the inviscid four- or five-equation models for two species. The additional cost for the viscous four- and five-equation models, which is created by the evaluation of the viscous and diffusive fluxes, causes the moving mesh overhead to be closer to a $\sim$20% increase for the simulation cost. The cost further decreases on HPC infrastructure as communication and memory bandwidth become increasingly costly on the simulation run time. These effects can cause the inviscid five-equation model to reduce down to a 15% increase in cost, as opposed to the 40% that may be obtained for simulations on a single core.

3.2.4 Time integration

The method of lines formulation for PDEs requires a spatial discretisation for the differential equation, whilst leaving the temporal component of the PDEs continuous. This reduces the system to a set of ODEs,

$$\frac{\partial \boldsymbol{U}}{\partial t} = \boldsymbol{L}(\boldsymbol{U}) \tag{3.88}$$

In this form, $\boldsymbol{L}(\boldsymbol{U})$ will be composed of inviscid, viscous, and source terms depending on the governing equations in use. As a set of ODEs, the time integration may then be performed using any number of schemes, however the technique used throughout this thesis is the two-stage second-order TVD Runge-Kutta scheme (Gottlieb & Shu, 1998).

$$\boldsymbol{U}^{(1)} = \boldsymbol{U}^n + \Delta t \boldsymbol{L}(\boldsymbol{U}^n) \tag{3.89}$$

$$\boldsymbol{U}^{n+1} = \frac{1}{2}\boldsymbol{U}^n + \frac{1}{2}\boldsymbol{U}^{(1)} + \frac{1}{2}\Delta t \boldsymbol{L}(\boldsymbol{U}^{(1)}) \tag{3.90}$$

For the inviscid, hyperbolic problem, the time step size of the integration step is limited by the CFL condition,

$$C_{\text{CFL}} = \frac{\Delta t S_{\max}}{\Delta x}, \tag{3.91}$$

which restricts the time-step size Δt so that $C_{\text{CFL}} \in (0, 1]$. However, depending upon the scheme employed, the maximum CFL allowed for stability can change. For the Godunov-type method employed, a simple estimate of the time step size may be done in either of the following approaches:

$$\Delta t_{CFL} = \frac{1}{m}\frac{\min(\Delta x, \Delta y, \Delta z)}{S_{\max}}, \tag{3.92}$$

$$\Delta t_{CFL} = \frac{1}{m}\min_i\left(\frac{\Delta x_i}{|u_i| + c}\right), \tag{3.93}$$

where m stands for the number of dimensions for the simulation (1-D, 2-D, or 3-D), and the maximum signal speed is estimated from the velocity and speed of sound, $S_{\max} = |u| + c$. For viscous problems, the time step restrictions for the viscosity, diffusion, and conductivity are based off the recommendations of Cook (2009):

$$\Delta t_{\mu} = \frac{\rho \min(\Delta x_i^2)}{2\mu} \tag{3.94}$$

$$\Delta t_{\kappa} = \frac{\rho c_v \min(\Delta x_i^2)}{2\kappa} \tag{3.95}$$

$$\Delta t_D = \frac{\min(\Delta x_i^2)}{2D}. \tag{3.96}$$

The time step restriction is then suggested to be evaluated by

$$\Delta t = C_{\text{CFL}} \min\left(\Delta t_{CFL}, \Delta t_{\mu}, \Delta t_{\kappa}, \Delta t_{D}\right), \tag{3.97}$$

where a custom CFL coefficient C_{CFL} can be prescribed for the simulation.

3.2.5 Low Mach correction

At the finer scales of turbulence, the velocities of the eddies decrease from the viscous interactions until the energy is dissipated into heat. Previously, Godunov-type methods have struggled with simulations of turbulent motion as at the low Mach numbers the schemes provide a disproportionate amount of dissipation, requiring excessively fine grids to counteract. Thornber *et al.* (2008*a*) showed that this dissipation scales according to $\Delta u^2\, a/\Delta x$ and entropy is generated proportional to $1/a$. Kolmogorov (1991) instead predicts that the dissipation rate should scale according u^3/l, and the entropy generation should scale with $1/a^2$. For the fifth-order reconstruction scheme of Kim & Kim (2005), the correction proposed by Thornber *et al.* (2008*b*) was to modify the extrapolated primitive variables in the reconstruction process. The corrected variables, u^{LM}, are calculated according to,

$$u_L^{LM} = \frac{u_L + u_R}{2} + min(max(M_L, M_R), 1)\frac{u_L - u_R}{2} \tag{3.98}$$

$$u_R^{LM} = \frac{u_L + u_R}{2} + min(max(M_L, M_R), 1)\frac{u_R - u_L}{2} \tag{3.99}$$

For supersonic flows where the Mach number is greater than unity, $M = u/c$, the reconstructed variables will take on their original values. For subsonic flows, the modification changes the relative velocity difference to be in line with the larger Mach number, effectively cancelling out the speed of sound scaling observed in the dissipation rate. For the fifth order reconstruction with the low Mach correction, the correct behaviour is obtained with a fifth order dissipation rate ($\propto \Delta x^5$). With this correction, the inherent numerical viscosity of the scheme allows for an effective sub-grid model for modelling turbulent flows as an implicit large eddy simulation (Thornber *et al.*, 2010, 2017, 2011; Thornber & Zhou, 2015, 2012; Groom & Thornber, 2020; El Rafei *et al.*, 2019; El Rafei & Thornber, 2020, 2024; Grinstein *et al.*, 2024).

3.2.6 Strain rates

The work of this thesis introduces a novel approach to simulating applied uniform strain rates. The work of Rogallo (1981) introduces applied strain rates using a deforming reference frame. The domain is transformed, which also transforms the solution variables, and the resulting strain

rates are applied through source terms. The alternative approach here is to explicitly apply the physical strain rates to the domain. To enforce the desired strain rates, the domain moves with the strain rate using the ALE moving mesh motion described in §3.2.3 and moving symmetry plane boundary conditions.

The mean velocity flow field that depends on the desired velocity gradients, $\partial\bar{u}_i/\partial x_j$, is calculated by

$$\bar{u}_i(x,t) = \frac{\partial \bar{u}_i}{\partial x_j} x_j. \tag{3.100}$$

The desired velocity gradient may be a function of time, depending upon the desired velocity profile. Using the definition of strain-rate,

$$S_{ij}(x,t) = \frac{1}{2}\left(\frac{\partial u_i}{\partial x_j} + \frac{\partial u_j}{\partial x_1}\right), \tag{3.101}$$

the normal strain-rates ($i = j$) are directly equal to the corresponding velocity gradient, simplifying the notation style to be used. Positive normal strain rates correspond to expansion, and negative will correspond to compression. The expansion factor, which represents the ratio of the domain length in direction i at time t to the original length is given by,

$$\Lambda_i(t) = \exp\left[\int_0^t \bar{S}_{ii}(t')dt'\right]. \tag{3.102}$$

If there is no strain in direction i, the expansion factors remain unity. The total change in volume of the domain is the product of the expansion factors for each direction:

$$\Lambda_{Total} = \Lambda_1\Lambda_2\Lambda_3. \tag{3.103}$$

In an expansion or compression process, the mass within the strained domain should be conserved. If the process is isentropic, with negligible dissipative heating, then the density and pressure can be calculated using the expansion factor in equation 3.102 (Durbin & Zeman, 1992).

$$\rho(t) = \rho_0 \Lambda_{\text{Total}}^{-1}(t) \tag{3.104}$$

$$p(t) = p_0 \Lambda_{\text{Total}}^{-\gamma}(t) \tag{3.105}$$

For multiple fluids in a strained domain, the fluid densities will change at the same rate, maintaining the density ratio and Atwood number, as long as the fluids have the same specific heat ratio, γ. If the specific heat ratios are different, the pressure of the fluids will be different, generating waves and causing one fluid to compress and the other to expand to achieve a pressure equilibrium. A uniform pressure profile is important to avoid any unnecessary Rayleigh-Taylor effects, whereby vorticity is generated through baroclinicity. To ensure that the background

expansion process does not generate a mean pressure gradient, the momentum equation in one-dimension can be solved for a uniform velocity gradient.

$$\rho\frac{\partial u}{\partial t} + \rho u\frac{\partial u}{\partial x} = -\frac{\partial p}{\partial x} + \rho g. \tag{3.106}$$

With the substitution of equation (3.100) and $\partial p/\partial x = 0$, the solution requires

$$g = \left(\frac{d\bar{S}}{dt} + \bar{S}^2\right) x \tag{3.107}$$

for the potential force, g. Typically, in rapid-distortion theory, the expression $d\bar{S}/dt + \bar{S}^2$ is set to be zero (Durbin & Zeman, 1992; Cambon *et al.*, 1993). This constrains the systems being modelled to what is labelled the constant velocity case in §3.2.6. By including this potential term, different mean velocity gradient profiles can be modelled (Yu & Girimaji, 2007). Verification of the implementation of the applied strain rate framework into FLAMENCO in appendix B.

Besides the computational cost of the moving mesh, as outlined in §3.2.3, the compression of the domain causes the simulation to become more expensive due to the reduced allowed time-step size. For a domain compressing in n dimensions with a uniform strain rate, the smallest cell length will scale with Λ, whilst the density and pressure will scale with $\Lambda_{\text{Total}} = \Lambda^n$. The allowed CFL time step size is can be approximated by using the ideal gas speed of sound as the signal speed,

$$\Delta t_{\text{CFL}} = \frac{\Delta x(t)}{\sqrt{\frac{\gamma p(t)}{\rho(t)}}} \tag{3.108a}$$

$$= \Delta t_0 \Lambda^{1+n(\gamma-1)/2} \tag{3.108b}$$

where Δt_0 is the original time-step size prior to any strain. For compression cases, with $\Lambda < 1$, the allowed time-step size is restricted, requiring a larger number of time-steps to achieve the desired physical simulation time. Whilst lower values of γ somewhat reduce this impact, as shown in figure 3.6, throughout the thesis $\gamma = 5/3$ is used, making the simulations more expensive than using $\gamma = 1.4$ for the fluids. The usage of $\gamma = 5/3$ is chosen to match the properties used in previous simulations of unstrained RMI (Thornber *et al.*, 2017; Walchli & Thornber, 2017). The utilisation of $\gamma = 5/3$ is commonly used as at high densities and temperatures, as achieved in ICF and supernovae, as the fluids become ionised and can be approximated as a monatomic gas.

Constant velocity

The first strain rate profile arises from a domain growing or shrinking with a constant boundary velocity, denoted V_0. Likewise, any unperturbed packet of fluid will maintain its original velocity

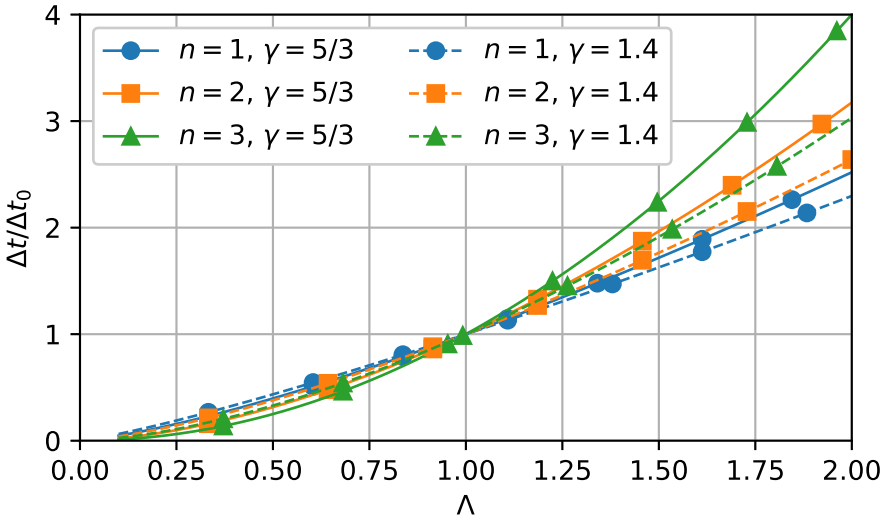

Figure 3.6: Change in time-step size as a function of the expansion factor (Λ), the specific heat ratio (γ), and the number of dimensions under strain (n).

throughout the strain profile. For a domain with an initial length of L_0, the domain length as a function of time varies linearly by,

$$L(t) = L_0 + V_0 R(t - t_0) \tag{3.109}$$

where $R(\phi) = \max(0, \phi)$ is the ramp function, t_0 is the initial time at which strain is applied and $t - t_0$ indicates the time since strain is initially applied. Initialised with a linear velocity profile, the mean strain rate is initially given by $\bar{S}_0 = V_0/L_0$. The mean strain rate will change as the length of the domain changes. The time-varying strain rate may be expressed as a function of the initial strain rate.

$$\bar{S}(t) = \frac{V_0}{L(t)} \tag{3.110a}$$

$$= \frac{\bar{S}_0}{1 + \bar{S}_0 R(t - t_0)} \tag{3.110b}$$

The expansion factor for the constant velocity case is simply given by,

$$\Lambda(t) = 1 + \bar{S}_0 R(t - t_0). \tag{3.111}$$

As previously mentioned, the constant velocity case is the default case used in rapid-distortion theory as it maintains homogeneity in the flow without any potential forcing.

Constant strain rate

The second strain rate profile used is designed for a constant strain rate. For the system with strain applied at time t_0, the strain rate is defined by,

$$\bar{S}(t) = \bar{S}H(t - t_0) \tag{3.112}$$

where $H(\phi)$ is the Heaviside step function, equal to unity for $\phi \geq 0$ and zero otherwise. For a constant strain rate, the domain will grow exponentially as the expansion factor only requires integrating a constant.

$$\Lambda(t) = \exp\left[\bar{S}R(t - t_0)\right] \tag{3.113}$$

In this configuration, the flow must accelerate in order for the domain to grow exponentially. To accelerate the flow without a pressure differential, thereby isolating the strain rate effects from RT effects, a potential forcing is required. Using a constant strain rate in equation (3.107) reduces the required potential term to,

$$g = \bar{S}^2 x \tag{3.114}$$

Strain rate non-dimensionalisation

The magnitude of strain rates observed will vary depending upon the application, hence the necessity for non-dimensionalisation. In rapid-distortion theory, the strain rate is normalised by using the turbulence to mean-shear timescale ratio, $\mathcal{S}k/\epsilon$, where $\mathcal{S} = (2\bar{S}_{ij}\bar{S}_{ij})^{1/2}$ (Pope, 2000). For the investigation of RMI in the linear regime, an alternative turbulent timescale is used, which is the initial eddy turnover time for the instability, $\lambda/\dot{h}_0$, where $\dot{h}_0$ is the initial growth rate of the mixing layer and λ is the effective initial wavelength. The strain rate is then non-dimensionalised as,

$$\hat{S}(t) = \frac{\bar{S}(t)\lambda}{\dot{h}_0}, \tag{3.115}$$

representing the ratio of the initial eddy turnover time to the strain timescale. For the constant-velocity cases, which has a time-varying strain rate, the initial strain rate will be utilised, $\hat{S}_0 = \hat{S}(t = t_0)$. The unstrained case corresponds to $\hat{S} = 0$, with the strain contribution increasing with the magnitude of $\hat{S}$. The benefit of this non-dimensionalisation is that it couples nicely with the common dimensionalisation of time for RMI,

$$\tau = \frac{t\dot{h}_0}{\lambda}. \tag{3.116}$$

This allows for the substitution, $\bar{S}t = \hat{S}\tau$, which commonly occurs as observed in the expansion factor in equations (3.111) and (3.113). As a result, the expansion factor is proportional to $\hat{S}\tau$. Therefore, to simulate large values of $\hat{S}$ until late time (large τ) will require a mesh that is suitable for the resulting large change in domain size.

It is possible to estimate values of $\hat{S}$ for a variety of problems. The Taylor-Sedov blast-wave has a post-shock velocity profile that is roughly linear, with an approximate strain rate of $\bar{S} \approx 4/(5(\gamma+1)t)$, which is inversely proportional to time. Including an interface that interacts with the blast-wave at time t_0 (and ignoring any alterations to the profile as a result), the non-dimensional strain rate across the interface is given by

$$\hat{S}_{TS} = \frac{t_0}{t}\frac{2\pi}{aklAt}. \tag{3.117}$$

The wavelength is replaced with the effective wavelength of the spherical harmonic mode l, and the initial growth rate has been decomposed into the impulsive contribution of Richtmyer (1960). Assuming initial linearity of $ak = 0.01$, Atwood number $At = 0.5$, and a dominant mode of $l = 60$, the peak non-dimensional strain rate contribution is 20.9 at $t = t_0$, but this rapidly decreases with time. By the time the shock wave has reached a radius of twice the initial interface radius, the value of $\hat{S}$ reduces to 3.7. In inertial confinement fusion, the fuel-ablator interface may reach a speed of 200 km s^{-1} at a radius of 200 μm, around a $4.5\times$ convergence. Assuming a linear velocity profile, or isotropic strain rates, this gives an axial strain rate of $-1/$ns. Using the initial conditions of $\lambda = 2\mu$m and $\dot{h}_0/h_0 = -63/$ns (Weber *et al.*, 2023), along with an initial perturbation size of 20 nm (Marinak *et al.*, 2001) gives $\hat{S} = -1.6$. Implosion simulations of El Rafei *et al.* (2019) have the interface move at an almost constant velocity between the initial shock and the re-shock. Prior to re-shock, at a convergence factor of 2.7, the strain rate may be estimated to be -1.2/ns, which for the two narrowband cases gives $\hat{S} = -0.54$ and $\hat{S} = -0.27$. In these applications, it is evident that the timescales of the turbulence and strain are of a similar order of magnitude, and the strain contribution should not be ignored.

CHAPTER 4

Influence of Axial Strain

4.1 Introduction

In convergent geometry the instability growth is modified by both radial (axial) strain rate and angular (transverse) strain rate and these effects are taken into account in the Bell-Plesset linear perturbation theory. In planar shock tube experiments, RMI and RTI may be influenced by compression/expansion of the mixing zone due to axial strain rates from transient waves (Vetter & Sturtevant, 1995; Li *et al.*, 2019, 2021). For the bulk overturning motion seen in the RTI tilted-rig case (Read, 1984; Youngs, 1989; Andrews *et al.*, 2014; Ferguson *et al.*, 2023), the interface is stretched in the transverse direction and thinned in the axial direction. The absence of a persevering mean strain rate normal to the interface is one of the key differences between planar RMI and converging RMI. Simulations have been performed on RMI in cylindrical geometry which show that the velocity difference between the edges of the mixing layer, labelled the stretching/compression effect, is a significant contributor to the growth rate of the instability (Ge *et al.*, 2020, 2022). An analysis of the mean mass fraction profile by Ge *et al.* (2022) shows that a mixing layer's width will grow due to three contributions: the velocity difference across the mixing layer, the turbulent/penetrative growth from the fluctuating field, and molecular diffusion of the fluids.

In general multidimensional compressible flows, RM/RT mixing layers are influenced by both axial and transverse strain rates. The purpose of the present chapter is to focus on the effect of axial strain rate and study this in detail for simple test cases. This is performed by conducting simulations of planar geometry RMI-induced mixing layers with an applied mean axial strain rate. By isolating the axial strain rate, the geometric convergence component of the Bell-Plesset effect is removed. In convergent geometry, the radial and angular strain rates are not easily decoupled. This planar configuration is therefore unique in its ability to be able to isolate the

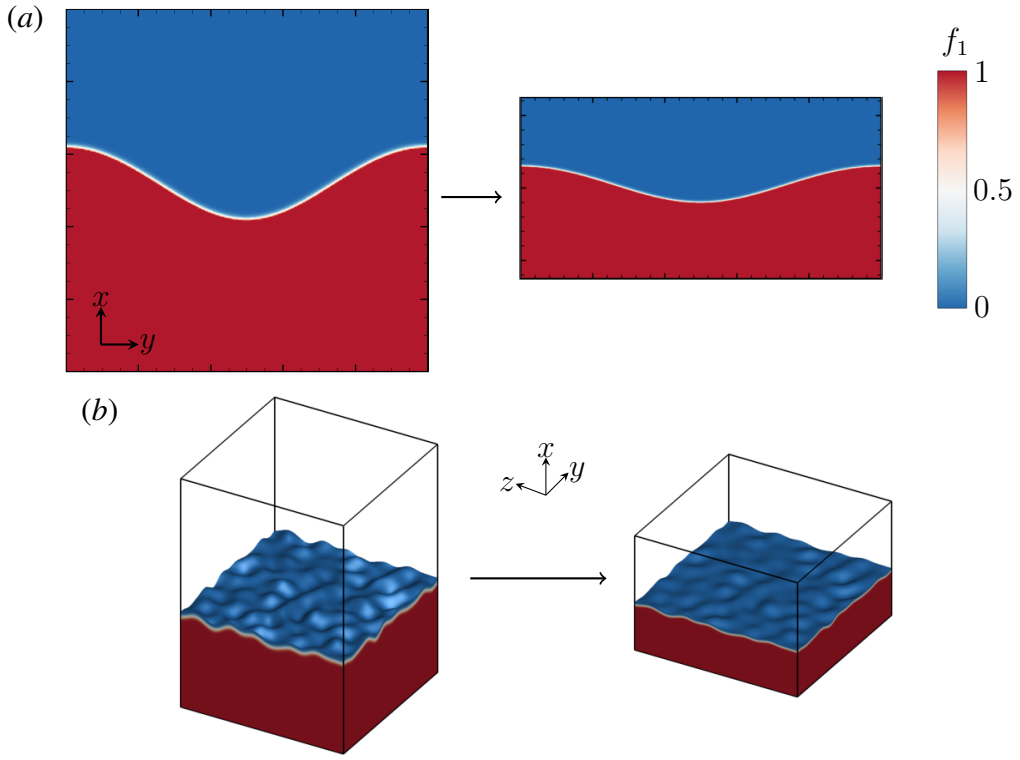

Figure 4.1: Change of domain size and amplitude for systems compressed with axial strain by a factor of two in the x-direction. (a) Two-dimensional system with a single mode perturbation; (b) Three-dimensional system with a multimode perturbation, bound by the $f_1 = 0.01$ iso-surface.

effect of a mean strain rate normal to the interface and determine how it affects the development of RMI and the transition to a self-similar mixing layer.

Section 4.3 analyses the linear regime of a 2D single-mode instability using resolved numerical simulations, and compares the results with the corresponding linear potential flow model. Section 4.4 looks at strained implicit large eddy simulations (ILES) of multi-modal narrowband RMI, and assesses the ability of a Buoyancy-Drag model to capture the growth rate.

4.2 Problem formulation

4.2.1 Axial strain rate

Using the strain rate framework outlined in §3.2.6, axial strain rates are applied in the x-direction. Figure 4.1 demonstrates the impact of the strain for two static systems, i.e. the configurations will not change or evolve in the absence of the applied strain rate. The applied axial strain will directly stretch or compress the x-extent of the domain, as well as the interface amplitudes or mixing layer width. For simplicity, $\bar{S}$ will be used to refer to the axial strain rate, $\hat{S}$ refers to the non-dimensionalised strain rate, and $\Lambda(t)$ refers to the axial expansion factor.

4.2.2 Governing equations

The two-dimensional resolved simulations use the five-equation, quasi-conservative model of Thornber *et al.* (2018), listed in section 3.1.2. The implicit large eddy simulations in section 4.4 use the inviscid version of the five-equation model.

4.2.3 Numerical methods

The numerical methods are primarily described in section 3.2. As there is a linear velocity profile, the fluid domain will grow or shrink according to the strain rate and strain profile. In order to accurately capture the instability growth, the mesh of the simulated domain is moved with the fluid. A moving mesh with FLAMENCO has previously been used (El Rafei & Thornber, 2020), and has been validated in a similar code employing volume fraction governing equations (Probyn *et al.*, 2014).

To maintain the linear velocity profile during strain application, the boundary conditions in the direction of strain are inviscid moving walls. The ghost cells are calculated by copying the cell symmetrically opposite the wall. The velocity of the ghost cells is mirrored relative to the wall velocity, as opposed to zero. For example, at the upper boundary, the normal velocity for the first ghost cell ($nx + 1$) is calculated by,

$$u_{nx+1} = 2u_{Wall} - u_{nx}. \tag{4.1}$$

The wall velocity, u_{Wall}, is given by the expected velocity as per the strain profile.

4.3 Two-dimensional single mode

4.3.1 Potential Flow

A potential flow model for an axially strained system needs to incorporate the velocity gradient of the flow as well as the change in density. The linearised potential flow model by Epstein (2004) includes the consideration of a compression ratio for the planar geometry model. The compression rate, $\gamma_\rho = \dot{\rho}/\rho$, is considered uniform in both fluids about the interface and creates a background fluid velocity given by,

$$\bar{u}_1(x,t) = \dot{x}_0(t) - \gamma_\rho(t)(x - x_0(t)) \tag{4.2}$$

where $x_0(t)$ is the mean interface position, and $\dot{x}_0(t)$ is the mean interface velocity. This rate of compression is related to the mean strain rate by $\sum \bar{S}_{ii} = -\gamma_\rho$. For the case of only an axial

strain rate, $\gamma_\rho = -\bar{S}(t)$, the background fluid velocity is,

$$\bar{u}_1(x,t) = \dot{x}_0(t) + \bar{S}(t)(x - x_0(t)) \tag{4.3}$$

which matches the velocity profile expected for a uniform velocity gradient of $\bar{S}(t)$. The resulting solution provided by Epstein (2004) for this case is given by,

$$\left(\bar{S}(t) + \frac{\mathrm{d}}{\mathrm{d}t}\right)\frac{\mathrm{d}}{\mathrm{d}t}\left(a_k\rho\right) = k\frac{\rho_2 - \rho_1}{\rho_2 + \rho_1}g_p a_k \rho \tag{4.4}$$

where a_k is the amplitude of the mode with wave number k, and $g_p = -(1/\rho)[\partial p(x_0,t)]/\partial x$ represents the fluid acceleration at the unperturbed interface due to the pressure gradient, and not the acceleration from external potential. Equation (4.4) can be written more clearly as,

$$\ddot{a}_k - \frac{\mathrm{d}}{\mathrm{d}t}\left(\bar{S}a_k\right) = k\frac{\rho_2 - \rho_1}{\rho_2 + \rho_1}g_p a_k. \tag{4.5}$$

Now considering the impulsive limit for a single-mode RMI with $g_p = \Delta u \delta(t)$, where Δu is the change in interface velocity, equation (4.5) will integrate to

$$\dot{a} = a\bar{S}(t) + U_0 \tag{4.6}$$

with

$$U_0 = a_0 k\frac{\rho_2 - \rho_1}{\rho_2 + \rho_1}\Delta u \tag{4.7}$$

as prescribed by Richtmyer (1960). This solution suggests a new growth rate that is the sum of the RMI velocity as well as the background velocity from the strain rate. As such, for the case of $\bar{S}(t) = 0$, equation (4.6) will reduce to the linear growth rate expected for RMI. For the case with no RMI velocity, the amplitude will grow with the domain as determined by the expansion factor. Solutions where both terms are presented will depend upon the strain rate profile. It is possible to write a generalised solution using a form similar to Flaig *et al.* (2018); Lombardini *et al.* (2014) by introducing the intermediate variable $\alpha(t)$,

$$a(t) = \alpha(t)\exp\left[\int_0^t \bar{S}(t')dt'\right]. \tag{4.8}$$

The exponential component is identical to the expansion factor, $\Lambda(t)$, as defined in equation (3.102). The resulting differential equation is,

$$\dot{\alpha}(t) = U_0\Lambda(t)^{-1}, \tag{4.9}$$

which in turn provides the general solution,

$$a(t) = a_0\Lambda(t) + U_0\Lambda(t)\int_0^t \Lambda^{-1}(t')dt'. \tag{4.10}$$

where $a_0 = a(0) = \alpha(0)$. This general solution has two distinct terms. The first term of the solution corresponds to the initial amplitude that is expanding/compressing with the domain due to the strain rate. The second term represents a more complicated relationship between the RMI velocity and the strain rate. In the absence of a strain rate, the expansion factor will remain one, and the expression will collapse to the standard RMI impulsive solution of $a_0 + U_0 t$. For the two prescribed strain rate profiles in §4.2.1, an exact solution can be obtained. For constant strain rate applied from time t_0, the expansion factor is an exponential after the time of strain offset. The solution for the system is

$$a(t > t_0) = (a_0 + U_0 t_0) e^{\bar{S}(t-t_0)} + \frac{U_0}{\bar{S}} \left(e^{\bar{S}(t-t_0)} - 1 \right). \tag{4.11}$$

For the constant velocity profile, it is easier to characterise the flow in terms of the initial strain rate, $\bar{S}_0$, see equation (3.110). The expansion factor for this case is a linear expression, which gives the resulting equation,

$$a(t > t_0) = (a_0 + U_0 t_0) \left(1 + \bar{S}_0 (t - t_0) \right) + \frac{U_0}{\bar{S}_0} \left(1 + \bar{S}_0 (t - t_0) \right) \ln \left(1 + \bar{S}_0 (t - t_0) \right). \tag{4.12}$$

In both equations the solutions are not defined for a mean strain rate of zero due to its presence in the denominator. Taking the Taylor series of the expressions will show that the solutions collapse down to the linear growth rate as the strain rate approaches zero.

Equations (4.11) and (4.12) can be non-dimensionalised by dividing by the wavelength and introducing the non-dimensional time, $\tau = t U_0 / \lambda$, and the non-dimensionalised strain rate, $\hat{S} = \bar{S} \lambda / U_0$. Substituting the non-dimensionalisations and setting the initial strain time $t_0 = 0$ for simplicity gives the non-dimensionalised equations,

$$\frac{a(t)}{\lambda} = \frac{a_0}{\lambda} e^{\hat{S}\tau} + \frac{1}{\hat{S}} \left(e^{\hat{S}\tau} - 1 \right) \tag{4.13}$$

for constant strain rate, and

$$\frac{a(t)}{\lambda} = \frac{a_0}{\lambda} \left(1 + \hat{S}_0 \tau \right) + \frac{1 + \hat{S}_0 \tau}{\hat{S}_0} \ln \left(1 + \hat{S}_0 \tau \right) \tag{4.14}$$

for constant velocity. The amplitude growth rate for a specific strain rate profile is therefore dependent upon the initial linearity (a_0/λ) and the non-dimensional strain rate value, $\hat{S}$. A more complicated non-dimensionalisation can be done using the general solution layout provided by equation (4.10). The resulting equation takes the form,

$$\frac{a(t)}{\lambda \Lambda(t)} = a_0 + \hat{\tau} \tag{4.15}$$

where $\hat{\tau} = U_0 \hat{t} / \lambda$ and

$$\hat{t} = \int_0^t \Lambda^{-1}(t') dt'. \tag{4.16}$$

This solution normalises the amplitude with respect to the domain expansion, collapsing the solution down to a straight line in the linear regime. The alternate time $\hat{t}$ hides the complexities of the strain rate, however for the unstrained case it will reduce to standard time.

4.3.2 Initial conditions

The simulations were conducted on a two-dimensional domain, with inviscid walls in the x-direction and periodic boundary conditions in the y-direction. The fluids were set up in a heavy-to-light configuration at a 3:1 density ratio, resulting in an Atwood number of 0.5. Instead of a shock wave and amplitude perturbation, a velocity perturbation was used to replicate the linear growth rate of RMI (Thornber *et al.*, 2010). The velocity potential is given by

$$\phi(x,t) = \text{sgn}(x_1 - x_0)\frac{U_0}{k}\cos(kx_2)e^{-k|x_1-x_0|}, \tag{4.17}$$

about the mean interface position, x_0. The analytic perturbation is made divergence free by using the vector potential, A_i.

$$u_1 = -\frac{\partial\phi}{\partial x_1} = \frac{\partial A_3}{\partial x_2} - \frac{\partial A_2}{\partial x_3} \tag{4.18a}$$

$$u_2 = -\frac{\partial\phi}{\partial x_2} = -\frac{\partial A_3}{\partial x_1} \tag{4.18b}$$

The vector potential is calculated by,

$$\Phi = \int \phi \,\mathrm{d}x_1 = -\frac{U_0}{k^2}\cos(kx_2)e^{-k|x_1-x_0|} \tag{4.19}$$

$$A_2 = -\frac{\partial\Phi}{\partial z} \tag{4.20}$$

$$A_3 = \frac{\partial\Phi}{\partial y}. \tag{4.21}$$

Whilst the potential and perturbation decays to zero as $x_1 \to \pm\infty$, the vector potentials are multiplied by a factor to ensure that they decay to zero at the finite x_1 boundaries of the domain (Thornber *et al.*, 2010).

The initialisation allows a simple initial growth rate of 1m/s to be used and requires an initial amplitude of $a_0 = 0$. As the initial amplitude is zero, the growth of the instability will be entirely due to the second term of the derived equations that represent the coupling between the RMI growth rate and the strain rate. The flat interface is initialised with a diffuse interface of the form,

$$f_1 = \frac{1}{2}\left(1 - \text{erf}\left(\frac{\sqrt{\pi}(x_1 - x_0)}{h}\right)\right) \tag{4.22}$$

where h is the initial diffusion width set to $\lambda/64$.

Table 4.1: Fluid properties for the linear regime cases.

Property	Fluid 1	Fluid 2	Units
Density, ρ	3	1	kg/m^3
Pressure, p	100	100	kPa
Molecular Mass, m	90	30	g/mol
Viscosity, μ	1.953125×10^{-4}	1.953125×10^{-4}	Pa s
Specific Heat Ratio, γ	5/3	5/3	
Lewis Number, Le	1	1	

The pressure was initialised at a uniform value of 100kPa throughout the domain. Using this pressure, the Mach number of the flow can reach up to 0.6 at the boundaries of the domain, however the turbulent Mach number remains around 0.004 throughout the simulation. The Reynolds number, $Re = U_0\lambda/\nu$, was set to 2048, which is sufficiently high that the linear regime growth rate is not impacted by viscosity (Walchli & Thornber, 2017). The kinematic viscosity for the multi-species system was calculated by $\nu = (\mu_1 + \mu_2)/(\rho_1 + \rho_2)$, and the same dynamic viscosity was used for both fluids. The Prandtl and Schmidt numbers were set to unity for both fluids, ensuring a Lewis number of one for calculating the diffusivity (see equation (3.22)). The initial properties of each fluid are provided in table 4.1. This configuration with a non-zero Atwood number, diffusivity, and a flat interface means that an initial asymmetry develops between the bubble and the spike due to the difference in the mass and volume fraction diffusive fluxes, caused by the density difference of the two fluids. This phenomenon does not affect the later time amplitudes or ratio.

For the specified fluid parameters and amplitude growth, it is difficult to ascribe a particular equivalent shock initialisation as the initial interface is flat, giving an amplitude and amplitude growth rate of zero for the equivalent problem. An analogous problem could be defined for a given shock strength by assuming some finite amplitude. With initial conditions of $p = 36.12\,\text{kPa}$, $\rho_1 = 1.76\,\text{kg m}^{-3}$, $\rho_2 = 0.56\,\text{kg m}^{-3}$, and $ak = 0.015$, then the post-shock conditions and amplitude growth rate of $U_0 = 1\,\text{m s}^{-1}$ would be achieved with a shock strength of $Ma = 1.8439$.

As the domain is expected to grow or shrink depending upon the sign of the imposed mean strain rate, different grids are used for the compression and the expansion cases. For the compression cases, the simulation was conducted on a grid of size $20\lambda \times \lambda$, to allow for the grid to compress by up to a factor of four without boundary effects inhibiting the growth of the instability. This grid is composed of initially square cells, which become rectangular as

Table 4.2: The strain rates, total simulation time, initial domain size, grid resolution, and final expansion factor for each of the linear regime cases.

Strain Profile	$\bar{S}_0$ (s^{-1})	$\hat{S}_0$	Simulation time (s)	Initial domain size (m^2)	Grid resolution	Λ_F
Unstrained	0.0	0.0	0.02	1.0×0.2	2560×128	1.00
Constant velocity	-37.50	-7.50	0.02	4.0×0.2	2560×128	0.25
Constant velocity	-18.75	-3.75	0.02	4.0×0.2	2560×128	0.625
Constant velocity	75.0	15.0	0.02	1.0×0.2	2560×128	2.50
Constant velocity	150.0	30.0	0.02	1.0×0.2	2560×128	4.00
Constant strain rate	-70.0	-14.0	0.02	4.0×0.2	2560×128	0.25
Constant strain rate	-35.0	-7.0	0.02	4.0×0.2	2560×128	0.50
Constant strain rate	35.0	7.0	0.02	1.0×0.2	2560×128	2.00
Constant strain rate	70.0	14.0	0.02	1.0×0.2	2560×128	4.00

the simulation progress, shrinking with the domain in the x-direction. For the expansion and unstrained cases, a grid of size $5\lambda \times \lambda$ was used, however the cell density was four times higher in the x-direction to allow the domain to expand up to a factor of four and still maintain the desired resolution in all directions. Besides the unstrained case, four cases were simulated for each strain profile. Listed in table 4.2, each profile has two expansion cases with positive strain rates, and two compression cases with negative strain rates.

4.3.3 Results

The final interfaces are plotted for the largest magnitude strain rate cases in figure 4.2. The difference in amplitude is evident between the compression and expansion cases, with around a factor of three difference in size. The strain rate has also affected the diffusive thickness of the interface, making it thicker for the expansion cases, which may inhibit the roll-up of secondary instabilities. The diffuse thickness has not scaled proportionally with the expansion factor as the diffusion rate is modified by the change in species gradient from the strain rate, resulting in a diffusive thickness that is proportionally less thick for the expansion cases when accounting for the expansion factor.

To measure the amplitude of the single-mode RMI, the interface position is taken to be along the isocontour line for the volume fraction where $f_1 = 0.5$. The amplitude is calculated by

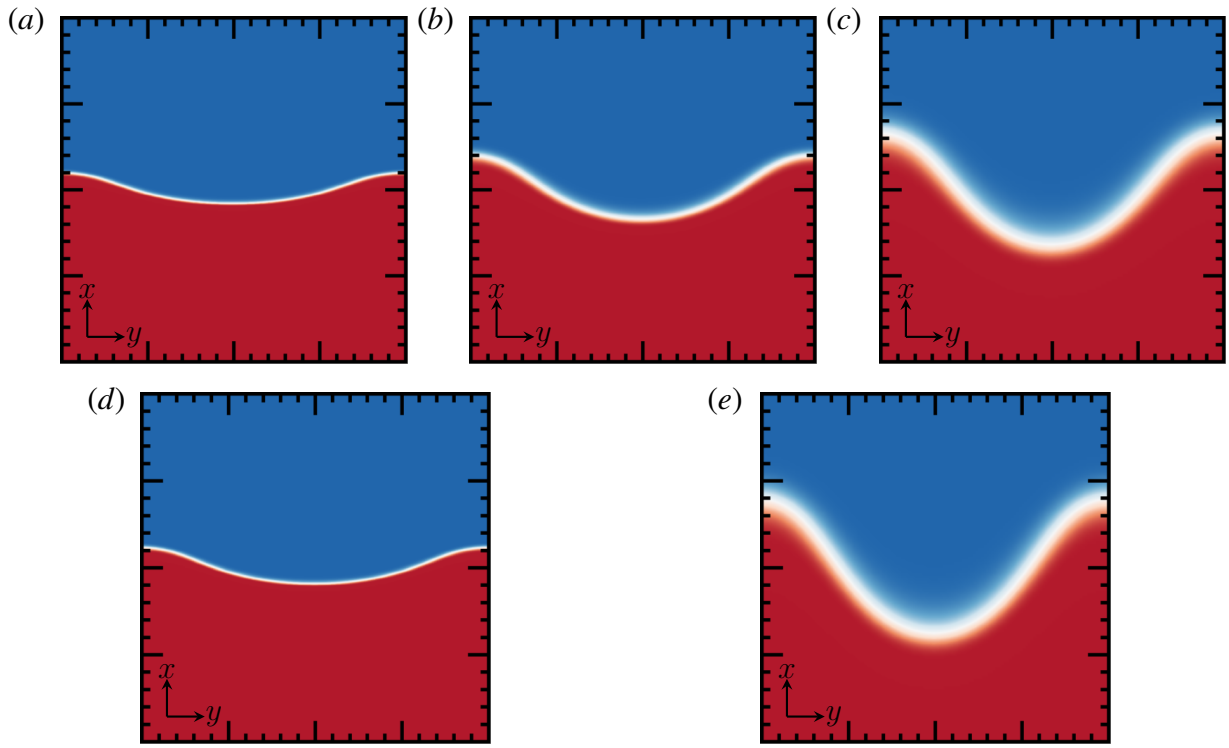

Figure 4.2: Visualisation of the volume fraction at $\tau = 0.1$ for the 2D single-mode simulations. Heavy fluid ($f_1 = 1$) is red, light fluid ($f_1 = 0$) is blue. Major ticks indicate a distance of $\lambda/4$; (*a*) Constant boundary velocity, $\hat{S}_0 = -7.5$, (*b*) Unstrained case, (*c*) Constant boundary velocity, $\hat{S}_0 = 30$, (*d*) Constant strain rate, $\hat{S} = -14$; (*e*) Constant strain rate, $\hat{S} = 14$.

taking the difference of the maximum and minimum x-position of the interface isocontour line,

$$a = 0.5 \left[\max(x_{f_1=0.5}) - \min(x_{f_1=0.5}) \right]. \tag{4.23}$$

The non-dimensionalised amplitude is plotted in figure 4.3, along with the theoretical solutions given in equations (4.13) and (4.14) as derived from the model by Epstein (2004). All cases initially start off with a linear growth rate, aligned with the unstrained growth rate. This is expected as the RMI contribution is proportional to t, whilst the strain is a higher order correction which provides a smaller contribution for early time. The cases with a negative strain rate grow more slowly in time, and the positive strain rate cases grow much faster. For the most strongly compressed constant velocity case, the growth-rate of the instability becomes negative, meaning the domain compression is reducing the amplitude faster than the instability is naturally growing. The theoretical model does manage to predict this behaviour in compression and matches the simulation result nicely. By $\tau = 0.1$, the theory tends to over-predict the amplitude of all the strained cases to some degree, as well as the unstrained case. At the final time, the difference between the model and simulation increases with the strain rate value, being larger for the expansion cases and smaller for the compression cases.

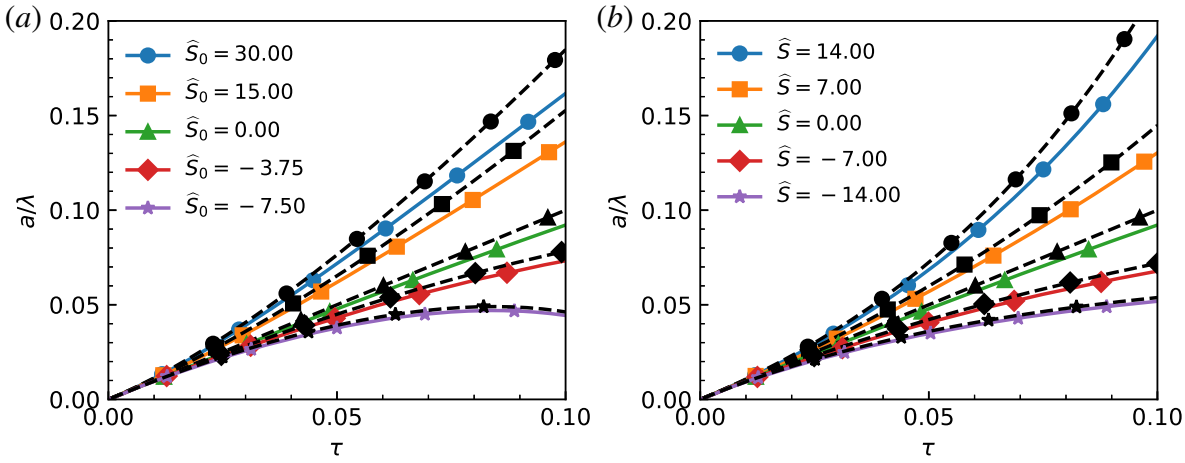

Figure 4.3: Amplitude of the single-mode linear regime for (a) constant boundary velocity and (b) constant strain rate. Solid lines indicate numerical results, dashed lines indicate linear model.

The percentage error is plotted in figure 4.4 as a function of the non-dimensional amplitude, showing the expansion cases reaching a larger percentage error than the compression. In this form, it can be seen that the error follows a roughly linear relationship with the amplitude. The compression cases which use an initially coarser grid in the y-direction show larger fluctuations in the early time due to the division of small values and the coarser grid. These oscillations in the error decrease as the grid becomes finer and as the amplitude values get larger with time. Given the roughly linear dependence of the error on the amplitude, the cause of the error is likely due to the mode saturation, as even the unstrained case diverges from linear theory. The error remains under 10% in magnitude whilst $a/\lambda < 0.1$, which is considered to be the cut-off for the linear regime (Brouillette, 2002). The actual growth rates simulated here are potentially slightly larger than what would be expected from a shock initialisation, as the vorticity deposited into the fluid due to the transmitted/reflected waves will inhibit the instability growth rate (Probyn *et al.*, 2021).

To see how the instabilities grow with respect to the domain size, it is possible to plot using the alternate non-dimensionalisaton listed in equation (4.15). Figure 4.5 shows the theoretical results all fall onto a single line, with the simulation results appearing close underneath. The simulation results are still expected to be below the theoretical growths due to the growth slowing down as the amplitude of the mode increases. It is interesting to see that when accounting for the domain growth, the $\hat{S}_0 = -7.5$ case shows approximately linear growth, suggesting it is still growing in the linear regime, but the growth is also being continually offset by the domain compression, which resulted in the net negative growth rate seen in figure 4.3. With this non-dimensionalisation the saturation time does not correspond to a specific value of $\hat{\tau}$, with the results diverging from the linear trend at different points along the plot.

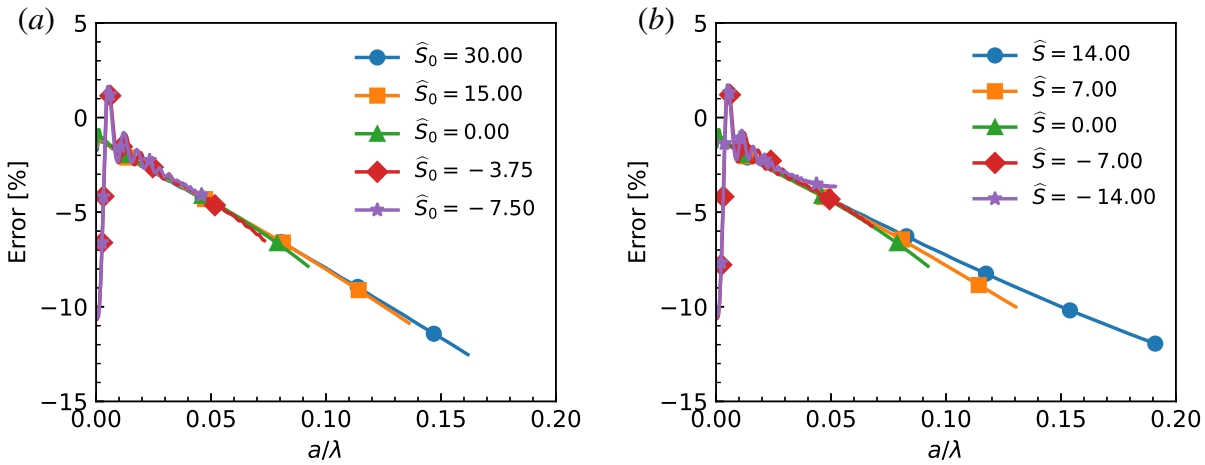

Figure 4.4: Error in the amplitude for the linear regime under (*a*) constant velocity and (*b*) constant strain rate.

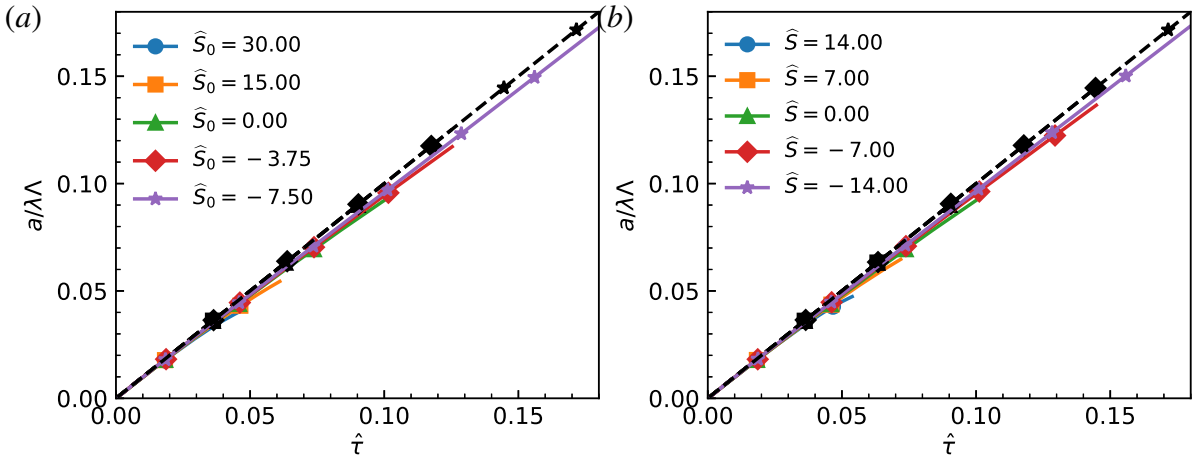

Figure 4.5: Amplitude of the single-mode linear regime for (*a*) constant velocity and (*b*) constant strain rate. Solid lines indicate numerical results, dashed lines indicate linear model.

4.4 Self-similar mixing layer

At late-time, RMI can induce a self-similar mixing layer, as indicated by quantities such as the mean volume-fraction collapsing down to a single curve when non-dimensionalised by the width of the mixing-layer, and the molecular mixing fraction, Θ, approaching an asymptotic value. The effect of axial strain on the development of multimode RMI has not been investigated, and it is unknown if the mixing layer reaches self-similarity. Using the three-dimensional quarter-scale narrowband case from the θ-group collaboration (Thornber *et al.*, 2017), the effects of axial strain rates on multimode RMI can be examined. Axial strain is added prior to the time at which the mixing layer achieves self-similarity, at a non-dimensional time of $\tau = 1$. This allows for stronger interaction between the strain rate and the turbulence in the anisotropic, inhomogeneous mixing layer than if the strain was applied at a later time. Following the original θ-group

simulations which were conducted using ILES, simulations of the strained mixing layer are also conducted using ILES. Additional modelling is performed using the buoyancy-drag model to determine the accuracy of recommended strain corrections.

4.4.1 Models

Buoyancy-drag model

The buoyancy-drag mixing model is based on the work by Layzer (1955) and Baker & Freeman (1981). The model was extended to better describe turbulent mixing by Dimonte (2000); Hansom *et al.* (1990); Oron *et al.* (2001); Ramshaw (1998). A buoyancy-drag model was calibrated for the narrowband RMI case used in the θ-group collaboration (Thornber *et al.*, 2017), which required a modification to the calculation of the effective length scale to prevent excessive drag at early time (Youngs & Thornber, 2020*b*). This buoyancy-drag model consisted of two coupled ordinary differential equations,

$$\frac{dW}{dt} = V, \quad \frac{dV}{dt} = -\frac{V^2}{l^{\text{eff}}(\bar{\lambda}, W)}. \tag{4.24a}$$

The model measures the mixing layer width using the integral width of the mixing layer,

$$W = \int_0^{L_x} \bar{f}_1 \bar{f}_2 dx. \tag{4.25}$$

along with a corresponding growth-rate or velocity measure, V. The effective length scale in the drag term was fitted to the form,

$$\frac{l^{\text{eff}}}{\bar{\lambda}} = \max\left\{ a - b\left(1 - e^{-cW/\bar{\lambda}}\right), \frac{\theta}{1-\theta}\left(\frac{W}{\bar{\lambda}} - d\right)\right\}. \tag{4.26}$$

This model is for the RMI-induced mixing layer and does not try to model shock transition. The resulting differential equation for the velocity component has no buoyancy contribution, only a drag contribution. The model for narrowband RMI was extended to model separate bubble and spike heights by Youngs & Thornber (2020*a*) for a similar case to the quarter-scale θ group case.

$$\frac{dh_b}{dt} = V_b, \qquad \frac{dV_b}{dt} = -\frac{V_b^2}{l_b^{\text{eff}}(\bar{\lambda}, h_b)} \tag{4.27a}$$

$$\frac{dh_s}{dt} = V_s, \qquad \frac{dV_s}{dt} = -\frac{V_s^2}{l_s^{\text{eff}}(\bar{\lambda}, h_b)} \tag{4.27b}$$

where the effective length scales for the $At = 0.5$ case were fitted according to,

$$\frac{l_b^{\text{eff}}}{\bar{\lambda}} = \max\left\{ a_b - b_s\left(1 - e^{-c_b h_b/\bar{\lambda}}\right), \frac{\theta}{1-\theta}\left(\frac{h_b}{\bar{\lambda}} - d_b\right)\right\} \tag{4.28a}$$

$$\frac{l_s^{\text{eff}}}{\bar{\lambda}} = \max\left\{ a_s - b_s\left(1 - e^{-c_s h_b/\bar{\lambda}}\right), \frac{\theta}{1-\theta} R\left(\frac{h_b}{\bar{\lambda}} - d_s\right)\right\} \tag{4.28b}$$

Table 4.3: Buoyancy-drag coefficients for $At = 0.5$, narrowband RMI (Youngs & Thornber, 2020*a*,*b*)

Length scale	a	b	c	d
Integral Width	0.3	0.176	8.35	0.237
Bubble	0.7	0.297	6.0	0.283
Spike	1.4	1.19	0.8	0.70

For the $At = 0.5$ case, the ILES data (as far as the calculations were conducted) was accurately modelled with a late-time growth rate of $\theta = 1/3$, the theoretical value of Elbaz & Shvarts (2018), and this is the value of θ used in the models here. However, if the ILES calculations were continued to a much later time, it is likely the theoretical value of $\theta = 1/4$ (Soulard *et al.*, 2018) would be appropriate. The self-similar ratio of spike-to-bubble height for the spike drag length scale was fitted to the data with $R = 1.1$. The remaining coefficients are listed in table 4.3. The coefficients are the same as those previously published (Youngs & Thornber, 2020*a*,*b*) except for c_S and d_S which have been modified to better capture the spike growth for this case.

The bubble and spike heights used in these equations are based on novel integral quantities, first defined in Youngs & Thornber (2020*a*). These bubble and spike heights are approximately equal to the bubble and spike values obtained by using the 1% and 99% cut-off of the mean volume fraction, however by being integral quantities they are less sensitive to statistical fluctuations.

$$h_{b/s} = 1.1 h^{(2)}_{b/s} \tag{4.29a}$$

$$h^{(m)}_s = \left[\frac{(m+1)(m+2)}{2} \frac{\int_0^\infty x'^m \bar{f}_1 dx'}{\int_0^\infty \bar{f}_1 dx'} \right]^{1/m} \tag{4.29b}$$

$$h^{(m)}_b = \left[\frac{(m+1)(m+2)}{2} \frac{\int_{-\infty}^0 |x'|^m \bar{f}_2 dx'}{\int_{-\infty}^0 \bar{f}_2 dx'} \right]^{1/m} \tag{4.29c}$$

These expressions are for when f_1 corresponds to the denser fluid ($\rho_1 > \rho_2$) and is initially below the mean interface position ($x' < 0$). The integrals are taken with reference to the mean interface position ($x' = x - x_C$), which is defined by the position where there are equal bubble and spike volumes on either side,

$$\int_{-\infty}^{x_C} \bar{f}_2 dx = \int_{x_C}^{\infty} \bar{f}_1 dx. \tag{4.30}$$

Buoyancy-drag models have been applied in spherical geometry in the works of Miles (2004, 2009); El Rafei & Thornber (2020). The key modifications used to adjust the buoyancy-drag model were to use the time varying wavelength for the drag calculation, as well as to incorporate

the background velocity of the fluid into the growth of the instability. Using a uniform mean background velocity gradient, $\bar{S}$, the velocity difference at the ends of a layer of width W is given by $W\bar{S}$, giving the new ordinary differential equation for the width as

$$\frac{dW}{dt} = V + W\bar{S} \tag{4.31}$$

This is the same correction that arises from the linear regime model in equation (4.6). As the quarter-scale narrowband case already has a calibrated buoyancy-drag model for the unstrained case, it is a great candidate to use to test the accuracy of the background strain rate correction whilst using the same drag expression from the unstrained case. El Rafei & Thornber (2020) calibrated a buoyancy-drag model for a narrowband perturbation in spherical geometry, however the effective length scales for the bubbles and spikes were different to the planar case of Youngs & Thornber (2020*a*). The initial buoyancy-drag simulations were conducted using equations with the inclusion of the background velocity correction:

$$\frac{dW}{dt} = V + W\bar{S}, \qquad \frac{dV}{dt} = -\frac{V^2}{l^{\text{eff}}(\bar{\lambda}, W)} \tag{4.32a}$$

$$\frac{dh_b}{dt} = V_b + h_b\bar{S}, \qquad \frac{dV_b}{dt} = -\frac{V_b^2}{l_b^{\text{eff}}(\bar{\lambda}, h_b)} \tag{4.32b}$$

$$\frac{dh_s}{dt} = V_s + h_s\bar{S}, \qquad \frac{dV_s}{dt} = -\frac{V_s^2}{l_s^{\text{eff}}(\bar{\lambda}, h_b)} \tag{4.32c}$$

using the same drag expressions given in equations (4.26) and (4.28).

4.4.2 Initial conditions

ILES

The ILES cases use the same initialisation as the quarter-scale narrowband case from the θ-group collaboration (Thornber *et al.*, 2017). ILES is conducted here using the inviscid form of equation (3.27), instead relying on the inherent numerical dissipation in the shock capturing scheme to approximate the cascade and removal of energy from the large scales to the small scales in the high-Reynolds number limit. The original quarter-scale case used a domain given by $x \times y \times z = \mathcal{L}_x \times \mathcal{L} \times \mathcal{L} = 2.8\pi \times 2\pi \times 2\pi\text{m}^3$. In the $y-$ and $z-$directions, periodic boundary conditions were used, whilst outflow boundary conditions were applied in the $x-$direction. The quarter-scale case was set up in a heavy-to-light configuration with unshocked densities of $3\,\text{kg}\,\text{m}^{-3}$ and $1\,\text{kg}\,\text{m}^{-3}$, both with $\gamma = 5/3$. The shock position was initialised in the heavy-fluid at $x = 3.0\text{m}$ using a Mach 1.8439 shock. The initial Atwood number is $At = 0.5$, and the post-shock Atwood number is $A^+ = 0.487$. The interface position was given by

$$S(y, z) = 3.5 + A(y, z)$$

The perturbation $A(y,z)$ is the summation of Fourier modes in the range of $\lambda_{\text{min}} = \mathcal{L}/32$ and $\lambda_{\text{max}} = \mathcal{L}/16$, and a constant power spectrum is used for the perturbations. The desired overall amplitude of the initial perturbation is $0.1\lambda_{\text{min}}$, with the profile shown in figure 4.6. The amplitudes and phase for each mode are randomly generated from a Gaussian distribution using a Mersenne Twister algorithm. The Mersenne Twister algorithm is deterministic for a given seed, so the random coefficients are reproducible, which allows for recreation of the interface. The amplitudes of each mode are scaled to achieve the desired power spectrum and amplitude. A detailed description of the generation of the perturbation can be found in Thornber *et al.* (2010, 2017). The interface is initially diffuse using a volume-fraction profile of

$$f_1 = \frac{1}{2}\left(1 - \text{erf}\left(\frac{\sqrt{\pi}\,[x - S(y,z)]}{\delta}\right)\right) \tag{4.33}$$

where the initial diffuse thickness is $\delta = \mathcal{L}/128$ for the quarter-scale case. The fluids are given a velocity offset of $\Delta u = -291.575\,\text{m}\,\text{s}^{-1}$ to account for the change in velocity from the incident shock. This allows the interface to remain stationary after the passage of the shock.

As given in Thornber *et al.* (2017), the variance $\sigma^2(t) = \sum_{k_x,k_y} a^2/2 = \int_0^\infty P(k)dk$ is the superposition of the individual modes and in the linear regime may be approximated as,

$$\sigma^2(t) = (C\sigma_0 A t^+ \Delta u \bar{k} t)^2 \tag{4.34}$$

using the initial variance σ_0, and the weighted average wave number of perturbation,

$$\bar{k} = \sqrt{\frac{\int_0^\infty k^2 P(k)dk}{\int_0^\infty P(k)dk}}. \tag{4.35}$$

For the narrowband, constant power spectrum, the mean wave number is equal to $\bar{k} = \sqrt{7/12}k_{\text{max}}$. For the perturbation type, the plane averaged volume fraction profile is given by,

$$\bar{f}_1(x) = \frac{1}{2}\left(1 - \text{erf}\left(\frac{x}{\sqrt{2}\sigma}\right)\right). \tag{4.36}$$

This can be related to the integral width through the definition in equation (4.25), which gives the relation $W = 0.564\sigma$. The initial predicted growth-rate for the integral width is obtained using the time derivative of the variance in equation (4.34).

$$\dot{W}_0 = 0.564\bar{k}At^+C\sigma_0\Delta u \tag{4.37}$$

For the quarter-scale case, the initial growth-rate is $\dot{W}_0 = 12.649\,\text{m}\,\text{s}^{-1}$. Length scales are non-dimensionalised by the mean wavelength, $\bar{\lambda} = 2\pi/\bar{k}$, and time scales are non-dimensionalised by using the initial growth-rate and mean wavelength, $\tau = t\dot{W}_0/\lambda$. This is the same approach

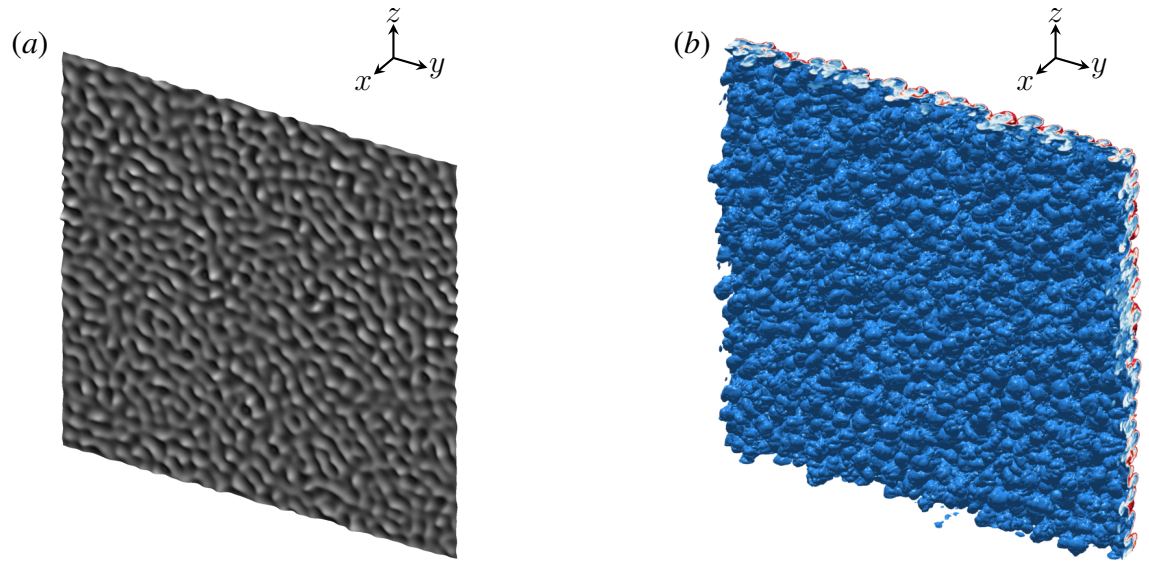

Figure 4.6: (*a*) Isosurface for volume fraction $f_1 = 0.5$ for the initial interface (*b*) Isosurfaces for $f_1 = 0.01$ (blue) and 0.99 (red) for the mixing layer at $\tau = 1$.

used in section 4.3, which enables the usage of the same non-dimensionalisation for the strain rate, $\hat{S} = \bar{S}\lambda/\dot{W}_0$. Other quantities are non-dimensionalised using $\dot{W}_0$, $\bar{\lambda}$, the cross-sectional area $4\pi^2$, and the mean post-shock density, $\bar{\rho}^+ = 3.51\ \mathrm{kg\,m^{-3}}$.

The application of the strain rates is applied to the simulation at $\tau = 1$, at which time the system is in the non-linear regime and bubble and spike structures have formed, as shown in figure 4.6. The strain rate is applied to the flow by adding a linear velocity gradient for the desired initial strain rate. As the main transmitted and reflected waves have left the domain, the outflow boundary conditions in the x-direction are replaced with moving inviscid walls, which allows the domain to maintain the background velocity gradient according to the prescribed strain rate profile. Four simulations were conducted for each strain profile, as listed in table 4.4, with two compressive strain rates and two expansive strain rates for each profile. The cases are run until a non-dimensional time of $\tau = 10$ or $\tau = 35$ depending upon the strain rate, such that the domain changes in length by a factor of two. For the expansion simulations, the solution at $\tau = 1$ is interpolated onto a grid with double the cells in the $x-$direction. This is to ensure that the simulations are able to resolve the same length scales as the unstrained case during the expansion, until $\Lambda(t) = 2$. Section 4.4.3 includes results that show the integral properties are unaffected by the introduction of walls for the unstrained simulation, and that the integral properties are converged for the expansion case using the base and refined mesh.

Table 4.4: The strain cases, total simulation time, domain size, grid resolution, and final expansion factor for each of the ILES cases.

Strain Profile	$\bar{S}_0$ (s^{-1})	$\hat{S}_0$	Simulation time (s)	Initial domain size (m^3)	Grid resolution	Λ_F
Unstrained	0.0	0.0	0.711	$2.8\pi \times 2\pi \times 2\pi$	720×512^2	1.00
Constant velocity	-2.50	-0.051	0.203	$2.8\pi \times 2\pi \times 2\pi$	720×512^2	0.54
Constant velocity	-0.625	-0.013	0.711	$2.8\pi \times 2\pi \times 2\pi$	720×512^2	0.57
Constant velocity	1.25	0.025	0.711	$2.8\pi \times 2\pi \times 2\pi$	1440×512^2	1.86
Constant velocity	5.0	0.102	0.203	$2.8\pi \times 2\pi \times 2\pi$	1440×512^2	1.91
Constant strain rate	-4.0	-0.081	0.203	$2.8\pi \times 2\pi \times 2\pi$	720×512^2	0.48
Constant strain rate	-1.0	-0.020	0.711	$2.8\pi \times 2\pi \times 2\pi$	720×512^2	0.50
Constant strain rate	1.0	0.020	0.711	$2.8\pi \times 2\pi \times 2\pi$	1440×512^2	2.00
Constant strain rate	4.0	0.081	0.203	$2.8\pi \times 2\pi \times 2\pi$	1440×512^2	2.08

Buoyancy-drag model

The buoyancy-drag model is initialised using the data provided in Youngs & Thornber (2020*a*). In this work, higher-resolution ILES simulations were conducted to ensure convergence at the early time of the narrowband RMI. As the buoyancy-drag model does not seek to capture the effects of shock compression, the model begins with an offset of $\tau = 0.08$. The initial conditions given are,

$$W_0 = 0.5642 C \sigma_0 \tag{4.38a}$$

$$h_{s0} = h_{b0} = 1.1 \times 2.0 C \sigma_0 \tag{4.38b}$$

$$V_0 = 0.5642 C \bar{k} \sigma_0 \Delta u A t \times F_W^{nl} \tag{4.38c}$$

$$V_{b0} = 1.1 \times 2.0 C \bar{k} \sigma_0 \Delta u A t \times F_b^{nl} \tag{4.38d}$$

$$V_{s0} = 1.1 \times 2.0 C \bar{k} \sigma_0 \Delta u A t \times F_s^{nl} \tag{4.38e}$$

with compression factor $C = 0.576$, and non-linearity factors: $F_W^{nl} = 0.85$, $F_b^{nl} = 0.54$, and $F_s^{nl} = 0.96$. The equations for the buoyancy-drag model are integrated without any strain rate applied until $\tau = 1$, after which the applied mean strain rate is included in the calculation by using the background velocity correction for the length scales, as shown in equation (4.31).

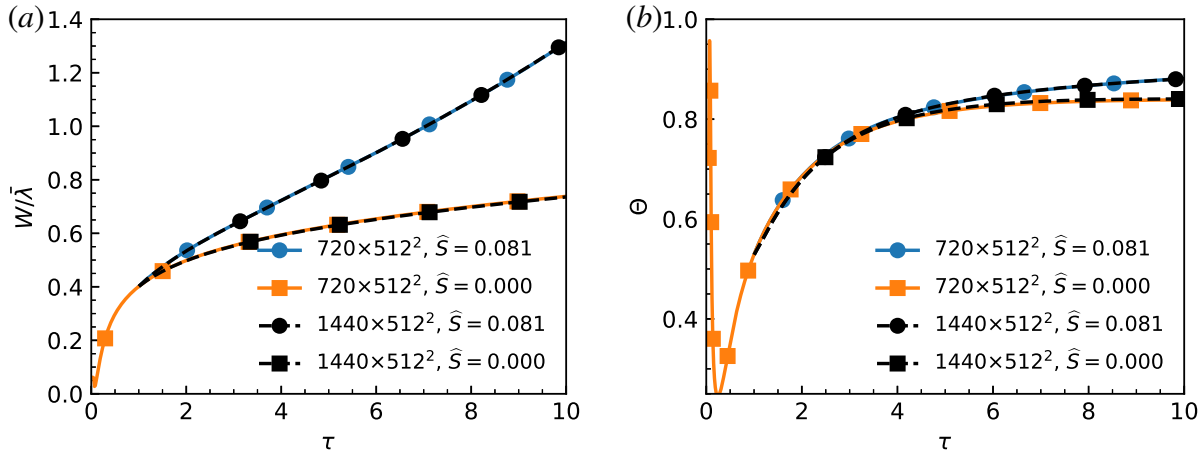

Figure 4.7: Effect of axial interpolation for (a) integral width, and (b) molecular mixing fraction. Solid lines indicate original mesh, dashed lines indicate refined mesh with interpolated solution.

4.4.3 Convergence

Implicit large eddy simulations are required to resolve the largest scales, leaving the smallest scales to be modelled by the numerical scheme of the code. Whilst the unstrained quarter-scale θ-group case is converged (Thornber *et al.*, 2017), the simulations with expansion strain-rates experience decreasing mesh resolution, which can increase the numerical dissipation. To mitigate this effect on the solution, the expansive cases use a solution interpolated onto a finer mesh with twice as many cells in the axial direction, ensuring the final expanded mesh size is not larger than the original mesh size. To show that the integral properties are converged, the unstrained and the constant-strain expansion case $\widehat{S} = 0.081$ were conducted with the original and refined mesh. The results in figure 4.7 show that the integral width and molecular mixing fraction are converged. The refined unstrained mesh also uses the wall boundary condition in the axial direction, showing that the inclusion of the walls in the x-direction doesn't affect the solution.

4.4.4 Results

Visualisations

Slices of volume fraction contours of the x-y plane for the constant velocity cases are shown in figure 4.8, with the solution at $\tau = 9.843$ shown in the left column, and $\tau = 34.451$ in the right column. The rows are organised by increasing strain rate, such that the strongest compression case is displayed in the top row, and the strongest expansion case is shown in the bottom row. For the same τ, the effect of the strain rate on the width of the mixing layer is evident, with the expansion cases growing much larger than the compression cases. The expansion cases appear to show more mixing within the mixing layer, showing larger amounts of intermediate

concentration, denoted by white in the images. The compression cases tend to show sharper transitions between regions of pure concentration, which may be expected as any diffusive widths are also being compressed.

A comparison of the 3D isosurfaces of the mixing layers for the same expansion factor is shown in figures 4.9 and 4.10. For the largest strain rate magnitudes, this occurs at a much smaller non-dimensional time, τ, than for the moderate magnitude strain rates. The mixing layer widths for the higher magnitude strain rate cases appear slightly smaller than the moderate strain rate cases, which is a likely result as the mixing layer has had less time to develop naturally from entrainment and diffusion; in the rapid limit for expansion, the mixing layer will grow only by the factor of $\Lambda(t)$, whilst a slower strain rate will have the turbulent growth of the mixing layer in addition. The bubble and spike structures are larger for the expansion cases, with the compression cases showing less variation in the isosurface position. Part of this appears to be due to the merger of bubbles and spikes into larger structures for the expansion cases compared to the compression cases. A comparison between different strain-profiles can be made by comparing adjacent figures. There are some slight visual differences of certain structures, however the overall morphology appears to be very similar between strain profiles for the same expansion factor.

Width and mix measures

The integral width of the mixing layer for both the ILES and buoyancy-drag cases is plotted in figure 4.11. Supporting the visualisations of the mixing layer, the expansion cases grow faster than the unstrained case, and the compression cases grow slower, even experiencing negative growth-rate. It is possible to observe a difference in the trajectories of the integral width curves between the constant strain rate and the constant velocity. For the expansion cases, the constant velocity has a strain rate that decreases in magnitude with time. This can be observed as the constant strain rate expansion cases have steeper gradients at the end of their simulations compared to the constant velocity, due to the integral width growing more from the layer stretching with the domain. For the compression cases, the constant velocity simulations have a strain rate that increases in magnitude (becomes more negative), and so the trajectory appears to be slightly more negative than the constant strain rate cases. The buoyancy-drag model does not align with the ILES simulation, except for the unstrained case for which it was calibrated. The buoyancy-drag model appears to overestimate the influence of the strain rate on the mixing layer, predicting a larger integral width for the expansion cases and a smaller integral width for the compression cases compared to what is observed from the ILES.

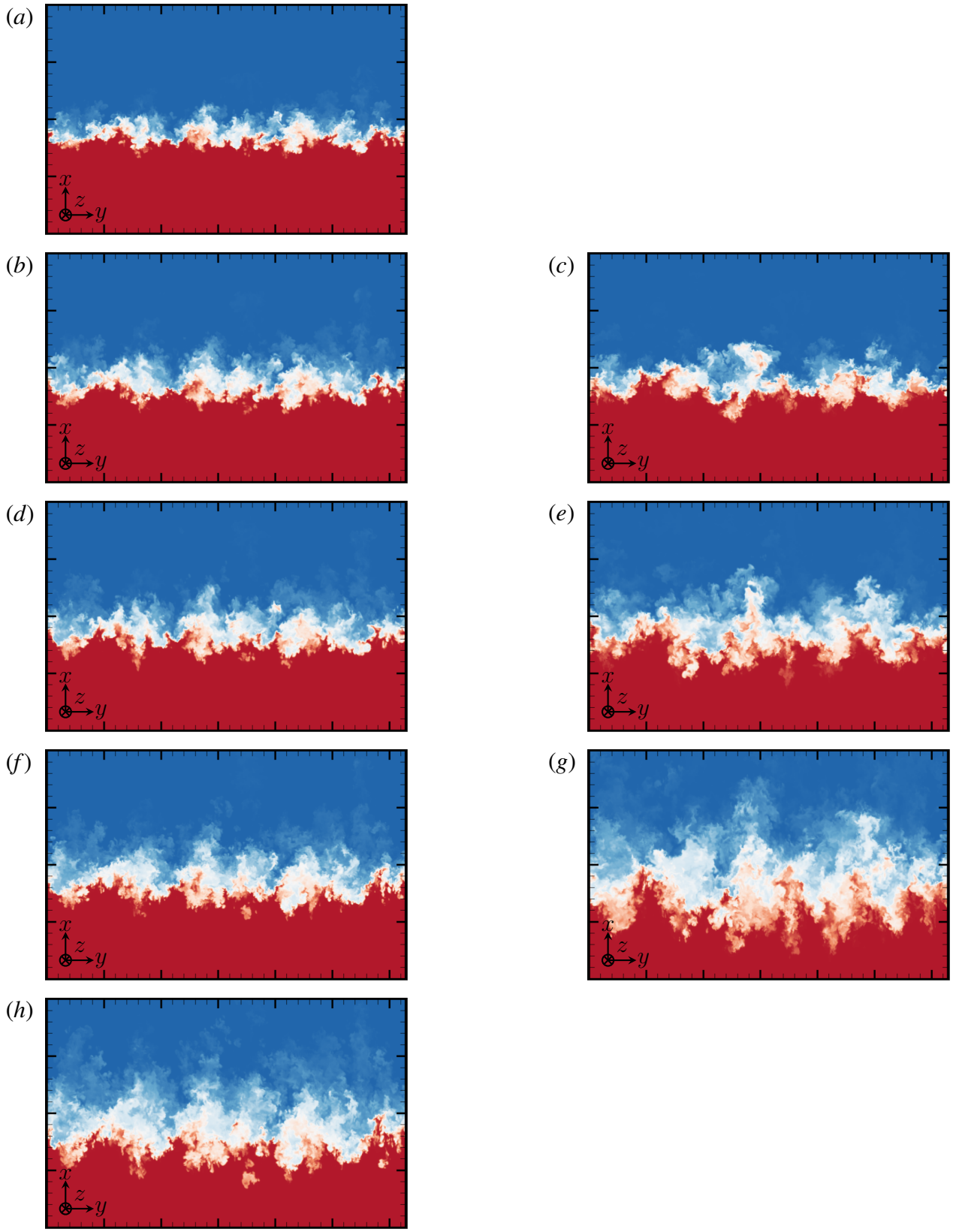

Figure 4.8: Contours of the volume fraction for the constant velocity ILES cases at $z = 0$. Heavy fluid ($f_1 = 1$) is red, light fluid ($f_1 = 0$) is blue. Major ticks on the axes correspond to $\Delta x = \Delta y = 1$m; (*a,b,d,f,h*) $\tau = 9.843$, (*c,e,g*) $\tau = 34.451$. (*a*) $\hat{S}_0 = -0.051$; (*b,c*) $\hat{S}_0 = -0.013$; (*d,e*) $\hat{S}_0 = 0$, (*f,g*) $\hat{S}_0 = 0.025$, (*h*) $\hat{S}_0 = 0.102$.

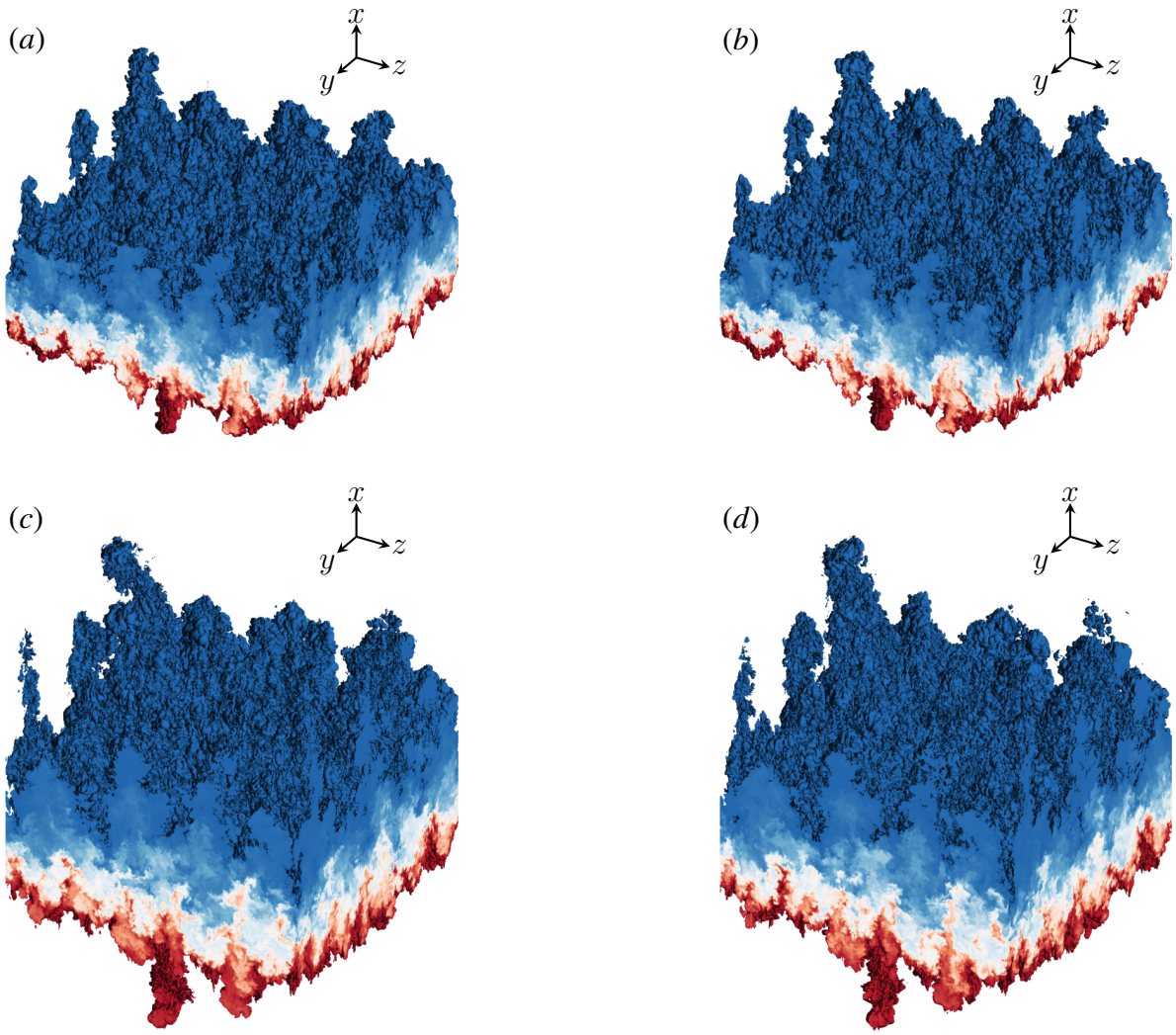

Figure 4.9: Contour of volume fraction f_1 for the expansion mixing layers at $\Lambda \approx 1.866$, bounded by $f_1 = 0.999$ (red) and $f_1 = 0.001$ (blue). (*a*) $\hat{S}_0 = 0.102$, $\tau = 9.55$, (*b*) $\hat{S} = 0.081$, $\tau = 8.66$, (*c*) $\hat{S}_0 = 0.025$, $\tau = 35.0$, (*d*) $\hat{S}_0 = 0.020$, $\tau = 31.7$.

The alternate non-dimensionalisation for the system is presented in figure 4.12, which in the linear regime was able to collapse the theoretical growth-rate down to a single straight line. The buoyancy-drag model results are included and show that with this non-dimensionalisation the buoyancy-drag predictions for all strain cases are almost equal to the unstrained ILES. There is a slight variation in the buoyancy-drag curves. This is due to the effective drag length scale not being self-similar under the transformation. The ILES strained results do not collapse down, instead the ILES compression cases grow at an increased rate compared to the unstrained and the ILES expansion cases have a decreased growth-rate. The failure of the buoyancy-drag model to accurately capture the physics of this anisotropic strain case suggests further corrections to the buoyancy-drag model are required, which will be explored in §4.4.4.

The plots for the bubble and spike heights are shown in figure 4.13 and 4.14 respectively. The

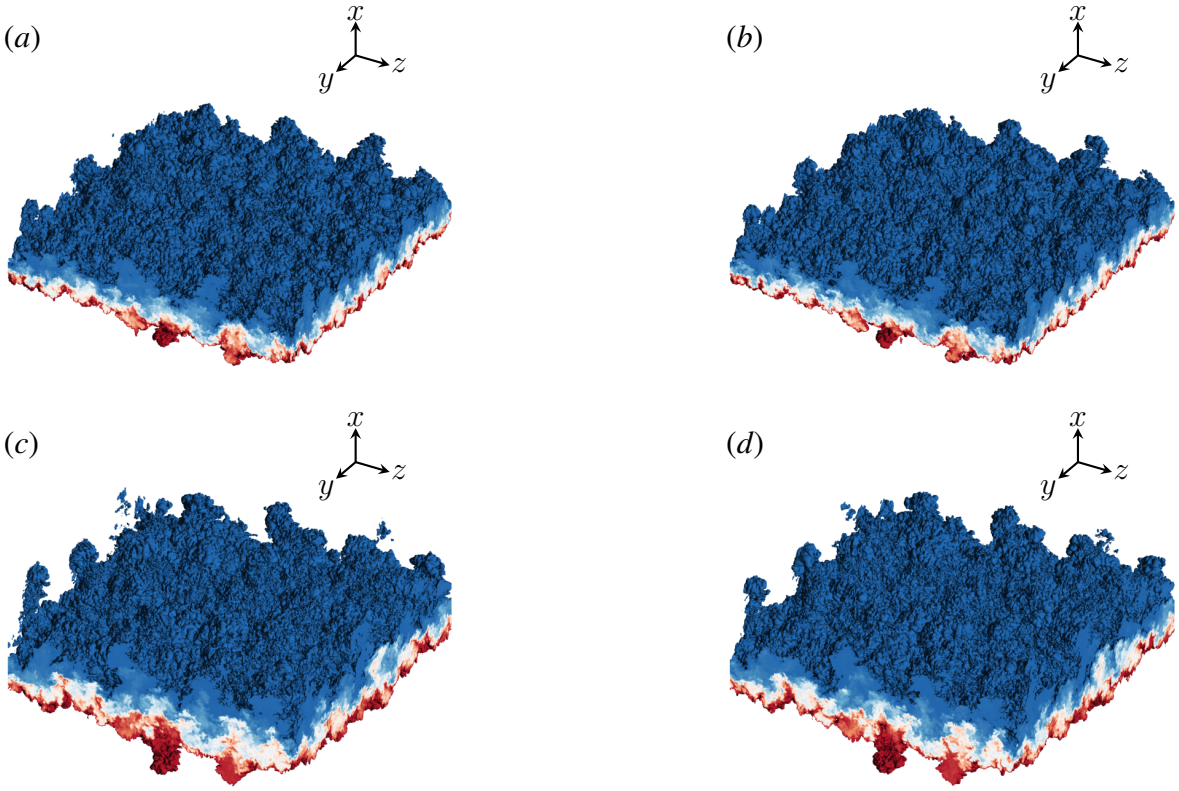

Figure 4.10: Contour of volume fraction f_1 for the expansion mixing layers at $\Lambda \approx 0.567$, bounded by $f_1 = 0.999$ (red) and $f_1 = 0.001$ (blue). (*a*) $\hat{S}_0 = -0.051$, $\tau = 9.55$, (*b*) $\hat{S} = -0.081$, $\tau = 7.97$, (*c*) $\hat{S}_0 = -0.013$, $\tau = 35.0$, (*d*) $\hat{S}_0 = -0.020$, $\tau = 28.9$.

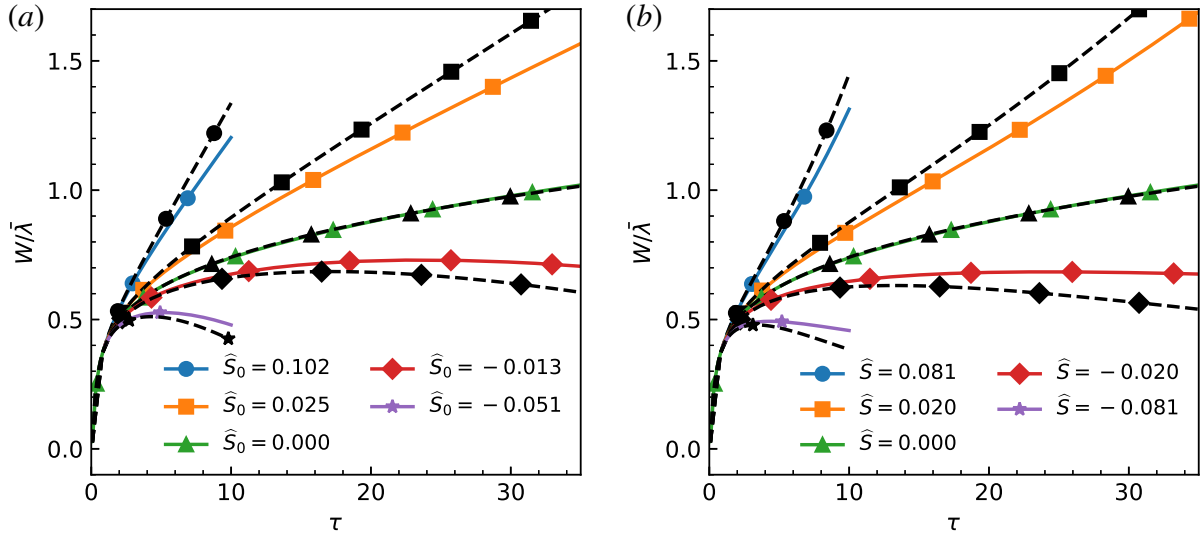

Figure 4.11: Integral width for (*a*) constant velocity, and (*b*) constant strain rate. Solid lines indicate ILES, dashed lines indicate buoyancy-drag.

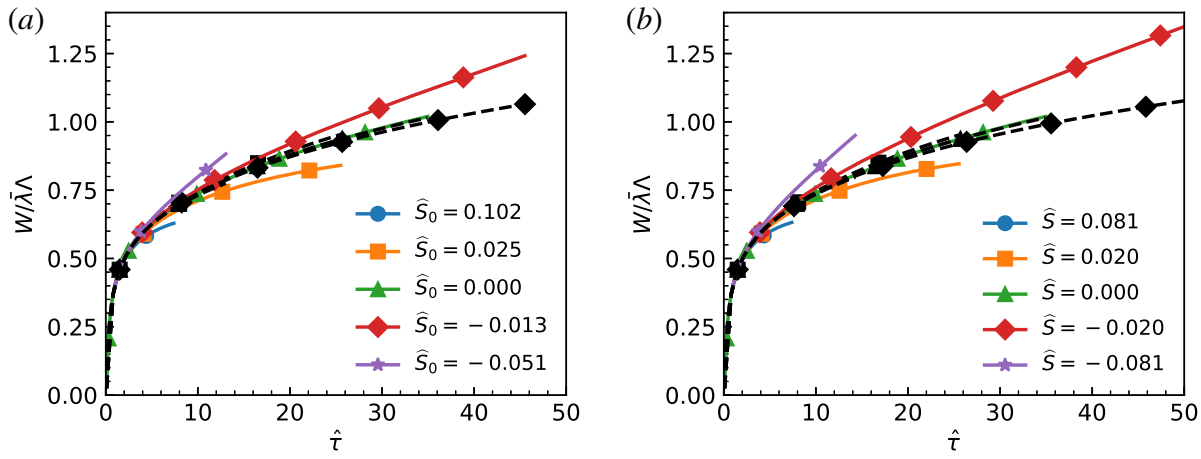

Figure 4.12: Alternate non-dimensionalisation for integral width for (*a*) constant velocity, and (*b*) constant strain rate. Solid lines indicate ILES, dashed lines indicate buoyancy-drag.

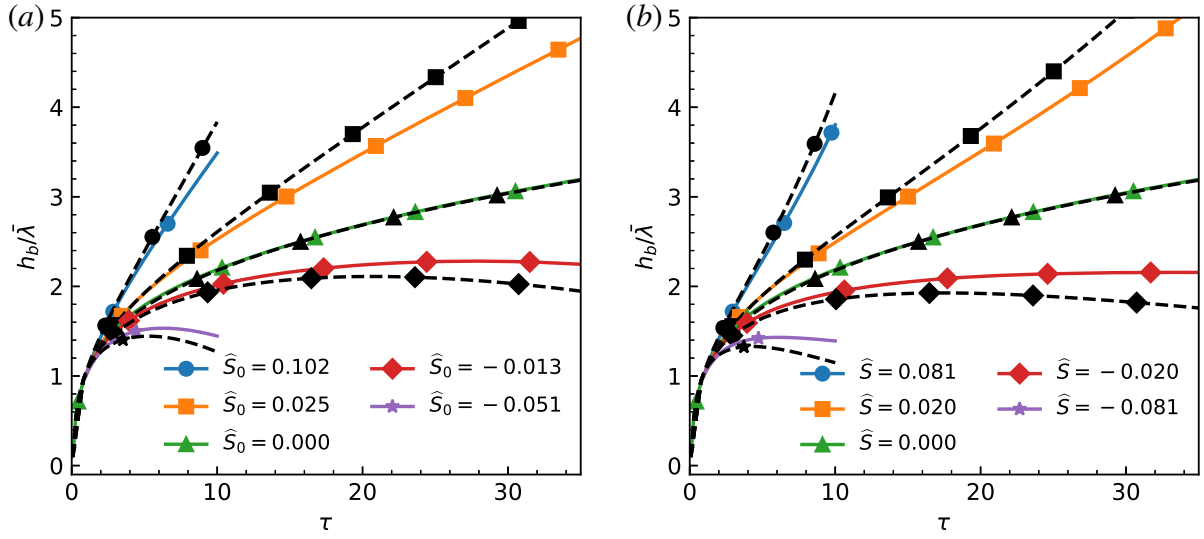

Figure 4.13: Bubble heights for (*a*) constant velocity, and (*b*) constant strain rate. Solid lines indicate ILES, dashed lines indicate buoyancy-drag.

bubble and spike heights behave in the same manner as the integral width, with both the bubble and spike heights increasing with positive strain rate and decrease with negative strain rate. The buoyancy-drag model again over-predicts the influence of the strain rate on the growth-rate.

The buoyancy-drag model for the spike height uses a drag term that is calculated from the bubble height, assuming the ratio of the two heights will achieve a self-similar ratio. For the quarter-scale narrowband case with Atwood number 0.5, the value used in the model is $R = 1.1$ (Youngs & Thornber, 2020*a*). Looking at the spike-to-bubble ratio in figure 4.15 the strain rate causes the ratios to diverge, increasing for expansion and decreasing for compression. This suggests the spike height is more affected by the strain rate than the bubble height.

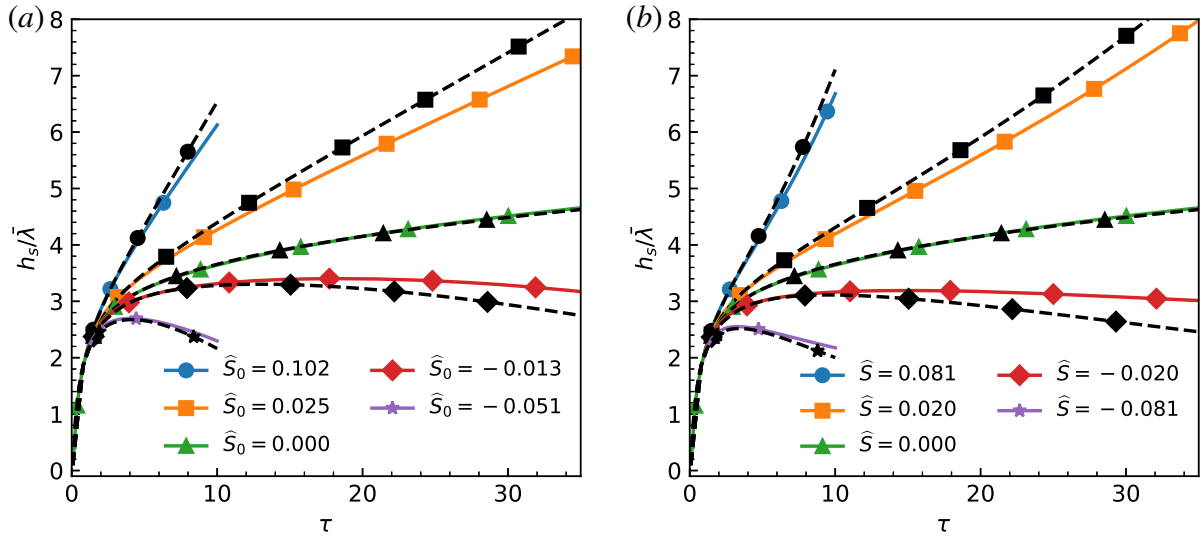

Figure 4.14: Spike heights for (*a*) constant velocity, and (*b*) constant strain rate. Solid lines indicate ILES, dashed lines indicate buoyancy-drag.

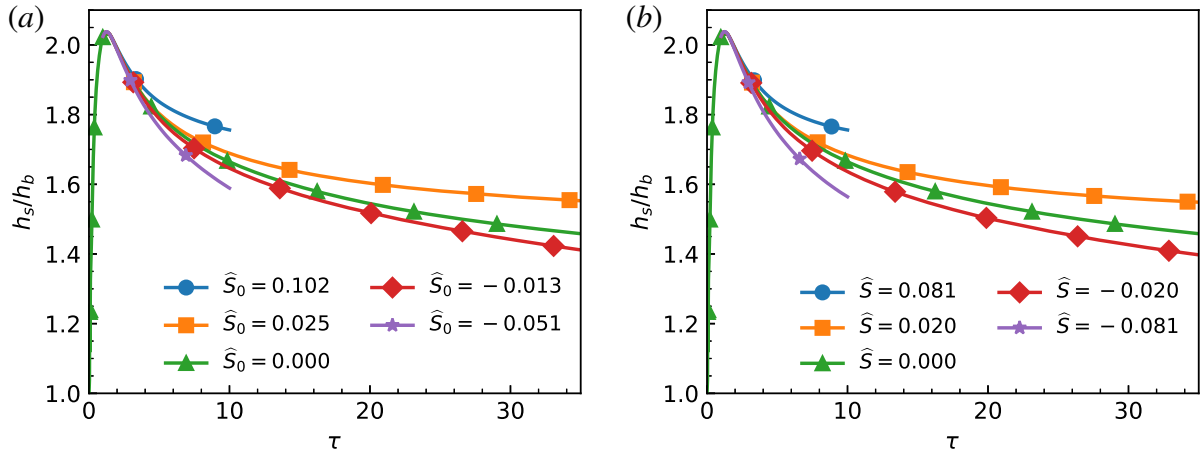

Figure 4.15: Ratio of spike-to-bubble height for (*a*) constant velocity, and (*b*) constant strain rate.

The molecular mixing fraction, an integral mixing measure, is calculated by,

$$\Theta(t) = \frac{\int \overline{f_1 f_2} dx}{\int \bar{f}_1 \bar{f}_2 dx} \tag{4.39}$$

where the overbar denotes a planar average in the homogeneous directions. The ILES result is plotted in figure 4.16, and included is FLAMENCO's value of Θ at the final time of $\tau = 246$ from the θ-group collaboration (Thornber *et al.*, 2017). In the present simulations, the unstrained case does not yet achieve this value and is instead slowly decreasing towards it. Immediately after perturbation, the strained cases appear to follow the same trajectory until around $\tau = 3$. Afterwards, the strain rates cause the molecular mixing fraction to change. The expansion cases surprisingly become more mixed, remaining above $\Theta = 0.85$. The compressed cases become less mixed, dropping below the steady-state value, and showing strong negative gradients at

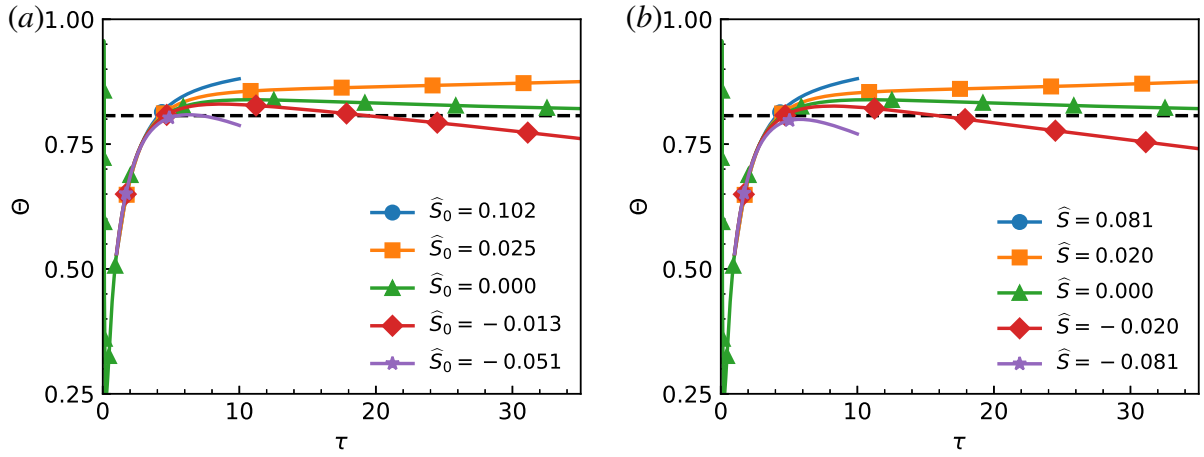

Figure 4.16: Integral mixing measures for the (*a*) constant velocity, and (*b*) constant strain rate. Solid lines indicate ILES results, dashed line is FLAMENCO's final value from Thornber *et al.* (2017).

the end of their simulations, suggesting they would continue to decrease in mixedness. The deviations from the self-similar asymptote suggest that the strain rates changes the behaviour of the mixing layer beyond the effect of changing the mixing layer's size through expansion or compression. This is analysed through the self-similarity of the volume fraction profiles in the following section.

Self-similarity

The denominator of the molecular mixing fraction is the integral width, computed from the mean volume fraction profile, $\bar{f}_1$, whilst the numerator is an integral over the mean volume fraction product, $\overline{f_1 f_2}$. The collapse of these two profiles is a key indication of when the mixing layer has reached a self-similar state. The spatial profiles for $\bar{f}_1$ and $\overline{f_1 f_2}$ are plotted at the end times of the simulations, $\tau = 9.843$ and 34.451, with constant velocity in figure 4.17 and constant strain rate in figure 4.18. The mean volume fraction profiles at the earlier time appear very similar, collapsing to the unstrained mean volume fraction profile. The profile for $\overline{f_1 f_2}$ shows an observable difference. Whilst the edges of the mixing layer appear to be similar, the peak of the profiles vary noticeably. A peak value of 0.25 would occur if every cell along the plane was 50% f_1 and 50% f_2. An increase in the peak of $\overline{f_1 f_2}$ for the expansion cases is indicative of greater homogeneity near the mixing layer centre. Likewise, the compression cases have a reduced maximum, suggesting that less mixing has occurred.

At late time, when only the data for the weaker strain cases is available, the effects of the strain rate on mixing becomes more prominent. There is some slight variation in the mean volume fraction profile on the bubble side. For the mean volume fraction product, the difference

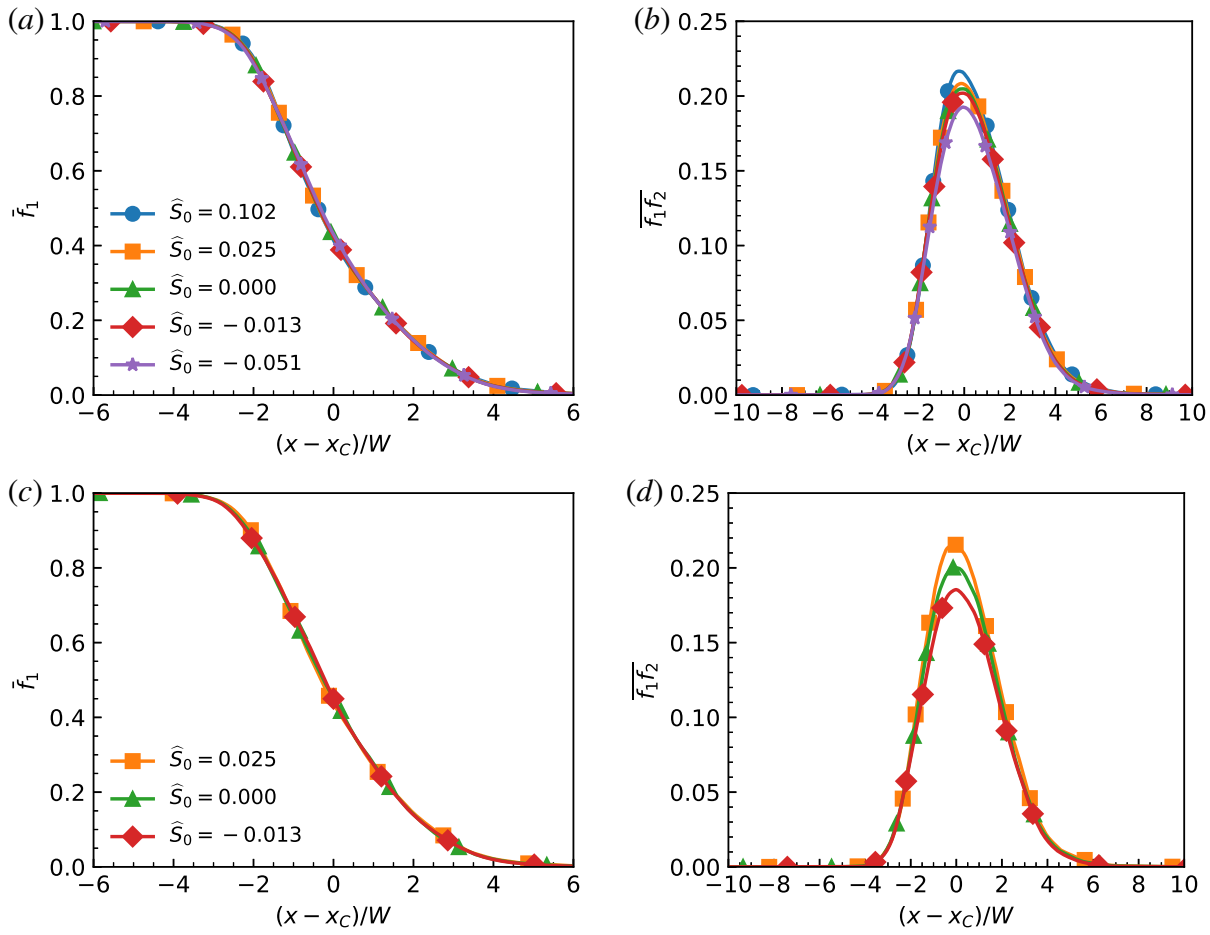

Figure 4.17: Planar averaged volume-fraction profiles for the constant velocity cases. (*a,b*) $\tau = 9.843$, (*c,d*) $\tau = 34.451$.

in the maxima at the centre of the mixing layer is evident, with the expansion case having a much larger peak than the unstrained and the compressed case. In the θ-group paper (Thornber *et al.*, 2017), the peak of $\overline{f_1 f_2}$ remains almost unchanged between $\tau = 25$ and $\tau = 196$. The difference observed in the mean volume fraction product reinforces the observation of the increased mixing (i.e. higher value of Θ) observed for the expansion case compared to the unstrained case, and suggests the axial strain rate causes the mixing layer to no longer collapse down to a self-similar profile.

Turbulent kinetic energy

The total turbulent kinetic energy in the domain, defined by,

$$TKE = \iiint \frac{1}{2} \rho u_i'' u_i'' \, \mathrm{d}x \, \mathrm{d}y \, \mathrm{d}z, \tag{4.40}$$

is plotted in figure 4.19. For all cases, the turbulent kinetic energy is decreasing due to dissipation. At late time, the unstrained case can be expected to fit a power-law spectrum of the form $t^{3\theta-2}$

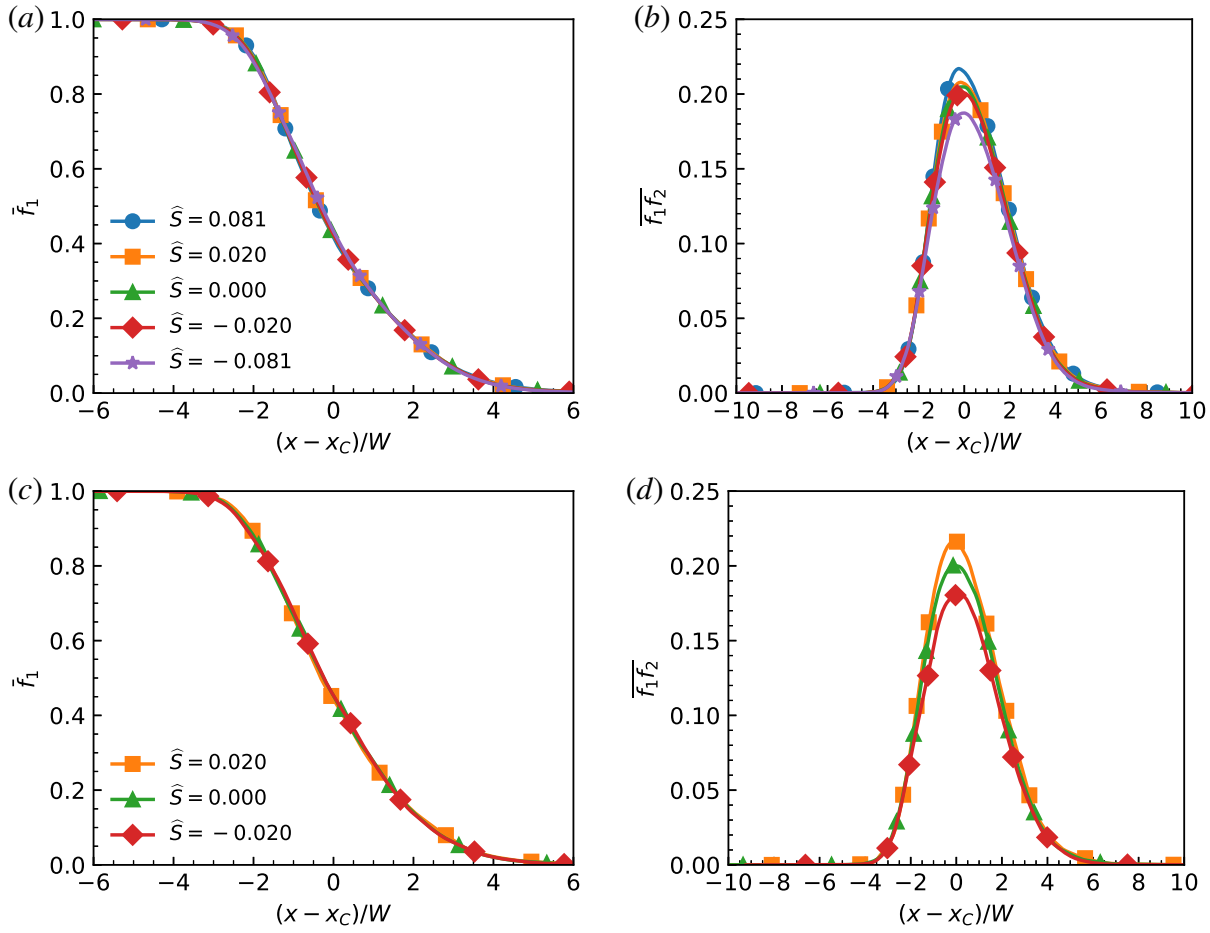

Figure 4.18: Planar averaged volume-fraction profiles for the constant strain rate cases. (*a,b*) $\tau = 9.843$, (*c,d*) $\tau = 34.451$.

(Thornber *et al.*, 2010). Whilst the unstrained case is heading towards this trend, the strained cases make a deviation. The compression cases show a larger amount of TKE compared to the unstrained domain, whilst the expansion cases show a decrease in the total turbulent kinetic energy. This is to be expected from the Reynolds stress transport equation, where the shear production contributes to the Reynolds stress as,

$$\frac{D\overline{\rho u_i'' u_j''}}{Dt} \propto -\overline{\rho u_i'' u_k''}\frac{\partial \tilde{u}_j}{\partial x_k} - \overline{\rho u_k'' u_j''}\frac{\partial \tilde{u}_i}{\partial x_k}. \tag{4.41}$$

In rapid-distortion theory, the primary contributions to the Reynolds stress are shear production and pressure scrambling. These simulations are not in the rapid-distortion limit, evident by the dominating role of dissipation on the evolution of the turbulent kinetic energy. With applied axial strain rates, there is a strong contribution from $\partial \bar{u}_1/\partial x_1$, which will only directly contribute to the x-turbulent kinetic energy. The directional components for the domain integrated turbulent kinetic energy can be calculated by,

$$TKX = \iiint \frac{1}{2}\rho u_1'' u_1'' \,\mathrm{d}x\,\mathrm{d}y\,\mathrm{d}z \qquad TKY = \iiint \frac{1}{2}\rho u_2'' u_2'' \,\mathrm{d}x\,\mathrm{d}y\,\mathrm{d}z. \tag{4.42}$$

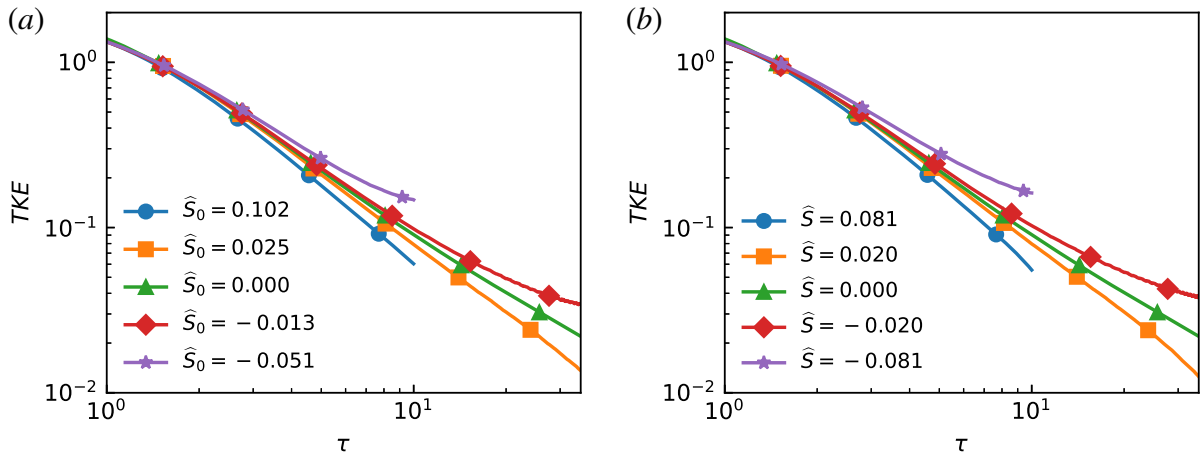

Figure 4.19: Total turbulent kinetic energy for (a) constant velocity, and (b) constant strain rate.

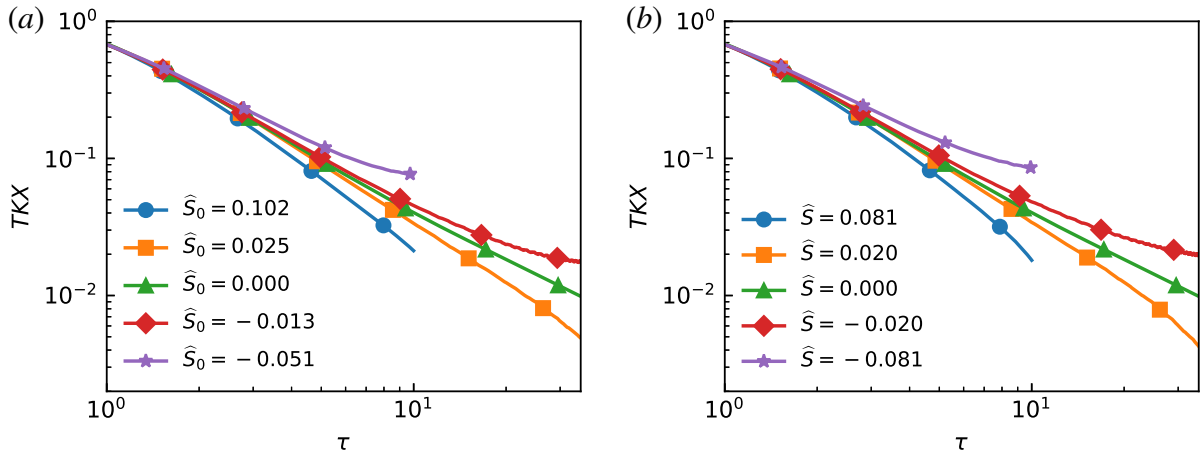

Figure 4.20: Turbulent kinetic energy in the x-direction for (a) constant velocity, and (b) constant strain rate.

The value of TKX is plotted in figure 4.20 and shows the same trend as the total turbulent kinetic energy. Due to the negative sign in the Reynolds stress equation, a negative strain rate corresponds to an increase in the turbulent kinetic energy, which is what is observed in the simulation results. For the y- and z-directions, the production terms are not expected to make the same level of contribution, as there is no applied mean strain rate to the flow. The y-turbulent kinetic energy is plotted in figure 4.21 and whilst it does show an increase in turbulent kinetic energy for the compression cases, and a decrease for the expansion, the contribution appears to be diminished compared to what is observed in the x-turbulent kinetic energy.

It can be expected that some turbulent kinetic energy will be redistributed from x to y and z due to the pressure scrambling. To see how the strain rates affect the distribution of the turbulent kinetic energy, it is possible to look at the level of anisotropy of the flow given by

$$TKR = \frac{2TKX}{TKY + TKZ}. \tag{4.43}$$

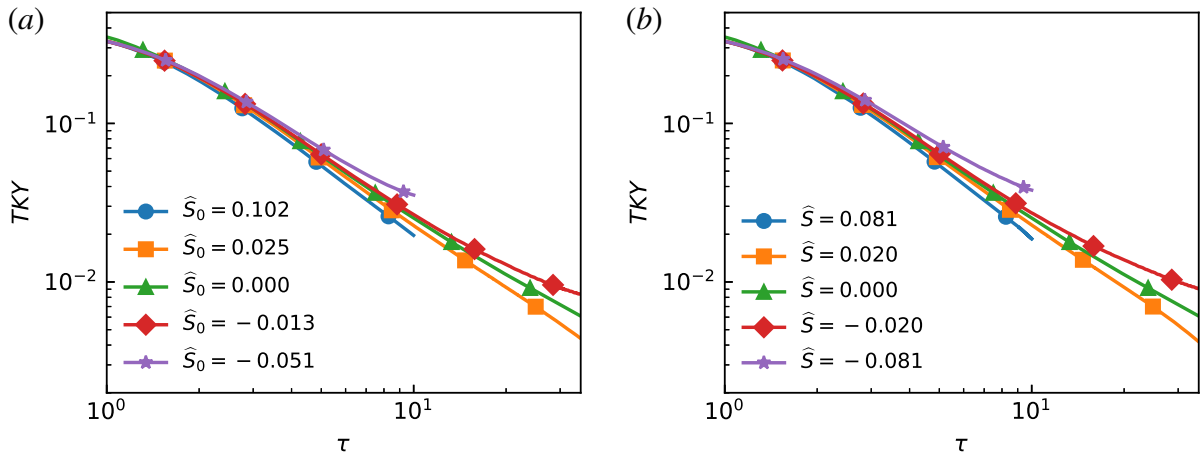

Figure 4.21: Turbulent kinetic energy in the y-direction for (a) constant velocity, and (b) constant strain rate.

For an isotropic flow, this value would collapse to one. As previously stated, RMI is observed to be persistently anisotropic both experimentally and in simulations, with FLAMENCO's anisotropy at $\tau = 246$ reaching $TKR = 1.49$ (Thornber *et al.*, 2017). The anisotropy is plotted in figure 4.22 and shows a strong divergence from the unstrained behaviour. This suggests that the pressure scrambling is not able to move the turbulent kinetic energy to/from the axial direction faster than it is removed/produced at the simulated strain rates. With insufficient turbulent kinetic energy redistribution, the strained simulations will not achieve the unstrained self-similar anisotropy, instead becoming more anisotropic during strain application. For the compression cases, the turbulent kinetic energy becomes focused towards the x-direction, reaching values above $TKR = 2$. The expansion cases have decreasing TKR, heading towards isotropy. The highest constant strain rate case shows that the decreasing trend continues past isotropy, and the turbulent kinetic energy is becoming focused in the transverse directions due to the removal of the axial turbulent kinetic energy by the mean velocity gradients. The changes in turbulent kinetic energy can explain the changes in the mixing layer growth-rate compared to the unstrained case. As the compression cases have increased axial velocity fluctuations, it is possible for the fluid to achieve greater entrainment of bulk pure fluid into the mixing layer, lowering Θ, whilst the expansion cases have lower entrainment, thus increasing Θ.

Vorticity

In compressible rapid-distortion theory, the vorticity equation has two linear contributions, the vortex stretching contribution for 3D flows and the compressibility contribution (Blaisdell *et al.*,

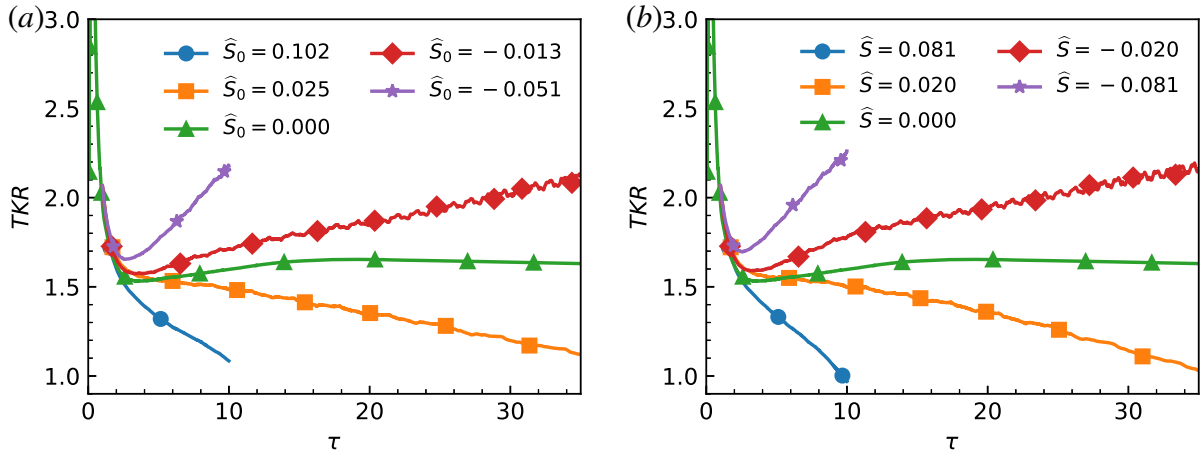

Figure 4.22: Anisotropy of the turbulent kinetic energy for (*a*) constant velocity, and (*b*) constant strain rate.

1996).

$$\frac{D\omega_i}{Dt} = \omega_j \frac{\partial u_i}{\partial x_j} - \omega_i \frac{\partial u_k}{\partial x_k} \tag{4.44}$$

where ω_i is the vorticity defined by,

$$\omega_i = \epsilon_{ijk} \frac{\partial u_k}{\partial x_j}, \tag{4.45}$$

and ϵ_{ijk} is the Levi-Civita symbol. If equation (4.44) is considered with only the mean axial strain rate, the contributions to the in-plane vorticity, ω_x, will cancel out. The out-of-plane components do not experience vortex stretching directly from the mean strain rate, but will decrease from the compressibility term for expansion cases, and increase for the compression cases. In figure 4.23, the total enstrophy of the domain is plotted. The enstrophy is given by,

$$\Omega = \iiint \rho \omega_i \omega_i \, \mathrm{d}x \, \mathrm{d}y \, \mathrm{d}z. \tag{4.46}$$

Due to the interpolation process onto the finer grid for the expansion cases, the initial enstrophy is artificially increased in the direction of the cell-splitting. The total enstrophy decreases with time, dominated by the dissipation contribution like the turbulent kinetic energy. Compared to the unstrained case, the expansion cases decrease faster, whilst the compression cases decrease at a slower rate. By including the dissipation, a rudimentary model can be created for the enstrophy components in each direction.

$$\frac{\partial}{\partial t} \begin{pmatrix} \Omega_x \\ \Omega_y \\ \Omega_z \end{pmatrix} = -2\bar{S}_{11} \begin{pmatrix} 0 \\ \Omega_y \\ \Omega_z \end{pmatrix} - \epsilon_\Omega \tag{4.47}$$

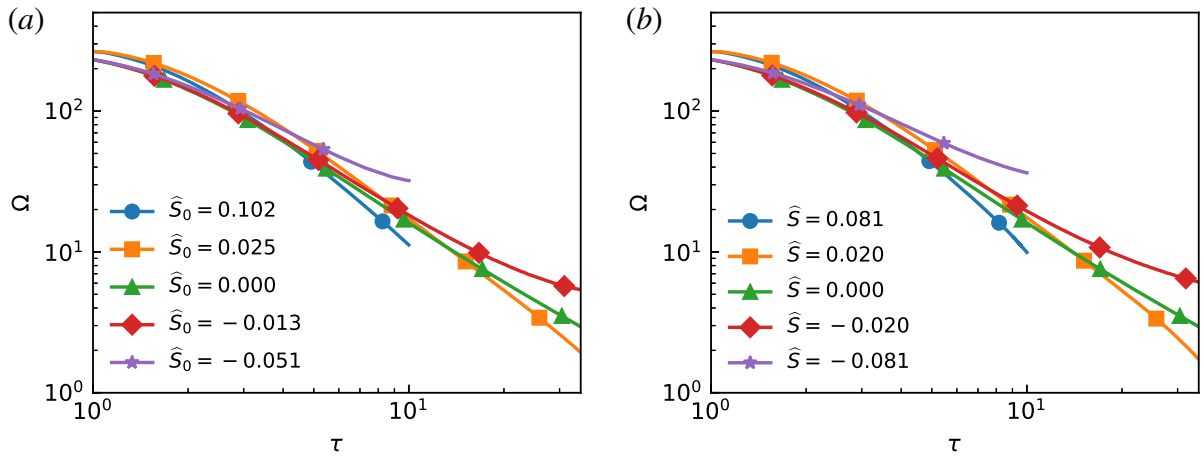

Figure 4.23: Total enstrophy for (*a*) constant velocity and (*b*) constant strain rate.

The dissipation rate, ϵ_Ω, is a function of the enstrophy component and is modelled using the unstrained strain rate case. The unstrained vorticity components decay with a power law exponent $n = 1.4$,

$$\Omega \propto \left(\frac{\tau}{\tau_0}\right)^{-n}. \tag{4.48}$$

Equating the derivative and the dissipation rate, and rearranging to remove time dependence gives the expression,

$$-\epsilon_\Omega = -\frac{n}{\tau_0 \Omega_0^{1/n}} \Omega^{(n+1)/n}. \tag{4.49}$$

Assuming the strained cases maintain this quasi-equilibrium relationship between the enstrophy and enstrophy dissipation rate, the model in equation (4.47) is closed assuming some initial condition values, τ_0 and Ω_0.

Looking at the in-plane component of vorticity in figure 4.24, there is a small spread in the values. The derived enstrophy model suggests that Ω_x should remain unchanged from the unstrained case (hence the model's omission from the plot), however there is a slight variation in the direction consistent with the compressibility effects.

An example of the out-of-plane contribution is shown in figure 4.25 for the ω_y^2 component. Also plotted is the enstrophy model for each case, solved using the values at $\tau = 3$ for the initial conditions of the differential equation. The model is well aligned with the ILES results, accurately predicting the relative decrease in enstrophy for the expansion cases and relative increase for the compression cases as compared to the unstrained case. This out-of-plane vorticity can be considered responsible for moving fluid through the mixing layer, whilst the in-plane vorticity mixes the fluid within the layer. Whilst the in-plane vorticity is slightly decreased for the expansion cases, the decrease in the out-of-plane vorticity is larger. The expansion cases observe

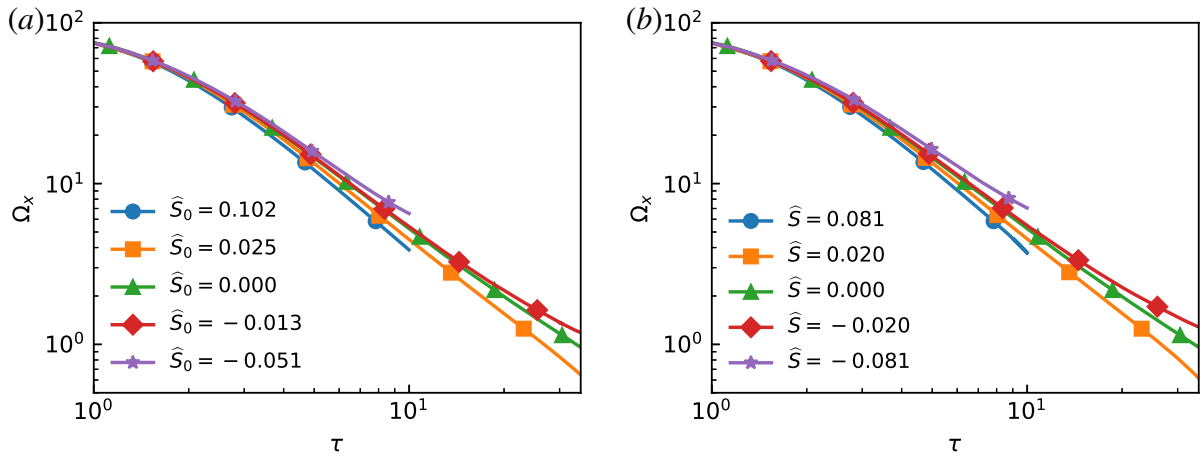

Figure 4.24: Enstrophy in the $y - z$ plane for (a) constant velocity and (b) constant strain rate.

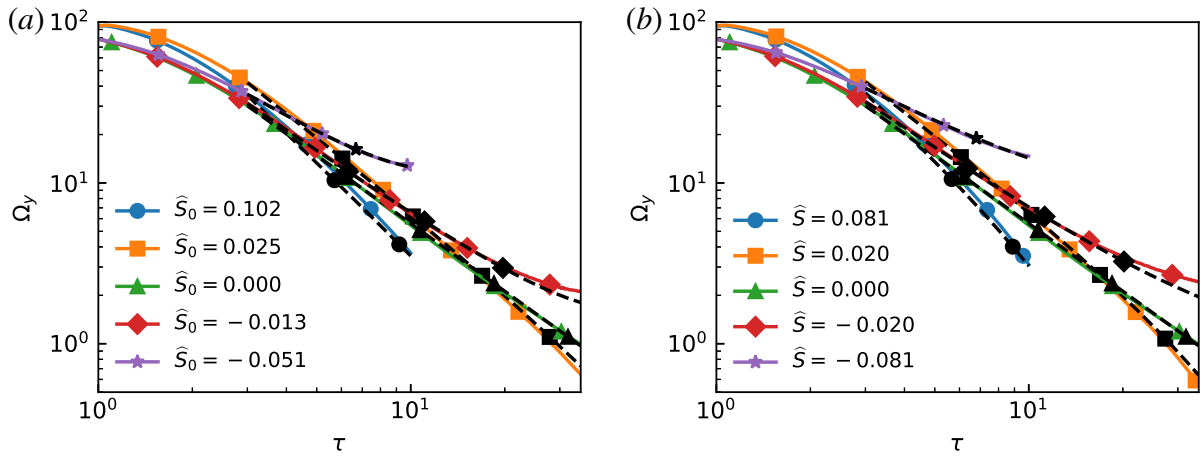

Figure 4.25: Enstrophy in the $x - z$ plane for (a) constant velocity and (b) constant strain rate. Solid lines indicate ILES results, dashed lines indicate enstrophy model.

a relative increase in the in-plane vorticity as a result, and this aligns with the observed increase in the $\overline{f_1 f_2}$ profile and mixedness of the layer. In contrast, the compression cases see a relative decrease in the in-plane vorticity compared to the out-of-plane vorticity. This phenomenon can also be explained simply by thinking of the axis of the effective mixing vortices being tilted in the direction of the strain rate. For expansion, the axis is tilted towards the x-axis, causing more mixing in the in-plane direction as opposed to the out-of-plane direction. For compression, the vortex axis is tilted to point orthogonal to the x-axis, causing less in-plane mixing.

Turbulent mass flux

The turbulent mass flux is a quantity that only arises in variable-density and compressible flows, resulting from the velocity fluctuations that are correlated to the density fluctuations.

$$a_i = \frac{\overline{\rho' u_i'}}{\bar{\rho}} = \overline{-u_i''} = \tilde{u}_i - \bar{u}_i \tag{4.50}$$

The turbulent mass flux is responsible for the conversion of potential energy to turbulent kinetic energy, and is a factor in the source term for the density-specific-volume covariance. A transport equation for the turbulent mass flux is common in turbulence models for hydrodynamic instabilities, with the equation first derived by Besnard *et al.* (1992). As the flow is primarily one-dimensional, the transverse components should be statistically zero, and analysis can focus on the axial component (Wong *et al.*, 2022). The axial turbulent mass flux has a source term from the mean velocity gradient, similar to the Reynolds stress transport equation,

$$\frac{Da_1}{Dt} \propto a_1 \frac{\partial \bar{u}_1}{\partial x_1}. \tag{4.51}$$

Whilst this source term is included in the BHR k-S-a model(Banerjee *et al.*, 2010), it is excluded in the k-L-a model (Morgan & Wickett, 2015) as it was deemed insignificant for the cases considered. The profile for the axial turbulent mass flux is plotted in figure 4.26 near the simulation end times. As expected from the transport equation, the compression cases maintain larger values of a_1. The profiles are asymmetric for all cases, showing a greater skew to the right, toward the lighter fluid, which was also observed in the work of Wong *et al.* (2022) for RMI before and after re-shock. Wong *et al.* (2022) also observed the peaks of the profiles tending towards the heavy fluid, however this was for plots of $\bar{\rho}a_1$. The same trend would be visible if $\bar{\rho}a_1$ profiles were plotted for the strain cases, however the density scaling has been avoided as the density varies between the cases due to the compression or expansion, which further exacerbates the difference between the profiles.

Buoyancy-drag

The results in figures 4.11, 4.13, and 4.14 show that the background velocity correction is not sufficient to predict the growth of RMI with axial strain. This is in part due to the vortex tilting that arises due to the axial strain rate, causing a change in the entrainment and mixing. Three correction terms are proposed for the velocity equation in the buoyancy-drag model, corresponding to the equivalent terms of $d/dt(\bar{S}W)$. The corrections are chosen to take this form such that the strain rate contributions are isolated and the same effective drag length scale can be used for all cases. For the three mixing layer length scales, the new equations are given by,

$$\frac{\mathrm{d}W}{\mathrm{d}t} = V + W\bar{S}, \qquad \frac{\mathrm{d}V}{\mathrm{d}t} = -\frac{V^2}{l^{\text{eff}}(\bar{\lambda}, W)} + C_1\bar{S}V + C_2\bar{S}^2W + C_3\dot{\bar{S}}W, \tag{4.52}$$

$$\frac{\mathrm{d}h_b}{\mathrm{d}t} = V_b + h_b\bar{S}, \qquad \frac{\mathrm{d}V_b}{\mathrm{d}t} = -\frac{V_b^2}{l_b^{\text{eff}}(\bar{\lambda}, h_b)} + C_{b_1}\bar{S}V_b + C_{b_2}\bar{S}^2h_b + C_{b_3}\dot{\bar{S}}h_b, \tag{4.53}$$

$$\frac{\mathrm{d}h_s}{\mathrm{d}t} = V_s + h_s\bar{S}, \qquad \frac{\mathrm{d}V_s}{\mathrm{d}t} = -\frac{V^2}{l_s^{\text{eff}}(\bar{\lambda}, h_b)} + C_{s_1}\bar{S}V_s + C_{s_2}\bar{S}^2h_s + C_{s_3}\dot{\bar{S}}h_s. \tag{4.54}$$

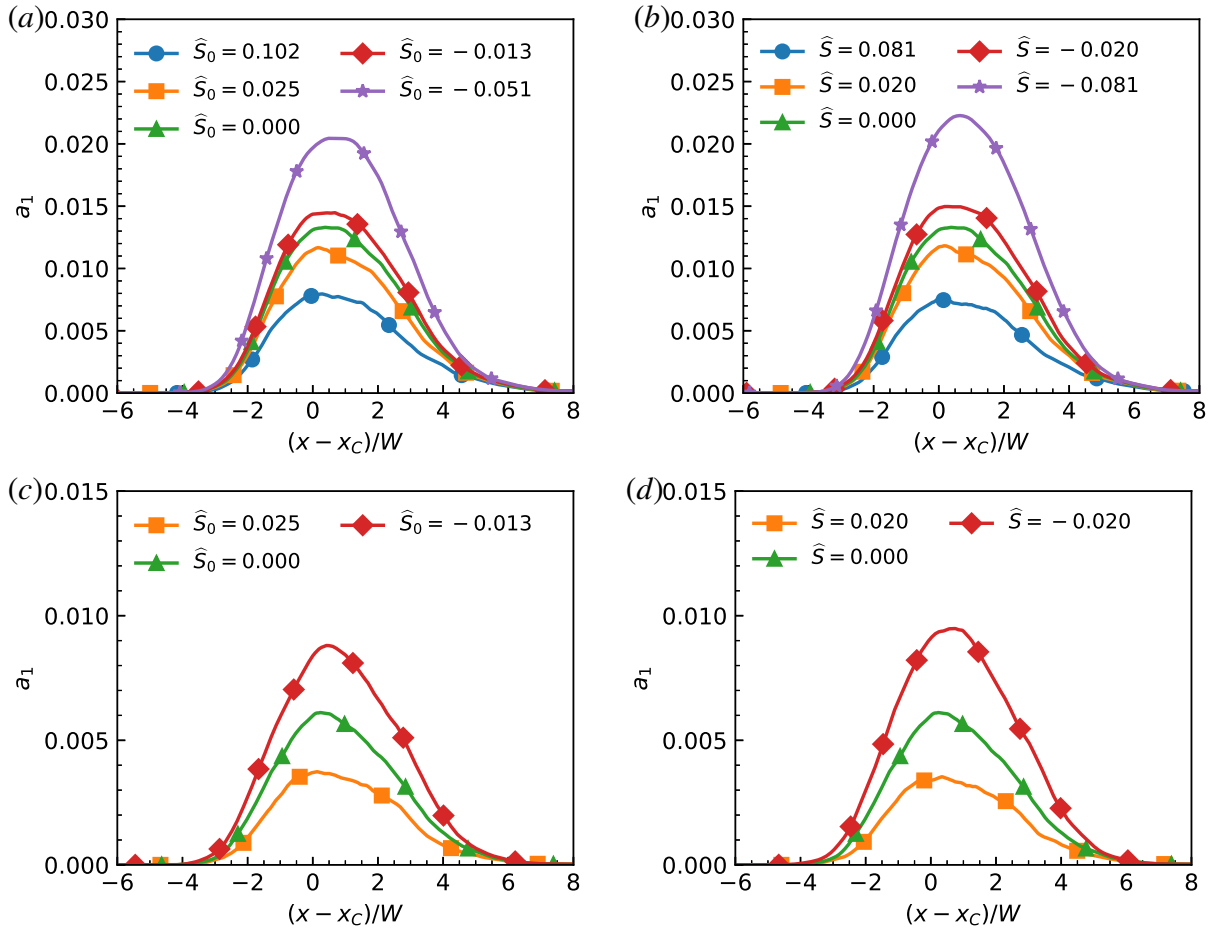

Figure 4.26: Axial turbulent mass flux for (*a,c*) constant velocity cases, and (*b,d*) constant strain rate cases. (*a,b*) $\tau = 9.843$, (*c,d*) $\tau = 34.451$.

The method used to calculate the optimum coefficients uses all strain cases for the optimisation process and uses the covariance matrix from the optimisation process to estimate the uncertainty in the coefficients. Each length scale coefficient set, referred to by $\hat{\theta}$, was optimised separately by minimising the corresponding error, $S(\hat{\theta})$, between the ILES results and the corrected buoyancy-drag model for the strained cases. For a given set of coefficients, the buoyancy-drag equations were numerically integrated using an ordinary differential equation solver. The mean square residual for each strain case was calculated, and the total error was taken to be the sum of the mean square residuals. Minimisation of the summated mean square residuals was performed by the Broyden–Fletcher–Goldfarb–Shanno algorithm Nocedal & Wright (2006). The minimisation process also returns the inverse Hessian, $H_{\hat{\theta}}^{-1}$ for the coefficient set used. The covariance matrix, $\hat{V}$, is estimated by scaling the inverse Hessian by the reduced chi-squared statistic χ^2,

$$\hat{V} = \chi^2 H_{\hat{\theta}}^{-1} \tag{4.55a}$$

$$\chi^2 = S(\hat{\theta})/(n-p) \tag{4.55b}$$

Table 4.5: Optimised coefficients for the buoyancy-drag model.

Lengthscale	C_1	C_2	C_3
Integral Width	-1.863 $\pm$ 0.039	0.162 $\pm$ 0.058	0.056 $\pm$ 0.074
Bubble	-1.504 $\pm$ 0.056	0.113 $\pm$ 0.079	0.041 $\pm$ 0.109
Spike	-1.665 $\pm$ 0.046	0.076 $\pm$ 0.147	0.001 $\pm$ 0.195

where n is the number of data-points used, and p is the degrees of freedom (Vugrin *et al.*, 2007). The variance of each coefficient corresponds to the trace of the covariance matrix. The optimised coefficients and the standard deviations are listed in table 4.5.

The C_1 coefficient for all length scales has the largest magnitude and the smallest uncertainty. The range of values for C_1 are spread from -1.5 for the bubble to -1.86 for the integral width, suggesting the buoyancy-drag model requires a strain drag term that replicates the decreased growth from the vortex stretching in expansion cases, and increased growth for compression cases. The C_2 coefficients are all positive, showing a tighter spread but differing by up to a factor of two between length scales. Unlike the C_1 term which may be positive or negative depending upon the sign of the strain rate, the C_2 term is always positive, causing the correction to increase the growth-rate for all strained cases. The C_3 term only activates for the constant velocity cases, whereby it opposes the C_2 term. The optimised coefficients for C_3 were the smallest coefficients of the three. For all length scales, the two standard deviation confidence interval for C_3 includes zero, suggesting the coefficient is not statistically significant.

The corrected buoyancy-drag model for the integral width is presented in figure 4.27. The corrected model is well aligned to the ILES results. Likewise, the corrected model for the bubble height is plotted in figure 4.28, and also shows close agreement. The results for the spike height are plotted in figure 4.29, and it is seen that this model does not perform as well as the others, as it is not able to capture the compression cases. The reason that the corrected model does not work for the spikes could be due to the usage of the bubble height in the effective length scale for the spike drag. Whilst the effective length scales for the bubble and spike for the unstrained case can be approximated as a function of the bubble height in the work of Youngs & Thornber (2020*a*), this may not be the case for the strained cases presented here. This may be in part due to the changing spike-to-bubble ratio, as shown in figure 4.15.

A physical meaning for the correction terms can be obtained by analysing the turbulent kinetic energy. A simplified one-dimensional equation for the mean turbulent kinetic energy

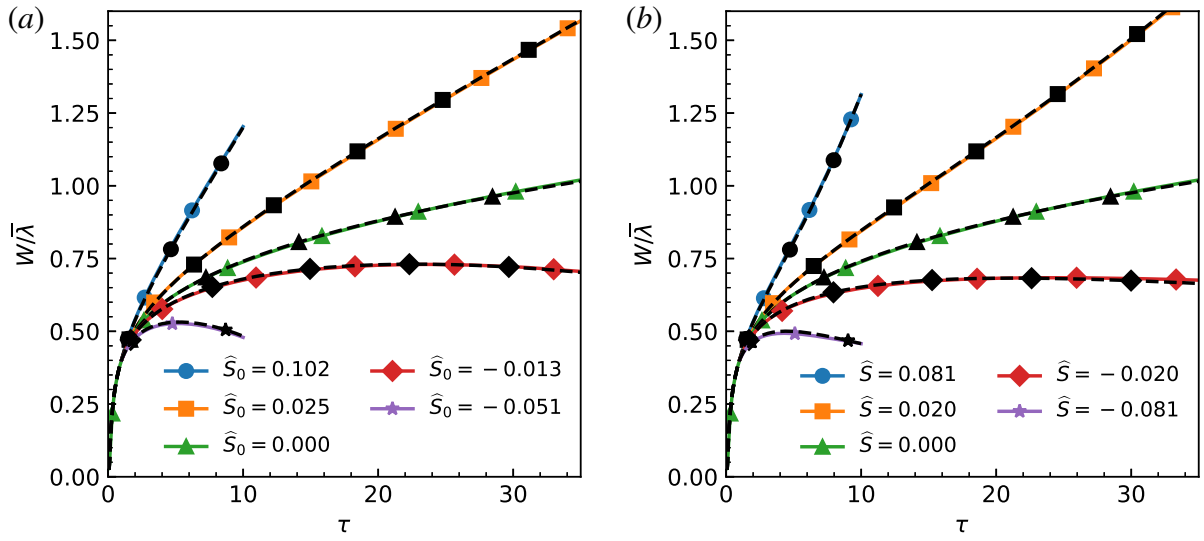

Figure 4.27: Corrected buoyancy-drag model for the integral width. (*a*) Constant velocity, and (*b*) constant strain rate. Solid lines indicate ILES results, dashed lines indicate buoyancy-drag model.

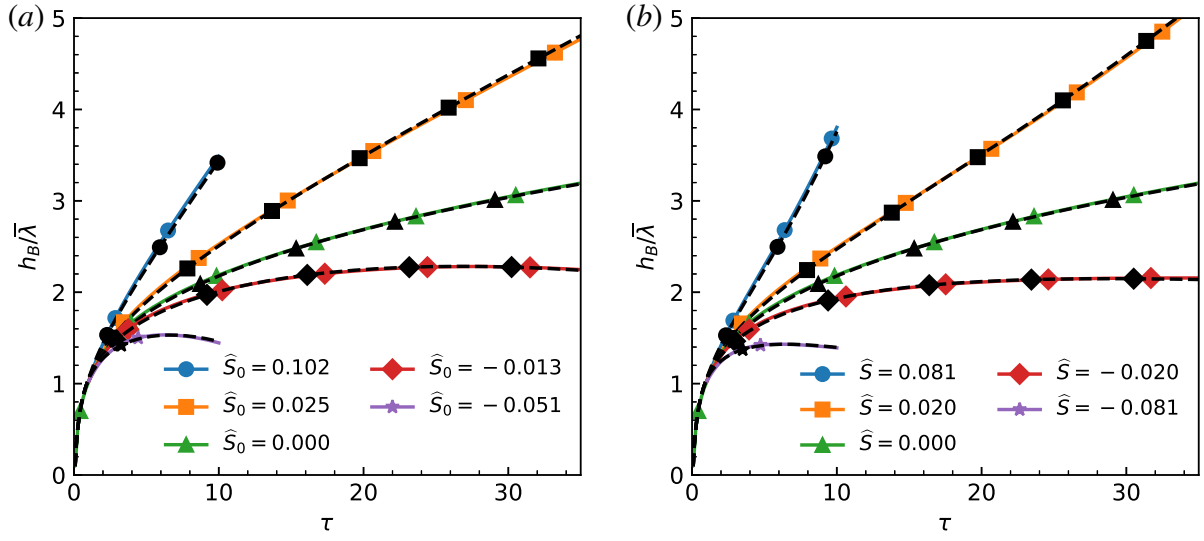

Figure 4.28: Corrected buoyancy-drag model for bubbles. (*a*) Constant velocity, and (*b*) constant strain rate. Solid lines indicate ILES results, dashed lines indicate buoyancy-drag model.

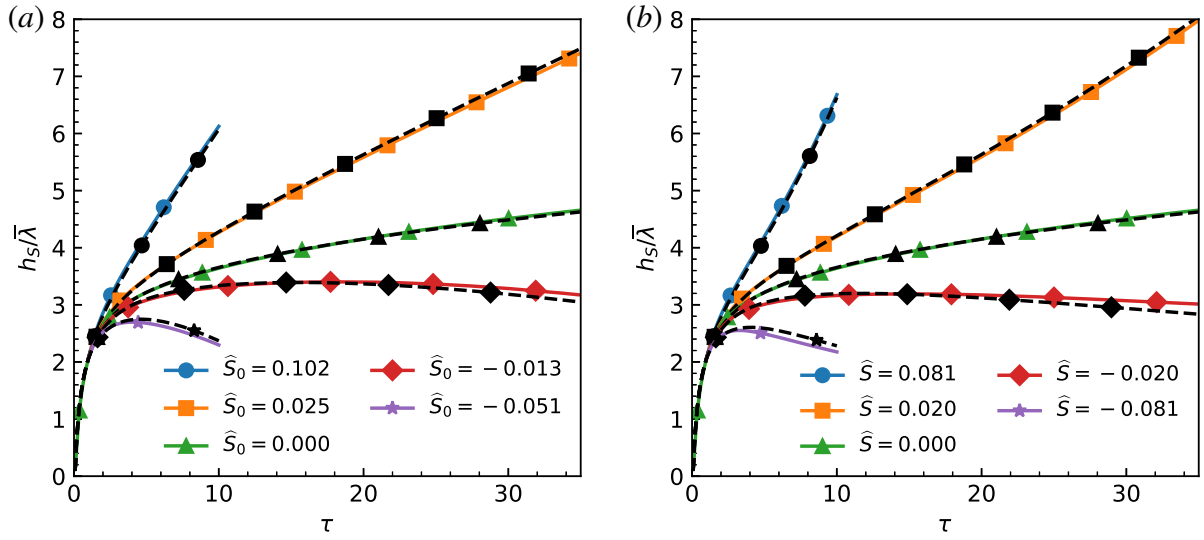

Figure 4.29: Corrected buoyancy-drag model for spikes. (*a*) Constant velocity, and (*b*) constant strain rate. Solid lines indicate ILES results, dashed lines indicate buoyancy-drag model.

may be considered, with the form

$$\bar{\rho}\frac{Dk}{Dt} = -\bar{\rho}\widetilde{u_1''u_1''}\frac{\partial \tilde{u}_1}{\partial x_1} - \bar{\rho}\epsilon. \tag{4.56}$$

It is possible to adapt the equation for the evolution of the turbulent velocity, $V = \sqrt{2k}$. Introducing a turbulent length scale L, the Reynolds stress is modelled using a Boussinesq eddy viscosity assumption,

$$\bar{\rho}\widetilde{u_i''u_j''} = \frac{2}{3}\bar{\rho}k\delta_{ij} - \mu_T\left(\frac{\partial \tilde{u}_i}{\partial x_j} + \frac{\partial \tilde{u}_j}{\partial x_i} - \frac{2}{3}\frac{\partial \tilde{u}_k}{\partial x_k}\delta_{ij}\right) \tag{4.57a}$$

$$\mu_T = C_\mu \bar{\rho} V L \tag{4.57b}$$

and the dissipation is given by,

$$\epsilon = C_\epsilon \frac{V^3}{L}. \tag{4.58a}$$

Assuming only the axial strain rate, $\tilde{S}_{11} = \partial \tilde{u}_1/\partial x_1$, is non-negligible then the turbulent velocity evolves according to,

$$\frac{DV}{Dt} = -C_\epsilon\frac{V^2}{L} - \frac{1}{3}V\tilde{S}_{11} + \frac{4}{3}C_\mu L\tilde{S}_{11}^2. \tag{4.59}$$

This equation bears similarity to the corrected buoyancy-drag model. The first term ($\propto V^2/L$) is the drag term, which originally corresponded to the dissipation of turbulent kinetic energy. The second and third terms are the results of the inclusion of the shear production for the turbulent kinetic energy, and have the same form as the two additional terms introduced to the buoyancy-drag model that were found to have statistically significant values. It is evident then that the introduced terms to the buoyancy-drag model correspond to the effects of shear production on the mixing layer.

4.5 Conclusion

The influence of axial strain rate on the Richtmyer-Meshkov instability has been investigated by applying a mean velocity gradient to the flow. Two different strain rate profiles were utilised, a constant velocity profile and a constant strain rate profile. These profiles were enforced in the fluid domain by using a moving mesh, inviscid moving walls boundary conditions, and source terms for the constant strain rate profile. This method allows for the controlled application of strain rates in planar geometry, mimicking the strain rates observed in convergent geometry.

A linear potential flow model for RMI and RTI with an axial strain rate, as done by Epstein (2004), predicts the RMI growth rate to be the sum of the impulsive velocity and the background velocity difference, $\dot{a} = U_0 + a\bar{S}_{11}$. Resolved two-dimensional simulations of a single-mode RMI at *Re*= 2048 were conducted to investigate the model for the linear regime, and utilised a velocity perturbation initialisation. The simulation results showed agreement with the model, in particular with tracking the negative growth for compression cases. The error in the model was proportional to the amplitude, which indicated the error was associated with mode saturation, which is expected for RMI.

The effects of the strain rate on the development of a self-similar mixing layer were conducted by applying strain to the quarter-scale θ-group case (Thornber *et al.*, 2017), a three-dimensional, multimode, narrowband RMI-induced mixing layer. The simulations were conducted using implicit large eddy simulation, with axial strain applied from $\tau = 1$, prior to the mixing layer achieving self-similarity. The axial strain increased the mixing layer width for expansion cases and decreased the width for compression cases, however, the effect of the strain rate on the mixing growth was less than expected. Under strain, the mixing layer no longer converged to the same self-similar state. The mixedness of the mixing layer increased for the expansion cases and decreased for the compression cases, whilst the turbulent kinetic energy became more focused towards the axial direction under compressive strain and shifted towards the transverse directions under the expansive strain. This is a result of the shear production of turbulent kinetic energy from the mean velocity gradients, adding axial turbulent kinetic energy for compressive strain and removing the axial turbulent kinetic energy for expansion cases. The shear production was not balanced out by pressure scrambling to re-balance the turbulent kinetic energy, which as a result caused the compression cases to achieve greater entrainment and decreased the mixedness, whilst the expansion cases had decreased entrainment and increased mixedness.

The Buoyancy-Drag model calibrated for the unstrained, narrowband RMI (Youngs & Thornber, 2020*a*,*b*) was modified to include the background velocity difference, as done for the linear regime and has also been done previously for convergent Buoyancy-Drag models (Miles,

2009; El Rafei & Thornber, 2020). This model was not accurate for the strained cases, and overestimated the influence of the strain rate as it did not take into account the shear production contribution which opposes the background stretching caused by the velocity gradient. Three correction terms were proposed to correct the velocity evolution under the axial strain rate. The coefficients for each term were calibrated to fit the strain cases. Whilst the third term was not found to be statistically significant, the optimised Buoyancy-Drag model was able to match the ILES results.

CHAPTER 5

Influence of Transverse Strain

5.1 Introduction

The instabilities of ICF and supernova do not occur in planar geometry, causing the behaviour of RMI and RTI to differ from the canonical, planar cases. Convergent geometry, used to describe both cylindrical and spherical geometry, is well described in the linear regime limit by Bell–Plesset effects (Penney & Price, 1942; Bell, 1951; Plesset, 1954). Whilst the work of Bell (1951) was limited to looking at the compressible and incompressible cases where one fluid was of negligible density, Plesset (1954) instead considered the incompressible limit between two fluids for any density ratio. The combined modelling of the two approaches is common, and the modified growth rate can be nicely expressed as a differential equation for the amplitude that depends on the fluid compression rate, radius, and radius convergence rate (Epstein, 2004). Bell–Plesset models have been validated against experiments for single-mode convergent RMI (Vandenboomgaerde *et al.*, 2018) and divergent RMI (Li *et al.*, 2020; Zhang *et al.*, 2023). Models have been adjusted to account for re-shock in single-mode simulations (Flaig *et al.*, 2018), and have also been able to predict multimode initial conditions prior to mode saturation (El Rafei *et al.*, 2019). Weakly non-linear models which account for higher-order harmonics for incompressible RTI have been derived for cylindrical geometry (Wang *et al.*, 2015) and spherical geometry (Zhang *et al.*, 2017). The experiments of Luo *et al.* (2019) for convergent, cylindrical RMI are able to be predicted by the model of Zhang *et al.* (2017) until a non-dimensionalised time of 1.

Whilst planar geometry RMI will not typically experience the compression rates or convergence rates associated with convergent geometry, it is possible to reproduce these effects. Epstein (2004) re-derived the Bell–Plesset model for cylindrical and spherical geometry, as well as a model for planar geometry with a compression rate. The compression rate used was

equivalent to a mean strain rate in the direction normal to the interface, hence labelled an axial strain rate. The axial strain rate acts to stretch or compress the mixing layer, depending upon the sign of the strain rate. Li *et al.* (2019, 2021) observed the influence of this term due to the strain rates that manifest across the mixing layer due to transient waves passing through. Ge *et al.* (2020, 2022) analysed the mixing layer's growth in cylindrical geometry, decomposing the growth into two main components: the compression/stretching effect from the axial strain rate, and the turbulent growth from fluctuating velocity. In Chapter 4, the development of RMI from the linear to self-similar regime was analysed. The model of Epstein (2004) was able to describe the linear regime, but was inaccurate as the mixing layer transitioned to turbulence. The shear production from the strain rate opposed the strain rate effects, increasing the mixing layer growth under compression and decreasing growth under expansion.

A strain rate formulation can provide an alternate understanding of the modifications of the instability growth in convergent geometry, splitting the contributions into axial and transverse strain rates as opposed to compression and convergence rates. The effect of axial strain rate will stretch or compress the mixing layer, however, the role of transverse strain rate is not as clear. The transverse strain rate corresponds to the convergence rate, but it is also a component of the compression rate; an incompressible model requires the axial strain rate and transverse strain rates to summate to zero. It is therefore difficult to isolate the transverse strain rate in convergent geometry. In planar geometry, there is no effective radius to consider for the convergence rate, as compared to the compression rate, which has an analogue in the axial strain rate. In order to better understand the transverse strain rate contribution, a method of modelling convergence is performed in planar geometry, using transverse strain rates to replicate the effects of convergence.

In §5.2 the definition of the convergence rate for convergent modelling is analysed and shown to be the same as a transverse strain rate for planar geometry, and the methods used to apply the transverse strain rates and simulate the flow are outlined. In §5.3 a linear regime model for planar geometry with axial and transverse strain rates is derived. The results are compared to the model for convergent geometry, as well as to simulations of the linear regime under transverse strain are conducted. The analysis of an RMI-induced multimode narrowband mixing layer under transverse strain rates is performed in §5.4 using an implicit large eddy simulation (ILES).

5.2 Problem formulation

5.2.1 Transverse strain rate

The transverse directions for the problems considered are in the plane of the initial interface (which at late-time represents the direction of homogeneity), and are orthogonal to the direction of growth for the amplitude or mixing layer. Transverse strain will modify the wavelength of a static perturbation but will not adjust the amplitude. This is presented in figure 5.1 for the transverse compression of both a two-dimensional system and a three-dimensional system. In both configurations, the wavelength size has been modified, however the amplitudes and x-extent are unchanged. The perturbations are more non-linear after compression, as the amplitude-to-wavelength ratio has increased. The perturbations in these demonstrative configurations are not evolving in time, as there is no instability development and the only velocity present is a linear velocity profile that allows the domain to compress without the generation of acoustic waves. The linear velocity profile in the y-direction is given by,

$$u_2(y,t) = \bar{S}_{22}(t)\, y, \tag{5.1}$$

where $\bar{S}_{22}(t) = \partial u_2/\partial y$ is a spatially uniform strain rate that can vary with time. Positive values of $\bar{S}_{22}$ correspond to expansion, and negative values to compression.

For the wavelength aligned with the transverse direction, the wavelength will vary according to

$$\lambda = \lambda_0 \exp\left[\int_{t_0}^{t} \bar{S}_{22}(t')dt'\right], \tag{5.2}$$

for a mean transverse strain rate $\bar{S}_{22}$, and with initial wavelength λ_0 at time t_0 that is aligned with $\bar{S}_{22}$. It is useful to define the transverse expansion factor which is used throughout the paper:

$$\Lambda(t) = \exp\left[\int_{0}^{t} \bar{S}_{22}(t')dt'\right]. \tag{5.3}$$

The transverse expansion factor represents the multiplicative change in the transverse length scale, as shown in equation (5.2) for the wavelength. The expansion factor is greater than one for expansion, and between zero and one for compression.

The transverse strain rate plays a role in the modelling of convergent geometry. In convergent geometry, the linear regime solutions are functions of the convergence rate of the interface radius, $\gamma_R = \dot{R}/R$, and the fluid compression rate, $\gamma_\rho = \dot{\rho}/\rho$. The equation for conservation of mass shows that the compression rate is equal to the negative sum of the strain rates:

$$\frac{1}{\rho}\frac{D\rho}{Dt} = -div(\boldsymbol{u}), \tag{5.4}$$

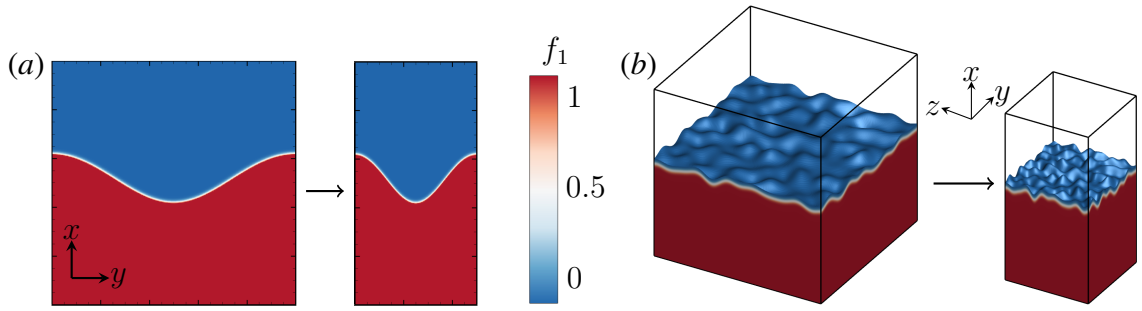

Figure 5.1: Change of domain size and wavelength for systems compressed with transverse strain by a factor of two. (*a*) Two-dimensional system with a single mode perturbation and compressed in y; (*b*) Three-dimensional system with a multimode perturbation, compressed in y- and z-directions, and bound by the $f_1 = 0.01$ iso-surface.

where the divergence of the velocity field is the trace of the strain tensor, which takes on different forms depending upon the coordinate system used. The convergence rate can be re-written in terms of the local flow field, with the mean radial velocity corresponding to the mean interface velocity:

$$\gamma_R = \left.\frac{\bar{u}_r(r,t)}{r}\right|_{r=R}. \tag{5.5}$$

In spherical geometry, the polar strain rate and azimuthal strain rate are given by

$$S_{\theta\theta} = \frac{u_r}{r} + \frac{1}{r}\frac{\partial u_\theta}{\partial \theta}, \tag{5.6a}$$

$$S_{\varphi\varphi} = \frac{u_r}{r} + \frac{1}{r}\left(\frac{\partial u_\varphi}{\partial \varphi} + u_\theta \cos(\theta)\right). \tag{5.6b}$$

The velocity component u_θ represents the velocity in the polar direction θ, whilst u_φ represents the velocity in the azimuthal direction φ. In the case of spherically symmetric flow, the mean flow has no polar or azimuthal component. The mean polar and azimuthal strain rates at the interface radius are therefore equal to the convergence rate:

$$\gamma_R = \left.\bar{S}_{\theta\theta}\right|_{r=R} = \left.\bar{S}_{\varphi\varphi}\right|_{r=R}. \tag{5.7}$$

These circumferential strain rates, $\bar{S}_{\theta\theta}$ and $\bar{S}_{\varphi\varphi}$, are of course orthogonal to the direction of growth of a spherically symmetric mixing layer which will grow in the radial direction. This fulfils the definition outlined for the transverse direction, which is further emphasised by considering the transverse strain rate in terms of the variation of the wavelength. Angular perturbations in spherical or cylindrical geometry will have an effective wavelength which scales with the radius of the interface. With this proportionality, $R \propto \lambda$, the convergence rate is equivalent to

$$\gamma_R = \frac{\dot{\lambda}}{\lambda}. \tag{5.8}$$

In planar geometry there is no mean interface radius, only an arbitrary interface position. The application of a transverse strain rate is possible, stretching or compressing the domain in the transverse direction. Evaluating equation (5.8) with the equation (5.2) shows that $\gamma_R = \bar{S}_{22}$.

Therefore, the transverse strain rate in convergent geometry is equal to the convergence rate and also contributes to the compression rate. The application of a transverse strain rate in planar geometry is possible, allowing for an investigation into the effects of convergence through planar simulations. The validity of this approach is further illustrated in §5.3.1 where the linear regime model in planar geometry is expanded to include a transverse strain rate in the background flow.

An outline of the strain rate profiles and non-dimensionalisation are provided in §3.2.6, which details the constant velocity and constant strain rate profiles used, as well as the non-dimensionalised strain $\hat{S}$.

5.2.2 Governing equations

The number fraction model of Thornber *et al.* (2018) represents an extension of the non-conservative five-equation model of Allaire *et al.* (2002) and Massoni *et al.* (2002) to include the effects of viscosity and diffusion. For the resolved 2-D simulations in section 5.3 the full viscous model is used. For the implicit large eddy simulations in section 5.4, the inviscid volume fraction model is used, representing the high Reynolds number limit. The full equations are stated in equation (3.27).

5.2.3 Numerical methods

The equations are solved using FLAMENCO, a finite-volume algorithm that is nominally fifth-order in space and second-order in time. Full implementation details can be found in section 3.2. With the inclusion of the mean velocity gradients in the simulation, the mesh is deformed with the mean velocity gradients by using an Arbitrary Lagrange-Eulerian moving mesh scheme (Thomas & Lombard, 1979; Farhat *et al.*, 2001; Luo *et al.*, 2004). By deforming the mesh with the specified strain rate profile, the simulation enforces the desired mean velocity gradient. The boundary conditions in the direction of the applied strain rates are moving, reflecting free-slip walls, such that the ghost cell quantities are symmetric with respect to the boundary and the strain rate profile is maintained through the ghost cells.

5.3 Two-dimensional linear regime

5.3.1 Linear potential flow

During the initial stages of instability growth, the evolution of the modes can be described analytically. A common methodology is to use a potential flow formulation to derive the analytical behaviour, as is done for the Bell-Plesset effects for RMI and RTI in convergent geometry (Penney & Price, 1942; Bell, 1951; Plesset, 1954). The Bell-Plesset equations can be simplified by using a strain rate framework, which becomes almost identical for planar, cylindrical, and spherical geometries. This model is validated for transverse strain in planar geometry, showing that the model is accurate while in the linear regime.

Convergent models

The differential equation provided by Epstein (2004) for the amplitude growth rate in spherical geometry is

$$\left(-\gamma_\rho - \gamma_R + \frac{d}{dt}\right)\frac{d}{dt}\left(a_l \rho R^2\right) = \gamma_0^2\left(a_l \rho R^2\right). \tag{5.9}$$

where a_l is the spatial amplitude of the spherical harmonic perturbation of degree l, $Y_l^m(\theta,\varphi)$. The driving term, γ_0^2 is given by

$$\gamma_0^2 = \frac{l(l+1)}{R}\frac{\rho^+ - \rho^-}{l\rho^+ + (l+1)\rho^-}g_p, \tag{5.10}$$

where ρ^+ and ρ^- are densities above and below the interface respectively, and g_p is the linearised pressure acceleration at the interface, $g_p = -(1/\rho)[\partial p/\partial x]_{r=R}$.

To obtain a strain rate formulation, the compression rate and convergence rate are converted to the strain rates equivalents,

$$\gamma_\rho = -\bar{S}_{11} - 2\bar{S}_{22}, \tag{5.11a}$$

$$\gamma_R = \bar{S}_{22}, \tag{5.11b}$$

where $\bar{S}_{11}$ is the mean radial/axial strain rate and $\bar{S}_{22}$ is the symmetric transverse strain rate. This assumes a spherically symmetric mean velocity profile, with a singular transverse strain rate, $\bar{S}_{22} = \bar{S}_{\theta\theta} = \bar{S}_{\varphi\varphi}$. Expanding the derivatives and simplifying gives the solution

$$\ddot{a}_l + \dot{a}_l\left(\bar{S}_{22} - \bar{S}_{11}\right) + a_l\left(-\bar{S}_{11}\bar{S}_{22} - \dot{\bar{S}}_{11}\right) = \gamma_0^2 a_l. \tag{5.12}$$

The same process can applied to the solution for cylindrical geometry given by Epstein (2004) with

$$\left(-\gamma_\rho + \frac{d}{dt}\right)\frac{d}{dt}\left(a_l \rho R\right) = \gamma_0^2\left(a_l \rho R\right). \tag{5.13}$$

The cylindrical model neglects activity in the longitudinal direction, such that the perturbations are only a function of polar coordinate, $\cos(l\theta)$. The compression rate is given by $\gamma_\rho = -\bar{S}_{11} - \bar{S}_{22}$, which is different to the spherical model, which has an extra $\bar{S}_{22}$ component. The resulting equation as a function of the strain rates is identical to equation (5.12), with the adjustment for the driving term,

$$\gamma_0^2 = \frac{l}{R}\frac{\rho^+ - \rho^-}{\rho^+ + \rho^-} g_p. \tag{5.14}$$

This similarity shows the strain rate formulation provides a more standardised and universal method to describe the effects of the convergent geometry on the amplitude growth for instabilities.

Planar model

To reproduce the differential equation for the growth rate in convergent geometry, both axial and transverse strain rates need to be applied in the planar geometry. The background fluid velocities, denoted with an overbar, are then given by

$$\bar{u}_1(x,t) = \dot{x}_0(t) + \bar{S}_{11}(x - x_0(t)), \tag{5.15}$$

$$\bar{u}_2(y,t) = \bar{S}_{22} y, \tag{5.16}$$

where x_0 is the mean interface position, $\dot{x}_0$ is the mean interface velocity, and the transverse velocity is stationary at $y = 0$. The velocity potential, $\bar{u}_i = \partial\Phi/\partial x_i$, for the background flow is then

$$\Phi(x,y,t) = \Phi_0(t) + \dot{x}_0(x - x_0) + \frac{1}{2}\bar{S}_{11}(x - x_0(t))^2 + \frac{1}{2}\bar{S}_{22} y^2. \tag{5.17}$$

The potential field is linearised about the mean interface,

$$U(x,y,t) = U_0 + g_{U_x}(x - x_0) + g_{U_y} y, \tag{5.18}$$

where $g_{U_x} = [\partial U/\partial x]_{x=x_0}$ and $g_{U_y} = [\partial U/\partial y]_{y=0}$. The pressure field is likewise linearised, only allowing for a pressure gradient in the x-direction,

$$p(x,t) = p_0 - \rho g_p (x - x_0). \tag{5.19}$$

where $g_p = -(1/\rho)[\partial p/\partial x]_{x=x_0}$. The acceleration of the interface is the sum of the potential and pressure acceleration,

$$\ddot{x}_0 = g_{U_x} + g_p. \tag{5.20}$$

To take into account the transverse expansion or compression, the perturbed interface uses a time-varying wave-number,

$$x_{int}(y,t) = x_0(t) + a_k(t)\cos(k(t)y) \tag{5.21}$$

where $k(t) = 2\pi/\lambda(t)$. The amplitude $a_k(t)$ corresponds to a specific wave number $k(t)$. Under a transverse strain rate of S_{22}, the expansion factor will scale the wavelength, and therefore the wave-number evolves as

$$k(t) = k_0 \exp\left[-\int_{t_0}^{t} S_{22}(t')dt'\right], \tag{5.22}$$

where $k_0 = 2\pi/\lambda_0$ is the reference wave-number at some time t_0. For simplicity, the dependence of k, a, x_{int}, and the strain rates will not be written further. The corresponding incompressible velocity potential is given by

$$\phi_k^+ = b_k^+ \cos(ky)\exp\left[-kx\right], \tag{5.23}$$

$$\phi_k^- = b_k^- \cos(ky)\exp\left[kx\right], \tag{5.24}$$

where the $+$ superscript denotes the fluid above the interface ($x > x_0$), and the $-$ superscript denotes for below the interface ($x < x_0$). Both terms decay to zero as x heads towards the relative infinity. The total velocity potential is then given by

$$\phi^{\pm} = \Phi + \phi_k^{\pm}. \tag{5.25}$$

The $b_k^{\pm}$ terms can be removed by equating the interface velocity (total time derivative of equation (5.21)) with the fluid's x-velocity at the interface (x-derivative of equation (5.25)):

$$\frac{dx_{int}}{dt} = \left.\frac{\partial \phi^{\pm}}{\partial x}\right|_{x=x_{int}}, \tag{5.26}$$

$$b_k^{\pm} = \pm\frac{a_k\bar{S}_{11} - \dot{a}_k}{k}\exp\left[\pm k x_{int}\right], \tag{5.27}$$

$$\phi_k^{\pm} = \pm\frac{a_k\bar{S}_{11} - \dot{a}_k}{k}\cos(ky)\exp\left[\mp k(x - x_{int})\right]. \tag{5.28}$$

The Bernoulli equation for unsteady, irrotational flow is given by

$$\frac{\partial \phi}{\partial t} + \frac{1}{2}u_i u_i + U + \frac{p}{\rho} = 0. \tag{5.29}$$

The equation is evaluated at the perturbed interface, equating the pressure on each side of the interface, $p^+ = p^-$. The cosine harmonic of the solution provides the equation,

$$\ddot{a}_k + \dot{a}_k\left(\bar{S}_{22} - \bar{S}_{11}\right) + a_k\left(-\bar{S}_{11}\bar{S}_{22} - \dot{\bar{S}}_{11}\right) = a_k k g_p A t, \tag{5.30}$$

where the Atwood number is given by $At = (\rho^+ - \rho^-)/(\rho^+ + \rho^-)$. The differential equation is identical to the solution obtained from the spherical model in equation (5.12), except for the different driving term on the right-hand side. The wave-number in the driving term is slightly different between the models due to the geometry. The cylindrical wave-number in the model is l/R, which can be derived by taking the wavelength as $2\pi R/l$. For the spherical harmonic, the effective wavelength can be calculated using Jeans' relation, giving $\lambda = 2\pi R/\sqrt{l(l+1)}$ (Jeans, 1997; Wieczorek & Meschede, 2018). The cylindrical model uses the standard Atwood number definition, whilst the spherical model uses the definition, $At = \sqrt{l(l+1)}(\rho^+ - \rho^-)/(l\rho^+ + (l+1)\rho^-)$. For large mode numbers l, the spherical Atwood number will approach the value from the standard definition.

The planar model was derived for a two-dimensional flow, however it produces the same differential equation as the three-dimensional spherical model. A third dimension could be added to the planar model, such that the interface is a function of y and z, however the same solution is obtained for a uniform transverse strain rate in both directions, such that all wavelengths are affected uniformly.

For the case with only axial strain rate, $\bar{S}_{22} = 0$, the differential equation collapses down to

$$\ddot{a}_k - \frac{d}{dt}\left(a_k \bar{S}_{11}\right) = a_k k g_p At. \tag{5.31}$$

This model was investigated in Chapter 4 for RMI, which showed the model was accurate within the linear regime. For only a transverse strain rate, $\bar{S}_{11} = 0$, the equation becomes

$$\ddot{a}_k + \dot{a}_k \bar{S}_{22} = a_k k g_p At. \tag{5.32}$$

For a single-mode RMI where the shock provides the acceleration $g_p = \Delta u \delta(t)$, the amplitude growth rate is

$$\dot{a}(t) = U_0 \exp\left[-\int_0^t \bar{S}_{22}(t')dt'\right], \tag{5.33}$$

where U_0 is the impulsive velocity as specified by Richtmyer (1960),

$$U_0 = a_0 k_0 \Delta u At. \tag{5.34}$$

This solution shows an amplification of the growth rate $\dot{a}$ as the system compresses, or a reduction as the system expands. The solution can also be written as

$$\dot{a}(t) = a_0 k(t) \Delta u At, \tag{5.35}$$

showing the linear growth rate scales as if the impulse was applied at the current wave-number, as opposed to the initial wave-number.

5.3.2 Initial conditions

The cases were simulated in a two-dimensional domain with a 3:1 density ratio for the two fluids. The single-mode instability is initialised with a velocity perturbation instead of an amplitude perturbation and shock interaction. The velocity perturbation is designed to produce an initial linear growth rate, as described in Thornber *et al.* (2010) and Chapter 4. Starting from a flat interface, the velocity perturbation is designed to grow at a velocity of $U_0 = 1\,\mathrm{m\,s^{-1}}$ for the initial wavelength of $\lambda_0 = 0.2\,\mathrm{m}$. The fluid properties for the initial conditions are given in table 5.1. As the initial amplitude of the instability starts from zero, there is no directly equivalent shock-induced RMI, but a comparison can be made if a small, finite amplitude is assumed. For example, a shock strength of Ma=1.8439 impacting the ideal gases with initial Atwood number of 0.52 at pressure $p = 36\,\mathrm{kPa}$ will give approximately the same parameters for an initial linearity of $ak = 0.015$. Smaller shock strengths can be used, requiring larger initial amplitudes to compensate. As the viscous and diffusive five-equation model (see equation (3.27)) is in use, the initial interface is diffuse, defined by an error function for the volume-fraction profile,

$$f_1 = \frac{1}{2}\left(1 - \mathrm{erf}\left(\frac{\sqrt{\pi}(x_1 - x_0)}{h}\right)\right), \tag{5.36}$$

where h is the initial diffusion width set to $\lambda/64$. The initial Reynolds number of the system is given by

$$\mathit{Re} = \bar{\rho} U_0 \lambda_0 / \bar{\mu} = 2048, \tag{5.37}$$

where the initial wavelength, average density, average viscosity, and the prescribed linear amplitude growth rate have been used. This Reynolds number is sufficiently high that the amplitude growth rate is not significantly affected by the viscosity, as seen in Walchli & Thornber (2017) for unstrained RMI.

A total of eight strain cases are conducted, four cases for each strain profile, split between expansion and compressive strain rates, as listed in table 5.2. The high-magnitude expansion strain rate cases expand by a factor of four, which requires the initial mesh to four times denser in the y-direction. These cells for the expansion case are initially skewed, but become closer to cubic as the simulations progress. The compression cases in contrast start with an isotropic mesh, but the cells become skewed as the domain compresses.

5.3.3 Results

Visualisations of the volume fraction contour for the unstrained case and the high-magnitude strain rate cases for each profile are shown in figure 5.2. Each plot is scaled to the final wavelength

Table 5.1: Fluid properties for the linear regime cases.

Property	Fluid 1	Fluid 2	Units
Density, ρ	3	1	$\mathrm{kg\,m^{-3}}$
Pressure, p	100	100	kPa
Molecular Mass, W	90	30	$\mathrm{g\,mol^{-1}}$
Viscosity, μ	1.953125×10^{-4}	1.953125×10^{-4}	Pa s
Specific Heat Ratio, γ	5/3	5/3	
Lewis Number, Le	1	1	

Table 5.2: The strain rates, total simulation time, domain size, grid resolution, and final expansion factor for each of the linear regime cases.

Strain Profile	$\bar{S}_0$ ($\mathrm{s^{-1}}$)	$\hat{S}_0$	Simulation time (s)	Initial domain size ($\mathrm{m^2}$)	Grid resolution	Λ_f
Unstrained	0.0	0.0	0.02	1.0×0.2	640×128	1.00
Constant velocity	-37.50	-7.50	0.02	1.0×0.2	640×128	0.25
Constant velocity	-18.75	-3.75	0.02	1.0×0.2	640×512	0.62
Constant velocity	75.0	15.0	0.02	1.0×0.2	640×512	2.50
Constant velocity	150.0	30.0	0.02	1.0×0.2	640×128	4.00
Constant strain rate	-70.0	-14.0	0.02	1.0×0.2	640×128	0.25
Constant strain rate	-35.0	-7.0	0.02	1.0×0.2	640×128	0.50
Constant strain rate	35.0	7.0	0.02	1.0×0.2	640×512	2.01
Constant strain rate	70.0	14.0	0.02	1.0×0.2	640×512	4.06

of the simulation, where the compression cases have a wavelength that is 16 times smaller than the expansion cases. Relative to the final wavelengths, the compression cases have a much larger value of $a/\lambda(t)$, displaying the formation of penetrating bubbles and spikes that are beginning to roll-up. The unstrained case is around the limit of the linear regime ($a \leq 0.1\lambda$), and the interface appears to be well described by a cosine function. For comparison, the expansion cases show a very small $a/\lambda(t)$ value, suggesting it is still within the linear regime.

As the interface is yet to roll-up and remains smoothly connected, the mean interface position is taken along the $f_1 = 0.5$ volume fraction isocontour line. The amplitude of the interface is taken to be half of the distance between the maximum and minimum of the isocontour,

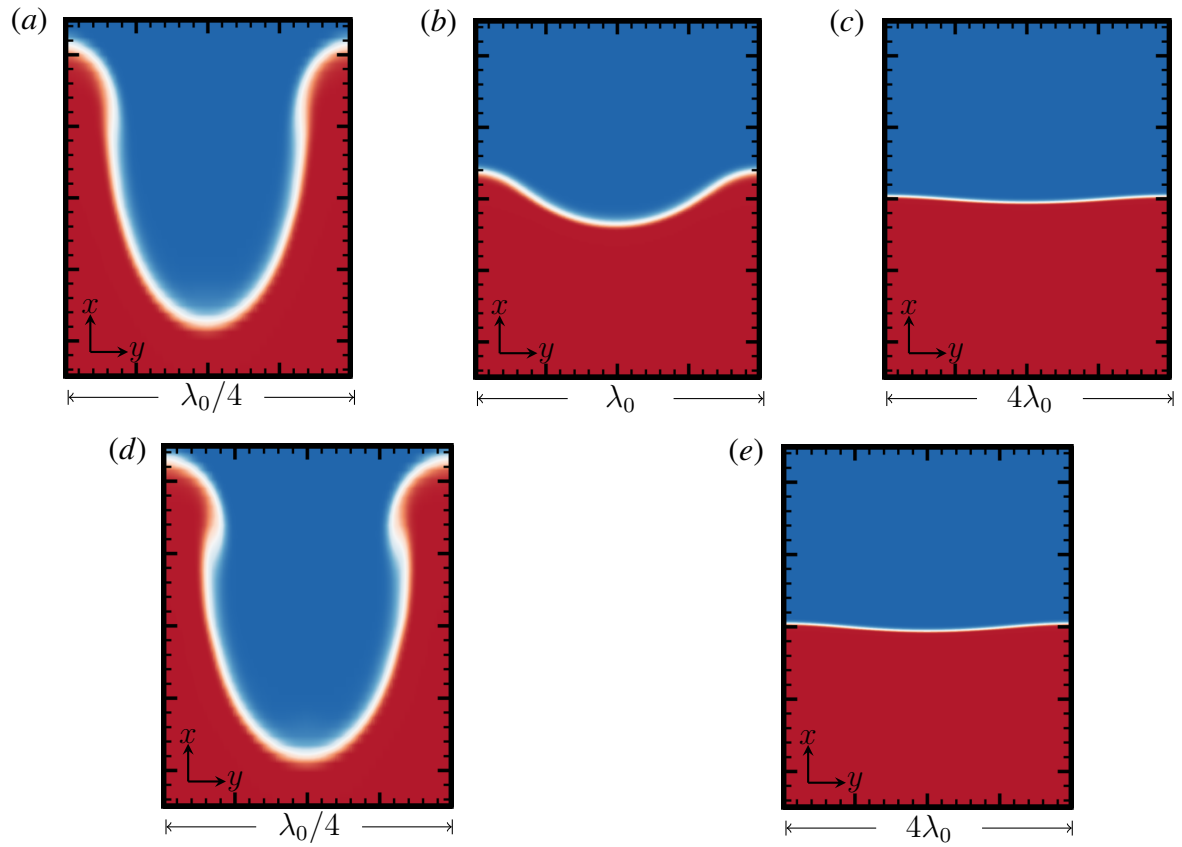

Figure 5.2: Interface at $\tau = 0.1$ for the 2-D single-mode simulations. Heavy fluid ($f_1 = 1$) is red, light fluid ($f_1 = 0$) is blue. Major ticks indicate a distance of $\lambda(t)/4$, with the final wavelength marked below the plot. (*a*) Constant velocity, $\hat{S}_0 = -7.5$; (*b*) Unstrained case; (*c*) Constant velocity, $\hat{S}_0 = 30$; (*d*) Constant strain rate, $\hat{S} = -14$; (*e*) Constant strain rate, $\hat{S} = 14$.

representing the peak and trough of the perturbation, given by

$$a = 0.5 \left(\max(x_{f_1=0.5}) - \min(x_{f_1=0.5}) \right). \tag{5.38}$$

A second-order interpolation scheme is used to locate the minimum and maximum isocontour positions from the simulation's cell average values. The amplitudes non-dimensionalised by the initial wavelength are plotted in figure 5.4, along with the theoretical model given in equation (5.35). The simulation results show that the expansion cases grow the slowest and the compression cases grow the fastest. The model is able to accurately predict the growth rate of the expansion cases, with a small final error for the unstrained case, which can be attributed to saturation as the mode becomes non-linear. The compression cases have a larger error, with the high magnitude compression (negative) strain rate cases the least accurate at the final simulation time. These cases have the largest amplitudes, such that they can be expected to be saturating by the final simulation time, as observed in the volume fraction contour plots of figure 5.2. It is worthwhile to instead look at the performance of the model when plotting as a function of the amplitude non-dimensionalised by the time-varying wavelength, as done in figure 5.5. The

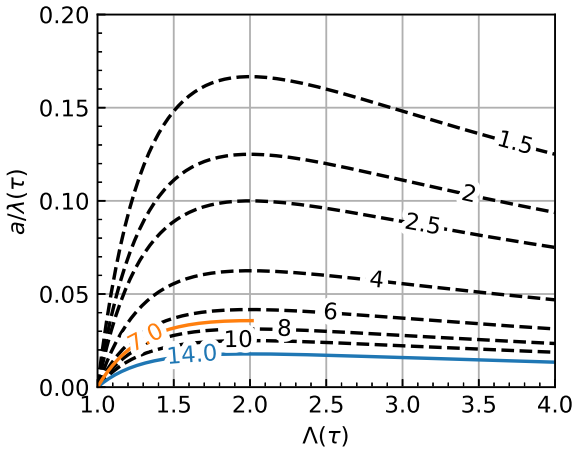

Figure 5.3: Amplitude growth as a function of the transverse expansion for the specified non-dimensionalised constant strain rates. Solid lines indicate numerical results, black dashed lines indicate linearised potential theory.

same trends can be observed in these plots, with the expansion cases growing the slowest and the compression cases growing the fastest. For the highest magnitude expansion cases, the growth of $a/\lambda(t)$ goes negative, a result of the wavelength growing faster than the amplitude. For highly strained expansion cases, requiring at least $\hat{S} \geq 2.5$, the perturbation will remain in the linear regime permanently. This is shown in figure 5.3 where the case reaches a maximum value of $a/\Lambda = 0.1$ before decreasing. The theory suggests that all transverse expansion cases will have a stationary point at $\Lambda(\tau) = 2$, after which the relative amplitude will begin to decrease.

The performance of the model confirms that the perturbation becomes non-linear depending upon the time-varying wavelength and not the initial wavelength. Figure 5.6 reinforces this by plotting the error between the model and simulation as a function of $a/\lambda(t)$. After some initial noise from the interpolation approximating the peak/trough of the initially flat interface, the error profile collapses to a rather straight line for the unstrained and compression cases. The expansion cases fall within the general trend, however the highly expanded cases are not monotonically increasing for $a/\lambda(t)$. The constant strain rate case of $\hat{S} = 14$ shows a final trajectory towards the origin, decreasing in error magnitude and $a/\lambda(t)$.

5.4 Self-similar mixing layer

The RMI-induced mixing layer becomes self-similar at late-time, exhibiting asymptotic values for quantities such as the mixedness and anisotropy of the turbulent kinetic energy. The quarter-scale case from the θ-group is utilised to investigate how the application of transverse strain rates affects the development of the mixing layer towards the self-similar state. Several models are

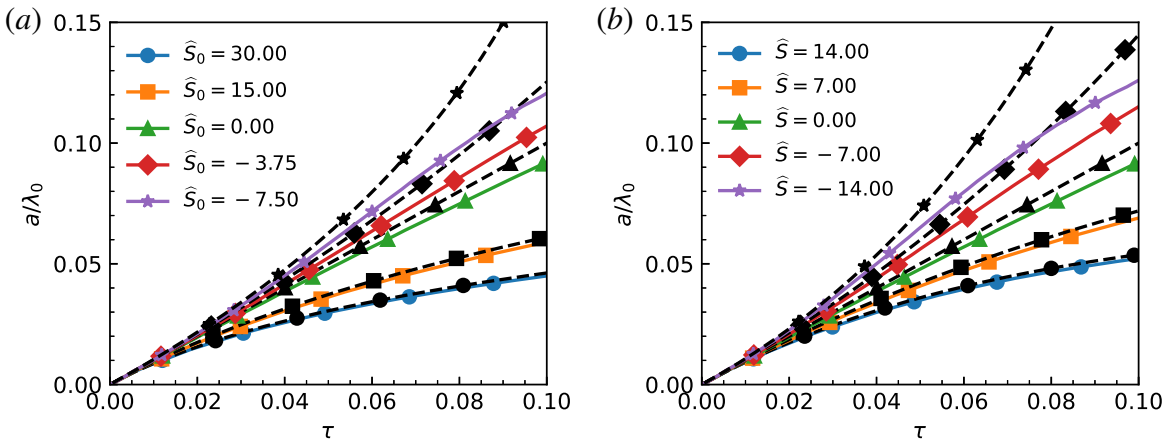

Figure 5.4: Amplitude of the single mode linear regime, non-dimensionalised for the initial wavelength for (*a*) constant velocity and (*b*) constant strain rate. Solid lines indicate numerical results, dashed lines indicate the linearised potential model.

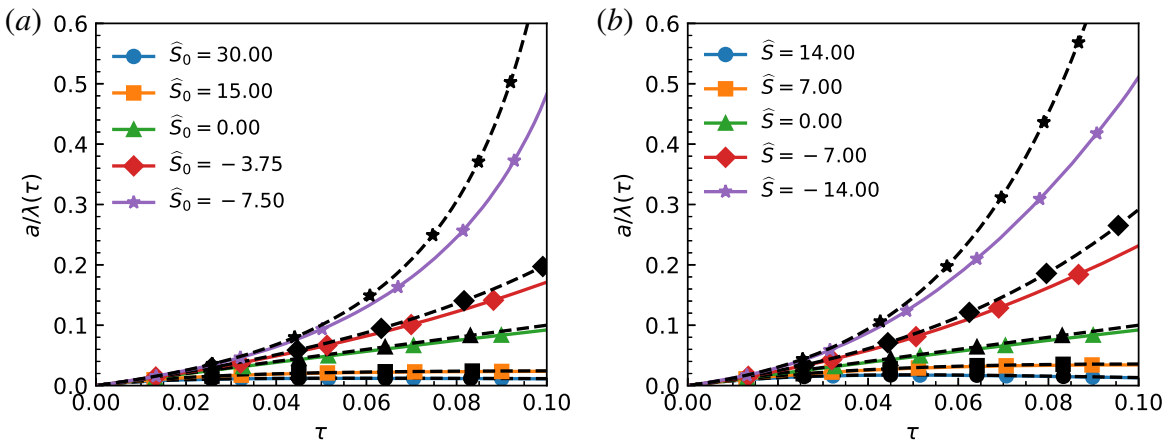

Figure 5.5: Amplitude of the single mode linear regime, non-dimensionalised by the time-varying wavelength for (*a*) constant velocity and (*b*) constant strain rate. Solid lines indicate numerical results, dashed lines indicate the linearised potential model.

proposed in order to capture the effects of the transverse strain rate and to help further understand how strain affects the mixing layer behaviour.

5.4.1 Initial conditions

ILES cases are conducted using the quarter-scale narrowband case from the θ-group collaboration (Thornber *et al.*, 2017). Relying on the dissipation of the numerical scheme to dissipate kinetic energy at the high wave numbers at a rate determined by the cascade from the large scales, the simulations are conducted in FLAMENCO using the inviscid five-equation model presented in equation (3.27). With the omission of the viscous, diffusive and conductive fluxes, the

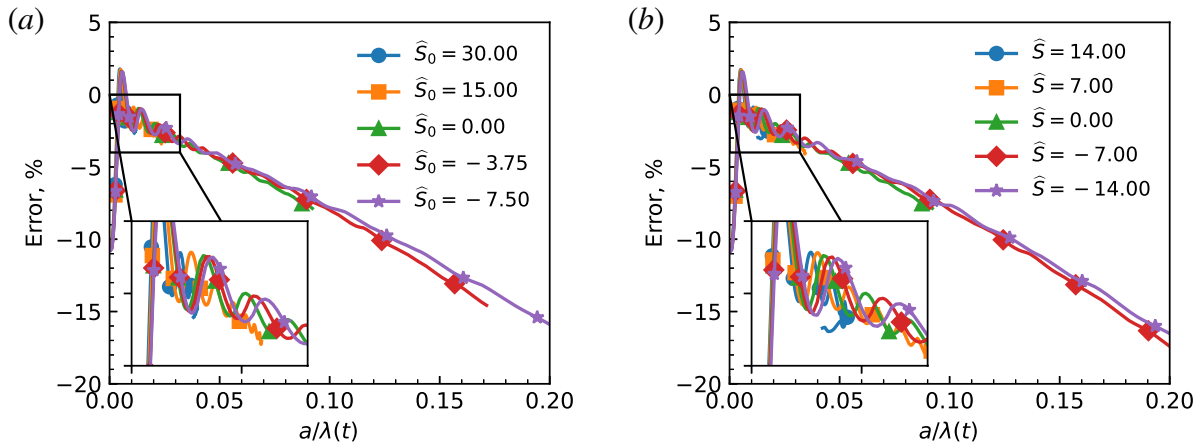

Figure 5.6: Error in the amplitude for the linear regime under (*a*) constant velocity and (*b*) constant strain rate.

simulations represent the high-Reynolds number limit. The ILES simulations conducted use the same initialisation but have a slightly different domain set-up. The initial domain size is the same, with size $x \times y \times z = \mathcal{L}_x \times \mathcal{L} \times \mathcal{L} = 2.8\pi \times 2\pi \times 2\pi \mathrm{m}^3$, however the boundary conditions are different. Whilst the original quarter-scale case used periodic boundary conditions in the y- and z-directions, for the application of transverse strain rates with moving mesh, it is necessary to use symmetry plane boundary conditions in FLAMENCO. An alternative approach to this could be to use the modelling approach of Rogallo (1981) to transform the domain and solve for the fluctuations. The x-direction boundary conditions remain as outflows. The fluids are initially set-up in a heavy-to-light order, with the mean interface position at $x = 3.5\,\mathrm{m}$, and the shock initialised below $x = 3\,\mathrm{m}$. The unshocked densities of the heavy and light fluids are $3\,\mathrm{kg\,m^{-3}}$ and $1\,\mathrm{kg\,m^{-3}}$ respectively. Both fluids have $\gamma = 5/3$, and the initial shock strength of Mach 1.8439 achieves a four-fold increase in the shocked heavy fluid. The interface between the heavy and light fluid is perturbed with a narrowband spectrum, using a constant power spectrum from $\lambda_{\mathrm{min}} = \mathcal{L}/32$ to $\lambda_{\mathrm{max}} = \mathcal{L}/16$. The amplitude and phase of each mode is randomly generated from a Gaussian distribution. The random numbers and initial spectrum are reproducible, as a specific seed is used with the Mersenne Twister algorithm. These amplitudes are scaled to ensure the amplitude of the final spectrum is equal to $0.1\lambda_{\mathrm{min}}$. The interface also uses a diffuse thickness, given by

$$f_1 = \frac{1}{2}\left(1 - \mathrm{erf}\left(\frac{\sqrt{\pi}\,[x - S(y,z)]}{\delta}\right)\right), \tag{5.39}$$

where diffuse thickness of $\delta = \mathcal{L}/128$ is used, and $S(y,z)$ is the perturbation spectrum:

$$S(y,z) = 3.5 + \sum_{k_y,k_z} a_0 \cos\left(k_y y + k_z z + \phi\right). \tag{5.40}$$

To offset the velocity difference imparted by the shock, the velocity in the domain is given an offset of $\Delta u = -291.575\,\mathrm{m\,s^{-1}}$, allowing the interface to remain close to stationary after shock transition. The length scales are non-dimensionalised by the mean wavelength, $\bar{\lambda} = \sqrt{12/7}\lambda_{\text{min}}$, and the velocities are non-dimensionalised by the initial growth rate of the integral width, $\dot{W}_0 = 12.649\,\mathrm{m\,s^{-1}}$, where the integral width is defined by

$$W = \int_0^{\mathcal{L}_x} \bar{f}_1 \bar{f}_2 dx. \tag{5.41}$$

Further details on how these properties are calculated can be found in Thornber *et al.* (2010, 2017). Other variables are non-dimensionalised using a combination of $\bar{\lambda}$, $\dot{W}_0$, the mean post-shock density for the unstrained case $\bar{\rho}^+ = 3.51\,\mathrm{kg\,m^{-3}}$, and the cross-sectional area $4\pi^2$.

The transverse strain rates are applied at $\tau = 1$, when the mixing layer is beginning to transition. The strain rates are applied by adding the mean velocity gradient to the flow profile and moving the mesh with the prescribed strain rate profile. Eight strain cases are conducted as listed in table 5.3. There are four strain cases for each strain rate profile, which can be further subdivided into two expansion cases and two compression cases. The simulations are conducted until the domain changes in size by around a factor of two. In order to resolve the expansion cases, the solution is interpolated on a mesh with twice as many cells in the $y-$ and $z-$directions, which is to ensure the simulations resolve the same minimum scale at the late time as the unstrained case. As shown in Appendix 5.4.2, the cases are converged for the integral properties such as the integral width and molecular mixedness, ensuring the strain rate effects on these properties are independent of the mesh resolution. The simulations are conducted to less extreme expansion factors compared to ICF problems, which can obtain compression factors of 15-18 for the moderate implosion schemes, and 30-40 for the high implosions schemes (Lindl *et al.*, 2014; Olson *et al.*, 2016). Despite this, the range of strain rates investigated are representative of practical application and capture a noticeable change in the development of the mixing layer.

5.4.2 Convergence

For the employed simulations that are based upon the quarter-scale θ-group case (Thornber *et al.*, 2017), it is necessary to be certain that the simulations are adequately resolved under the applied strain rates. As the simulations are ILES, they do not attempt to resolve to the Kolmogorov scale, and instead simulate the larger scales whilst relying on the inherent numerical dissipation of the solver to model the smallest scales. The original quarter-scale θ-group case utilised 512 cells in each transverse direction, and the same mesh was used for the compression strain rate cases.

Table 5.3: The strain cases, total simulation time, domain size, grid resolution, and final expansion factor for each of the ILES cases.

Strain Profile	$\bar{S}_0$ (s^{-1})	$\hat{S}_0$	Simulation time (s)	Initial domain size (m^3)	Grid resolution	Λ_F
Unstrained	0.0	0.0	0.711	$2.8\pi \times 2\pi \times 2\pi$	720×512^2	1.00
Constant velocity	-2.50	-0.051	0.203	$2.8\pi \times 2\pi \times 2\pi$	720×512^2	0.54
Constant velocity	-0.625	-0.013	0.711	$2.8\pi \times 2\pi \times 2\pi$	720×512^2	0.57
Constant velocity	1.25	0.025	0.711	$2.8\pi \times 2\pi \times 2\pi$	720×1024^2	1.86
Constant velocity	5.0	0.102	0.203	$2.8\pi \times 2\pi \times 2\pi$	720×1024^2	1.91
Constant strain rate	-4.0	-0.081	0.203	$2.8\pi \times 2\pi \times 2\pi$	720×512^2	0.48
Constant strain rate	-1.0	-0.020	0.711	$2.8\pi \times 2\pi \times 2\pi$	720×512^2	0.50
Constant strain rate	1.0	0.020	0.711	$2.8\pi \times 2\pi \times 2\pi$	720×1024^2	2.00
Constant strain rate	4.0	0.081	0.203	$2.8\pi \times 2\pi \times 2\pi$	720×1024^2	2.08

Table 5.4: Test cases employed for the convergence study. Check-marks indicate the mesh used for results in the chapter, circles indicate meshes used for convergence study.

Cells	$\widehat{S} = -0.081$	$\widehat{S} = 0.0$	$\widehat{S} = 0.081$
720×512^2	✓	✓	○
1080×768^2	○	○	○
720×1024^2		○	✓

The expansion cases used a mesh with 1024 cells across, interpolating the original solution onto the finer mesh, in order to maintain the resolution at maximum expansion at the end of the simulations. To show that the integral properties of the simulations are converged, simulations are performed from $\tau = 1$ with various meshes, interpolating the original solution onto the new meshes. The three meshes used are listed in table 5.4, which consist of the original mesh, the transversely refined mesh used for expansion, and a moderately refined mesh which was refined in the axial and transverse directions.

The simulations are conducted for the unstrained case and the two high-magnitude constant strain rate cases, $\hat{S} = \pm 0.081$, until a time of $\tau = 10$. The results for the integral width and molecular mixing fraction are plotted in figure 5.7. The results for the integral width show a very small difference between the 512 cells cases and the higher resolution cases, with the higher resolution cases showing a slightly smaller integral width, but following the same identifiable trends dependent upon the strain rate. The same observation can be made for the molecular

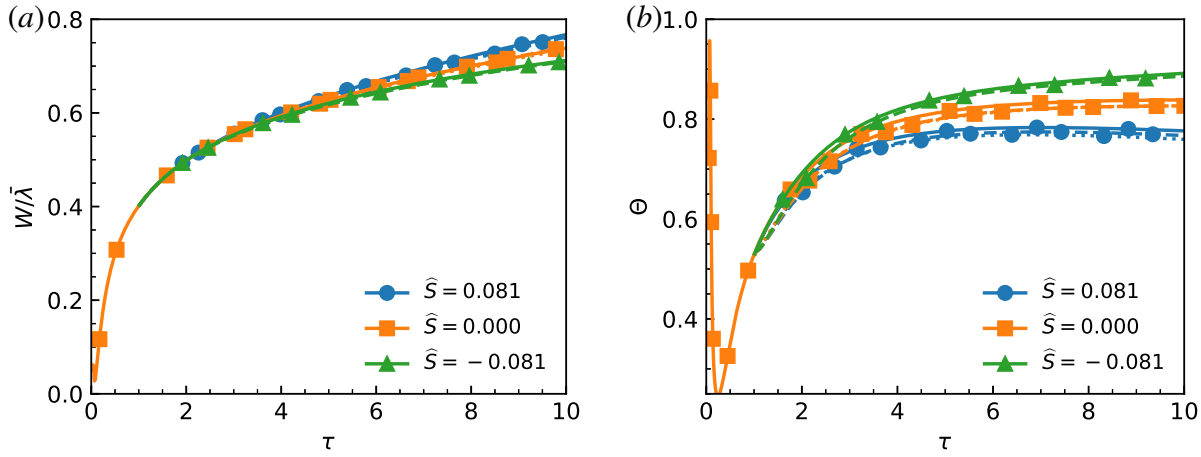

Figure 5.7: Convergence of constant strain rate simulations under transverse compression for (a) integral width and (b) molecular mixing fraction. Solid lines indicate results for 512 cells across, dashed lines for 768 cells, dotted lines for 1024 cells.

mixing fraction, where the mixedness is slightly decreased with the increased mesh resolution, but the same trends are discerned.

5.4.3 Results

Visualisations

Slices of volume fraction contours for the constant velocity cases are shown in figure 5.8 for the middle x-y plane of the simulations. The left column shows $\tau = 9.84$ for all cases, whilst the right column shows the results for the low-magnitude strain rate cases at the later time of $\tau = 34.35$. Due to the varying domain width with time, the scale of each plot is varied to fit the slice within the column. The compression cases appear to be dominated by several large structures, whilst the expansion cases maintain more distinct small structures in the mixing layer which have not been broken down by turbulent mixing.

Isosurfaces of the volume fraction at $f_1 = 0.01$ and $f_1 = 0.99$ are shown in figure 5.9 for the expansion cases at $\Lambda \approx 1.82$, and in figure 5.10 for the compression cases at $\Lambda \approx 0.57$. The scale used in the expansion plots is different to the scale used for the compression plots, so a visual comparison of the mixing layer thickness between expansion and compression cases is not an accurate representation. For the lower magnitude strain rate cases, the specified expansion factor is achieved at a later non-dimensional time. This is evident from the increased mixing layer thickness observable for the (c) and (d) subplots compared to (a) and (b). These later time plots also show the penetration of a vortex ring into the heavy fluid. For the expansion cases, the structure remains intact, but for the compression cases, the structure has bifurcated. This may be

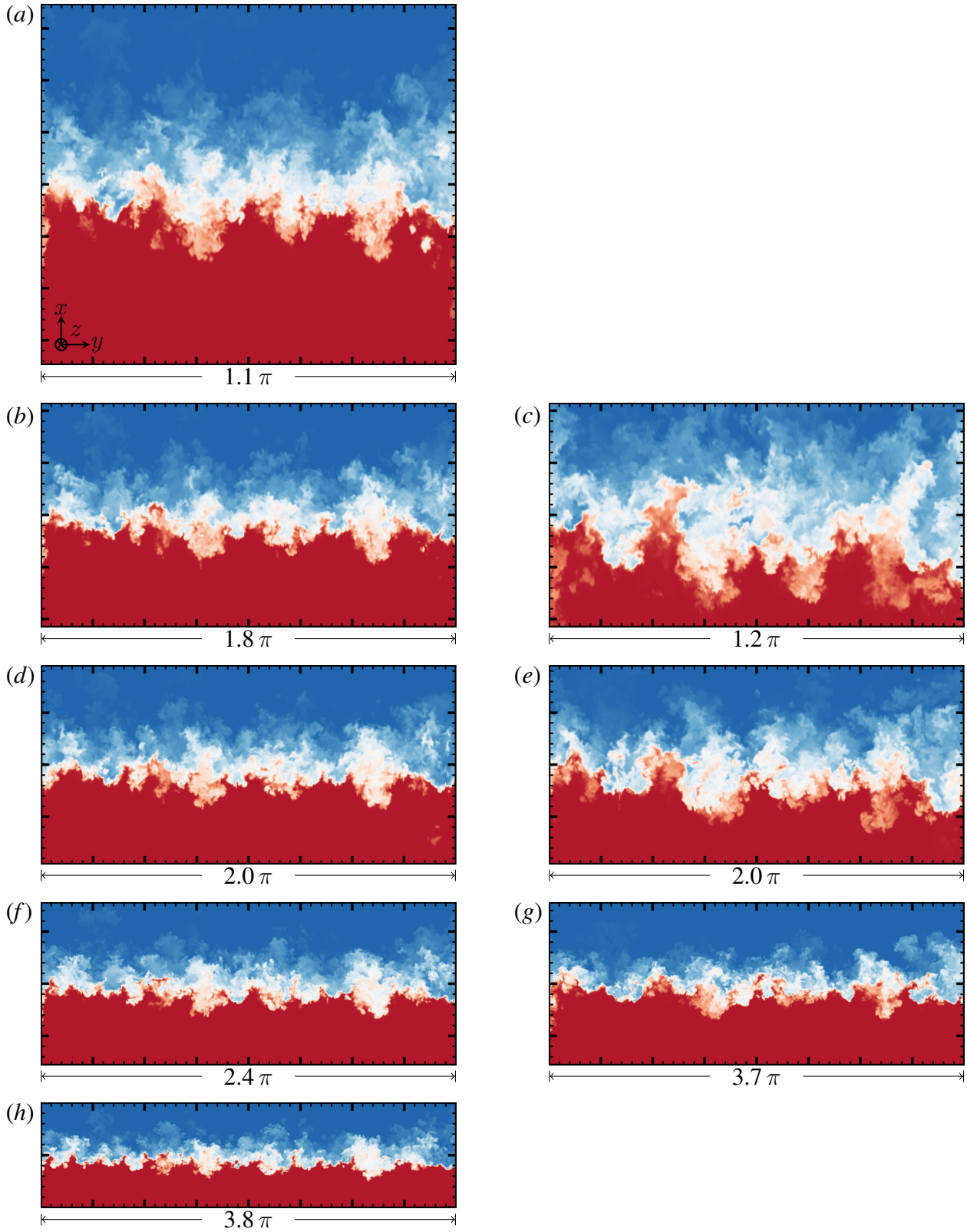

Figure 5.8: Contours of the volume fraction for the constant velocity ILES cases at the centre x-y plane ($z = \mathcal{L}(t)/2$): (*a,b,d,f,h*) $\tau = 9.843$; (*c,e,g*) $\tau = 34.451$; (*a*) $\hat{S}_0 = -0.051$; (*b,c*) $\hat{S}_0 = -0.013$; (*d,e*) $\hat{S}_0 = 0$; (*f,g*) $\hat{S}_0 = 0.025$; (*h*) $\hat{S}_0 = 0.102$. Heavy fluid ($f_1 = 1$) is red, light fluid ($f_1 = 0$) is blue. Major ticks on the axes correspond to $\mathcal{L}(t)/8$;

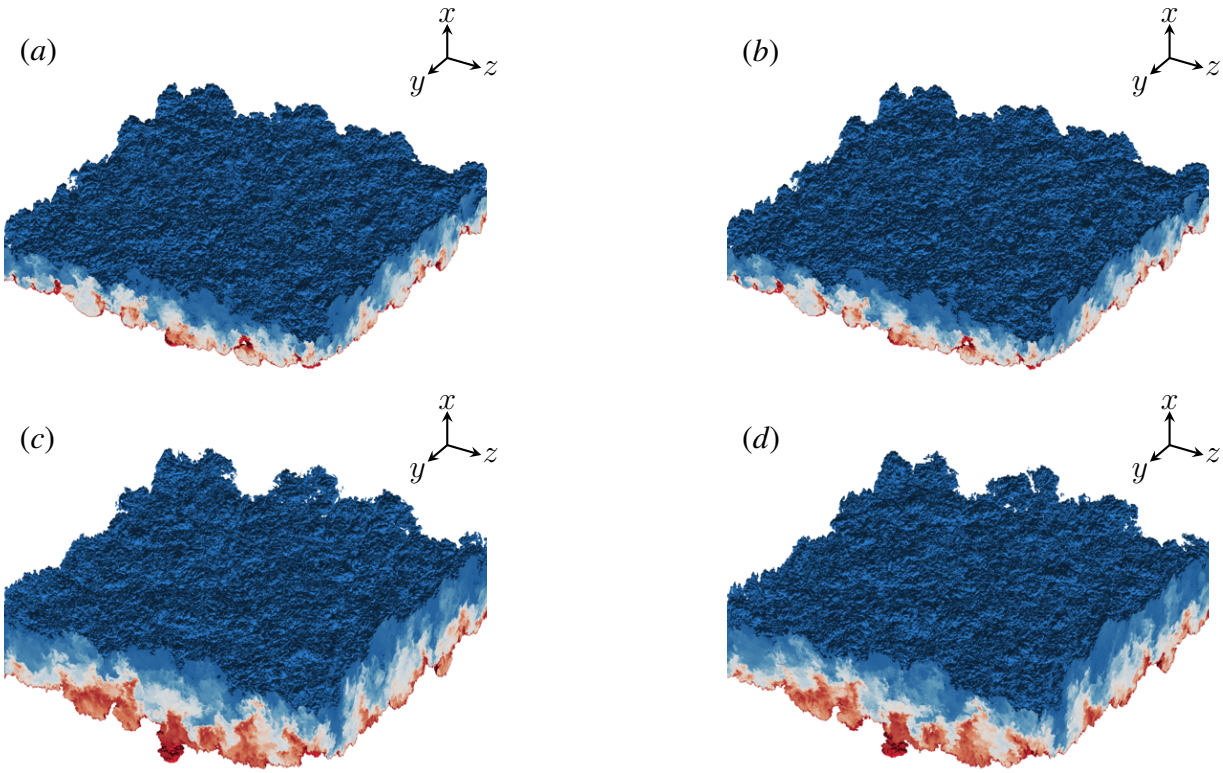

Figure 5.9: Contour of volume fraction f_1 for the expansion mixing layers at $\Lambda \approx 1.82$, bounded by $f_1 = 0.99$ (red) and $f_1 = 0.01$ (blue). (*a*) $\hat{S}_0 = 0.102$, $\tau = 9.05$, (*b*) $\hat{S} = 0.081$, $\tau = 8.37$, (*c*) $\hat{S}_0 = 0.025$, $\tau = 33.5$, (*d*) $\hat{S}_0 = 0.020$, $\tau = 30.5$

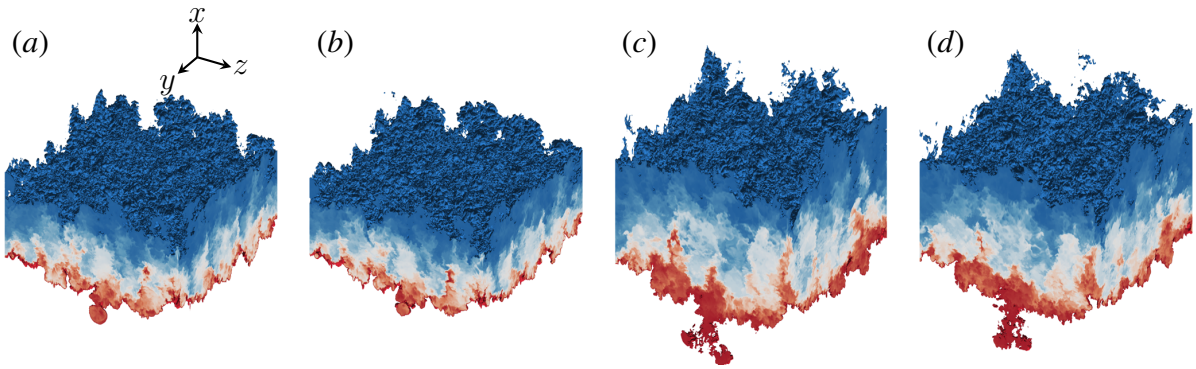

Figure 5.10: Contour of volume fraction f_1 for the expansion mixing layers at $\Lambda \approx 0.57$, bounded by $f_1 = 0.99$ (red) and $f_1 = 0.01$ (blue). (*a*) $\hat{S}_0 = -0.051$, $\tau = 9.45$, (*b*) $\hat{S} = -0.081$, $\tau = 7.88$, (*c*) $\hat{S}_0 = -0.013$, $\tau = 34.9$, (*d*) $\hat{S}_0 = -0.020$, $\tau = 28.5$

the result of vortex tilting and the vortex ring being pinched by the compressive strain. Vortex pinching has been investigated by Marshall & Grant (1994) for planar strain configurations, where expansive and compressive strain rates are applied in perpendicular directions in the plane of the vortex ring. For sufficiently high strain rates, this can cause the vortex ring to deform into an elliptical shape and curve into the third dimension, eventually pinching at the centre and producing two smaller vortex rings.

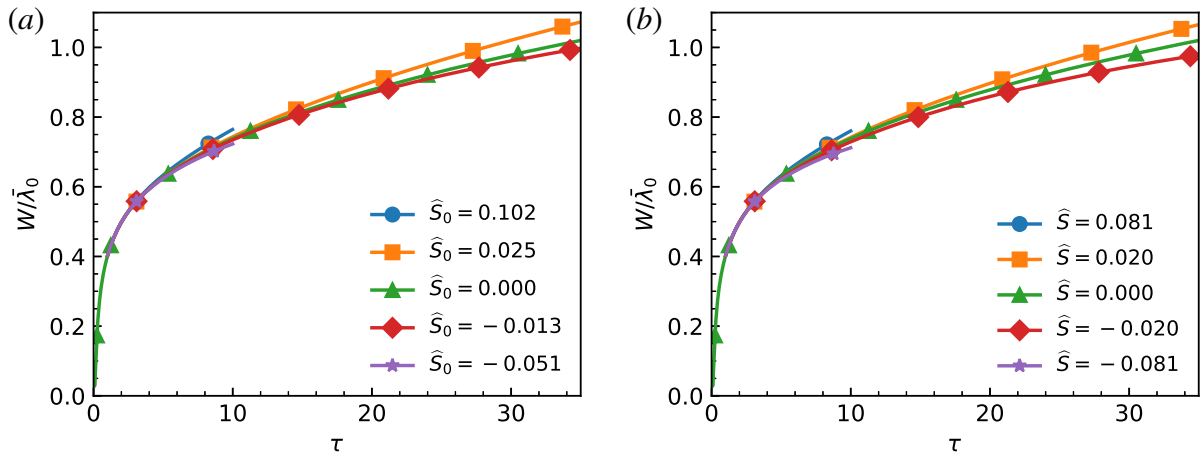

Figure 5.11: Integral width for (*a*) constant velocity, and (*b*) constant strain rate.

Width and mix measures

The integral width of the mixing layer normalised by the initial mean wavelength of the interface is plotted in figure 5.11. The cases with applied expansion transverse strain rates show a slight increase in the integral width, whilst the compression cases show a decrease. This behaviour is the opposite of what was observed in the linear regime, where transverse compression increased the growth and was well captured by the Bell-Plesset model. El Rafei *et al.* (2019) also noted that once the modes begin to saturate, Bell-Plesset models fail to accurately predict the growth of the mixing layer for the spherical implosion. This observed trend demonstrates that the influence of the transverse strain rate on the transitional and turbulent mixing layer is fundamentally different from the linear regime and can not be modelled by the same approach. It is also important to note that the integral widths of transverse strain rate cases are much closer to the unstrained simulation than was observed for cases with axial strain rates in Chapter 4, where the strain rate causes the mixing layer to stretch/compress directly from the background velocity difference. This is a similar observation to the one made by Lombardini *et al.* (2014) which noted the compression effects were larger than the convergence effects for the analysed implosion profile. As the quarter-scale θ-group case is initialised with a narrowband perturbation and a uniform power spectrum, all the perturbation modes are non-linear at the time of strain application. Different behaviour could be observed for a broadband spectrum, where the high wave-number modes will saturate much earlier than the low wave-number modes, which can remain linear for a longer time (Groom & Thornber, 2020). The high wave-number modes will transition to a turbulent state which observes the reduced growth for compression, meanwhile the growth rate of the low wave-number modes would be amplified by transverse compression causing an increased mixing layer growth rate.

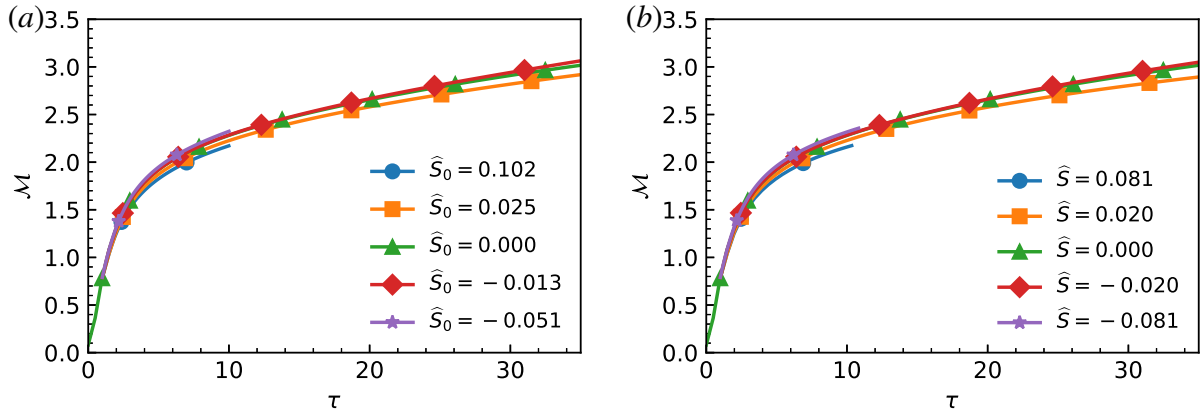

Figure 5.12: Mixed mass for (*a*) constant velocity and (*b*) constant strain rate.

The mixed mass is an alternate measure of the mixing layer, and measures how much of one fluid has mixed with another. An attractive feature of the mixed mass is the ability to derive the evolution equation for the mixed mass from the mass fraction transport equation (Zhou *et al.*, 2016):

$$\mathcal{M} = \int 4\rho Y_1 Y_2 dV \tag{5.42}$$

The profiles of the mixed mass are plotted in figure 5.12, and show a different trend compared to the integral width. For the mixed mass, the compression cases achieve slightly higher growth and the expansion cases achieve less growth. As the name mixed mass suggests, it is not purely a measure of the width of the mixing layer but also has dependence upon mixedness of the mixing layer, whereas the integral width depends on the mean volume fraction profile. Therefore, depending upon the choice of measurement metric for the mixing layer development, the influence of the transverse strain rate will change signs. The increased mixedness of the compression cases represents a more mixed or homogeneous composition in the mixing layer as compared to the unstrained, and likewise a less mixed layer for the expansion cases. The compression cases show a smaller deviation from the unstrained case compared to the expansion cases. As the change in mixedness is opposing the change in mixing layer width for the mixed mass results, it is not surprising that the deviation is larger for the expansion cases. The expansion cases are becoming less mixed, which is a simpler task compared to making the mixing layer even more mixed for the compression cases. The mixedness of the mixing layer is further explored using the molecular mixing fraction below.

Due to the different densities of the fluids (i.e. non-zero Atwood number), asymmetries form in the development of the mixing layer. The penetration structures of the heavy fluid into the light fluid (spikes) tends to be larger than the penetration of the light fluid into the heavy fluid (bubbles). The spike-to-bubble heights will toward a constant ratio if the growth rates of the

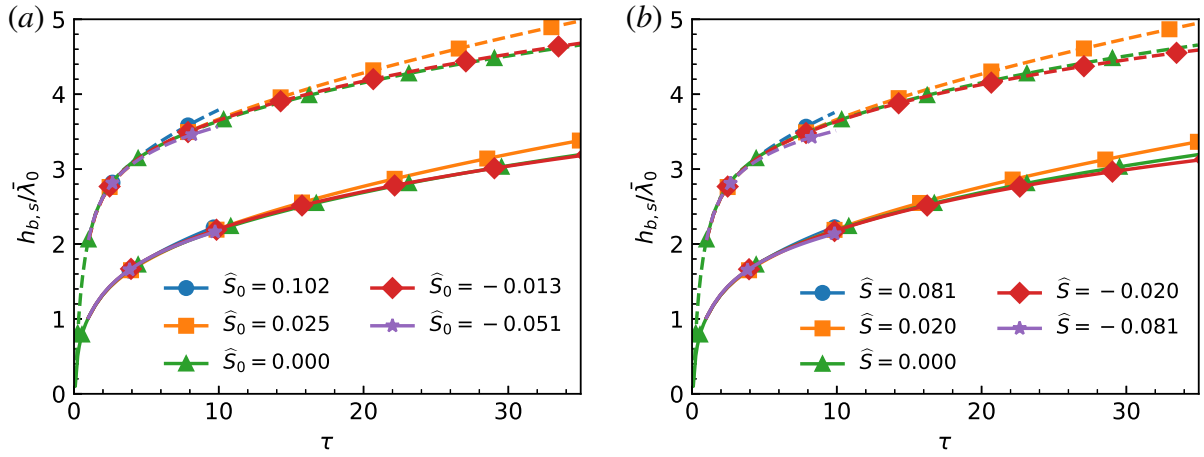

Figure 5.13: Bubble and spike heights for (*a*) constant velocity and (*b*) constant strain rate. Solid lines indicate bubble height, dashed lines indicate spike height.

spikes and bubbles both follow the same power law growth rate, i.e. $\theta_s = \theta_b$ (Thornber *et al.*, 2017; Mikaelian & Olson, 2020). The bubble and spike heights of the mixing layer are defined relative to the mixing layer centre x_C, taken to be the planar location where there is an equal volume of penetrating fluid on either side:

$$\int_{-\infty}^{x_C} \bar{f}_2 dx = \int_{x_C}^{\infty} \bar{f}_1 dx \tag{5.43}$$

To reduce the impact of statistical fluctuations, the bubble and spike heights used are based off the integral measure proposed by Youngs & Thornber (2020*a*):

$$\bar{h}_b^{(m)} = \left[\frac{(m+1)(m+2)}{2} \frac{\int_{-\infty}^{0} |x'|^m (1-\bar{f}_1) dx'}{\int_{-\infty}^{0} (1-\bar{f}_1) dx'} \right]^{1/m}, \tag{5.44a}$$

$$\bar{h}_s^{(m)} = \left[\frac{(m+1)(m+2)}{2} \frac{\int_{0}^{\infty} |x'|^m \bar{f}_1 dx'}{\int_{0}^{\infty} \bar{f}_1 dx'} \right]^{1/m}. \tag{5.44b}$$

The integrals are taken with respect to the mixing layer centre, $x' = x - x_C$, and the integral terms of the denominator are equal to the volume of the penetrating fluid on either side of the mixing layer centre. These definitions provided assume that fluid 1 is located below fluid 2 in the x-direction and that $\rho_1 > \rho_2$. The bubble and spike heights plotted in figure 5.13 use the heights $h = 1.1\bar{h}^{(2)}$ which were found to be well aligned with the heights measured by the 1% and 99% mean volume-fraction cut-off but are less sensitive to statistical fluctuations (Youngs & Thornber, 2020*a*).

The bubble and spike heights show the same behaviour as observed for the integral width, with the expansion cases growing slightly compared to the unstrained simulation. The compression cases tend to have smaller heights than the unstrained cases, however the influence of the transverse compression appears to be smaller, such that the results are closer to the unstrained

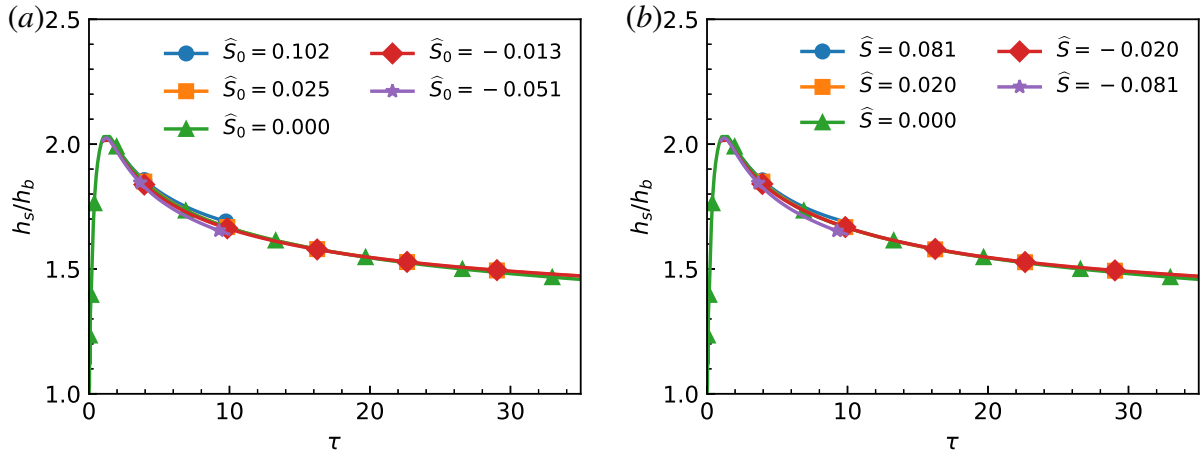

Figure 5.14: Ratio of spike-to-bubble height for (*a*) constant velocity and (*b*) constant strain rate.

simulation results. Despite this, the ratio of the spike height to bubble height shows a common trend with the unstrained case, as shown in figure 5.14. The effect of convergence doesn't appear to change the growth rate of the bubble and spike heights disproportionately, displaying the same self-similar ratio between the heights as seen for unstrained simulations.

To better quantify the mixedness of the mixing layer, which is suggested to change by the discrepancy in the behaviour between the mixed mass and the integral width, the molecular mixing fraction and the non-dimensionalised mixed mass are used. The molecular mixing fraction measures how well the species in the mixing layer are mixed, as measured by the volume fraction. A value of $\Theta = 0$ means complete segregation, whilst $\Theta = 1$ corresponds to perfect homogeneity in the plane. The molecular mixing fraction is calculated by,

$$\Theta(t) = \frac{\int \overline{f_1 f_2} dx}{\int \bar{f}_1 \bar{f}_2 dx}. \tag{5.45}$$

At late-time, a steady Θ indicates that a mixing layer has become self-similar. Included in figure 5.15 is the final value of Θ from the quarter-scale case using FLAMENCO in the θ-group collaboration at a time of $\tau = 246$. The unstrained quarter-scale case simulation can be observed to be approaching the self-similar value marked by the black, dashed line. The strained cases do not appear to be approaching the same asymptote. Instead, the compression cases show an increasing mixedness and the expansion cases are decreasing.

This is the same trend as observed when axial strain rates are applied to the mixing layer, such that a decrease in turbulent growth of the mixing layer corresponds to an increase in the mixedness. The difference between the transverse and axial strain rates is that the decreased turbulent growth occurs for compressive transverse strain rates, whilst the decreased turbulent growth occurs for expansive axial strain rates, as shown in Chapter 4. The compressive transverse strain rates

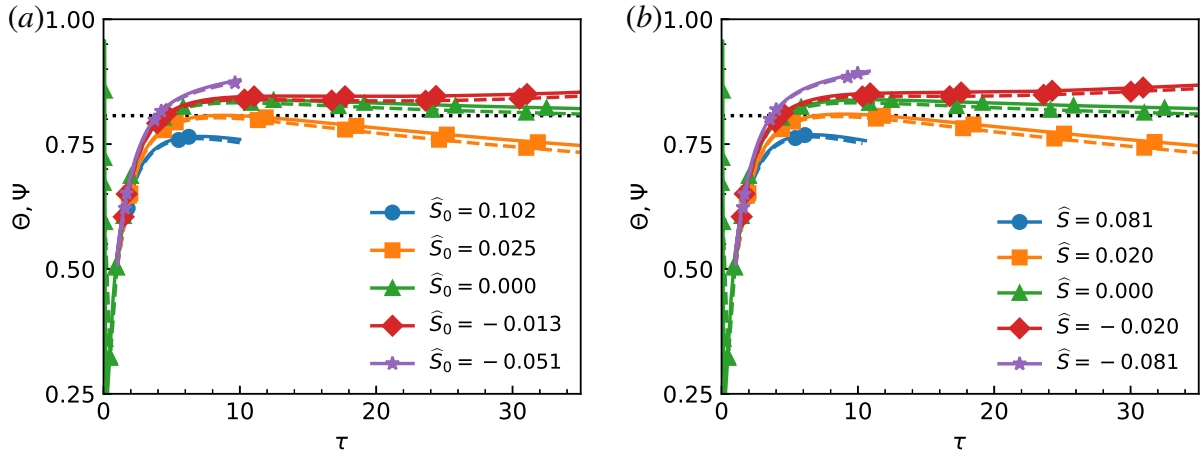

Figure 5.15: Mixing measures for the (*a*) constant velocity and (*b*) constant strain rate. Solid lines indicate Θ, dashed lines indicate Ψ, dotted line is FLAMENCO's final Θ value at $\tau = 246$ (Thornber *et al.*, 2017).

can be expected to enhance the turbulence in the transverse direction through shear-production, which allows greater mixing, as shown in the results. This clearly affects the self-similarity of the simulation, potentially converging to a different self-similar state, or not converging at all. The normalised mixed mass is also plotted in figure 5.15, using the definition

$$\Psi = \frac{\int \rho Y_1 Y_2 dV}{\int \bar{\rho} \bar{Y}_1 \bar{Y}_2 dV}. \tag{5.46}$$

The results for Θ and Ψ are well aligned, with the values of Ψ attaining slightly smaller values compared to Θ. This behaviour has previously been observed in several other studies (Zhou *et al.*, 2016, 2020; El Rafei & Thornber, 2020).

Self-similarity

To further investigate the self-similarity of the simulation, the two contributions of the molecular mixing fraction may be analysed: the mean volume fraction profile $\bar{f}_1$, and the mean volume fraction product $\overline{f_1 f_2}$. These terms correspond to the denominator and numerator of the molecular mixing fraction, and for a self-similar mixing layer these profiles will collapse under non-dimensionalisation.

The profiles of $\bar{f}_1$ and $\overline{f_1 f_2}$ are plotted in figure 5.16 for the constant velocity cases, and in figure 5.17 for the constant strain rate cases. The profiles are shown at two different times, corresponding to the end times of the high strain rate cases, $\tau = 9.843$, and the end time of the low strain rate cases, $\tau = 34.451$. All cases are visible for the early time, whilst at the late time only information for the low strain rate cases are available. The mean profile of f_1 is plotted in the sub-figures (a) and (c). The mean volume fraction profile does not appear to vary

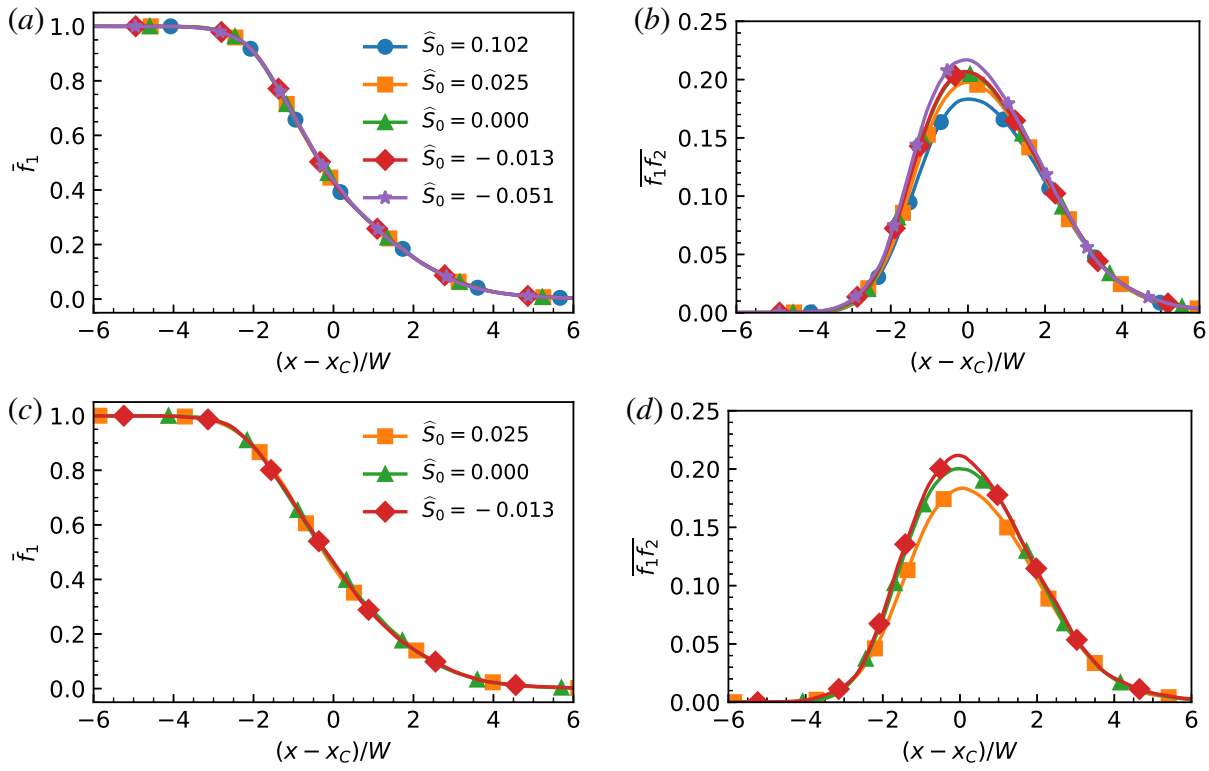

Figure 5.16: Planar-averaged volume-fraction profiles for the constant velocity cases: (*a,b*) $\tau = 9.843$; (*c,d*) $\tau = 34.451$

from the unstrained solution for both strain profiles and at both times shown. The evolution of the mean volume fraction profile for the quarter-scale θ-group case almost collapsed to a single profile, however the profile slightly smoothed out with time around the inflection points at $(x - x_C)/W = -2$ and 2.5. The agreement between the strain cases and the unstrained case is suggestive that the bubble and spike heights grow in the same proportion as in the unstrained case, reinforcing the results in figure 5.14.

The mean volume fraction product shown in subplots (b) and (d) of figures 5.16 and 5.17 show a larger deviation from the unstrained case. Whilst the unstrained quarter-scale θ-group case was self-similar in the centre of the mixing layer for the mean volume fraction product, the strained cases do not match the profile, explaining the different Θ values obtained. The compression cases which possessed the largest Θ values have a larger peak value of $\overline{f_1 f_2}$, representing greater mixing at the centre of the mixing layer. This is due to the shear-production increasing the mixing, with the larger magnitude strain rates showing larger changes in the mean product. The low-magnitude strain rates can be observed to deviate further away from the unstrained profile as the simulation progresses, showing that the strained cases have not achieved a self-similar state.

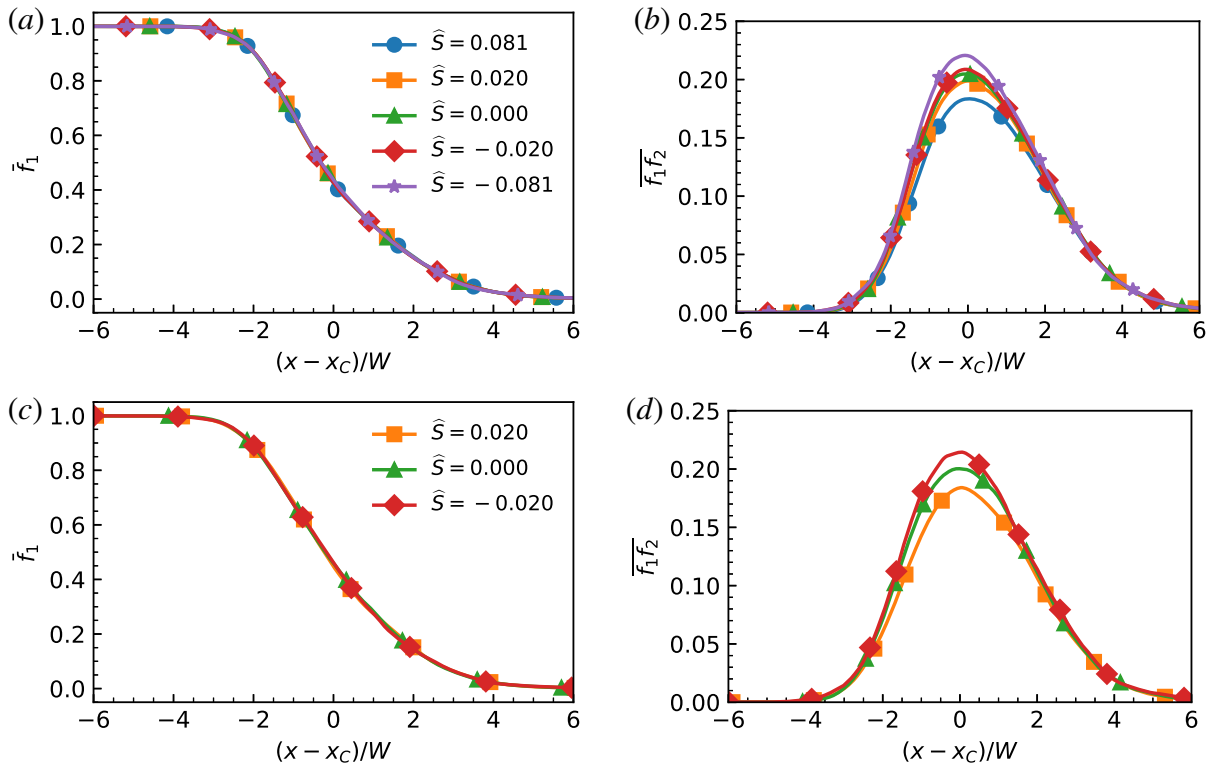

Figure 5.17: Planar-averaged volume-fraction profiles for the constant strain rate cases: (*a,b*) $\tau = 9.843$; (*c,d*) $\tau = 34.451$

Turbulent kinetic energy

Under transverse strain rates, the shear-production contribution to the turbulent kinetic energy clearly affects the mixedness of the mixing layer. The total turbulent kinetic energy in the domain is calculated by

$$TKE = \iiint \frac{1}{2} \rho u_i'' u_i'' \, \mathrm{d}x \, \mathrm{d}y \, \mathrm{d}z, \tag{5.47}$$

where the Favre fluctuations u_i'' are calculated from the flow field with the mean velocity gradients removed. To compare to the simulation results of TKE, it is possible to define a simple model. As the quantity has been integrated over the domain, fluxes may be neglected and the model consists of shear production and dissipation,

$$\frac{\mathrm{d}TKE}{\mathrm{d}t} = \mathcal{P} - \varepsilon \tag{5.48}$$

It has also been assumed that there is negligible buoyancy production at this stage, and for simplicity it is assumed that the pressure-rate-of-strain tensor has no net effect on the turbulent kinetic energy, and only redistributes energy. Analysis of the turbulent kinetic energy budgets shows that the pressure-rate-of-strain has a net contribution to the turbulent kinetic energy for the unstrained case, however the significance of this term decreases with time (Thornber *et al.*,

2019). A compressible model for the pressure-dilation will include contributions to the total turbulent kinetic energy, whereas incompressible models do not. The compressible model of Sarkar (1992) includes pressure-dilation contributions which are weighted by the turbulent Mach number, however the mean turbulent Mach number in the strained simulations is below 0.03, calculated using the planar-averaged turbulent kinetic energy. Using dimensional analysis, the dissipation rate is taken to be on the order of $\sim u^3/l$ (Thornber *et al.*, 2010; Groom & Thornber, 2020),

$$\varepsilon = C_\epsilon \frac{TKE^{3/2}}{W\sqrt{M}} \tag{5.49}$$

where the integral width W is interpolated from the simulation data and used as the length scale, and M is the mass within the mixing layer, $M = 4\pi^2\bar{\rho}_0 W$. An additional coefficient of $C_\epsilon = 1/140$ is included to calibrate the dissipation rate to match the unstrained simulation. To accurately calculate the shear production contributions it is necessary to also evolve the turbulent kinetic energy components for each direction, given by

$$TKX = \iiint \frac{1}{2}\rho u_1'' u_1'' \,\mathrm{d}x\,\mathrm{d}y\,\mathrm{d}z, \qquad TKY = \iiint \tfrac{1}{2}\rho u_2'' u_2'' \,\mathrm{d}x\,\mathrm{d}y\,\mathrm{d}z. \tag{5.50}$$

Assuming homogeneity in the y- and z- directions allows for the simplification of $TKY = TKZ$, and by definition the total turbulent kinetic energy will be equal to $TKE = TKX + 2TKY$. The model for the turbulent kinetic energy components is based upon Reynolds stress transport equations composing of production $(\mathcal{P})$, pressure-rate-of-strain tensor $(\mathcal{R})$, and isotropic dissipation where each direction uses a third of the total dissipation rate specified in equation (5.49),

$$\frac{d}{dt}\begin{pmatrix} TKX \\ TKY \end{pmatrix} = \begin{pmatrix} 0 \\ \mathcal{P}_{22} \end{pmatrix} + \begin{pmatrix} \mathcal{R}_{11} \\ \mathcal{R}_{22} \end{pmatrix} - \frac{1}{3}\varepsilon. \tag{5.51}$$

The shear production only acts in the transverse direction due to the applied transverse strain rate and is calculated by $\mathcal{P}_{22} = 2(TKY)\bar{S}$. The total production for TKE is the sum of the production terms for y and z, resulting in $\mathcal{P} = 2\mathcal{P}_{22}$. The pressure-rate-of-strain tensor is calculated using the LRR-IP model by Launder *et al.* (1975), which is a combination of the return-to-isotropy model by Rotta (1951) and the isotropisation of production model by Naot *et al.* (1970). The LRR-IP model is commonly used for Reynolds stress transport models for compressible turbulent mixing (Grégoire *et al.*, 2005; Schwarzkopf *et al.*, 2011). Adjusting the

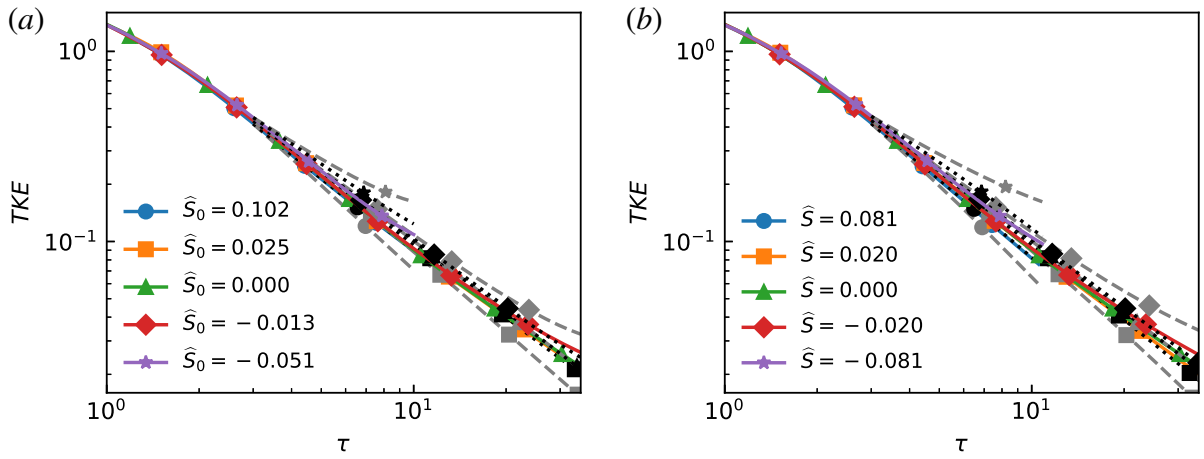

Figure 5.18: Total turbulent kinetic energy for (*a*) constant velocity and (*b*) constant strain rate. Solid lines indicate ILES, gray dashed lines indicate the turbulent kinetic energy model, and black dotted lines indicate the corrected turbulent kinetic energy model.

model to use the domain integrals instead of the Reynolds stress terms gives the expressions:

$$\mathcal{R}_{11} = -C_R \frac{\varepsilon}{TKE}\left(TKX - \frac{1}{3}TKE\right) - C_2\left(-\frac{1}{3}\mathcal{P}\right), \tag{5.52a}$$

$$\mathcal{R}_{22} = -C_R \frac{\varepsilon}{TKE}\left(TKY - \frac{1}{3}TKE\right) - C_2\left(\mathcal{P}_{22} - \frac{1}{3}\mathcal{P}\right). \tag{5.52b}$$

The C_R term is responsible for the return to isotropy and is active for the unstrained and strained cases, whilst the C_2 term is for the isotropisation of production and will only be active for the strain cases. Whilst Launder (1996) suggests a value of $C_R = 1.8$, RMI-induced mixing layers remain anisotropic, so the value was modified to improve the agreement with the unstrained simulation, using a value of unity here in order to accurately predict the TKX and TKY components. With a value of $C_R = 1$, the unstrained system will maintain the initial anisotropic distribution of turbulent kinetic energy across the three directions. To align with the observed relationship between C_R and C_2 in Launder (1996), the value of C_2 was set to 0.77 which should allow the model to still describe free shear flows.

The application of the model for TKE is shown in figure 5.18 alongside the simulation results. The simulation data shows the expected trends of the compression cases having greater TKE due to the positive shear-production contribution. However, the model, as shown in dashed grey lines, over-predicts the influence of the strain rate on the total turbulent kinetic energy. The results for the model for the transverse component, TKY, is shown in figure 5.19 and shows the same trend.

The inaccuracy of the predicted total energy in the domain suggests the model is not accurate, with an issue for either the pressure-rate-of-strain tensor or the dissipation rate closure. For the pressure-rate-of-strain tensor, excessive shear production for the strain cases could be caused

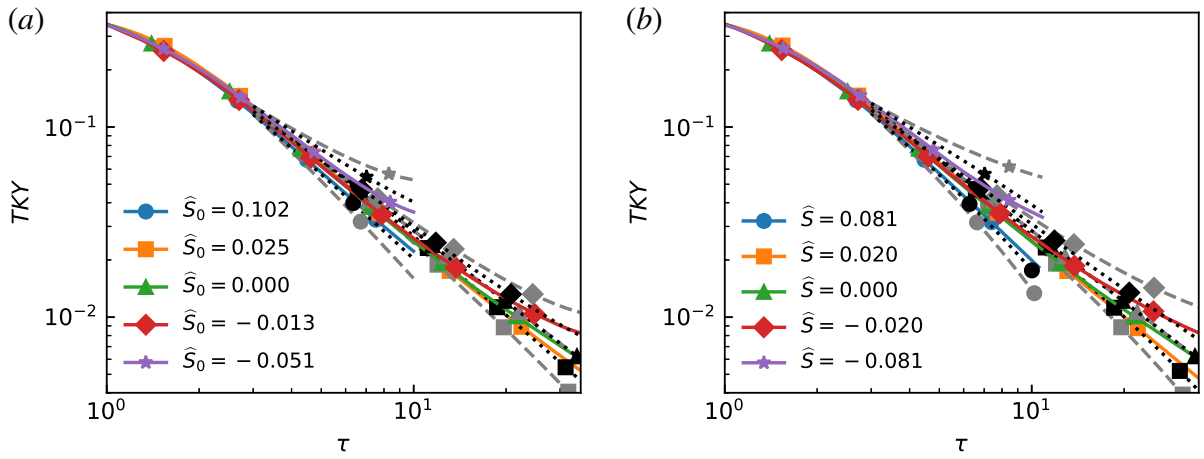

Figure 5.19: Turbulent kinetic energy in the y-direction for (a) constant velocity and (b) constant strain rate. Solid lines indicate ILES, gray dashed lines indicate the turbulent kinetic energy model, and black dotted lines indicate the corrected turbulent kinetic energy model.

by the model not accurately capturing the redistribution of the energy between the transverse and axial directions. For the compression cases, the alignment with ILES would improve if the transverse energy was redistributed to the axial direction, decreasing the transverse energy and the shear production contribution whilst increasing the TKX component. By the same process, redistribution of energy for the expansion cases should result in lower TKX. The results from the ILES in figure 5.20 show the opposite trend, with instead the expansion cases exhibiting slightly higher TKX than the unstrained case, implying that the energy is not just being redistributed into/from TKX for the strain-cases. Instead, the issue lies with the modelling of the total dissipation rate. It is commonly assumed in turbulence models that bulk compression or expansion will scale the turbulent length scale (Dimonte & Tipton, 2006; Besnard *et al.*, 1992). To account for the transverse compression, the turbulent length scale is modified to scale with the geometric mean of the expansion factors:

$$\varepsilon = C_\epsilon \frac{TKE^{3/2}}{W\sqrt{M}\Lambda^{2/3}} \tag{5.53}$$

As the strain rates are only applied in two out of the three dimensions, the resulting scale is to the power of 2/3. The results for this corrected model are also plotted in figures 5.18 and 5.19 as the black dotted lines, which show an improved agreement with the simulation results. The modified dissipation rate counteracts the effect of shear production, reducing the deviation from the unstrained case. This modification improves the TKE estimates to align with the ILES simulation results. The corrected model and the simulation results for TKX are plotted in figure 5.20, with the original model omitted due to the proximity of the data-lines. The combination of the return-to-isotropy, isotropisation of production, and strain-dependent dissipation is able to produce similar results to the simulations, showing that the influence of the strain rates on TKX

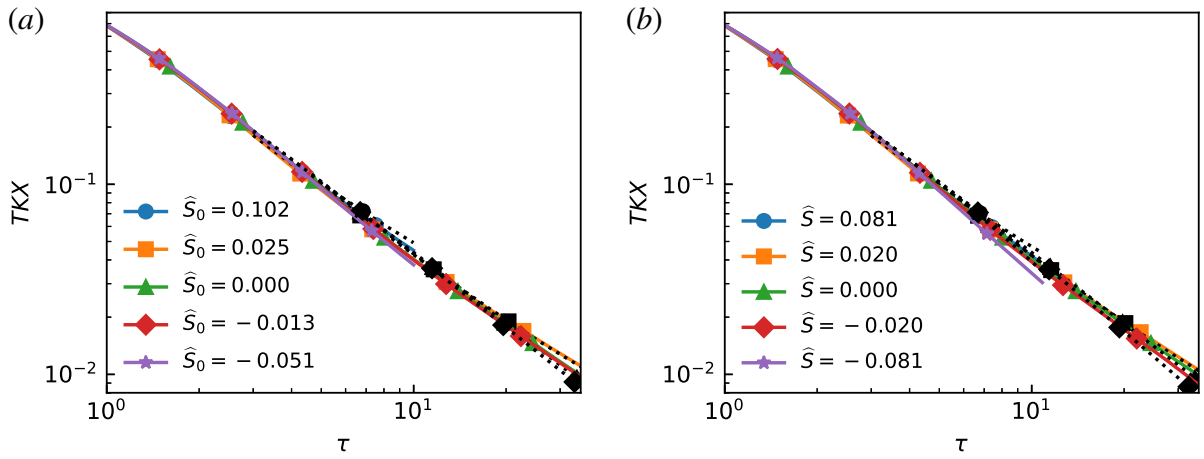

Figure 5.20: Turbulent kinetic energy in the x-direction for (a) constant velocity and (b) constant strain rate. Solid lines indicate ILES, and black dotted lines indicate the corrected turbulent kinetic energy model.

amounts to very little variation from the unstrained case. The expansion cases do have slightly higher TKX, which can explain the increased integral width for the expansion cases. By having a larger TKX, the mixing layer is able to entrain slightly more fluid, resulting in an increased growth rate.

The turbulent kinetic energy anisotropy can be calculated from the components using the equation:

$$TKR = \frac{2TKX}{TKY + TKZ}. \tag{5.54}$$

RMI has been shown to be persistently anisotropic, biased in the x-direction. The unstrained case achieves an anisotropy value of 1.49 at the final time of $\tau = 246$ from FLAMENCO in the θ-group collaboration (Thornber *et al.*, 2017). The simulation results in figure 5.21 show the unstrained case plateauing near this final value. The strained cases diverge from the asymptotic value, and it is observed that the expansion cases obtain larger values of TKR, becoming more anisotropic due to the shear production removing turbulent kinetic energy in the transverse directions. The compression cases head towards isotropy, with the compression amplifying the transverse turbulent kinetic energy. Such behaviour is also observed in spherical simulations, such as by Wang *et al.* (2023) and El Rafei *et al.* (2019) between the first and second re-shock. The anisotropy from the turbulent kinetic energy model is also plotted in figure 5.21. The unstrained case maintains a constant anisotropy due to the assignment of $C_R = 1.0$, keeping the model and ILES profiles closely aligned, with the main deviation between the two profiles arising from the slight increase in the ILES anisotropy which cannot be reproduced by the model. For the unstrained case, the model which uses the original LRR-IP coefficients is also plotted, which shows a much faster trend to isotropy than is observed from the simulation. Using a value of

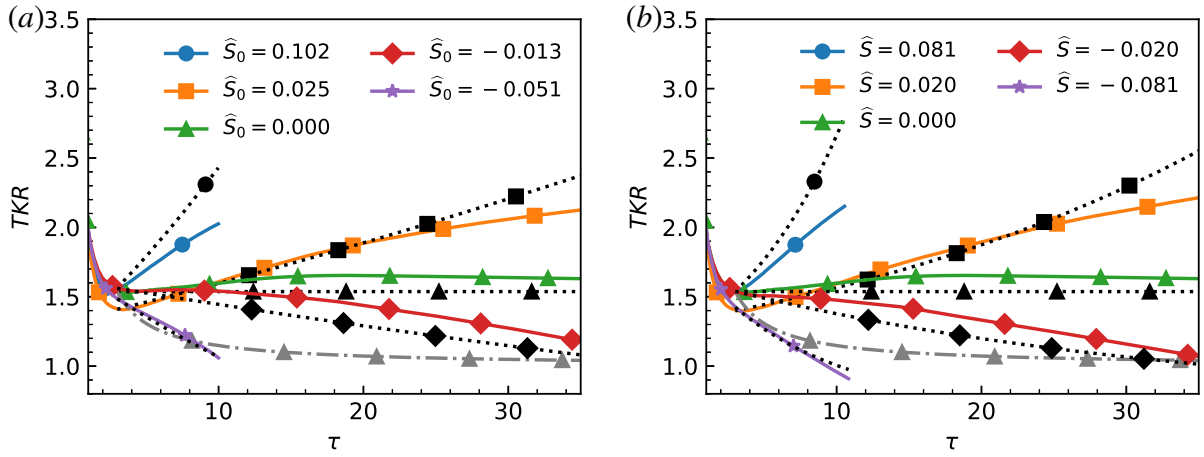

Figure 5.21: Anisotropy of the turbulent kinetic energy for (a) constant velocity and (b) constant strain rate. Solid lines indicate ILES, black dotted lines indicate the corrected turbulent kinetic energy model, and grey dot-dash lines indicate the turbulent kinetic energy model with the original LRR-IP coefficients.

$C_R = 1.8$ causes the anisotropy to exponentially decay towards the isotropic value of $TKR = 1$. The half-life of the anisotropy, that is the time required for the anisotropic deviation from unity to reduce by a factor of one-half, is around 2.5τ for the original coefficients of the LRR-IP model. The corrected turbulent kinetic energy model's anisotropy predictions for the strain cases shows reasonable agreement, with the anisotropy being driven by the shear production but is slightly counteracted by the isotropisation of production term in the model. The largest deviations between the model and ILES results occurs for the expansion cases, with the ILES showing reduced anisotropic growth, suggesting some tendency towards either isotropy or the original anisotropic value. The pressure-rate-of-strain modelling is simplified in its assumptions of zero total production and the treatment of the return to isotropy modelling, which is calibrated for the unstrained behaviour. For RMI, a more accurate model may involve a return to anisotropy approximation, causing the system to decay towards a specified anisotropy ratio of turbulent kinetic energy.

For the derived model, there is no inherent limitation on the domain for strain rates or expansion factors for validity. As the equations are based upon the physical transport equations, the models can be simplified in the rapid distortion limit to only consider the terms that are weighted by the strain rate. Comparison to experimental results for large strain rates or compressions may differ due to the introduction of physics not considered, such as equation of state and viscosity.

Spectra

For DNS cases where the flow field is completely resolved, the results are independent of the mesh and the numerical scheme used. In contrast, implicit large eddy simulations depend on numerical dissipation to stabilise the flow and dissipate the energy at the smallest scales. This numerical dissipation rate depends upon the numerical scheme and the grid resolution. Using an anisotropic mesh will affect the dissipation rate, and affects the size and orientation of the vortices that can be resolved. ILES should be converged for the largest scales of the flow, however the smaller scales will vary depending on the schemes used. This is demonstrated in the cross-code comparison of the θ-group collaboration for the standard case (Thornber *et al.*, 2017). The simulations conducted all converge to the same integral width, however, there is a large variance in the turbulent kinetic energy power spectra measured. In this regard, the simulations conducted are converged for the macro-properties reported, the anisotropic mesh does not affect these results. However, properties of the smaller scales which are not converged will have dependence. This can be observed by looking at the distribution of the turbulent kinetic energy across the scales of the domain, which is performed by using the radial power spectra of the transverse velocity components at the mixing layer centre. The one-dimensional radial power spectrum for the velocity component in direction i is calculated by

$$E_i(\kappa) = \widehat{\psi_i}^{\dagger}\widehat{\psi_i} \tag{5.55}$$

where $\widehat{(\ldots)}$ denotes the two-dimensional Fourier transform, the radial wave-number is given by $\kappa = \sqrt{\kappa_y^2 + \kappa_z^2}$, and the spectra is density weighted by using $\psi_i = \sqrt{\rho}u_i''$. The spectra of the velocities in the two transverse directions, E_y and E_z, are averaged to create the E_{yz} spectrum, as it is assumed the $y-z$ plane is isotropic. The resulting spectra are plotted in figure 5.22 for $\tau = 9.84$ and $\tau = 34.45$. It is evident that the compression cases have more turbulent kinetic energy in the transverse direction as $E_{yz}(\kappa)$ increases as the strain-rate decreases for all κ. As the wave-numbers are normalised by the mean wave-number of the initial perturbation spectrum, $\bar{k}$, the effect of the transverse strain-rate on the resolved spectrum can be observed. The maximum resolvable wave-number scales with the inverse of the expansion factor, increasing with time for compression and decreasing for the expansion. This effect can also be observed due to the change in the wave-number corresponding to the peak of the energy spectra. It should also be noted that the expansion cases are initially able to resolve to a higher wave-number due to the interpolation onto a finer mesh.

To determine the spectrum power-law, the spectrum data was fit to a single power law curve and to a segmented curve consisting of two power laws. To determine between the two models,

the Bayes information criterion (BIC) was used,

$$BIC = n\ln(\hat{\sigma}^2) + k\ln(n) \tag{5.56}$$

where n is the number of wave-number samples used for the fit, k is the number of parameters used in the model (two for linear and four for segmented), and $\hat{\sigma}^2$ is the mean-squared error between the spectrum data and the optimised model. To prevent over-fitting, the model with the lowest BIC should be chosen. As the BIC is weighted by both the mean-square error and the number of parameters, BIC aims to essentially select the model with the smallest error and least number of parameters required. The above equation is valid for cases where the residuals are normally distributed, which was found to be an accurate representation of the residuals observed. The range to fit over can change the results of the fit, as noted by Pfefferlé & Abarzhi (2020). The range used here is selected to be κ_l and κ_r given by,

$$\kappa_l = 4\kappa_{\text{E-max}} \quad \text{where} \quad \max(E_{yz}(\kappa)) = E_{yz}(\kappa_{\text{E-max}}) \tag{5.57a}$$

$$\kappa_r = \kappa_{\text{E-min}} \quad \text{where} \quad \min(E_{yz}(\kappa)) = E_{yz}(\kappa_{\text{E-min}}) \tag{5.57b}$$

The upper limit is usable in this form as FLAMENCO has non-negligible energy at the highest wave-numbers when performing ILES, whilst other codes show a regime akin to a dissipation range (Thornber *et al.*, 2017). The lower bound is taken to be a multiple of the wave-number with the highest energy, and this helps avoid the fitting at lower κ than the inertial range. The spectrum for the unstrained simulation was the only simulation that had a lower BIC for the single power law fit. The unstrained spectrum has a power law trend of -1.53 as reported in table 5.5. This value is close to the -3/2 value proposed for RMI (Zhou, 2001; Thornber *et al.*, 2010). The strain cases with the segmented fit show two different power laws, as listed in table 5.5. The first section of the inertial range is shallower than the -1.5 trend expected for RMI-induced mixing layers, instead ranging between -1.28 and -1.41 for the power law trend. The higher wave-number space requires a steeper fit, ranging between -1.84 and -2.26, clearly in excess of even the Kolmogorov power law of -5/3. It has been observed that for high-wave numbers in flows with shear strain that the energy spectra scales relative to κ^{-2} (Hunt & Carruthers, 1990). Whilst the power laws recorded here fluctuate away from these values, it is possible that the spectrums for the strain cases are a composition of the RMI and shear strain scaling laws.

Turbulent mass flux

In compressible flows, the turbulent mass flux, $a_i = \tilde{u}_i - \bar{u}_i = -\overline{u_i''}$, represents the difference between the mean and density weighted velocities. The turbulent mass flux is commonly used in

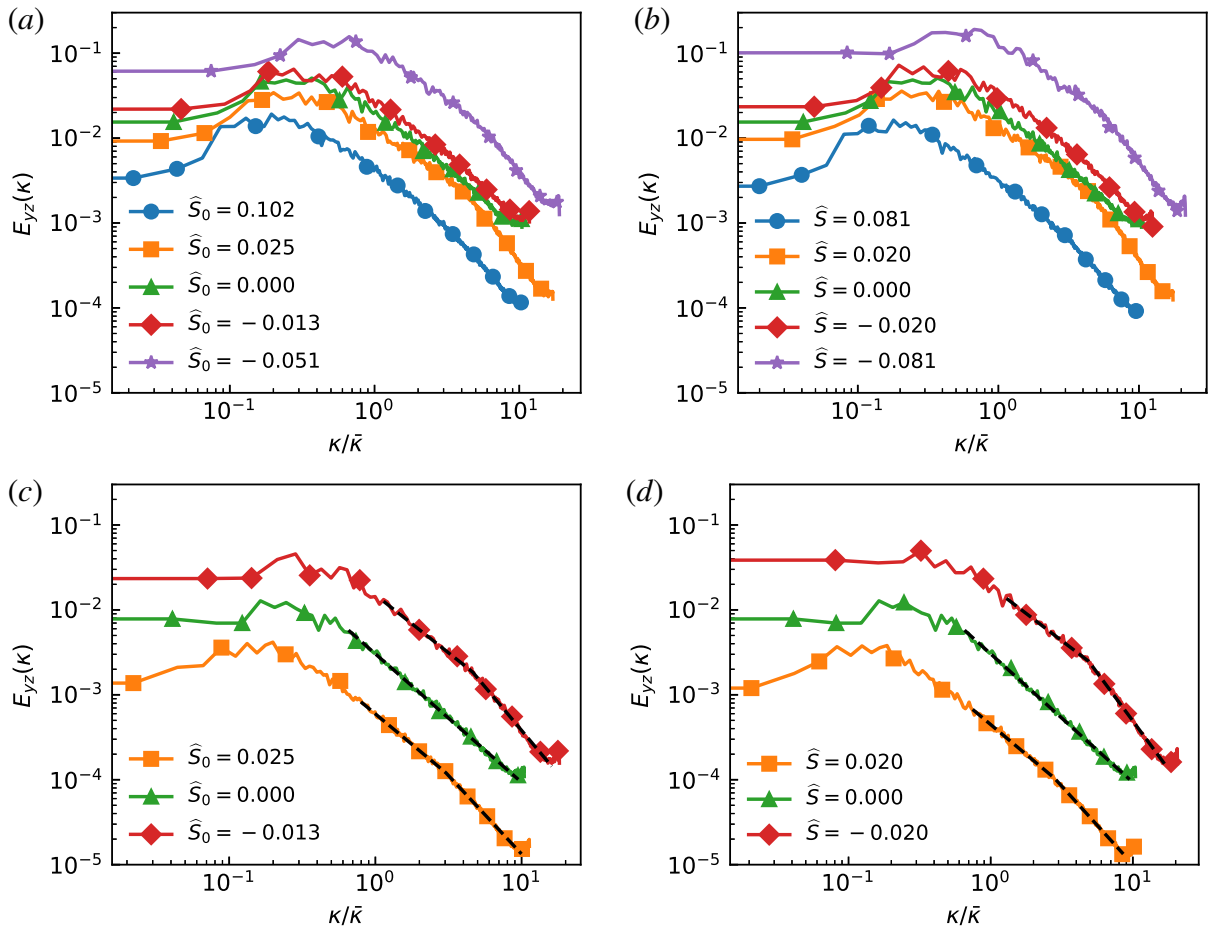

Figure 5.22: Spectrum for the transverse fluctuating turbulent kinetic energy component at the mixing layer centre for (a,c) constant velocity, and (b,d) constant strain-rate. (*a,b*) $\tau = 9.84$, (*c,d*) $\tau = 34.45$.

Strain Profile	$\hat{S}_0$	Power law 1	Power law 2
Unstrained	0.0	-1.51	-
Constant velocity	-0.013	-1.36	-2.05
Constant velocity	0.025	-1.44	-1.85
Constant strain-rate	-0.020	-1.28	-2.26
Constant strain-rate	0.020	-1.41	-1.84

Table 5.5: Power law scaling for the transverse turbulent kinetic energy spectra at $\tau = 34.45$

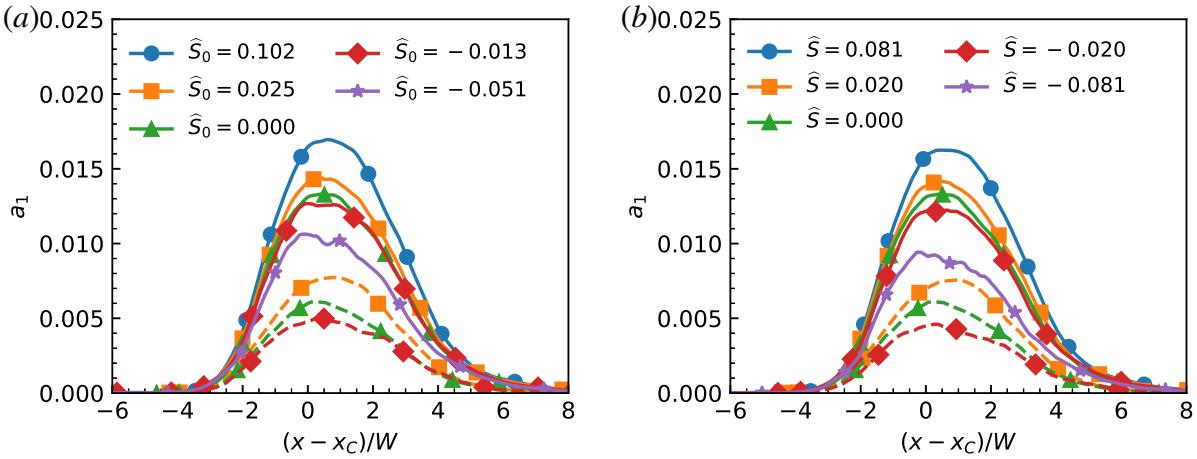

Figure 5.23: Turbulent mass flux for (a) constant velocity, and (b) constant strain rate. Solid lines indicate results at $\tau = 9.843$, dashed lines indicate results at $\tau = 34.451$.

closure of compressible Reynolds-averaged Navier-Stokes models, as the generation of turbulent kinetic energy (or the production of the Reynolds stresses) from potential energy is proportional to the turbulent mass flux. With the transverse velocity-gradients removed, the homogeneity of the y-z plane means that a_2 and a_3 should statistically be zero for the plane. The axial component, a_1 is not zero, and is plotted in figure 5.23 for all cases at $\tau = 9.843$ (solid lines), and for the unstrained and low-magnitude strain rate cases at $\tau = 34.451$ (dashed lines). The results show the compression cases have a decreased amount of axial turbulent mass flux compared to the unstrained case. The turbulent mass flux can be generated by a term equivalent to shear production,

$$\frac{\partial \bar{\rho} a_i}{\partial t} \propto -\bar{\rho} a_j \frac{\partial \bar{u}_i}{\partial x_j}, \tag{5.58}$$

and with the applied strain rates in the transverse direction, this term will act on components a_2 and a_3, not a_1. The components a_2 and a_3 will remain statistically zero, however the influence of the strain rate will affect the standard deviation/second moment of the u_i'' distribution, which is the turbulent kinetic energy and investigated in §5.4.3. Under axial strain rates, a_1 is amplified under compression as observed in Chapter 4, the opposite of the trend observed in figure 5.23. This decrease in a_1 matches the behaviour observed for TKX which decreased under compression due to the change in dissipation rate, showing that the effect of the modified turbulent length scale and dissipation rate is observable with the turbulent mass flux as well.

Enstrophy

The modelling of the pressure-dilatation tensor can be avoided by analysing the vorticity or enstrophy of the flow. The vorticity is defined by the curl of the velocity field,

$$\omega_i = \epsilon_{ijk}\frac{\partial u_k}{\partial x_j}. \tag{5.59}$$

For a compressible, viscous fluid, the transport equation for the vorticity components is given by Kida & Orszag (1990); Porter *et al.* (2015) as

$$\begin{aligned}\frac{\partial \omega_i}{\partial t} + \frac{\partial}{\partial x_j}\left(u_j\omega_i\right) = \omega_j\frac{\partial u_i}{\partial x_j} + \frac{\epsilon_{ijk}}{\rho^2}\frac{\partial \rho}{\partial x_j}\frac{\partial p}{\partial x_k} \\ + \frac{1}{Re_0}\left[\frac{1}{\rho}\frac{\partial^2\omega_i}{\partial x_j\partial x_j} - \frac{\epsilon_{ijk}}{\rho^2}\frac{\partial\rho}{\partial x_j}\left(\frac{\partial^2 u_k}{\partial x_l x_l} + \frac{1}{3}\frac{\partial^2 u_l}{\partial x_k \partial x_l}\right)\right].\end{aligned} \tag{5.60}$$

The domain integrated enstrophy components will be defined by integrating the density-weighted enstrophy over the domain,

$$\Omega_{ij} = \iiint \rho\omega_i\omega_j \,\mathrm{d}V. \tag{5.61}$$

For simplicity the notation of $\Omega_x = \Omega_{11}$ will be used for directional components, and $\Omega = \Omega_{ii}$ will be used to denote the total enstrophy respectively. The transport equation for the enstrophy components can be obtained by integrating the equation over the time-varying domain. It is also assumed that after $\tau = 1$, the pressure in the simulation is uniform in space and the baroclinic source term can be neglected. As the simulations were performed as ILES, the viscous effects were represented implicitly through the numerical scheme used to solve the flow (Grinstein *et al.*, 2007). As a result, the final term which is inversely proportional to the Reynolds number is replaced with a symbolic dissipation rate:

$$\frac{\mathrm{d}}{\mathrm{d}t}\begin{pmatrix}\Omega_x\\ \Omega_y\\ \Omega_z\end{pmatrix} = \begin{pmatrix}\Omega_x\frac{\partial\bar{u}_1}{\partial x_1}\\ \Omega_y\frac{\partial\bar{u}_2}{\partial x_2}\\ \Omega_z\frac{\partial\bar{u}_3}{\partial x_3}\end{pmatrix} - \begin{pmatrix}\Omega_x\\ \Omega_y\\ \Omega_z\end{pmatrix}\frac{\partial\bar{u}_i}{\partial x_i} - \varepsilon_\Omega \tag{5.62}$$

The source terms on the right-hand side correspond to the vortex stretching, vortex compression, and dissipation. The vortex stretching amplifies the vorticity in the direction of the strain rate, causing vortices to tilt towards the strained axis for expansion or away in the case of compression. The vortex compression term scales all vorticity components according to the mean compression rate. In the rapid distortion limit, the dissipation is neglected, as it occurs on a larger timescale than the strain (Hunt & Carruthers, 1990; Blaisdell *et al.*, 1996). The present simulations are

not in the rapid distortion limit, with the dissipation still playing a dominant role. In order to model the dissipation, the self-similar solution of the vorticity will be utilised. With a late-time power scaling of $\Omega \propto \tau^{-1.4}$ (Zhou *et al.*, 2020), then for the unstrained case the enstrophy and dissipation rate will be modelled according to

$$\Omega = \Omega_0 \left(\frac{\tau}{\tau_0} \right)^{-n}, \tag{5.63}$$

$$\varepsilon_\Omega = -\frac{d\Omega}{d\tau} = \frac{n}{\Omega_0^{1/n} \tau_0} \Omega^{(n+1)/n}. \tag{5.64}$$

The dissipation rate has been expressed in equation (5.64) as function of the current value of the enstrophy as opposed to a function of time, allowing the dissipation rate to maintain dependence or proportionality to the simultaneous enstrophy value. The dissipation rate also depends on a prescribed power law decay exponent and some initial conditions to scale it accordingly. Each enstrophy component is assumed to maintain this dissipation scaling, using the respective enstrophy component to calculate the corresponding dissipation rate. The model equation for the x- and y-component can be re-written, now using the dissipation model and substituting in the transverse strain rate, to take the form

$$\frac{\mathrm{d}}{\mathrm{d}\tau} \begin{pmatrix} \Omega_x \\ \\ \Omega_y \end{pmatrix} = \begin{pmatrix} 0 \\ \\ \Omega_y \hat{S} \end{pmatrix} - 2\hat{S} \begin{pmatrix} \Omega_x \\ \\ \Omega_y \end{pmatrix} - \frac{n}{\tau_0} \begin{pmatrix} \Omega_{x0}^{-1/n} \Omega_x^{(n+1)/n} \\ \\ \Omega_{y0}^{-1/n} \Omega_y^{(n+1)/n} \end{pmatrix}. \tag{5.65}$$

The results for this model are plotted in figure 5.24 for Ω_X and in figure 5.25 for Ω_Y. Whilst the unstrained and compression cases start from the same initial enstrophy values, the expansion cases have a higher initial value due to the interpolation on to the finer mesh. The interpolation process conserves the velocity components, ensuring the domain-integrated velocity and velocity derivatives are unchanged. The interpolation process however can steepen local gradient calculations, and as the enstrophy depends upon these gradients, the domain-integrated enstrophy is not conserved and will increase. For DNS, the flow field should be adequately resolved and smooth meaning that such effects are small under refinement, however for ILES the effect is observable in the flow-field following bulk refinement. The difference in the calculated enstrophy is larger for Ω_x which represents the enstrophy in the homogeneous y-z plane which was interpolated in both directions, whilst Ω_y represents the out-of-plane direction which includes the unchanged axial direction. Despite this, the trends of the enstrophy components is clear. The combination of the vortex stretching and vortex compression terms create a source term that linearly scales with the negative of the strain rate. It is observed in the plots that the expansion cases show a stronger decrease in enstrophy than the unstrained case, whilst the compression cases show a relative increase in the enstrophy components. For Ω_x, the compression cases

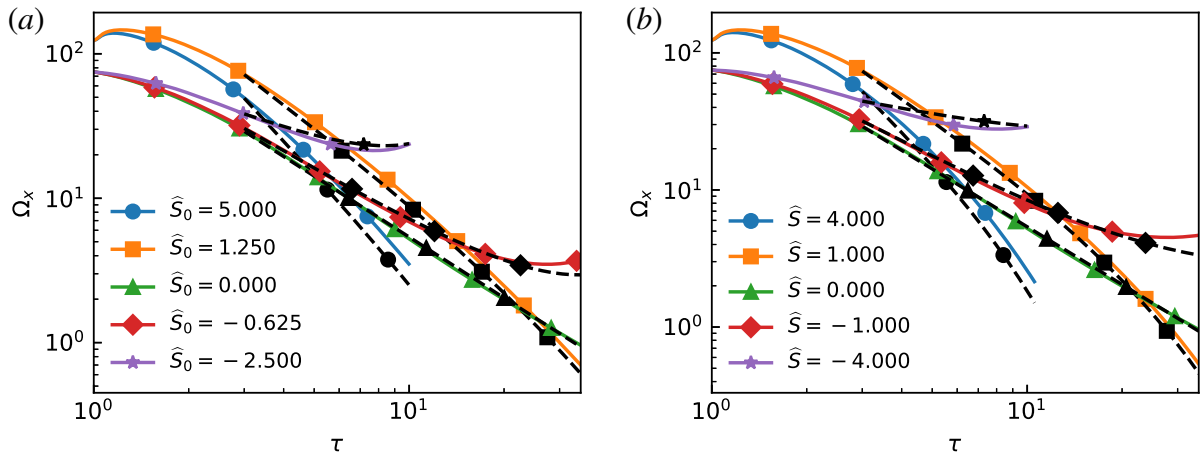

Figure 5.24: Enstrophy in the $y - z$ plane for (a) constant velocity and (b) constant strain rate. Solid lines indicate ILES, dashed lines indicate the enstrophy model.

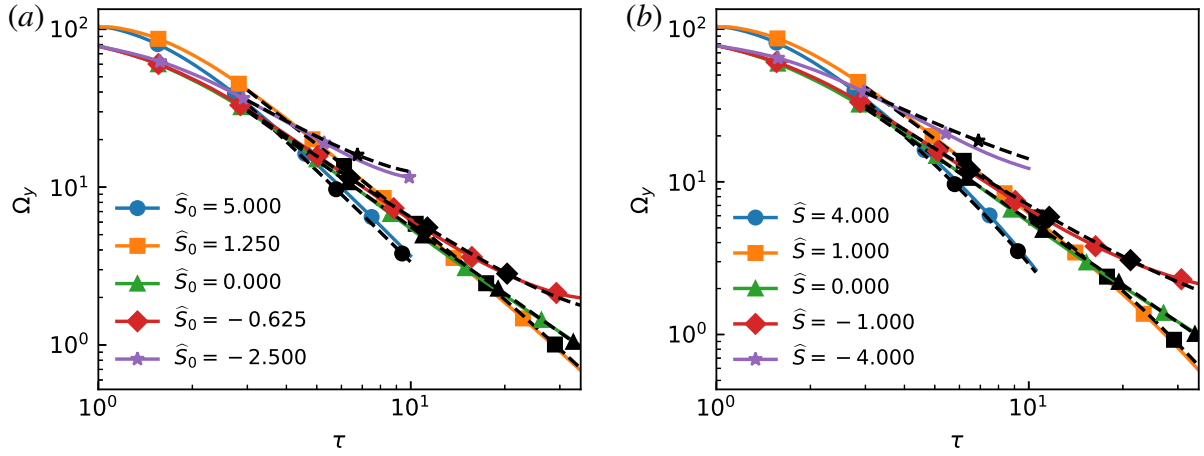

Figure 5.25: Enstrophy in the $x - z$ plane for (a) constant velocity and (b) constant strain rate. Solid lines indicate ILES, dashed lines indicate the enstrophy model.

even achieve a net production at the final simulation times. The model in the plots starts at $\tau = 3$, as after this time the unstrained case matches the self-similar decay profile, as show by the agreement with the model. The model accurately predicts the trends for the strain-simulation and doesn't require additional scaling for the dissipation rate, unlike the turbulent kinetic energy. The changes in Ω_x agree with the observation of increased mixedness within the mixing layer; higher vorticity in the y-z plane should correspond to greater mixing to achieve more in-plane homogeneity. The out-of-plane vorticity which corresponds to Ω_y would be expected to help move the two fluids through the mixing layer, however it does not appear to have a noticeable effect on the mean volume fraction profile of $\bar{f}_1$, and instead may just aid in the total mixedness. The change in enstrophy may serve as an indicator of the change in mixedness for the mixing layer. In contrast, the turbulent kinetic energy serves as a better indicator of the effects of how the strain rate affects the growth rate of the mixing layer.

Buoyancy-drag model

The computational cost of fully simulating and resolving turbulent mixing layers drives the necessity for simpler models that provide swift estimates of the mixing layer growth. One such model is the buoyancy-drag model, which uses coupled ordinary differential equations (ODEs) that can be solved with greater ease than partial differential equations. This methodology was inspired by the modelling of bubble penetration in the $At = 1$ case for RTI by Layzer (1955), however there have been many works trying to derive and calibrate the buoyancy-drag model to accurately represent the RMI and RTI for all Atwood numbers (Baker & Freeman, 1981; Dimonte, 2000; Hansom *et al.*, 1990; Oron *et al.*, 2001; Ramshaw, 1998). The simplicity of the buoyancy-drag model has also inspired other models, such as the K-L turbulence model (Dimonte & Tipton, 2006) which collapses to the buoyancy-drag model under a self-similar analysis. The most relevant buoyancy-drag model to the cases investigated here are the models calibrated to the quarter-scale θ-group case by Youngs & Thornber (2020*a*,*b*). The integral width, bubble height, and spike height are each governed by a pair of ODEs:

$$\frac{\mathrm{d}W}{\mathrm{d}t} = V, \qquad \frac{\mathrm{d}V}{\mathrm{d}t} = -\frac{V^2}{l^{\text{eff}}(\bar{\lambda}, W)}, \tag{5.66a}$$

$$\frac{\mathrm{d}h_b}{\mathrm{d}t} = V_b, \qquad \frac{\mathrm{d}V_b}{\mathrm{d}t} = -\frac{V_b^2}{l_b^{\text{eff}}(\bar{\lambda}, h_b)}, \tag{5.66b}$$

$$\frac{\mathrm{d}h_s}{\mathrm{d}t} = V_s, \qquad \frac{\mathrm{d}V_s}{\mathrm{d}t} = -\frac{V_s^2}{l_s^{\text{eff}}(\bar{\lambda}, h_b)}. \tag{5.66c}$$

The growth of the heights (W, h_b, h_s) is equal to the respective velocity component (V, V_b, V_s) in the unstrained buoyancy-drag model. As this model is calibrated for the RMI-induced mixing layer, the velocity ODE only contains a drag term, however for RTI flows a buoyancy term is also included. Youngs & Thornber (2020*b*) calibrated the effective drag length scale used in the drag term for the integral width to accurately predict the early-time growth. This analysis was extended to the bubble and spike heights in Youngs & Thornber (2020*a*). The drag length scales for each height are given by

$$\frac{l^{\text{eff}}}{\bar{\lambda}} = \max\left\{a - b\left(1 - e^{-cW/\bar{\lambda}}\right), \frac{\theta}{1-\theta}\left(\frac{W}{\bar{\lambda}} - d\right)\right\}, \tag{5.67a}$$

$$\frac{l_b^{\text{eff}}}{\bar{\lambda}} = \max\left\{a_b - b_s\left(1 - e^{-c_b h_b/\bar{\lambda}}\right), \frac{\theta}{1-\theta}\left(\frac{h_b}{\bar{\lambda}} - d_b\right)\right\}, \tag{5.67b}$$

$$\frac{l_s^{\text{eff}}}{\bar{\lambda}} = \max\left\{a_s - b_s\left(1 - e^{-c_s h_b/\bar{\lambda}}\right), \frac{\theta}{1-\theta}R\left(\frac{h_b}{\bar{\lambda}} - d_s\right).\right\} \tag{5.67c}$$

The effective length scale for each equation is a piece-wise function that transitions between a drag length scale dependent upon the spectrum perturbation to a drag length scale that scales

Table 5.6: Buoyancy-drag coefficients for $At = 0.5$, narrowband RMI (Youngs & Thornber, 2020*a*,*b*)

Lengthscale	a	b	c	d
Integral width	0.3	0.176	8.35	0.237
Bubble	0.7	0.297	6.0	0.283
Spike	1.4	1.19	0.8	0.70

linearly with the outer length scale. For the late-time growth, a theoretical power-law value of $\theta = 1/3$ was used, based upon the work of Elbaz & Shvarts (2018). It is important to note that the bubble and spike are expected to grow self-similarly, and so the drag terms for the spike height are calculated using the bubble height and a calibrated fit value of $R = 1.1$ for spike-to-bubble height to describe the asymptotic proportionality. The remaining coefficients of the drag length scale equations are listed in table 5.6, based off the values in the original works (Youngs & Thornber, 2020*a*,*b*). As the bubble and spike heights were calibrated to a slightly different case, the values of c_S and d_S are updated to provide a more accurate fit to the present unstrained model. For the simulation of alternative RMI configurations, such as changing the initial spectrum or Atwood number, alternative coefficients are necessary. This is evident as the cases considered in Youngs & Thornber (2020*a*) for $At = 0.5$ and $At = 0.9$ use different coefficients, different spike-to-bubble ratio R, and a different length scale function for the early time.

In the planar configuration, there is no variation in the mean wavelength used to calculate the effective drag length scale. For spherical geometry, Miles (2004, 2009) utilised the time-varying wavelength as the drag length scale, whilst El Rafei & Thornber (2020) calibrated a buoyancy-drag model by fitting the effective drag length scale as a function of the time-varying wavelength, $l^{\text{eff}}/\bar{\lambda}(t) = f(\bar{\lambda}(t), W/\bar{\lambda}(t))$. The effective drag length scale can be calculated from equation (5.66) using the form,

$$l^{\text{eff}} = -\frac{\dot{W}^2}{\ddot{W}}. \tag{5.68}$$

As this equation relies on the second derivative of the integral width measurements, it is inherently noisy. The noise in the profile was reduced through a down-sampling of the data. In figure 5.26, there are two variations of the effective drag length scale for the integral width plotted. The first is as a function of $W/\bar{\lambda}(t)$, denoted by the dotted lines, which corresponds to the approach used by El Rafei & Thornber (2020). For the strain-cases presented, the profiles do not collapse upon the unstrained case. The low-magnitude compression cases do show alignment with the

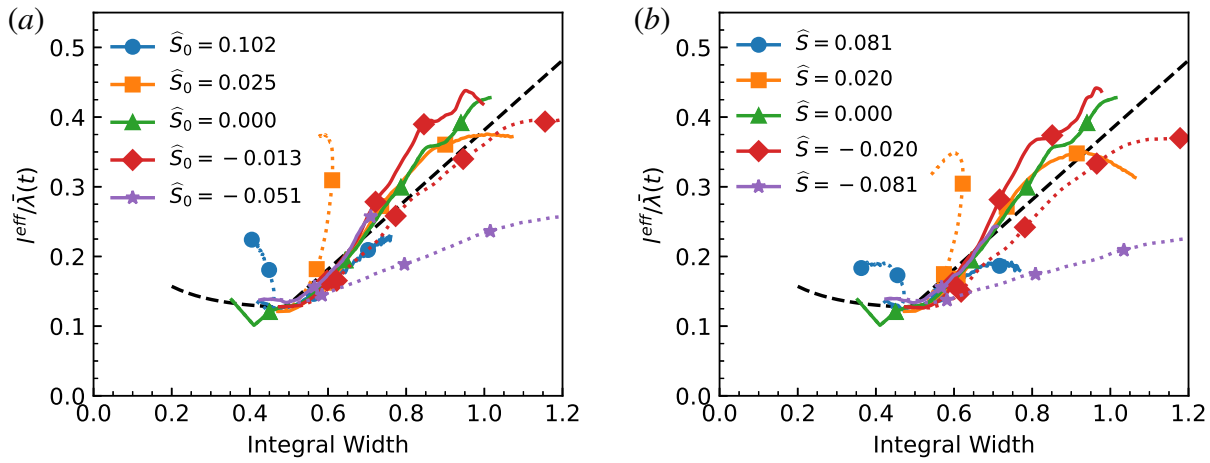

Figure 5.26: Effective drag length scale as a function of non-dimensionalised integral width for (*a*) constant velocity and (*b*) constant strain rate. Solid lines indicate integral width non-dimensionalised by $\bar{\lambda}_0$, dotted lines indicate integral width non-dimensionalised by $\bar{\lambda}(t)$, and dashed lines indicate planar narrowband effective length scale model.

unstrained model, and also possess a similar gradient to the unstrained case, as was observed by El Rafei & Thornber (2020). The effective drag length scale variation as a function of $W/\bar{\lambda}_0$ is denoted by the solid lines, which all fall within the vicinity of the unstrained model.

The collapse of the effective drag length scale profiles suggests the model to be used for the transverse strain cases should be function of $W/\bar{\lambda}_0$,

$$\frac{l^{\text{eff}}}{\bar{\lambda}(t)} = \max\left\{a - b\left(1 - e^{-cW/\bar{\lambda}_0}\right), \frac{\theta}{1-\theta}\left(\frac{W}{\bar{\lambda}_0} - d\right)\right\}. \tag{5.69}$$

In this form, the original effective drag length scale calculation is used, however the effective drag length scale is proportionally scaled to the time-varying wavelength.

To validate this model, the equations are integrated in time using the initial conditions provided in Youngs & Thornber (2020*a*). An offset of $\tau = 0.08$ is used to align the buoyancy-drag model with the simulations, as the buoyancy-drag model is fitted to the post-shock behaviour and does not describe the shock transition. The initial heights and velocities are given by

$$W_0 = 0.5642C\sigma_0, \tag{5.70a}$$

$$h_{s0} = h_{b0} = 1.1 \times 2.0C\sigma_0, \tag{5.70b}$$

$$V_0 = 0.5642C\bar{k}\sigma_0\Delta uAt \times F_W^{nl}, \tag{5.70c}$$

$$V_{b0} = 1.1 \times 2.0C\bar{k}\sigma_0\Delta uAt \times F_b^{nl}, \tag{5.70d}$$

$$V_{s0} = 1.1 \times 2.0C\bar{k}\sigma_0\Delta uAt \times F_s^{nl}, \tag{5.70e}$$

with compression factor $C = 0.576$, and non-linearity factors: $F_W^{nl} = 0.85$, $F_b^{nl} = 0.60$, and $F_s^{nl} = 1.0$. The solution for all cases are identical until $\tau = 1$, after which the transverse strain

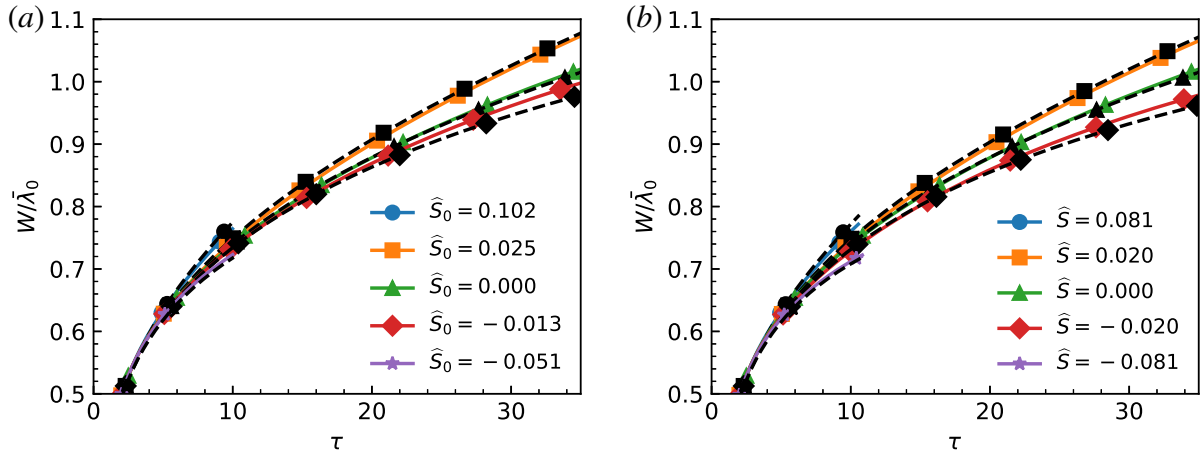

Figure 5.27: Buoyancy-drag model for integral width: (*a*) constant velocity and (*b*) constant strain rate. Solid lines indicate ILES results, dashed lines indicate the buoyancy-drag model.

rates will begin to change $\bar{\lambda}(t)$ and the effective drag length scale. The results for integral width are plotted in figure 5.27, and the buoyancy-drag model shows good alignment for all cases except for the weak compression cases. This trend is also observed for bubble heights in figure 5.28 and the spike heights in figure 5.29. The increased growth for the weak compression cases could be a result of the redistribution of the turbulent kinetic energy from the transverse direction to the axial direction, which is causing some additional growth for these components. Such behaviour could be accounted for by including additional terms in the drag length scale that would correspond to the shear production terms, as was done in Chapter 4. The modification to the drag length scales also implies that the self-similar growth rate is permanently modified after the period of strain. For a constant value of Λ, using equation (5.69) permits a power-law growth rate of the form $W \propto t^{\hat{\theta}}$ for RMI, where the new growth rate is given by,

$$\hat{\theta} = \theta \frac{\Lambda}{\theta(\Lambda - 1) + 1}, \tag{5.71}$$

whereby $\hat{\theta}$ decreases for transverse compression ($\Lambda < 1$), and increases for expansion ($\Lambda > 1$).

5.5 Conclusion

The influence of transverse strain rates on the Richtmyer–Meshkov instability, or more generally for anisotropic, inhomogeneous mixing-layers, has been investigated by applying transverse strain rates to simulations in planar geometry. Within the linear regime, a linearised potential flow model was derived to predict how the application of the transverse strain rate would affect the initial RMI perturbation growth. Using the strain rate framework, the solution obtained was found to be equivalent to the Bell–Plesset results, meaning that strained planar simulations can

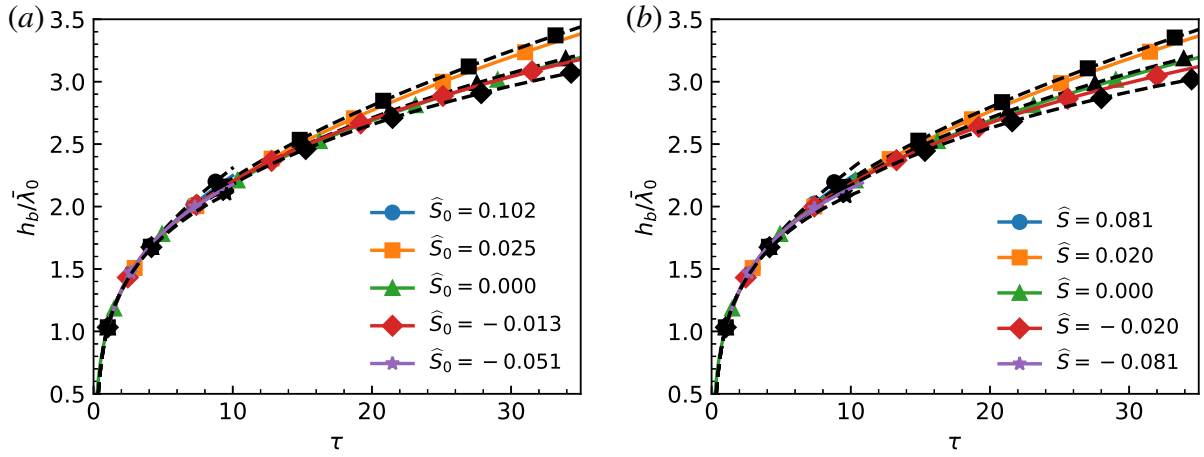

Figure 5.28: Buoyancy-drag model for bubble height: (*a*) constant velocity and (*b*) constant strain rate. Solid lines indicate ILES results, dashed lines indicate the buoyancy-drag model.

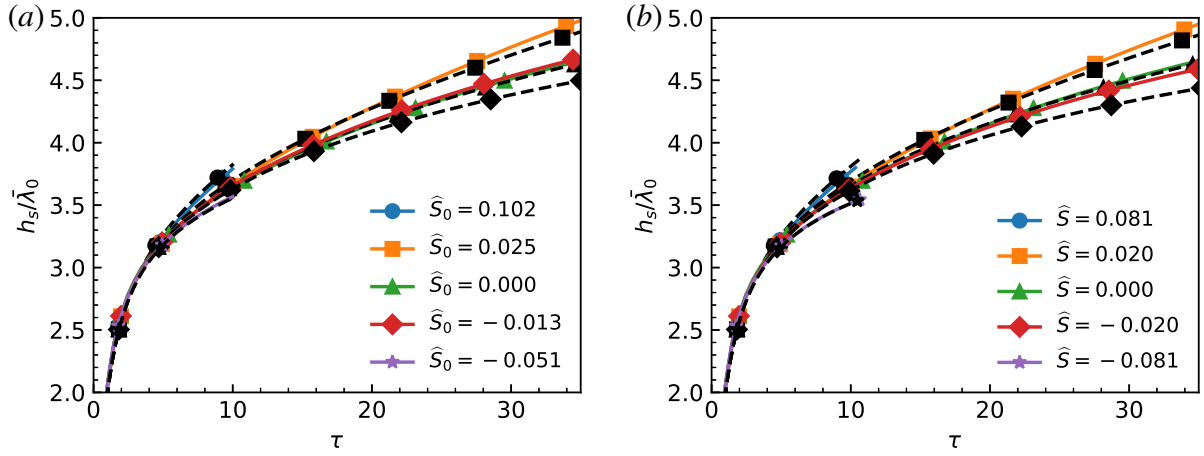

Figure 5.29: Buoyancy-drag model for spike height. (*a*) constant velocity and (*b*) constant strain rate. Solid lines indicate ILES results, dashed lines indicate the buoyancy-drag model.

replicate the behaviour of convergent simulations in the linear regime. Resolved two-dimensional numerical simulations were conducted in planar geometry, applying expansive or compressive strain rates. The simulations and model showed agreement while the amplitude was smaller than the time-varying wavelength, $a < 0.1\lambda(t)$, with compressive strain rates amplifying the instability growth-rate whilst expansive strain rates inhibit the growth.

To investigate the effects of transverse strain rates in the transitional and self-similar regime, strained simulations were conducted using the quarter-scale θ-group case as the initial conditions. These implicit large eddy simulations were initialised at $\tau = 1$ from the original case, a multimode narrowband RMI-induced mixing layer. Unlike the linear regime, the ILES results show that the compressive strain rates cause the mixing layer to have a slightly decreased growth rate, whilst the expansion cases grow slightly faster. This change in growth rate is explained by the modification of the turbulent length scale with the applied strain rates. Whilst shear-production

from the mean velocity gradients will generate turbulent kinetic energy in the transverse direction under compressive strain rates, the turbulent length scale will decrease, increasing the dissipation rate inside the mixing layer. As a result, the axial turbulent kinetic energy will slightly decrease under compression as the increased dissipation rate will counteract the energy redistribution, and the mixing layer will attain a slightly decreased growth rate. This was further investigated by comparing the effective drag length scale for a Buoyancy-Drag model, showing that the effective drag length scale is best captured by linearly scaling the effective drag length scale with the time-varying mean wavelength, $l^{eff} = \bar{\lambda}(t) f(\bar{\lambda}_0, W)$.

The shear-production effect from the strain rate was observed to increase the transverse turbulent kinetic energy, albeit by a reduced amount due to the counteracting dissipation rate modification. This increase in transverse turbulent kinetic energy caused the mixing layer to no longer attain the same asymptotic self-similar state as the unstrained case. The anisotropy of the turbulent kinetic energy increased for expansion cases. The compression cases instead head towards isotropy, with some cases achieving greater turbulent kinetic energy in the transverse direction. The mixedness of the mixing layer was also affected, with the compression cases attaining higher levels of mixedness whilst the expansion cases became less mixed. These changes in mixedness are correlated with the changes in the turbulent kinetic energy and enstrophy.

CHAPTER 6

Turbulence modelling of anisotropic strain

6.1 Introduction

Reynolds-Averaged Navier-Stokes (RANS) models are an important tool used to predict the behaviour of hydrodynamic instabilities at a fraction of the cost of large-eddy simulation (LES) and direct numerical simulation (DNS). For practical problems such as astrophysical flows and ICF, it can be computationally intractable to completely resolve the complete range of length and time scales involved, driving the necessity for simplified models. For compressible turbulent mixing layers, Besnard *et al.* (1992) presented a comprehensive derivation of the Favre-averaged equations for variable-density turbulence. In Besnard *et al.* (1992), both a Reynolds stress model and a simpler three equation model were provided, forming the basis of the BHR model. Both models included an evolution equation for the turbulent kinetic energy dissipation rate (ϵ). Using the dissipation rate is a popular choice in other fields, given the prominence of the k-ϵ turbulence model Jones & Launder (1972); Launder & Spalding (1974); Wilcox (2006), and several other turbulence models designed for compressible turbulent mixing layers have also used the turbulent dissipation rate Grégoire *et al.* (2005); Morán-López & Schilling (2014); Morán-López *et al.* (2015). Whilst there is an equivalence between the transport equations, an alternative approach is to transport the turbulent length scale, as recommended in Besnard *et al.* (1992) and implemented by Dimonte & Tipton (2006) for the K-L model. For interfacial instabilities such as RTI and RMI, the initial turbulent length scale has a greater physical meaning than an initial dissipation rate, and also allows for easier self-similarity analysis at late-time where the turbulent length scale is assumed to be proportional to the mixing layer width. Improvements have been made to the K-L model to improve performance, through self-similarity analysis (Morgan & Greenough, 2016; Xiao *et al.*, 2020*b*,*a*; Zhang *et al.*, 2020), improved treatment of buoyancy production for the turbulent kinetic energy (Kokkinakis *et al.*, 2015), and realisability of the modelled Reynolds

stress (Kokkinakis *et al.*, 2020; Xiao *et al.*, 2021). Further developments to the BHR model and K-L model have occurred through the introduction of additional transport equations, resulting in a multitude of different models (Morgan & Wickett, 2015; Morgan *et al.*, 2018*a*,*b*; Morgan, 2021, 2022; Morgan *et al.*, 2023; Banerjee *et al.*, 2010; Denissen *et al.*, 2012; Schwarzkopf *et al.*, 2016; Braun & Gore, 2021). One of the lesser analysed components of the closure for the RANS models is the effect of bulk compression. The recommended modification by Reynolds (Reynolds, 1980, 1987) for the dissipation rate based upon isotropic compression in the rapid distortion regime for homogenous turbulence is equivalent to the term by Dimonte & Tipton (2006) for the turbulent length scale derived for conservation of mass of an eddy under isotropic compression (Morel & Mansour, 1982). Investigating isotropic compression of homogenous turbulence for sudden viscous dissipation, Campos & Morgan (2019) used the same expression for bulk compression but found it necessary to introduce a variable viscosity term in the length scale transport equation to align with DNS results. As noted previously, in practical applications, turbulent mixing layers are neither homogenous nor experiencing isotropic strain.

The goal of this chapter is to quantify the ability of the K-L turbulence model to capture the characteristics of turbulent mixing layers under anisotropic strain rates and propose an improved model formulation. The work focuses on the bulk compression term for the scaling of the turbulent length scale under strain. Section 6.2 introduces the equations of the K-L model, the method used to apply the uniform strain rates to the simulation domain, and the simulation cases conducted. In Sec. 6.3, the performance of the K-L model with different scaling approaches is presented, showing results for the integral width and the domain integrated turbulent kinetic energy. Further insight into the K-L model is obtained by performing a self-similar analysis of the K-L model to reduce it down to a buoyancy-drag model.

6.2 Computational Approach

6.2.1 Strain rates

In order to analyse the influence of the strain rates on the development of the turbulent mixing layer, it is necessary to quantify and control the strain rate. The application of uniform normal strain rates are achieved by applying mean velocity gradients to the simulation domain and moving the domain bounds with the specified strain rates, using boundary conditions which preserve the linear velocity profile. For planar geometry, the strain rates are considered separately in the axial direction ($\bar{S}_A$), representing strain rates in the direction of mixing for the inhomogeneous turbulent mixing layer, and in the transverse direction ($\bar{S}_T$), corresponding to strain rates in the

directions of the homogeneous plane.

$$\bar{S}_A = \frac{\partial \bar{u}_1}{\partial x_1} \tag{6.1}$$

$$\bar{S}_T = \frac{\partial \bar{u}_2}{\partial x_2} = \frac{\partial \bar{u}_3}{\partial x_3} \tag{6.2}$$

A combination of axial and transverse strain is possible, such as for isotropy ($\bar{S}_A = \bar{S}_T$) or for bulk incompressibility with zero divergence ($\bar{S}_A + 2\bar{S}_T = 0$).

The strain profiles, constant velocity and constant strain rate, are detailed in §3.2.6, along with the definition of the strain non-dimensionalisation.

6.2.2 Governing Equations

The simulations conducted use the K-L model, a two-equation RANS model that achieves closure by introducing transport equations for the turbulent length scale L and turbulent kinetic energy $\tilde{K} = \widetilde{u_i'' u_i''}/2$. The K-L governing equations are detailed in §3.1.3. The choice of coefficients will be discussed in Sec. 6.2.4.

6.2.3 Numerical Implementation

The K-L model is implemented into FLAMENCO using the numerical methods detailed in §3.2.

6.2.4 Problem Description

To investigate the capability of the K-L model to capture the effects of the uniform strain rates on the development of the turbulent mixing layer, one-dimensional RANS simulations are conducted with applied mean strain rates. The implicit large eddy simulations of the previous chapters were conducted to analyse the effects of the normal strain rates on the development of the Richtmyer-Meshkov induced mixing layer. These simulations were based upon the quarter-scale θ-group case (Thornber *et al.*, 2017) which simulated a narrowband multimode Richtmyer-Meshkov instability with a $Ma = 1.8439$ shock-wave initialising the instability in a heavy-to-light configuration, conducted at $At = 0.5$ with an ideal gas equation of state for the fluids. The strained simulations were conducted separately for axial strain rates in Chapter 4, and transverse strain rates in Chapter 5. At a time of $\tau = 1$, while the mixing layer is transitioning to turbulence, the strain rates are applied by modifying the velocity profile to achieve the desired velocity gradient, and the domain begins to move with the specified profile to capture the strain and preserve the velocity gradients.

Table 6.1: Properties of the implicit large eddy simulation cases. Simulations cases exist for *D*=A for the axial strain cases, and *D*=T for the transverse cases.

		Strain rate		
Label	Strain profile	$\bar{S}\ (s^{-1})$	$\hat{S}$	Final τ
S0	Unstrained	0.0	0.0	35
*D*CV-2	Constant Velocity	-2.5	-0.051	10
*D*CV-1	Constant Velocity	-0.625	-0.013	35
*D*CV$+1$	Constant Velocity	1.25	0.025	35
*D*CV$+2$	Constant Velocity	5.0	0.102	10
*D*CS-2	Constant Strain	-4.00	-0.081	10
*D*CS-1	Constant Strain	-1.00	-0.020	35
*D*CS$+1$	Constant Strain	1.00	0.020	35
*D*CS$+2$	Constant Strain	4.00	0.081	10

The RANS simulation cases are based on the ILES data in Chapters 4 and 5. The ILES cases consist of an axial strain subset with eight strain cases, and a transverse strain subset with eight cases. These strain subsets use the same strain rate and strain profile combinations for the axial and transverse strain applications. Each case is labelled according to the strain direction, strain profile, and relative strain rate: $D\mathrm{C}X \pm n$, where D indicates direction (A for axial and T for transverse, CX indicates the strain profile (CV for constant velocity and CS for constant strain rate), and $\pm n$ indicates the ranked magnitude of the applied strain rate ($+n$ is expansive, $-n$ is compressive, larger n is larger magnitude strain rate). The specific strain rates for each case and the simulation run time are listed in Table 6.1. Visualisations of the ILES constant strain rate cases at the final simulation time are presented in Fig. 6.1 as two-dimensional slices. The figures are centred on the mixing layer and use the same scale across all plots, showing different domains widths for the transverse strain cases and different mixing layer heights for the axial strain cases due to the effects of the strain.

Whilst the ILES cases are three-dimensional, the homogeneity of the y–z planes allows the RANS simulations to be conducted as one-dimensional, using a mesh of 720 cells in the x-direction. The domain is initialised using the planar-averages of the initial conditions for the quarter-scale θ-group case. The fluids are set up in a heavy-to-light configuration with densities of 3 kg m^{-3} and 1 kg m^{-3} to achieve a 0.5 Atwood number. The shocked heavy fluid is initialised for $x < 3.5$ m using a $Ma = 1.8439$ shock for a pressure ratio of four. The interface between the two fluids is located at $x_0 = 3.5$ m with a diffuse error function profile. As the mean profile is applied, the diffusive thickness of the initial interface is taken to use the standard deviation

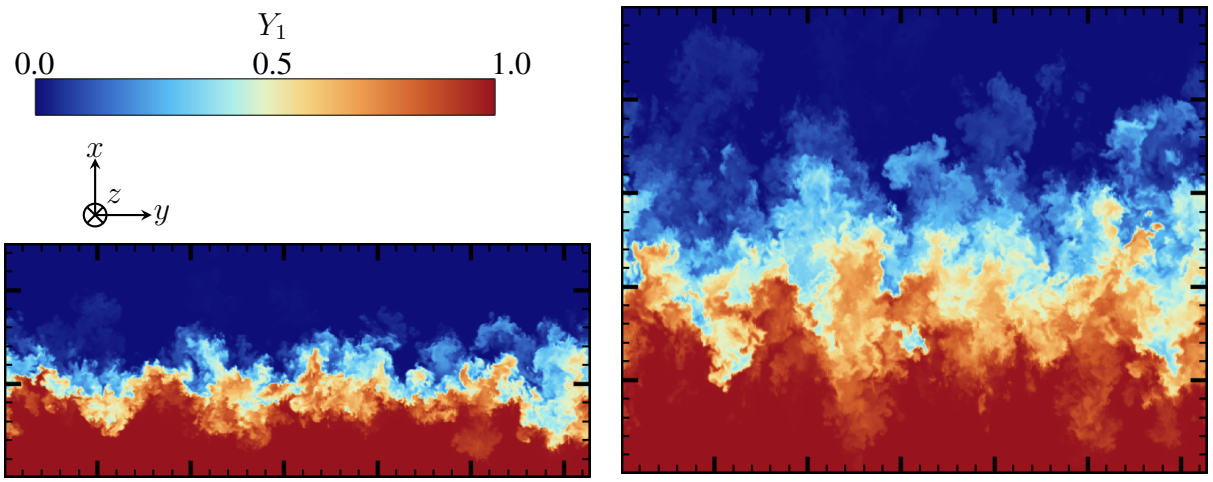

(a) Axial compression (ACS-1)

(b) Axial expansion (ACS+1)

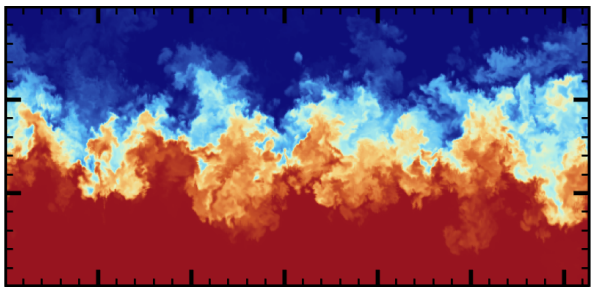

(c) Unstrained (S0)

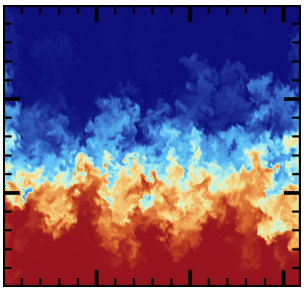

(d) Transverse compression (TCS-1)

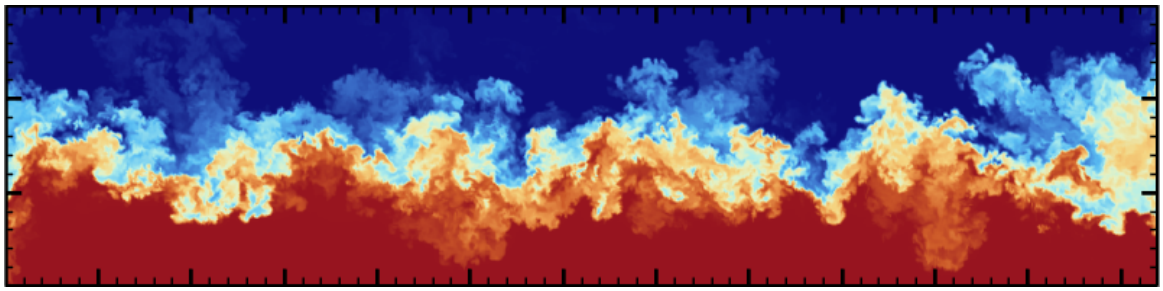

(e) Transverse expansion (TCS+1)

Figure 6.1: Contours of the mass fraction of species 1 at $\tau = 34.5$ along the centre-plane from the ILES constant strain rate cases. Major ticks indicate a distance of 1 m.

of the ILES perturbation spectrum as opposed to the original diffuse thickness. The volume fraction profile used to initialise the mass fraction profile is

$$\bar{f}_1(x) = \frac{1}{2}\left(1 - \operatorname{erf}\left(\frac{x - x_0}{\sqrt{2}\sigma_0}\right)\right). \tag{6.3}$$

The standard deviation σ_0 is $0.1\lambda_{\text{min}}$, where the initial perturbation wavelengths ranged between $2\pi/32$ and $2\pi/16$. The initial turbulent kinetic energy is set to a nominal value of $\tilde{K} = 1 \times 10^{-40}\text{m}^2\,\text{s}^{-2}$ throughout the domain, whilst the initial turbulent length scale is calibrated to reproduce the integral width of the unstrained ILES case, i.e. the original quarter-scale θ-group simulation. The details of the turbulent length scale are further discussed below. Both fluids use an ideal gas equation of state with $\gamma = 5/3$ and have an unshocked pressure of 100 kPa. The

whole domain has an initial velocity offset of $u_1 = -291.575\,\mathrm{m\,s^{-1}}$ to counteract the velocity shift from the interface-shock interaction, making the post-shock interface stationary. At the non-dimensional time $\tau = 1$, the strain is applied to the simulation domain, just as was performed with the ILES cases.

The K-L model in its current form is not capable of effectively capturing the growth rate of the mixing layer at all stages. Instead, the focus during model calibration is on predicting the late-time growth rate for the mixing layers. By calibrating the initial conditions of the K-L model to match the late-time integral width for the unstrained case, the RANS results are not aligned during the linear or transitional regimes. Improved alignment of results in these regimes may be possible with the introduction of an intermittency factor, which serves to quantify the local transition to turbulence and correspondingly limit the turbulent viscosity (Xie *et al.*, 2025). The utilisation of the RANS model at early time may also conflict with the requirement of the spectral gap. For unsteady flow which consists of low-frequency deterministic unsteadiness and turbulent fluctuations, it is necessary to have a separation of scales between the regimes (Sandberg & Zhao, 2022). If the two regimes overlap then the Reynolds-averaging is inaccurate, as it can not account for the interactions between the turbulence and deterministic unsteadiness. For RMI, and many other instabilities, the initial growth rate is deterministic and follows linear theory. After sufficient growth and development of secondary instabilities, the modes are no longer deterministic, developing into a turbulent mixing layer. For the narrowband initialisation considered, the turbulent mixing layer arises from the interaction of the initial high wavelength modes. The period in which there is a potential overlap is therefore limited to the transitional regime, whereas before the flow is deterministic and after it is turbulent. For cases with low-mode perturbations that take much longer to become turbulent, such as broadband spectra or the inverse chevron, the deterministic unsteadiness will remain for a greater duration.

Using the K-L model coefficients posited in Xiao *et al.* (2020*a*); Zhang *et al.* (2020), it is possible to capture the integral width of the unstrained case at late time, however the turbulent kinetic energy results are out by an order of magnitude. To provide a better comparison with the ILES data, the coefficients of the model were re-calculated so that both the integral width and turbulent kinetic energy results are aligned for the unstrained simulations. The coefficients used for the simulations in the present study are listed in Table 6.2, which were derived using the same methodology laid out in the aforementioned articles. The calibrating coefficient of α, which scales the Rayleigh-Taylor growth, was adjusted from the default value of 0.05 to 0.01 to improve the turbulent kinetic energy calculation. This is a smaller value than $\alpha = 0.025$, which is the observed coefficient for narrowband RTI simulations. The ability of the K-L model to capture the

Table 6.2: Coefficients for the K-L turbulence model. Previous coefficients come from Xiao *et al.* (2020*a*); Zhang *et al.* (2020)

Model	C_A	C_B	C_D	C_L	C_P	C_μ	N_H	N_K	N_L	N_Y
Previous	11.2	0.76	0.2	0.19	2/3	1.19	0.35	0.43	0.04	0.35
Current	5.01	0.34	0.2	0.19	2/3	1.19	1.74	2.14	0.19	1.74

influence of the strain rate on the RMI-induced mixing layer is not affected by this recalibration, as simulations conducted with the original coefficients of Xiao *et al.* (2020*a*); Zhang *et al.* (2020) demonstrated the same trends as observed in the results presented here-within. The choice of coefficients employed simply allow the turbulent kinetic energy comparison between the ILES and RANS results to be conducted more easily as the unstrained profiles are calibrated to be aligned.

6.2.5 Bulk compression closure

In the prescribed model, there are two coefficients which are not determined from the self-similarity analysis. The first is C_P, which is the contribution of the turbulent kinetic energy to the Reynolds stress components. The second term is the coefficient for the bulk compression of the turbulent length scale, C_C. The value of this term is typically $1/3$ under the assumption of conservation of mass in an eddy under isotropic compression (Dimonte & Tipton, 2006). If the mass inside the eddy is given by ρL^3, then for isotropic compression

$$\frac{dL}{dt} = \frac{1}{3} L \frac{\partial u_k}{\partial x_k}. \tag{6.4}$$

More generally, this approach will evolve the turbulent length scale according to the mean strain rate of the local flow field. In contrast, the multi-fluid model of Andrews (1992) scales the length scale with the negative of the strain tensor magnitude, whilst the multi-fluid of Youngs (1994) scales with the divergence but also considers the direction of the strain, using the strain in the direction of mixing as determined by the gradient of the species' volume or mass fraction. In the cases where the expansion/compression only occurs in n dimensions, Morel & Mansour (1982) consider the conservation of ρL^n instead. The resulting evolution of the length scale is

$$\frac{\mathrm{d}L}{\mathrm{d}t} = \frac{1}{n} L \frac{\partial u_k}{\partial u_k}. \tag{6.5}$$

Under anisotropic strain rates, length scales in different directions will vary depending upon the strain rate that is aligned with the length scale. Considering the axial and transverse strain rates, each strain rate will modify the corresponding length scale. From this, two alternative

Table 6.3: The $\hat{C}_C$ coefficients for the different bulk compression closures under different applied strain rates, representing the equivalent C_C coefficient/scaling of the velocity divergence for the specified applied strain rates.

	Applied strain rate		
Length scale closure	Axial strain	Isotropic strain	Transverse strain
Axial, S_A	1	1/3	0
Isotropic, S_I	1/3	1/3	1/3
Transverse, S_T	0	1/3	1/2

closures for the bulk compression term are introduced, which use either the axial strain rate or the transverse strain rate:

$$\frac{dL}{dt} = L\frac{\partial u_1}{\partial x_1} = LS_A, \tag{6.6}$$

$$\frac{dL}{dt} = L\frac{1}{2}\left(\frac{\partial u_2}{\partial x_2} + \frac{\partial u_3}{\partial x_3}\right) = LS_T. \tag{6.7}$$

Using the approach of Morel & Mansour (1982), the axial closure would be obtained if only axial strain was expected, whilst the transverse closure would be obtained under transverse strain.

These alternative closures for the bulk compression of the turbulent length scale can also be considered as using different C_C coefficients for the different cases. An equivalent C_C coefficient can be calculated for each type of strain application,

$$\hat{C}_C\frac{\partial u_k}{\partial x_k} = S_\phi \tag{6.8}$$

where S_ϕ represents the desired closure strain rate (S_A, S_T, or $S_I = \nabla \cdot u/3$), and $\hat{C}_C$ is the equivalent coefficient. These coefficients are given in Table 6.3. For isotropic strain rates, all three closures will reduce to the same scaling, as the mean strain rate is equivalent to the strain rate in any direction. Under pure axial strain, the transverse strain rate closure reduces $\hat{C}_C$ to zero as the bulk compression term will not activate, whilst the axial strain closure increases the coefficient to unity. The equivalent coefficients assume that the term only activates under bulk compression/expansion, however the utilisation of Favre averaged velocities in the divergence means that it is affected by the mixing of fluids at different densities.

Given the possibility of the axial, isotropic or transverse strain closure, the simulation cases listed in Table 6.1 were conducted for each closure, providing three sets of RANS data. The effect of the different approaches manifests in the initialisation of the flow variables in the domain. A common approach to initialising the interface for RMI is to apply a non-negligible L at the cells adjacent to the interface and zero elsewhere, whilst $\tilde{K}$ is set to a negligible value

Table 6.4: Values of L used for simulation initialisation

Axial closure	Isotropic closure	Transverse closure
0.515m	0.51m	0.50m

everywhere. When the shock interacts with the interface, the buoyancy production term will activate, generating turbulent kinetic energy at the interface. The amount of turbulent kinetic energy deposited, and the resulting growth rate, will depend on the initial value of L. The bulk compression term will also activate due to the velocity gradient across the shock, and as a result different initial L values are required under the different scaling schemes, as shown in Table 6.4. As the shock is compressive and acts in the axial direction, the axial strain closure simulations require a larger initial L value to counteract the resulting bulk compression of L and achieve the same post-shock growth rate prior to the application of strain. The listed values of L are obtained by calibrating the initial L value in the cells on either side of the interface to predict the unstrained growth rate. Outside the cells neighbouring the interface, the value of $L_0 = 1 \times 10^{-16}$ m is used.

6.3 Results and Discussion

6.3.1 Integral Width

The mixing layer width is measured here using the integral width, which is based upon the mean volume fraction profile,

$$W = \int \bar{f}_1 \bar{f}_2 dx. \tag{6.9}$$

The original ILES cases were conducted using the five-equation model of Allaire *et al.* (2002), which includes a transport equation for the volume fraction of each species. As the K-L model only transports the mean mass fraction, the volume fraction is calculated assuming equal temperature and pressure within the cell, allowing the volume fraction of species 1 to be calculated by

$$\bar{f}_1 = \frac{\tilde{Y}_1/W_1}{\sum_a \tilde{Y}_a/W_a}. \tag{6.10}$$

The molecular mass, W_a, of each species is $90\,\mathrm{g\,mol^{-1}}$ and $30\,\mathrm{g\,mol^{-1}}$ respectively, inline with the initial density ratio between the fluids. The integral width results for the simulations with axial strain rates applied are shown in Fig. 6.2 for the three K-L models and the ILES results. The

influence of the axial strain rate on the integral width demonstrates an increased integral width for expansive strain rates, as the velocity difference across the mixing layer causes the mixing layer to stretch/compress for positive/negative strain rates (Ge *et al.*, 2022). The K-L models are unable to capture the early-time growth of the mixing layer as the models are designed for late-time self-similar growth, and as a result are not well-designed for the transitional regime. Despite the underestimation of the mixing layer growth rate in the early time, the K-L models show the same increased growth rate under expansion strain as observed in the ILES. This stretching/compression effect arises from the velocity difference in the mean flow field, which is resolved by the simulation, allowing the simulations to capture this direct effect of the axial strain rate. The variation between the different bulk compression closure approaches arises from the turbulent growth which is dependent upon the turbulent viscosity, which is proportional to L and $\tilde{K}^{1/2}$. The value of L is modified by the bulk compression term, with greater variation of L under strain for configurations with larger $\hat{C}_C$ values. This effect on the mixing layer is evident as the axial strain closure with the applied axial strain ($\hat{C}_C = 1$) will have the largest modification of L from the bulk compression term, and is observed to overestimate the influence of the strain rates on the mixing layer. The model with the best performance, most accurately capturing the turbulent growth, is the transverse strain closure implementation with $\hat{C}_C = 0$, which is not modifying the turbulent length scale for the cases with only axial strain applied. The default closure with $\hat{C}_C = 1/3$ performs quite well for this problem, however the model can be observed to overestimate the influence of the integral width of the mixing layer. To compare the accuracy of the three implemented models, the mean absolute percentage error (MAPE) between the RANS results and the ILES data is recorded for the low-magnitude strain rate cases (cases ACV$\pm$1 and ACS$\pm$1) at the final time. The high-magnitude strain cases are omitted, as their final results are still polluted by the underestimation of the transitional regime by the K-L model. The MAPE of the four cases are recorded in Table 6.5, and shows the transverse closure to reduce the MAPE by a factor of four compared to the default isotropic closure, whilst the axial closure performs closer to $2.5\times$ worse.

Under applied transverse strain rates, the ILES obtains slightly larger growth rates for the expansive strain as compared to the unstrained simulation. In Pascoe *et al.* (2025*b*), this trend was considered the result of the turbulence length scale in the simulation stretching under expansion, which in turn effectively decreased the dissipation rate. A buoyancy-drag model calibrated to the unstrained case (Youngs & Thornber, 2020*b*) was modified for the applied transverse strain cases by scaling the unstrained effective drag length scale by the transverse expansion factor, with the resulting model able to accurately predict the integral width (Pascoe *et al.*, 2025*b*). For the K-L

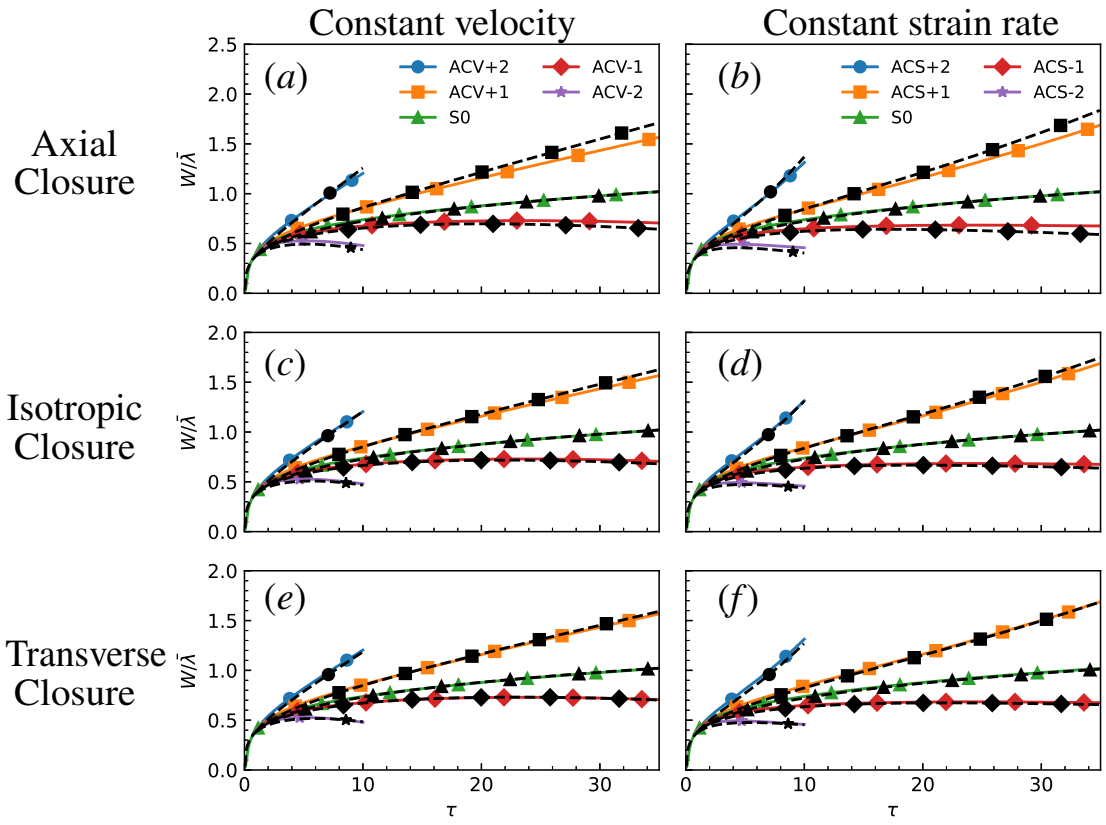

Figure 6.2: Integral width for simulations under the applied axial strain rate with (left) constant velocity profile and (right) constant strain rate profile. Solid lines indicate ILES, dashed lines indicate K-L model with (top) axial closure, (middle) isotropic closure, and (bottom) transverse closure for bulk compression.

Table 6.5: Mean absolute percentage error (MAPE) at the final simulation time for the low-magnitude strain cases. Closure model with lowest MAPE for each strain application are highlighted in bold text.

		MAPE	
Strain Direction	Closure	Integral Width	TKE
Axial	Axial	9.91	68.9
Axial	Isotropic	4.12	39.9
Axial	**Transverse**	**1.28**	**25.9**
Transverse	Axial	9.55	47.7
Transverse	Isotropic	3.77	20.4
Transverse	**Transverse**	**0.80**	**7.2**

model simulations, the integral width predictions vary, as shown in Fig. 6.3. Just as observed for the ILES, the K-L model results show only a small modification to the integral width, as the transverse strain does not directly stretch/compress the mixing layer as the axial strain does. The isotropic closure shows almost no variation of the integral width, as if the effects of shear production and bulk compression cancel each other out. Under compression, shear production will deposit turbulent kinetic energy and the bulk compression will reduce the turbulent length scale, which can effectively maintain a steady turbulent viscosity and growth rate. Using the axial closure, corresponding to $\hat{C}_C = 0$, causes the K-L model to incorrectly predict the sign of the change, with the expansion cases growing at a slower rate than the unstrained case. As there is no bulk compression for this closure and strain combination, the only effect would be shear production, which would decrease the turbulent kinetic energy and turbulent viscosity in turn, producing the observed results for expansive strain. Using the transverse strain closure improves the performance of the model, aligning to the ILES data more effectively than the isotropic or axial closure. The transverse closure has a larger effective C_C ($\hat{C}_C = 1/2$), causing the turbulent length scale to vary more under the transverse strain. The MAPE for the low-magnitude strain cases is listed in Table 6.5, and the results confirm that the transverse closure is the most well aligned of the three closure methods. Similar ratios are observed as for the applied axial strain cases, with the transverse closure of the turbulent length scale attaining a factor of four smaller MAPE than the isotropic closure.

6.3.2 Turbulent kinetic energy

The domain integrated turbulent kinetic energy is calculated by different methods for the ILES and RANS cases. For the ILES, cases the turbulent kinetic energy is evaluated using the Favre velocity fluctuations:

$$TKE = \iiint \frac{1}{2}\rho u_i'' u_i'' dV. \tag{6.11}$$

The RANS cases calculate the total turbulent kinetic energy by integrating the transported turbulent kinetic energy variable:

$$TKE = \iiint \bar{\rho}\tilde{K} dV. \tag{6.12}$$

The results for the axially strained cases are plotted in Figure 6.4. The ILES results show the impact of shear production, with the compressive strain cases obtaining a slight increase in TKE, whilst the compression cases decrease. The axial closure RANS cases show little variation in the TKE, which can be explained by the change in the turbulent length scale, affecting the dissipation

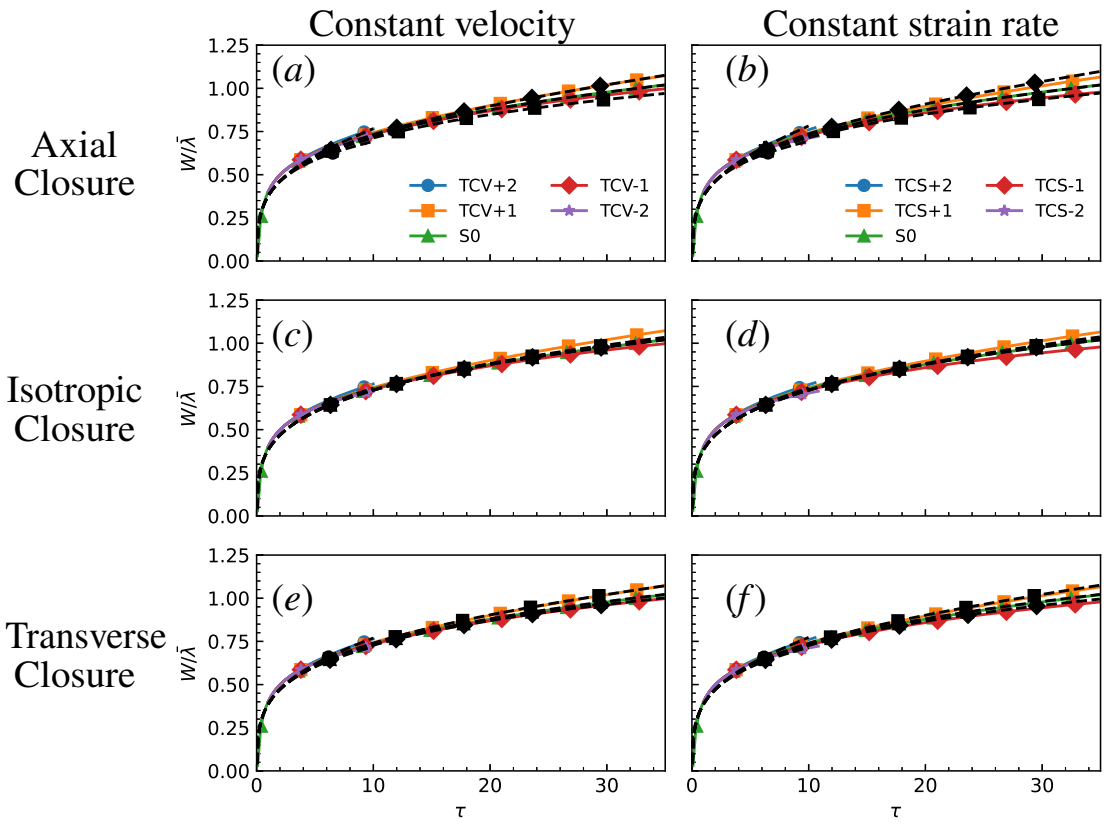

Figure 6.3: Integral width for simulations under the applied transverse strain rate with (left) constant velocity profile and (right) constant strain rate profile. Solid lines indicate ILES, dashed lines indicate K-L model with (top) axial closure, (middle) isotropic closure, and (bottom) transverse closure for bulk compression.

rate and counteracting shear production. In contrast, the transverse closure cases do a better job of capturing the effect of the strain rate on the TKE. The MAPE for low-magnitude strain cases are calculated in the same manner as was done for the integral width, and is reported in Table 6.5. The results show the same trend as for the integral width, with the transverse closure K-L model performing the best, and the axial closure model performing the worst. This is not surprising, as for the transverse closure to accurately capture the turbulent growth of the integral width, it would require more accurate representation of the turbulent viscosity and turbulent kinetic energy compared to the other methods. It is interesting to note that the transverse closure does a better job of capturing the TKE for the compressive cases, as compared to the expansion cases. As a two-equation model, the turbulent kinetic energy is assumed to be isotropic and is evenly divided across the three normal Reynolds stresses, as indicated by the $-C_P\bar{\rho}\tilde{K}\delta_{ij}$ contribution to $\bar{\tau}_{ij}$ in Eq. 3.36. The expansion cases tend towards isotropy for the TKE as the simulation continues, whilst the compression cases are anisotropic, with the TKE becoming more aligned with the x-direction (Pascoe *et al.*, 2024). It is interesting to note that the model performs better

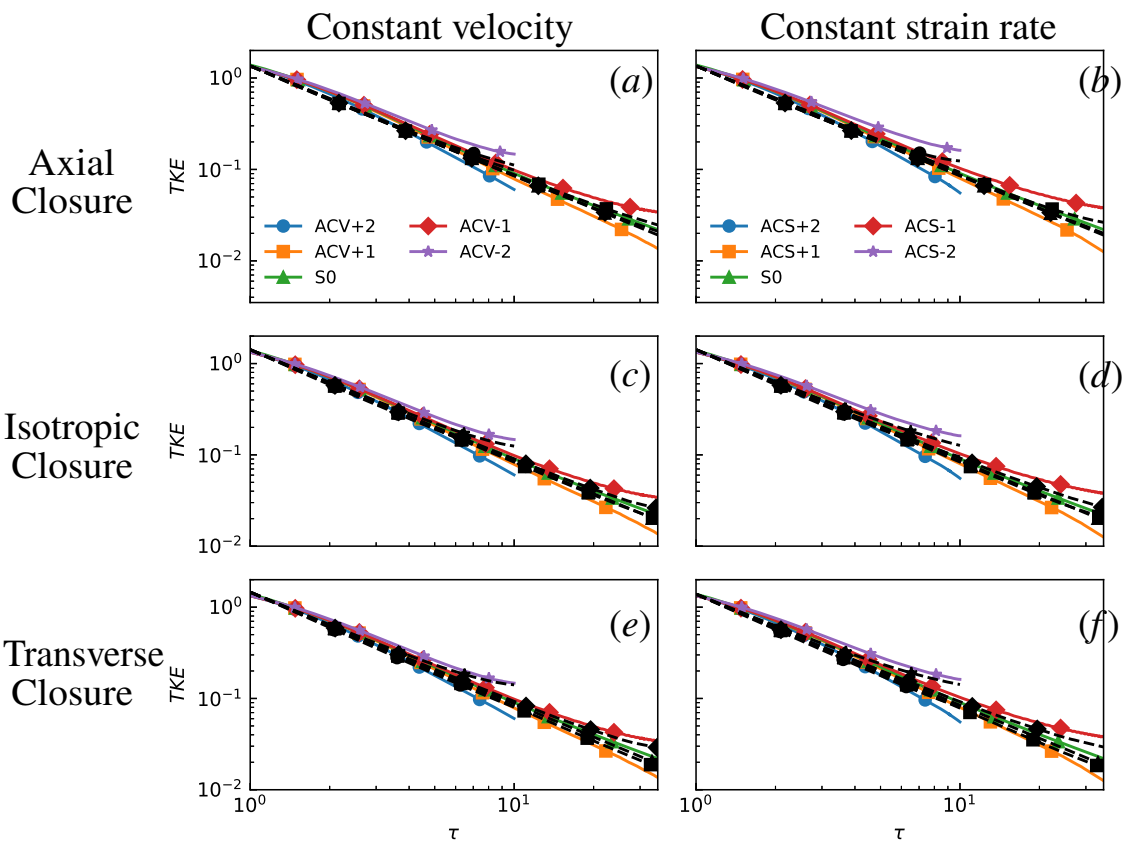

Figure 6.4: Turbulent kinetic energy for simulations under the applied axial strain rate with (left) constant velocity profile and (right) constant strain rate profile. Solid lines indicate ILES, dashed lines indicate K-L model with (top) axial closure, (middle) isotropic closure, and (bottom) transverse closure for bulk compression.

for these anisotropic cases than it does for the isotropic ones.

The domain integrated turbulent kinetic energy for the transverse strain cases is shown in Fig. 6.5. The ILES results show little variation as a result of the change in the turbulent length scale. A simple Reynolds stress model was calibrated to the unstrained case in Pascoe *et al.* (2025*b*), which showed that the TKE could be accurately estimated if the length scale for the TKE dissipation was made to scale with the geometric mean of the expansion factor in each direction. For compression, this means the length scale decreases and in turn increases the dissipation rate, counteracting shear production that adds energy into the mixing layer from the negative velocity gradients. The counteracting behaviour causes the tight spread observed in the ILES results. Again, the transverse closure appears to do the best job of capturing the tight spread, with the isotropic closure showing a slightly larger variation, and the axial closure overestimating the influence of the strain rate. This is not surprising then, as the axial closure will not modify the turbulent length scale directly ($\hat{C}_C = 0$), so there is no counteracting behaviour to shear production. The MAPE is reported in Table 6.5, with the transverse closure attaining

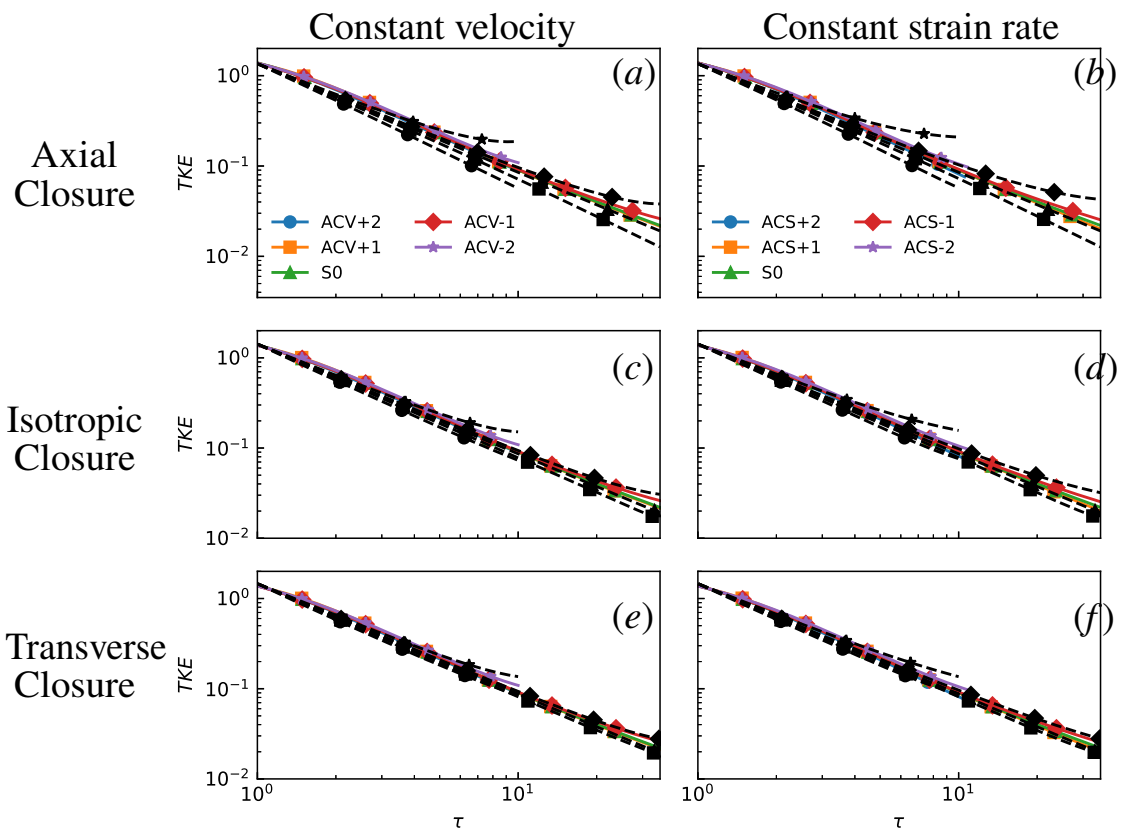

Figure 6.5: Turbulent kinetic energy for simulations under the applied transverse strain rate with (left) constant velocity profile and (right) constant strain rate profile. Solid lines indicate ILES, dashed lines indicate K-L model with (top) axial closure, (middle) isotropic closure, and (bottom) transverse closure for bulk compression.

the lowest error out of the three models.

The mean profiles for the turbulent kinetic energy are shown in Fig. 6.6 for the constant strain rate cases at the final time. For the unstrained case, the RANS simulations are identical and are able to reasonably predict the peak of the turbulent kinetic energy distribution. The RANS simulations, for all cases presented, are not able to predict the spike side turbulent kinetic energy, as the turbulent kinetic energy distribution is confined to the region in which the two fluids mix by the nature of the model. As the spike side is the region with the lowest density, the impact of this discrepancy is diminished by using $\bar{\rho}\tilde{K}$ for domain integration. The improvement of the transverse closure is most visible in cases ACS+1 and TCS-1, where the axial and isotropic closures overestimate the increase of turbulent kinetic energy. For cases ACS-1 and TCS+1, the isotropic closure has better alignment along the bubble side of the profile, however the transverse closure's slight overestimation allows for a better estimate of the domain integrated turbulent kinetic energy, as is done for the unstrained case.

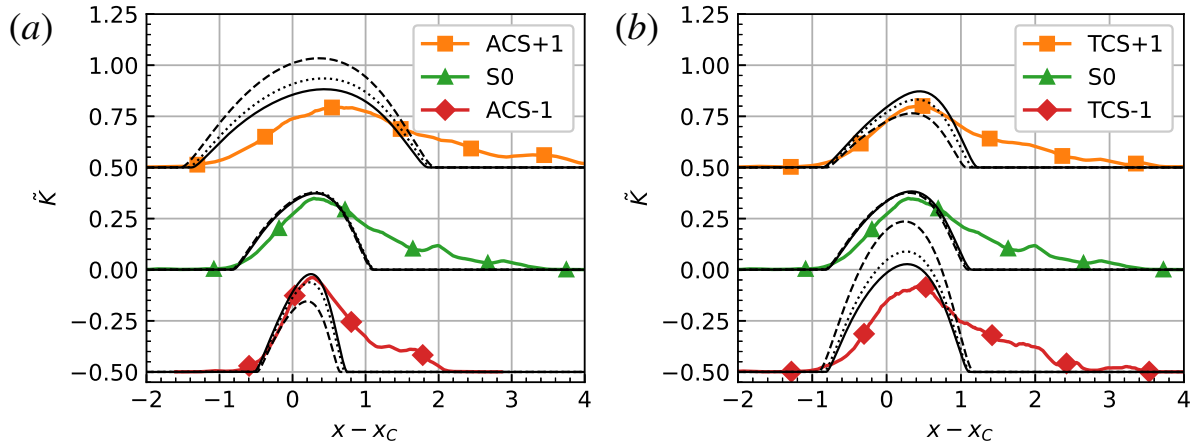

Figure 6.6: Mean turbulent kinetic energy profile at $\tau = 34.45$ for constant strain rate cases under (a) axial strain, and (b) transverse strain. Cases are displayed with a vertical offset of $\Delta\tilde{K} = 0.50$. Solid coloured lines represent ILES, solid black lines represent transverse closure, dotted black lines represent isotropic closure, and dashed black lines represent axial closure.

6.3.3 Turbulent mass flux velocity

The addition of a transport equation for the turbulent mass flux velocity, a_i, is the most common way to improve upon the two-equation models for compressible flows Besnard *et al.* (1992); Banerjee *et al.* (2010); Morgan & Wickett (2015). With the addition of the turbulent mass flux velocity, the system is able to more accurately treat the conversion of potential energy to turbulent kinetic energy and avoid the shock detection mechanism outlined in equation (3.38). After the shock transit, the influence of the turbulent mass flux is negligible for the developing turbulent mixing layer, as it only modifies the values of L and $\tilde{K}$ due to buoyancy production when $\partial\bar{p}/\partial x_i \neq 0$. The turbulent mass flux is calculated according to,

$$a_i = \tilde{u}_i - \bar{u}_i = \overline{-u_i''}. \tag{6.13}$$

Whilst the implemented K-L model does not calculate a_i, it is possible to estimate the value for a_i for incompressible flows Kokkinakis *et al.* (2019). At a sufficiently late time, the decaying turbulent mixing layer induced by RMI may become approximately incompressible. The value for a_1 can be approximated by using the Favre-weighted velocity from the simulation for $\tilde{u}_1$, and using $\bar{u}_1 = \bar{S}_A$. A comparison of the ILES results and the estimates from each closure is presented in Fig. 6.7 for the constant strain rate cases near the final time. The RANS results for the unstrained case are identical for all closures, showing agreement with the ILES results but not fully capturing the spike side profile. The transverse closure results provide the best overall estimate of the profile for the strained cases. The ordering and effect of the closure on the turbulent mass flux velocity is the same as observed for the turbulent kinetic energy. For this reason, the transverse closure is expected to be beneficial for models which also transport the

turbulent mass flux velocity, utilising the modified turbulent length scale for improved dissipation estimates.

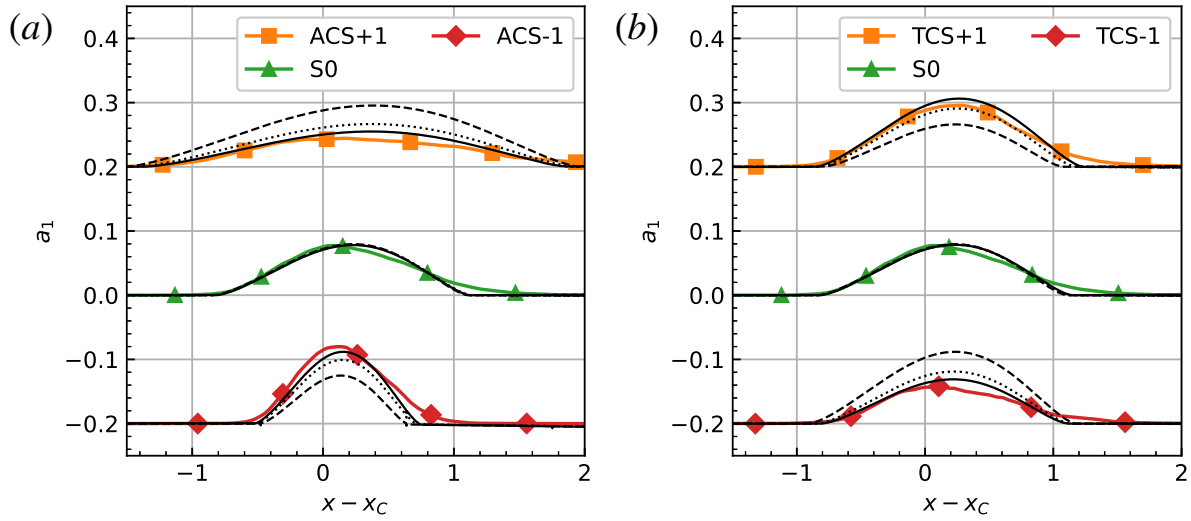

Figure 6.7: Turbulent mass flux velocity profile at $\tau = 34.45$ for cases under (a) axial strain, and (b) transverse strain. Cases are displayed with a vertical offset of $\Delta a_1 = 0.20$. Solid coloured lines represent ILES, solid black lines represent transverse closure, dotted black lines represent isotropic closure, and dashed black lines represent axial closure.

6.3.4 Reynolds Stress

One of the weaknesses of the K-L model is the inability to estimate the Reynolds-stresses, relying on the Boussinesq eddy viscosity assumption. In the presence of strong velocity gradients, as observed with shock waves, the Reynolds stress tensor can become non-realisable. There are different approaches to avoid this, such as only using the isotropic turbulent pressure component Dimonte & Tipton (2006), limiting the obtained stresses Kokkinakis *et al.* (2019), or modifying the eddy viscosity to ensure realisability Xiao *et al.* (2021). For the simulations conducted, negligible differences were obtained for the integral width and total turbulent kinetic energy, whether using the limited or unlimited Reynolds stress components. The Reynolds stress components are calculated using the Boussinesq eddy viscosity assumption for the RANS cases, according to

$$\widetilde{u_i u_j} = -\frac{\bar{\tau}_{ij}}{\bar{\rho}} = \frac{2}{3}\tilde{K}\delta_{ij} - \frac{\mu_T}{\bar{\rho}}\left(\frac{\partial \tilde{u}_i}{\partial x_j} + \frac{\partial \tilde{u}_j}{\partial x_i} - \frac{2}{3}\frac{\partial \tilde{u}_k}{\partial x_k}\delta_{ij}\right). \tag{6.14}$$

The axial ($\widetilde{u_1'' u_1''}$) and transverse ($\widetilde{u_2'' u_2''}$) stresses at the final time for the constant strain rate case are shown for the axially strained simulations in Fig. 6.8 and in Fig. 6.9 for the transversely strained simulations. The anisotropy of the Reynolds stress components is visible in the ILES

results; however, the RANS cases do not perform well at correctly predicting the ratio. This is most evident for the $\widetilde{u_1''u_1''}$ component for case ACS+1 which becomes non-realisable in the absence of any correction. This is accompanied by an overestimate of the transverse stress, however using the transverse closure minimises the under- and over-prediction of the stresses. Similar behaviour is observed for case TCS-1 which has non-realisable $\widetilde{u_1''u_1''}$ values at edges of the captured mixing layer. Part of the difficulty in the capturing the cases ACS+1 and TCS-1 is that near the final time, the turbulent kinetic energy is close to isotropic, which is visible in the ILES profiles. As the unstrained case starts with the anisotropic distribution, the application of the strain rates causes these two cases to become less anisotropic, which the Boussinesq eddy viscosity assumption does not predict.

The isotropic and axial closures allow for better estimates of $\widetilde{u_1''u_1''}$ for case ACS-1 in Fig. 6.8, whereas the transverse closure overestimates the stress. The other closures will then more accurately predict the shear production contribution. However, in the actual $\tilde{K}$ profile in Fig. 6.6, the profile is underestimated, a result of the closure which means the axial compression reducing the length scale and increasing the dissipation. In contrast, the transverse closure is consistent in the slight over-prediction of the turbulent kinetic energy.

Modelling the flow with a Reynolds stress model should improve the results due to the more accurate calculation of the shear production. However, the return to isotropy treatment of many models may not be well suited for the case considered, where the base case remains anisotropic at late time.

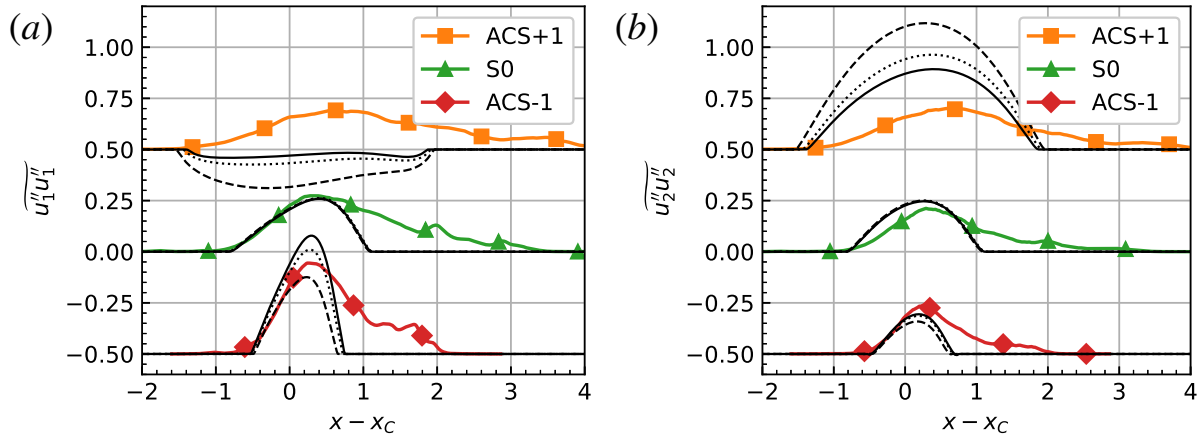

Figure 6.8: Reynolds stress components at $\tau = 34.45$ for cases with constant axial strain rates. (*a*) $\widetilde{u_1''u_1''}$, and (*b*) $\widetilde{u_2''u_2''}$. Cases are displayed with a vertical offset of $\Delta\widetilde{u''u''} = 0.50$. Solid coloured lines represent ILES, solid black lines represent transverse closure, dotted black lines represent isotropic closure, and dashed black lines represent axial closure.

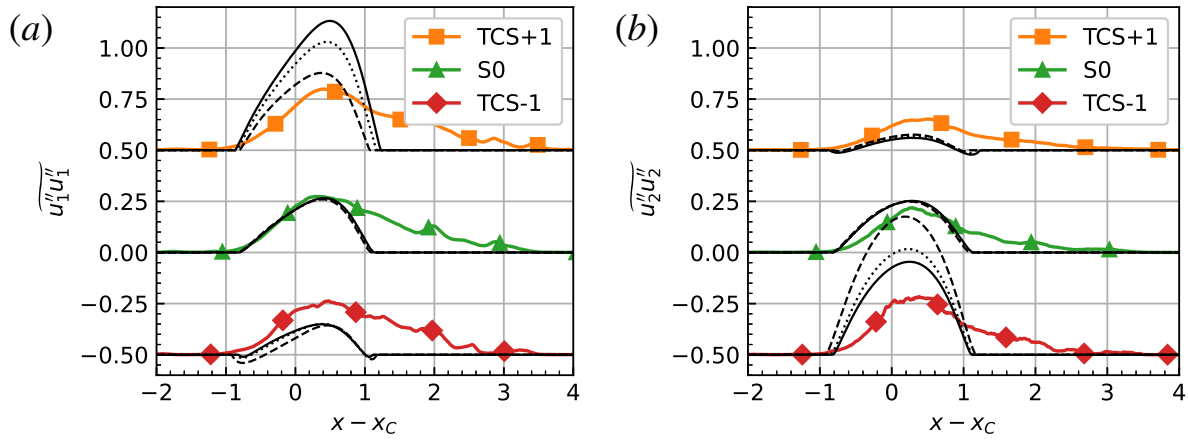

Figure 6.9: Reynolds stress components at $\tau = 34.45$ for cases with constant transverse strain rates. (*a*) $\widetilde{u_1'' u_1''}$, and (*b*) $\widetilde{u_2'' u_2''}$. Cases are displayed with a vertical offset of $\Delta \widetilde{u'' u''} = 0.50$. Solid coloured lines represent ILES, solid black lines represent transverse closure, dotted black lines represent isotropic closure, and dashed black lines represent axial closure.

6.3.5 Self-similar analysis of the K-L model

In order to better understand the K-L model's performance, it is possible to perform a self-similarity analysis of the governing equations. This will reduce the equations to the form of a buoyancy-drag model, a set of ordinary-differential equations for the evolution of the mixing layer width and mixing layer growth rate. Following the work in Xiao *et al.* (2020*b*,*a*); Zhang *et al.* (2020), the profiles of L and $\tilde{K}$ are given by self-similar profiles:

$$L(x,t) = L_0(t) X^r(x,t) \tag{6.15}$$

$$\tilde{K}(x,t) = \tilde{K}_0(t) X^s(x,t) \tag{6.16}$$

where the profiles are effectively separated into a magnitude component, and a spatial component using the transformed coordinates:

$$X(x,t) = 1 - \chi^2 \tag{6.17}$$

$$\chi(x,t) = \tfrac{x}{h(t)} \tag{6.18}$$

where h is half the mixing layer width. The non-dimensionalised spatial variables are limited to within the mixing layer, i.e. $\chi \in [-1, 1]$ and $X \in [0, 1]$. Previous works assumed the values of $r = 1/2$ and $s = 1$ such as in Dimonte & Tipton (2006) for the K-L model and Morgan & Wickett (2015) for the K-L-a model. Instead, Xiao *et al.* (2020*b*,*a*); Zhang *et al.* (2020) consider arbitrary values of s and r, with the constraint of $2r + s = 2$, in order to find the optimum fit to the models, ultimately using $s = 1.6$. The generalisation of the exponents meant that the self-similar equations did not separate easily into temporal and spatial contributions, and were solved by integrating over the mixing layer.

For the cases considered, the $\tilde{K}$ and L equations used will assume homogeneity in the transverse directions, and neglect the effects of density by assuming the flow is in the low-Atwood number limit.

$$\bar{\rho}\frac{D\tilde{K}}{Dt} = \frac{\partial}{\partial x_1}\frac{\mu_T}{N_K}\frac{\partial \tilde{K}}{\partial x_1} + \bar{\tau}_{ij}\frac{\partial \tilde{u}_i}{\partial x_j} - C_D\tilde{V}^3/L \tag{6.19a}$$

$$\bar{\rho}\frac{DL}{Dt} = \frac{\partial}{\partial x_1}\frac{\mu_T}{N_L}\frac{\partial L}{\partial x_1} + C_L\bar{\rho}\tilde{V} + \bar{\rho}LS_\phi \tag{6.19b}$$

The buoyancy production term for $\tilde{K}$ has been neglected, whilst the Reynolds stress contribution and the L compressibility term are included, two terms which are commonly ignored. For generality, the L bulk compression term has been represented as scaling with the arbitrary strain rate S_ϕ, where using the isotropic strain rate closure ($\nabla \cdot \boldsymbol{u}/3$) will provide the original model. To obtain a buoyancy-drag model, the self-similar profiles given in Eqs. (6.15) and (6.16) were substituted in, a Taylor series about $\chi = 0$ was taken to remove the spatial component, and the turbulent kinetic energy was transformed into the turbulent velocity using the relation $\tilde{K}_0 = \tilde{V}_0^2/2$. Assuming only normal velocity gradients are present, the gradients are replaced with the corresponding strain rate.

$$\begin{aligned}\frac{dL_0}{dt} &= \tilde{V}_0(t)\left(\frac{C_L N_L - 2C_\mu r\beta^2}{N_L}\right) + L_0 S_\phi \\ \frac{d\tilde{V}_0}{dt} &= -\frac{\tilde{V}_0^2(t)}{L_0(t)}\left(\frac{C_D N_K + C_\mu s\beta^2}{N_K}\right) + \frac{4}{3}C_\mu L_0(S_A - S_T)^2 \\ &\quad - \frac{1}{2}C_P(S_A + 2S_T)\tilde{V}\end{aligned} \tag{6.20a}$$

Typically, the evolution equation of L_0 will be transformed into the evolution equation of the mixing layer half width, h, as these terms are considered to be proportional by a constant within the regime of self-similarity.

$$\beta = \frac{L_0(t)}{h(t)} \tag{6.21}$$

As the integral width has been used as the measure of the mixing layer width in the previous sections, the system will be transformed by $\beta_W = L_0/W$. However, the assumption of self-similarity is not valid for the strained simulation cases. Under the application of axial and transverse strain, the turbulent kinetic energy anisotropy and the mixedness of the mixing layer do not approach an asymptotic value, instead deviating away from the unstrained case's self-similar behaviour (Pascoe *et al.*, 2024, 2025*b*). This is further evidenced by the variation of β_W for the RANS simulations conducted, shown in Figs. 6.10 and 6.11. The unstrained cases approach a final value of $\beta_W = 0.687$, suggesting the unstrained case has entered this regime of self-similar growth for the RANS model. It is possible to further validate this asymptotic value, as for a

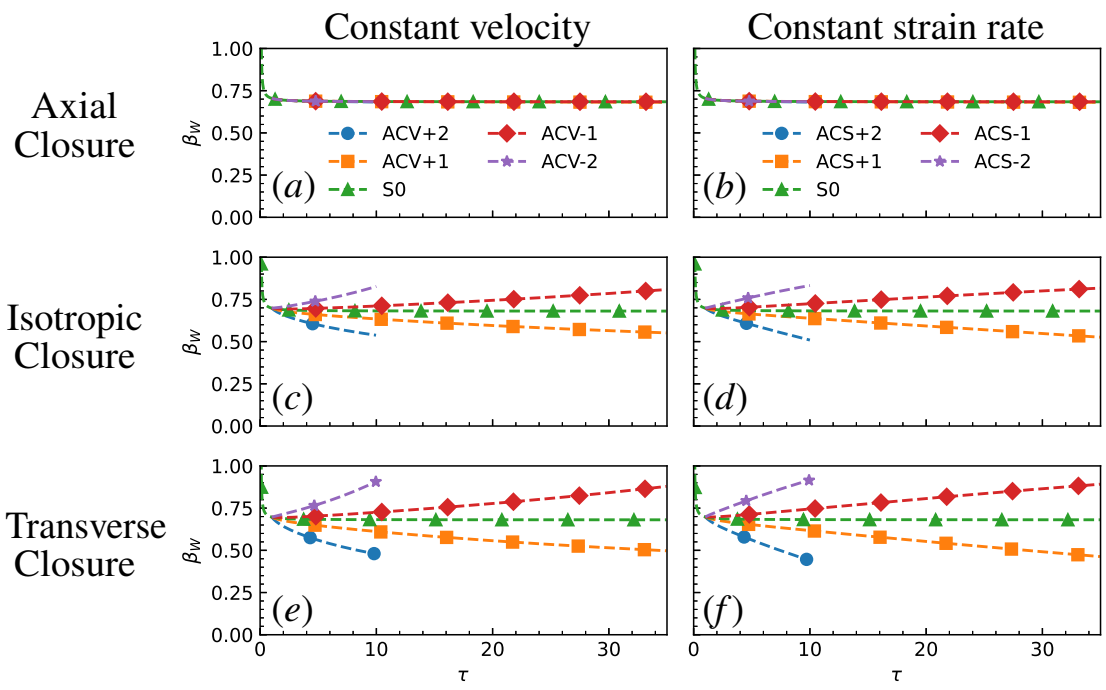

Figure 6.10: β_W for simulations under the applied axial strain rate with (left) constant velocity profile and (right) constant strain rate profile for the K-L model with (top) axial closure, (middle) isotropic closure, and (bottom) transverse closure for bulk compression.

linear mean volume fraction profile the integral width should be three times smaller than the half width, giving the relation of $\beta_W = 3\beta$. The theoretical value of β for the present model is calculated according to $\beta = 1/C_A$ (Xiao *et al.*, 2020*b*,*a*; Zhang *et al.*, 2020). The actual relation observed from the simulations is $\beta_W = 3.44\beta$, a slightly higher ratio due to the mean volume fraction profile not being linear. Whilst the unstrained cases plateau, the strained cases show a variation in β_W, suggesting that the peak value of L in the domain and the integral width do not grow in the same proportion for the isotropic and transverse closure cases. In contrast, the axial closure cases do maintain the late-time value of β_W. Whilst the self-similarity assumption simplifies the buoyancy-drag reduction analysis, it is not an accurate representation of the state of self-similarity for the ILES cases. This necessitates the inclusion of time dependence for β.

Adjusting both equations to use the integral width, the growth rate of the integral width is defined by

$$V_W = \tilde{V}_0 \frac{C_L N_L - 2C_\mu r \beta^2}{N_L \beta_W}. \tag{6.22}$$

Substituting and simplifying gives the new expressions:

$$\frac{dW}{dt} = V_W + \left(S_\phi - \frac{\dot{\beta}_W}{\beta_W} \right) W \tag{6.23a}$$

$$\frac{dV_W}{dt} = -\frac{V_W^2}{l^{\text{eff}}} + C_W (S - S_T)^2 W - \frac{1}{2} C_P (S_A + 2S_T) V_W + C_\beta V_W \tag{6.23b}$$

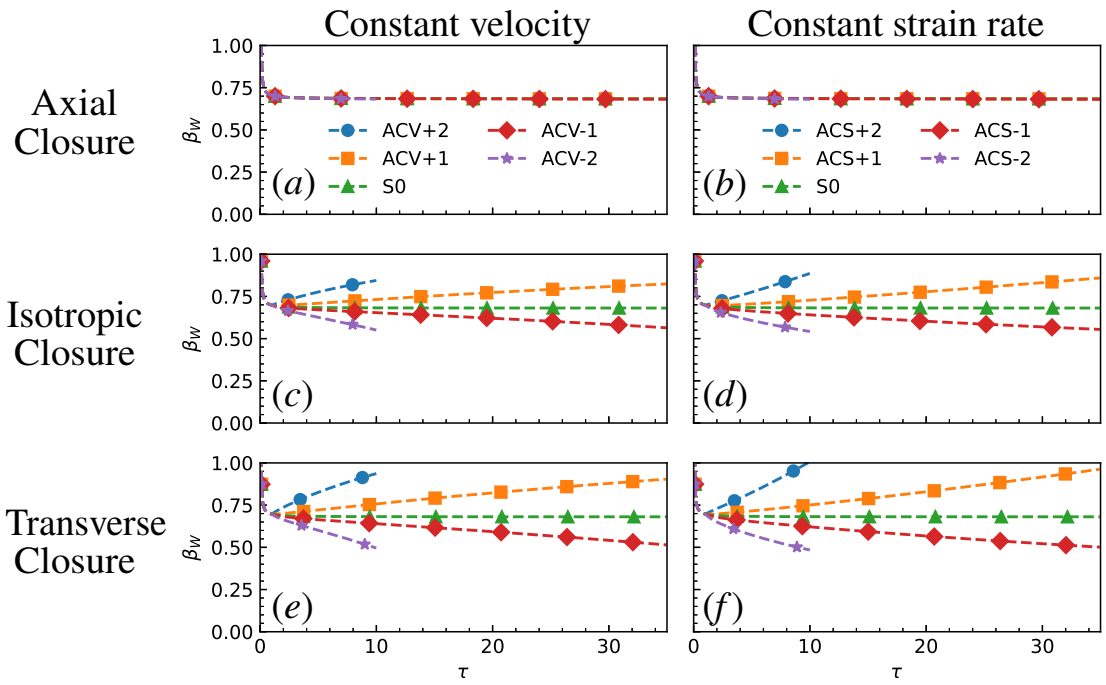

Figure 6.11: β_W for simulations under the applied transverse strain rate with (left) constant velocity profile and (right) constant strain rate profile for the K-L model with (top) axial closure, (middle) isotropic closure, and (bottom) transverse closure for bulk compression.

with the definitions

$$l^{\text{eff}} = \frac{N_K\left(C_L N_L - 2C_\mu r\beta^2\right)}{N_L\left(C_D N_K + C_\mu s\beta^2\right)}W \tag{6.24a}$$

$$C_W = \frac{4C_\mu(C_L N_L - 2C_\mu r\beta^2)}{3N_L} \tag{6.24b}$$

$$C_\beta = -\frac{\dot{\beta}_W}{\beta_W} - \frac{4C_\mu r\beta}{C_L N_L - 2C_\mu r\beta^2}\dot{\beta}. \tag{6.24c}$$

This derivation has not assumed a constant β or β_W, causing the derivatives of each to occur in the differential equations. The equations may be simplified to use only a single β term as they are proportional for a specified mean volume fraction profile. The model is greatly simplified by using constant β. It may be possible to empirically determine a relationship for the variation in β under strain for the specific bulk compression closure employed. For now, the analysis is conducted with the assumption of self-similarity between the turbulent length scale and the mixing layer width. Using this assumption reduces the model to,

$$\frac{dW}{dt} = V_W + S_\phi W \tag{6.25a}$$

$$\frac{dV_W}{dt} = -\frac{V_W^2}{l^{\text{eff}}} + C_W(S_A - S_T)^2 W - \frac{1}{2}C_P(S_A + 2S_T)V_W. \tag{6.25b}$$

In this model the growth of the integral width is dependent upon the velocity as well as a contribution from the background strain rate, $S_\phi W$. For the case of axial closure ($S_\phi = S_A$),

this contribution is identical to the RMI linear regime correction with axial strain, where the amplitude growth rate is the superposition of the amplitude growth rate and the background stretching contribution (Epstein, 2004; Pascoe *et al.*, 2024). It makes sense then that axial closure preserves the β_W ratio, as it allows the turbulent length scale to grow at the same rate as the integral width, where the integral width will naturally vary from the velocity difference across the mixing layer. Despite this, the transverse closure provides better performance for the model by adjusting the dissipation rate for the transverse strain expansion factor. Without any strain and with the coefficients provided in Table 6.2, the effective drag length scale is calculated to be $l^{\text{eff}} = 0.383W$, which for unstrained RMI suggests a power law growth $W = A(t - t_0)^\theta$, where $\theta = 0.277$. This is in between the prescribed coefficient used for the K-L model derivation of $\theta = 0.25$, and the late-time coefficient of $\theta = 0.292$ for the quarter-scale θ-group case (Thornber *et al.*, 2017).

The velocity equation has two additional terms that are dependent upon strain rate. These two terms are the result of shear production, a product of the Reynolds stress and velocity gradients. Similar terms were hypothesised and calibrated to improve the performance of a buoyancy-drag model for ILES cases under axial strain (Pascoe *et al.*, 2024). Whilst the C_W term will always act as a positive source for the evolution of the growth rate, the C_P contribution will depend upon the signs of the applied strain rate as expected for shear production contribution.

Given the clear separation in behaviour of the two length scales, the integral width which scales with axial strain and the turbulent length scale which scales with transverse strain, a two length scale approach could be used to generate a buoyancy-drag model. Whilst two length scales are employed in many modern RANS models, those length scales are used to separate the turbulence transport and destruction length scales (Schwarzkopf *et al.*, 2016; Morgan *et al.*, 2018*b*). In the derivation of the K-2L-a model, the turbulent length scale equation is considered to grow self-similarly with the mixing layer width, while the ratio between the turbulent transport and destruction length scale is not necessarily constant (Morgan *et al.*, 2018*b*).

Two further modifications have been made to obtain the buoyancy-drag model in Eq. 6.26 from Eq. 6.25. Firstly, the transverse strain contributions from shear production have been omitted from the evolution of the turbulent velocity growth to improve agreement with the transverse results. Whilst turbulent kinetic energy is added under compressive transverse strain, it is not distributed to the axial direction, which the isotropic model for $\tilde{K}$ does not account for and so causes the mixing layer growth rate to be incorrectly estimated. An alternate modification would be to scale the turbulent velocity more strongly with the transverse strain rate to counteract this effect. Secondly, the magnitude of the coefficient of the $S_A V_W$ term has been increased to

improve the alignment with the axial results, effectively increasing the strain drag. Whilst these modifications are phenomenological, they can be considered corrections to the prior removal of the terms which depended upon the time variation of β.

$$\frac{dW}{dt} = V_W + S_A W \tag{6.26a}$$
$$\frac{dL}{dt} = V_W + S_T L \tag{6.26b}$$
$$\frac{dV_W}{dt} = -\frac{V_W^2}{l^{\text{eff}}} + 0.143 S_A^2 L - 0.933 S_A V_W \tag{6.26c}$$
$$l^{\text{eff}} = 0.383 L \tag{6.26d}$$

For simplicity, both length scales are scaled by the turbulent velocity, as opposed to being different by a factor of β_W. For a case without applied strain, the proposed model will reduce down to the more typical two-equation model for buoyancy-drag modelling. The performance of the model is plotted in Figs. 6.12 and 6.13, using initial conditions of [W_0,L_0,V_{W0}]=[0.00638, 0.00638,1679] and an initial time offset of $\tau = 0.08$ to better align with the shock transition. The initial length scale values use the post-shock integral width (Thornber *et al.*, 2017; Youngs & Thornber, 2020*b*), as with the omission of the source term in the analysis the resulting buoyancy-drag is not able to capture the shock transition. As the model uses an effective drag length scale proportional to the turbulent length scale which is initialised the same as the integral width, it is unable to capture the linear and transitional regimes, just like the RANS model. The initial drag is very high due to the small turbulent length scale/integral width, requiring a very large initial velocity (36$\times$ larger than the theoretical growth rate (Thornber *et al.*, 2017; Youngs & Thornber, 2020*b*)) to counteract the drag. This could be rectified by using a piecewise effective drag length scale as done in the buoyancy-drag models of Youngs & Thornber (2020*b*,*a*). As the drag term is derived from the diffusion and dissipation terms for the turbulent kinetic energy, a modification to these terms could improve the performance of the K-L model in the early time. The late time performance of the derived buoyancy-drag model is well aligned with the ILES, and is far less computationally expensive to run than both the ILES and RANS simulations.

6.3.6 Equivalence of two-equation models

The bulk compression closure for the turbulent length scale can be generalised to other two-equation RANS models, such as for the K-ϵ model which transports the turbulent kinetic energy dissipation rate. Starting from the turbulent kinetic energy and the turbulent length scale, alternate formulations are obtained by using the transformation (Pope, 2000; Wilcox, 2006)

$$Z = C_Z K^m L^n. \tag{6.27}$$

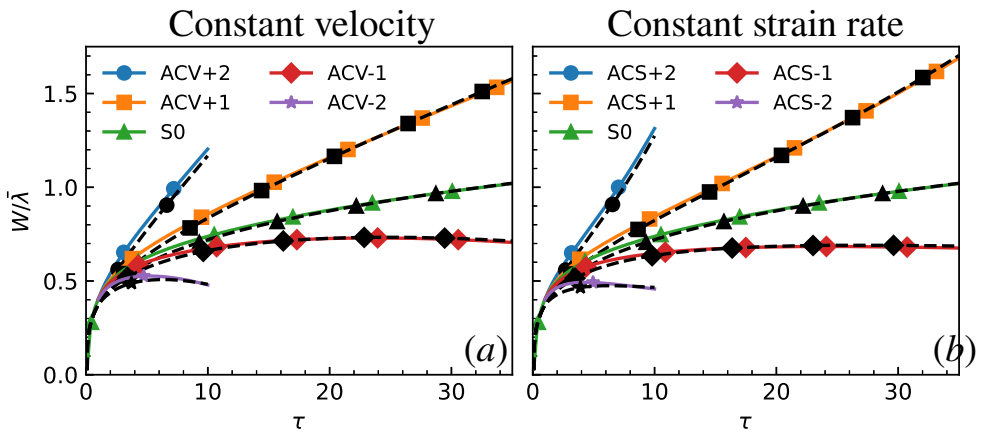

Figure 6.12: Buoyancy-drag model for simulations under the applied axial strain rate with (left) constant velocity profile and (right) constant strain rate. Sold line indicates ILES, dashed line indicates buoyancy-drag model from Eq. 6.26.

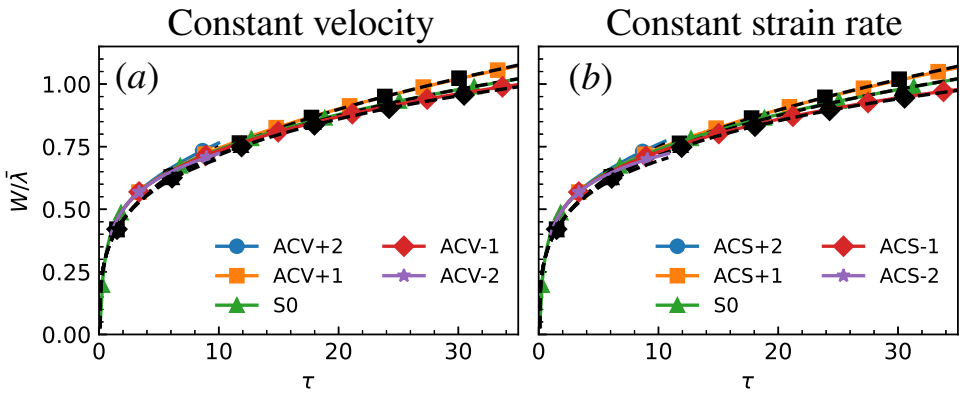

Figure 6.13: Buoyancy-drag model for simulations under the applied transverse strain rate with (left) constant velocity profile and (right) constant strain rate. Solid line indicates ILES, dashed line indicates buoyancy-drag model from Eq. 6.26.

Given the formulation of the dissipation of turbulent kinetic energy in Eq. 3.33e, for $Z = \epsilon$ the values of $m = 3/2$, $n = -1$, and $C_Z = 2\sqrt{2}C_D$ are obtained. The transport equation for Z is then obtained via

$$\bar{\rho}\frac{\tilde{D}Z}{\tilde{D}t} = m\frac{Z}{\tilde{K}}\bar{\rho}\frac{\tilde{D}\tilde{K}}{\tilde{D}t} + n\frac{Z}{L}\bar{\rho}\frac{\tilde{D}L}{\tilde{D}t} \tag{6.28}$$

$$= m\frac{Z}{\tilde{K}}\left[\frac{\partial}{\partial x_j}\left(\frac{\mu_T}{N_K}\frac{\partial K}{\partial x_j}\right) + \bar{\tau}_{ij}\frac{\partial \tilde{u}_i}{\partial x_j} + S_K - \bar{\rho}\epsilon\right] + n\frac{Z}{L}\left[\frac{\partial}{\partial x_j}\left(\frac{\mu_T}{N_L}\frac{\partial L}{\partial x_j}\right) + C_L\bar{\rho}\tilde{V} + \bar{\rho}LS_\phi\right] \tag{6.29}$$

where $\tilde{D}/\tilde{D}t = \partial/\partial t + \tilde{u}_i \partial/\partial x_i$ refers to the total derivative for the Favre-averaged flow field. For the turbulent dissipation rate, the equations evaluate to

$$\begin{aligned}\bar{\rho}\frac{\tilde{D}\epsilon}{\tilde{D}t} = \frac{\partial}{\partial x_j}\left(\mu_T\left(\frac{3}{2N_K}+\frac{1}{N_L}\right)\frac{\partial \epsilon}{\partial x_j}\right) + \frac{3}{2}\frac{\epsilon S_K}{K} + \frac{3}{2}\frac{\epsilon}{\tilde{K}}\bar{\tau}_{ij}^{(d)}\frac{\partial \tilde{u}_i}{\partial x_j} \\ - \left(\frac{3}{2}+\frac{C_L}{2C_D}\right)\bar{\rho}\frac{\epsilon^2}{\tilde{K}} - \left(\frac{3}{2}C_P\frac{\partial \tilde{u}_i}{\partial x_i} + S_\phi\right)\bar{\rho}\epsilon + C.D.\end{aligned} \tag{6.30}$$

On the right-hand side of Eq. 6.30, the terms represent diffusion, shear production, buoyancy production, dissipation, bulk compression, and cross-diffusion respectively for the turbulent dissipation rate. The re-arrangement of the diffusion terms for $\tilde{K}$ and L into the diffusion term for ϵ introduces cross-diffusion terms (Wilcox, 2006), which will depend upon the gradients of $\tilde{K}$, ϵ and density, but not the strain rates of the flow. For simplicity, these terms have not been included as the focus of this comparison is on the bulk compression. The Reynolds stress in the shear production term has been split into the deviatoric component $\bar{\tau}_{ij}^{(d)}$ and the isotropic component $-C_P\bar{\rho}K\delta_{ij}$. The isotropic component of the Reynolds stress combines with the bulk compression term for the turbulent length scale to produce the bulk compression term for the turbulent dissipation rate. For comparison, the transport equation for the turbulent dissipation rate in Morán-López & Schilling (2013, 2014); Gauthier & Bonnet (1990); Schilling (2015, 2021, 2024) is

$$\bar{\rho}\frac{\tilde{D}\epsilon}{\tilde{D}t} = \frac{\partial}{\partial x_j}\left[\left(\bar{\mu}+\frac{\mu_t}{\sigma_\varepsilon}\right)\frac{\partial \varepsilon}{\partial x_j}\right] + C_{\varepsilon 0}\frac{\varepsilon}{K}S_K + C_{\varepsilon 1}\frac{\varepsilon}{K}\tau_{ij}^{(d)}\frac{\partial \tilde{u}_i}{\partial x_j} - C_{\varepsilon 2}\frac{\rho\epsilon^2}{K} - \frac{2}{3}C_{\varepsilon 3}\rho\varepsilon\frac{\partial \tilde{u}_j}{\partial x_j} \tag{6.31}$$

where the form of S_K varies depending on the model, a physical viscosity $\bar{\mu}$ has been included in the diffusion term, and $\bar{\tau}_{ij}$ has been updated changed to use current notation. The values of σ_ϵ and $C_{\epsilon j}$ are model constants. The last term on the right-hand-side of Eq. 6.31 is the bulk compression term for the dissipation rate. For incompressible flows it is common to set the corresponding coefficient $C_{\epsilon 3}$ to zero, whilst for compressible flows a value of $C_{\epsilon 3} = 2$ is used to achieve the coefficient of $-4/3$ (Reynolds, 1987; Speziale & Sarkar, 1991). Using the default model coefficients for the K-L model with $C_P = 2/3$ and $S_\phi = \nabla \cdot \tilde{\mathbf{u}}/3$, the resulting bulk compression term for the turbulent dissipation rate is

$$-\left(\frac{3}{2}C_P\frac{\partial \tilde{u}_i}{\partial x_i} + S_I\right)\bar{\rho}\epsilon = -\frac{4}{3}\frac{\partial \tilde{u}_i}{\partial x_i}\bar{\rho}\epsilon, \tag{6.32}$$

giving the same expression as used for K-ϵ models. The model in Xie *et al.* (2021) neglects the contribution of the isotropic production from K in the derivation for the bulk compression closure of ϵ, instead attaining $C_{\epsilon 3} = 1/2$. For inhomogeneous turbulence with anisotropic strain, the transverse strain closure model for the bulk compression of the turbulent length scale

performed better than the default closure for isotropic strain. Using the transverse strain closure, the expression for the bulk compression of the turbulent dissipation rate becomes

$$-\left(\frac{3}{2}C_P\frac{\partial\tilde{u}_i}{\partial x_i}+S_T\right)\bar{\rho}\epsilon=-\left(\frac{\partial\tilde{u}_i}{\partial x_i}+S_T\right)\bar{\rho}\epsilon. \tag{6.33}$$

This expression is very similar, in essence swapping out a mean strain rate contribution (one third of the divergence) for the transverse strain contribution. Under isotropic strain, the expressions are identical in the low-Atwood number limit. The transformation process can be repeated for the K-ω model, using $m=1/2$, $L=-1$, and leaving C_ω as an arbitrary constant. The equivalent transport equation for the specific dissipation rate ω is

$$\begin{aligned}\bar{\rho}\frac{\tilde{D}\omega}{\tilde{D}t}=&\frac{\partial}{\partial x_j}\left(\mu_T\left(\frac{1}{2N_K}+\frac{1}{N_L}\right)\frac{\partial\omega}{\partial x_j}\right)+\frac{1}{2}\frac{\omega S_K}{K}+\frac{1}{2}\frac{\omega}{\tilde{K}}\bar{\tau}_{ij}^{(d)}\frac{\partial\tilde{u}_i}{\partial x_j}\\&-\left(\frac{C_D^{3/2}2^{1/2}}{C_\omega}+\frac{C_L2^{1/2}}{2C_\omega}\right)\bar{\rho}\frac{\omega^2}{\tilde{K}}-\left(\frac{1}{2}C_P\frac{\partial\tilde{u}_i}{\partial x_i}+S_\phi\right)\bar{\rho}\omega+C.D.\end{aligned} \tag{6.34}$$

The terms on the right-hand-side of Eqn. 6.34 are presented in the same order as for Eqn. 6.30. Evaluation of the bulk compression term with the default isotropic closure gives a scaling coefficient of $-2/3$. The 1988 Wilcox K-ω model (Wilcox, 1998) is given by

$$\bar{\rho}\frac{\tilde{D}\omega}{\tilde{D}t}=\frac{\partial}{\partial x_j}\left[\left(\mu+\frac{\mu_T}{\sigma_\omega}\right)\frac{\partial\omega}{\partial x_j}\right]+\gamma\frac{\omega}{\tilde{K}}\bar{\tau}_{ij}^{(d)}\frac{\partial\tilde{u}_i}{\partial x_j}-\beta\rho\omega^2-\gamma\frac{2}{3}\bar{\rho}\omega\frac{\partial\tilde{u}_k}{\partial x_k}. \tag{6.35}$$

The terms on the right-hand-side are diffusion, shear production, dissipation, and a bulk compression term which has been extracted from the shear production. This model does not have any buoyancy production, and it does not include the cross-diffusion term for simplicity. The coefficient $\gamma=13/25$ is calibrated for wall properties, but is very close to the derived factor of $1/2$ from the model equivalence. The bulk compression term in this K-ω model will then evaluate to around $-1/3$. Based off Morel & Mansour's derivation, Vuong & Coakley (1987); Coakley & Huang (1992) adjust the coefficient by assuming that one-dimensional rapid compression from shock waves is the primary activation of the bulk compression. This results in a scaling of the divergence by $-4/3$ as compared to the isotropic compression closure of $-2/3$. Using the transverse closure will result in the relation

$$-\left(\frac{1}{2}C_P\frac{\partial\tilde{u}_i}{\partial x_i}+S_T\right)\bar{\rho}\omega=-\left(\frac{1}{3}\frac{\partial\tilde{u}_i}{\partial x_i}+S_T\right)\bar{\rho}\omega \tag{6.36}$$

An interesting inclusion in the K-ω model is the 'Pope correction' (Pope, 1978; Wilcox, 2006), which modifies β in the dissipation term of ω. This modification was created due to the anomaly of the different spreading rates of the round-jet and plane-jet. The plane-jet is a

two-dimensional problem, whilst the round-jet is three-dimensional and will experience vortex stretching. The correction introduces a dependence upon χ, a non-dimensional measure of the vortex stretching. Whilst full details can be found in the aforementioned references, the non-dimensional measure for the vortex stretching in the K-ω model is given by

$$\chi_\omega = \left| \frac{\Omega_{ij}\Omega_{jk}\hat{S}_{ki}}{(\beta^*\omega)^3} \right| \tag{6.37}$$

For the strained simulations conducted, this correction would not contribute as χ would be zero due to the dependence on the rotation tensor of the flow.

A complication for the transverse closure is determining the transverse strain rate for more complicated case configurations. For turbulent mixing layers in standard configurations with clear distinctions between the axial direction (normal to the interface) and transverse direction (parallel to the interface or plane of homogeneity), identification of the transverse strain rate is a simple endeavour. For more complicated mixing layers and flow structures, the transverse direction may not be uniform in space or time. For example, the tilted rocket rig Read (1984); Youngs (1989); Andrews *et al.* (2014); Ferguson *et al.* (2023), which experiences anisotropic strain, is a popular validation case for RANS models as it is difficult to simultaneously capture the mixing layer width, turbulent kinetic energy, turbulent mass flux velocity and density-specific volume correlation Denissen *et al.* (2014); Morgan *et al.* (2023). To account for this, the transverse direction can be considered to be the homogenous plane and orthogonal to the direction of mixing. The direction of mixing can be determined by using the direction of the gradient vector for some quantity that varies through the mixing layer, such as the species mass fraction or turbulent kinetic energy. With this method, the local transverse strain rate can be calculated according to,

$$S_T = \frac{1}{n-1}\left[\begin{pmatrix}1\\1\\1\end{pmatrix} - \frac{\vec{\nabla}\phi}{|\vec{\nabla}\phi|}\right] \cdot \begin{pmatrix}\partial u_1/\partial x_1\\ \partial u_2/\partial x_2\\ \partial u_3/\partial x_3\end{pmatrix}, \tag{6.38}$$

where n is the number of dimensions of the true flow. The variable to determine the direction of mixing, ϕ, may vary depending upon the case, however the turbulent kinetic energy would likely remain useful in all contexts. As the conducted simulations here within are performed as one-dimensional but represent three-dimensional flows ($n = 3$), the gradient is evaluated in the x_1 direction, and the evaluated transverse strain rate from equation (6.38) reduces to the form used in equation (6.7). A two-dimensional flow however would not contribute a strain-rate in the third direction, hence the modified scaling factor.

The same closure for the bulk compression of the turbulent length scale should be valid for alternative RANS models that include additional equations, such as equations for the turbulent mass flux velocity, scalar variance, or density self-correlation. Two points of future investigation would be for the treatment of length scales in two length scale models, where the dissipation and transport length scales may be most accurately modelled with different bulk compression closures, and for Reynolds stress models which can more accurately predict the anisotropy of the turbulent kinetic energy.

6.4 Conclusion

The ability of the K-L turbulence model to predict the growth of a Richtmyer-Meshkov induced turbulent mixing layer under anisotropic strain was investigated through a series of simulations. Based upon the quarter-scale θ-group case Thornber *et al.* (2017), the strained ILES of Refs. Pascoe *et al.* (2024, 2025*b*) served as the basis for comparison. Three sets of simulations were conducted, each utilising a different closure for the treatment of the turbulent length scale under bulk compression of the fluid, a term that is not theoretically defined for anisotropic strains. The three closure approaches correspond to scaling the turbulent length scale with the axial strain rate, the transverse strain rate, and the default methodology of scaling with the mean strain. Under mean axial strain rates, the K-L model was able to predict the expansion/compression of the mixing layer due to the ability to resolve the velocity difference in the fluid flow which expands/compresses the mixing layer. The results for each closure differed in their ability to model the turbulent growth and the total turbulent kinetic energy, with the transverse strain closure performing the best of the three options. Similarly, the transverse strain closure performed the best of the three methods for both the integral width and turbulent kinetic energy. These results suggest that for modelling of turbulent mixing layers under anisotropic strain rates, such as observed in implosion and explosion profiles in spherical geometries, the performance of the K-L model can be improved through the modification of the bulk compression term for the turbulent length scale to instead vary with the transverse strain rate. A self-similarity analysis of the K-L model produced a buoyancy-drag model for modelling the mixing layer growth. The development of the model was limited by the assumption of the proportionality of the turbulent length scale and integral width, a common assumption for model calibration in K-L type models. To rectify this constraint, a three-equation buoyancy-drag model was developed, which evolves both the integral width and a turbulent length scale. With this design, the integral width is allowed to scale with the axial strain which stretches/compresses the mixing layer, whilst

the turbulent length scale scales with the transverse strain rate. Through the equivalence of two-equation RANS models, the closure for the bulk compression was also derived for the K-ϵ and K-ω models. Further avenues of research should be conducted to determine the proficiency of these modifications in describing other flow features.

CHAPTER 7

Conclusions and Further Research

7.1 Summary of current research

The impact of normal strain rates on instabilities and the development of turbulent mixing layers is an important consideration in many applications. Primarily, in convergent geometry the change in the radial position of the mixing layer, as observed in ICF implosions and supernova explosions, corresponds to large, anisotropic strain rates. Depending upon the strain, this may either inhibit or accelerate the mixing of fluids. Understanding the influence of the strain rates is an important step towards modelling and understanding the behaviour of these dynamic and complex systems. The aim of this thesis has been to analyse different aspects of the Richtmyer-Meshkov instability and the induced turbulent mixing layer under applied strain rates, aiming to develop models that explain the observed results. A novel approach of applying strain rates in planar geometry was implemented, allowing for simulations of controlled strain profiles to be conducted for fluids with the same specific heat ratios. This method allowed a decoupling of the axial and transverse strain rates that is not easily achievable in convergent geometries.

Chapter 4 focused on the effects of the axial strain rate on RMI-induced mixing layer development. A linearised potential flow model that includes the axial strain suggests that within the linear regime, the amplitude growth rate of an impulsively accelerated interface should grow from the superposition of the traditional RMI velocity and the velocity difference across the perturbation, where the velocity difference across the perturbation is proportional to the strain rate and the interface amplitude. Simply, expansive axial strain will cause the interface perturbation amplitudes to stretch, whilst compressive strain will cause the perturbation amplitudes to shrink. Validation of the model was performed by conducting two-dimensional single-mode simulations using a velocity perturbation initialisation. The simulations showed agreement with the linearised model, as long as the amplitude remained small relative to the

wavelength.

Axial strain rates were then applied to an RMI-induced turbulent mixing layer, based on the quarter-scale θ-group case, which used a narrowband perturbation initialisation between fluids with a 3:1 density ratio. These simulations were conducted as ILES, representing the high-Reynolds number limit of the flow. The applied strain rates had the same primary effect on the mixing layer — expansive strain rates would cause the mixing layer width to increase, whilst compressive strain rates would reduce the mixing layer width. Unlike the linear regime, the growth of the mixing layer was no longer a superposition of the mixing layer's turbulent growth rate and the background velocity difference. This was demonstrated through the implementation of a buoyancy-drag model which included the background velocity contribution to the growth of the mixing layer. This buoyancy-drag model over-predicted the influence of the strain rate on the mixing layer development. This discrepancy between the simulation and models results is due to shear production of turbulent kinetic energy from the axial strain rate. Under expansive strain, shear production will remove turbulent kinetic energy from the mixing layer, causing the turbulent growth rate of the mixing layer to decrease. Additional terms were introduced into the buoyancy-drag model to account for these effects, and the terms were calibrated to match the ILES results. Two correction terms were found to be significant, correlating to the terms that are expected from a self-similarity analysis of the turbulent kinetic energy transport equation with axial strain and a Boussinesq eddy-viscosity assumption. The effect of the shear production was also found to alter the self-similarity of the mixing layer. Whilst the unstrained case converged towards a constant late-time mixedness and anisotropy of turbulent kinetic energy, the application of axial strain caused a deviation from this profile. The shear production of axial turbulent kinetic energy is not proportionally redistributed to the transverse direction, which causes a shift in the anisotropy. Where the axial turbulent kinetic energy serves to mix the bulk, outer fluid into the mixing layer, the vorticity will mix the fluid within the mixing layer. Under compression, which observes an increase in axial TKE but only a small increase in the in-plane vorticity, the mixing layer is observed to grow faster and become less mixed. The non-dimensionalised mean volume fraction profile is relatively unchanged, whereas the value of $\overline{f_1 f_2}$ at the centre of the mixing layer increases for the expansion case and decreases for the compression cases.

The application of transverse strain is the focus of the work in Chapter 5. The solutions for the amplitude growth rate in the linear regime for spherical, cylindrical, and planar geometries are shown to be equivalent when using a strain rate framework in terms of the axial and transverse strain. This strain rate framework provides a more intuitive understanding of the Bell-Plesset effects on the mixing layer development as opposed to the compression rate and convergence

rate, which is not directly applicable to planar geometry. The application of transverse strain on the linear regime was conducted with two-dimensional simulations, confirming the model's predictions that the growth rate is amplified under compression and diminished under expansion. For sufficiently strong expansive strain, the mixing layer may remain in the linear regime indefinitely.

The same trends were not observed for the application of transverse strain to a turbulent mixing layer. Using the same quarter-scale θ-group case in Chapter 4, transverse strain rates were applied to the RMI-induced mixing layer. Whilst the linear regime theory suggests the compressive strain would amplify the growth rate, in the turbulent regime the compressive strain achieves a slight decrease in mixing layer width, and a slight increase for expansion. The transverse shear production of turbulent kinetic energy only created a slight change in the transverse component, increasing for compression and decreasing for expansion, but the change was less than would be expected. This energy was not found to be redistributed to the axial component, as the axial component of the turbulent kinetic energy was found to decrease under the compressive strain, where redistribution would have it increase. The missing energy for compression and additional energy for expansion is explained by using a modified dissipation rate that also depends upon the transverse expansion factor. As the domain compresses, so too does the turbulent length scale which is inversely proportional to the dissipation rate, creating a larger dissipation rate for compression and removing more energy, and vice versa for expansion. A simple Reynolds stress model for the domain integrated quantities was implemented and demonstrated the effect of the modified length scale in the dissipation rate, achieving greater alignment with the ILES results. The model also highlighted the inability of the standard pressure-rate-of-strain tensor to handle RMI-induced mixing layers – the standard assumption of return-to-isotropy does not hold for RMI, which remains anisotropic well into the late time. As a result, the closure had to be adjusted to reproduce the desired anisotropy for the unstrained case. The anisotropy predicted for the strain cases could be improved, by either a better closure for the pressure-rate-of-strain tensor or by modelling the spatial dimensions of the flow. Analysis of the effective drag length scale for the integral width showed that compared to the unstrained case, the drag length scale should scale linearly with the expansion factor, or the time-varying mean perturbation wavelength instead of the initial wavelength. This modification was made in the buoyancy-drag model to take into account the transverse strain rate. The resulting model performed well at estimating the integral width for the strained cases, although the compression cases showed slightly more growth than predicted by the model, potentially due to redistribution of the transverse turbulent kinetic energy into the axial direction.

The modelling of the axially and transversely strained ILES cases using the K-L turbulence model was investigated in Chapter 6, with a focus on the bulk compression closure for the turbulent length scale. Whilst existing closures describe the scaling of the turbulent length scale or turbulent dissipation rate for homogenous flows under isotropic strain, the correct closure for inhomogeneous flows with anisotropic strain is not evident. RANS models are a vital tool in engineering applications, such as in ICF capsule design, due to the reduced computational demand arising from the lower requirement for the resolution of scales as compared to DNS or LES. For the simulations to be useful they must be accurate, and so it is necessary to identify the most accurate closure for the bulk compression. As the y-z plane is statistically homogenous in planar RMI, the RANS simulations were conducted as one-dimensional and initialised using the planar-averages of the quarter-scale θ-group case. Three sets of simulations were conducted, each using a different closure model for the bulk compression. The isotropic closure uses the default closure of one-third of the divergence, representing the mean strain rate. The two alternative closures introduced were the axial strain rate closure and the transverse strain rate closure, which uses the axial and transverse strain rate for closure, respectively. The initial conditions for each set were calibrated to achieve the correct late-time integral width and TKE for the unstrained case. Despite this, limitations of the K-L model meant that the transitional stage of the simulation was not well captured. Whilst all three closures would perform the same under isotropic strain, the simulation results for the applied axial and transverse strain rates differ. All three closures are able to capture the axial strain effect which stretches/compresses the mixing layer, as this effect depends on the simulation resolving the velocity difference across the mixing layer. The difference arises from the turbulent growth, which is a function of the turbulent kinetic energy and the turbulent length scale. For both axial strain and transverse strain, the transverse closure achieves the most accurate results for the integral width and the TKE. The original isotropic closure performs reasonably well for the case, whilst the axial closure performs the worst. A self-similarity analysis of the equations highlight the failure of the axial strain closure as assuming the mixing layer remains self-similar, which it does not. The recommendation from these results is to adjust the bulk compression to use the transverse strain rates for improved modelling of mixing layers under anisotropic strain. This modification was also derived for the K-ϵ and K-ω models, through the equivalence of two-equation models.

7.2 Recommendations for future research

The conducted investigation into the influence of strain rates on the development of RMI-induced mixing layers leaves several avenues of future research open. A greater understanding of the late-time development can be achieved by conducting the simulations for an even longer duration. Longer simulations for the applied strain rates will achieve greater variations in the domain size. This is especially important for modelling ICF, where the interface radius can be reduced by a factor of 30-40 as the capsule implodes. Simulating to such a scale would require a greater amount of computational resources as the CFL time-step size decreases under convergence, and the mesh size needs to be increased to retain resolution of the small scales under expansion.

Three-dimensional simulations of anisotropic strain, as observed in practical applications, can serve to further validate or refine the existing models. The linearised potential flow model that accounts for the effects of axial and transverse strain rates includes a term that depends upon the product of the two strain rates. In the non-linear and turbulent regimes, a coupling between the two strain rates may result in the solution not being the superposition of the models derived separately for the axial and transverse strain rates. Simulating anisotropic strain rates to get high order statistics, whether DNS or ILES, will need to take care regarding the mesh motion. Moving the mesh geometry with the anisotropic strain creates anisotropic cells. The resulting anisotropic numerical dissipation may make convergence more difficult for investigations into the fine scales of the flow and DNS. It may be possible to avoid the issues of anisotropic meshes with an alternate implementation of moving mesh motion to preserve isotropic cells within the mixing layer. However, this may create additional numerical diffusion, as some aspects of the mesh would no longer be moving with the mean flow.

In ICF, the compression of the capsule is performed to achieve the pressure and temperature necessary for the fuel to undergo fusion. The temperature of the fuel therefore varies by several orders of magnitudes as is it converges. Research into sudden viscous dissipation has highlighted that the viscosity of a plasma has a stronger temperature dependence ($T \sim T^{5/2}$). Performing direct numerical simulations of an RMI-induced mixing layer under compression can be performed with the strain framework. As the domain compresses, the temperature of the fluid will increase, allowing for the effects of the viscosity's temperature dependence to be investigated. For the ILES simulations conducted, the lack of physical viscosity has meant that the shear production of TKE was the primary alteration to the evolution of the TKE, causing an increase for compression relative to the unstrained case. The ratio between shear production and dissipation will vary depending upon the viscosity scaling. For weak scaling, similar results to the ILES may be obtained, but at the strong scaling for plasmas the increased viscosity will

cause dissipation to dominate. Investigating this behaviour for several viscosity profiles will elucidate this behaviour, aiding with modelling and capsule design for ICF.

The simulations conducted have high non-dimensional strain rates for the linear regime simulations, and lower non-dimensional strain rates for the late-time multimode simulations. A more thorough investigation into the effect of the strain rate on the transitional mixing layer may be conducted with moderate strain rates. The limitation is that it takes some time for the flow to adapt and manifest the effects of the strain rate on the flow, however there is a limited number of eddy turnovers available within the transitional regime, making such observations difficult. For the ILES conducted, the application of strain could not be applied until the pressure within the domain had reached close to an equilibrium, otherwise pressure waves would bounce around within the domain due to the usage of moving inviscid walls as boundary conditions. This could be averted by initialising the multimode simulations with a velocity perturbation, as was done with the single-mode cases. The application of strain from the linear regime onwards for the multimode case would give a far greater understanding of the linear-to-transitional stage for the multimode case, which was not a focus of the work conducted.

The application of transverse strain with a broadband perturbation initialisation may produce interesting results due to different growth rates of each perturbation mode. The highest wave-numbers will saturate long before the low wave-number modes, allowing the mixing layer to reach a turbulent state prior to the low wave-number modes saturating. The mixing layer may then experience the influence of both regimes — under compressive strain the mixing layer may observe an increased growth from the amplified growth rate of the linear low wave-number modes, but also a decreased growth rate due to the increased dissipation rate caused by the compression of the turbulent length scale. To accurately resolve the low wave-number modes, it may also be necessary to improve the boundary condition treatment. The application of moving symmetry planes in the direction of strain limits the modes that can be resolved when transverse strain is applied. Periodicity allows the low odd wave-numbers to continue to evolve in the regions near the edges of the domain.

Due to the versatility of RANS models, it is worthwhile investigating the efficacy of using more complicated RANS models for capturing the effects of anisotropic strain. Where an alternate closure has been proposed for the single turbulent length scale, the modification necessary for two length scale models, scales for dissipation and turbulence, is not obvious. It may require one of the two or both to adapt the alternate scaling, or a new closure altogether. Likewise, Reynolds stress models that use anisotropic eddy viscosity will require consideration. The K-L model used assumes isotropy of the turbulent kinetic energy and eddy viscosity, hence

with these assumptions no longer applicable, it may not be necessary to have this anisotropic closure for the bulk compression. Additionally, the application of the derived RANS to other cases under anisotropic strain will further help validate the model.

References

Allaire, G., Clerc, S. & Kokh, S. 2002 A Five-Equation Model for the Simulation of Interfaces between Compressible Fluids. *Journal of Computational Physics* **181** (2), 577–616.

Amendt, P., Colvin, J. D., Tipton, R. E., Hinkel, D. E., Edwards, M. J., Landen, O. L., Ramshaw, J. D., Suter, L. J., Varnum, W. S. & Watt, R. G. 2002 Indirect-drive noncryogenic double-shell ignition targets for the National Ignition Facility: Design and analysis. *Physics of Plasmas* **9** (5), 2221–2233.

Andrews, M. J. 1992 An Experimental Study of Turbulent Mixing by the Rayleigh-Taylor Instabilities and a Two-Fluid Model of the Mixing Phenomena. In *Advances in Compressible Turbulent Mixing*, pp. 7–19. Lawrence Livermore National Laboratory.

Andrews, M. J. & Spalding, D. B. 1990 A simple experiment to investigate two-dimensional mixing by Rayleigh–Taylor instability. *Physics of Fluids A: Fluid Dynamics* **2** (6), 922–927.

Andrews, M. J., Youngs, D. L., Livescu, D. & Wei, T. 2014 Computational Studies of Two-Dimensional Rayleigh-Taylor Driven Mixing for a Tilted-Rig. *Journal of Fluids Engineering* **136** (091212).

Arnett, D. 2000 The Role of Mixing in Astrophysics. *The Astrophysical Journal Supplement Series* **127** (2), 213–217.

Arnett, W. D., Bahcall, J. N., Kirshner, R. P. & Woosley, S. E. 1989 Supernova 1987A. *Annual Review of Astronomy and Astrophysics* **27** (Volume 27, 1989), 629–700.

Baker, L. & Freeman, J. R. 1981 Heuristic model of the nonlinear Rayleigh-Taylor instability. *Journal of Applied Physics* **52** (2), 655–663.

Banerjee, A., Gore, R. A. & Andrews, M. J. 2010 Development and validation of a turbulent-mix model for variable-density and compressible flows. *Physical Review E* **82** (4), 046309.

Bell, G. I. 1951 Taylor instability on cylinders and spheres in the small amplitude approximation. *Tech. Rep.* LA-1321. Los Alamos Scientific Laboratory.

Bellman, R. & Pennington, R. H. 1954 Effects of Surface Tension and Viscosity on Taylor Instability. *Quarterly of Applied Mathematics* **12** (2), 151–162, arXiv: 43634128.

Besnard, D., Harlow, F. H., Rauenzahn, R. M. & Zemach, C. 1992 Turbulence transport equations for variable-density turbulence and their relationship to two-field models. *Tech. Rep.* LA-12303-MS. Los Alamos National Lab. (LANL), Los Alamos, NM (United States).

Betti, R. & Hurricane, O. A. 2016 Inertial-confinement fusion with lasers. *Nature Physics* **12** (5), 435–448.

Biamino, L., Jourdan, G., Mariani, C., Houas, L., Vandenboomgaerde, M. & Souffland, D. 2015 On the possibility of studying the converging Richtmyer–Meshkov instability in a conventional shock tube. *Experiments in Fluids* **56** (2), 26.

Blaisdell, G. A., Coleman, G. N. & Mansour, N. N. 1996 Rapid distortion theory for compressible homogeneous turbulence under isotropic mean strain. *Physics of Fluids* **8** (10), 2692–2705.

Boris, J. P. & Book, D. L. 1973 Flux-corrected transport. I. SHASTA, a fluid transport algorithm that works. *Journal of Computational Physics* **11** (1), 38–69.

Boris, J. P., Grinstein, F. F., Oran, E. S. & Kolbe, R. L. 1992 New insights into large eddy simulation. *Fluid Dynamics Research* **10** (4-6), 199–228.

Boureima, I., Ramaprabhu, P. & Attal, N. 2018 Properties of the Turbulent Mixing Layer in a Spherical Implosion. *Journal of Fluids Engineering* **140** (050905).

Bradley, P. A. 2014 The effect of mix on capsule yields as a function of shell thickness and gas fill. *Physics of Plasmas* **21** (6), 062703.

Bradley, P. A., Cobble, J. A., Tregillis, I. L., Schmitt, M. J., Obrey, K. D., Glebov, V., Batha, S. H., Magelssen, G. R., Fincke, J. R., Hsu, S. C., Krasheninnikova, N. S., Murphy, T. J. & Wysocki, F. J. 2012 Role of shocks and mix caused by capsule defects. *Physics of Plasmas* **19** (9), 092703.

Brasseur, M., Vandenboomgaerde, M., Mariani, C., Barros, D. C., Souffland, D. & Jourdan, G. 2021 Experimental generation of spherical converging shock waves. *Experiments in Fluids* **62** (7), 156.

Braun, N. O. & Gore, R. A. 2021 A multispecies turbulence model for the mixing and de-mixing of miscible fluids. *Journal of Turbulence* **22** (12), 784–813.

Brouillette, M. 2002 The Richtmyer-Meshkov Instability. *Annual Review of Fluid Mechanics* **34** (1), 445–468.

Brouillette, M. & Sturtevant, B. 1994 Experiments on the Richtmyer–Meshkov instability: Single-scale perturbations on a continuous interface. *Journal of Fluid Mechanics* **263**, 271–292.

Cabot, W. H. & Cook, A. W. 2006 Reynolds number effects on Rayleigh–Taylor instability with possible implications for type Ia supernovae. *Nature Physics* **2** (8), 562–568.

Cambon, C., Coleman, G. N. & Mansour, N. N. 1993 Rapid distortion analysis and direct simulation of compressible homogeneous turbulence at finite Mach number. *Journal of Fluid Mechanics* **257**, 641–665.

Campos, A. & Morgan, B. E. 2019 Direct numerical simulation and Reynolds-averaged Navier-Stokes modeling of the sudden viscous dissipation for multicomponent turbulence. *Physical Review E* **99** (6), 063103.

Casey, D. T., Smalyuk, V. A., Tipton, R. E., Pino, J. E., Grim, G. P., Remington, B. A., Rowley, D. P., Weber, S. V., Barrios, M., Benedetti, L. R., Bleuel, D. L., Bond, E. J., Bradley, D. K., Caggiano, J. A., Callahan, D. A., Cerjan, C. J., Chen, K. C., Edgell, D. H., Edwards, M. J., Fittinghoff, D., Frenje, J. A., Gatu-Johnson, M., Glebov, V. Y., Glenn, S., Guler, N., Haan, S. W., Hamza, A., Hatarik, R., Herrmann, H. W., Hoover, D., Hsing, W. W., Izumi, N., Kervin, P., Khan, S., Kilkenny, J. D., Kline, J., Knauer, J., Kyrala, G., Landen, O. L., Ma, T., MacPhee, A. G., McNaney, J. M., Mintz, M., Moore, A., Nikroo, A., Pak, A., Parham, T., Petrasso, R., Rinderknecht, H. G., Sayre, D. B., Schneider, M., Stoeffl, W., Tommasini, R., Town, R. P., Widmann, K., Wilson, D. C. & Yeamans, C. B. 2014 Development of the CD Symcap platform to study gas-shell mix in implosions at the National Ignition Facility. *Physics of Plasmas* **21** (9), 092705.

Chiravalle, V. P. 2006 The k-L turbulence model for describing buoyancy-driven fluid instabilities. *Laser and Particle Beams* **24** (3), 381–394.

Chow, F. K. & Moin, P. 2003 A further study of numerical errors in large-eddy simulations. *Journal of Computational Physics* **184** (2), 366–380.

Clark, D. S., Marinak, M. M., Weber, C. R., Eder, D. C., Haan, S. W., Hammel, B. A., Hinkel, D. E., Jones, O. S., Milovich, J. L., Patel, P. K., Robey, H. F., Salmonson, J. D., Sepke, S. M. & Thomas, C. A. 2015 Radiation hydrodynamics modeling of the highest

compression inertial confinement fusion ignition experiment from the National Ignition Campaign. *Physics of Plasmas* **22** (2), 022703.

Clark, D. S., Weber, C. R., Milovich, J. L., Pak, A. E., Casey, D. T., Hammel, B. A., Ho, D. D., Jones, O. S., Koning, J. M., Kritcher, A. L., Marinak, M. M., Masse, L. P., Munro, D. H., Patel, M. V., Patel, P. K., Robey, H. F., Schroeder, C. R., Sepke, S. M. & Edwards, M. J. 2019 Three-dimensional modeling and hydrodynamic scaling of National Ignition Facility implosions. *Physics of Plasmas* **26** (5), 050601.

Coakley, T. & Huang, P. 1992 Turbulence modeling for high speed flows. In *30th Aerospace Sciences Meeting and Exhibit*, p. 436. American Institute of Aeronautics and Astronautics.

Colella, P. & Woodward, P. R. 1984 The Piecewise Parabolic Method (PPM) for gas-dynamical simulations. *Journal of Computational Physics* **54** (1), 174–201.

Coleman, G. N. & Mansour, N. N. 1993 Simulation and Modeling of Homogeneous Compressible Turbulence Under Isotropic Mean Compression. In *Turbulent Shear Flows 8* (ed. Franz Durst, Rainer Friedrich, Brian E. Launder, Frank W. Schmidt, Ulrich Schumann & James H. Whitelaw), pp. 269–282. Berlin, Heidelberg: Springer.

Collaboration, T. I. D. I. 2024 Achievement of target gain larger than unity in an inertial fusion experiment. *Physical Review Letters* **132** (6), 065102.

Cook, A. W. 2009 Enthalpy diffusion in multicomponent flows. *Physics of Fluids* **21** (5), 055109.

Dahm, W. J. A. & Dimotakis, P. E. 1990 Mixing at large Schmidt number in the self-similar far field of turbulent jets. *Journal of Fluid Mechanics* **217**, 299–330.

Denissen, N. A., Fung, J., Reisner, J. M. & Andrews, M. J. 2012 Implementation and Validation of the BHR Turbulence Model in the FLAG Hydrocode. *Tech. Rep.* LA-UR-12-24386. Los Alamos National Lab. (LANL), Los Alamos, NM (United States).

Denissen, N. A., Rollin, B., Reisner, J. M. & Andrews, M. J. 2014 The Tilted Rocket Rig: A Rayleigh–Taylor Test Case for RANS Models. *Journal of Fluids Engineering* **136** (091301).

Dimonte, G. 2000 Spanwise homogeneous buoyancy-drag model for Rayleigh–Taylor mixing and experimental evaluation. *Physics of Plasmas* **7** (6), 2255–2269.

Dimonte, G. & Schneider, M. 1996 Turbulent Rayleigh-Taylor instability experiments with variable acceleration. *Physical Review E* **54** (4), 3740–3743.

Dimonte, G. & Schneider, M. 2000 Density ratio dependence of Rayleigh–Taylor mixing for sustained and impulsive acceleration histories. *Physics of Fluids* **12** (2), 304–321.

Dimonte, G. & Tipton, R. 2006 K-L turbulence model for the self-similar growth of the Rayleigh-Taylor and Richtmyer-Meshkov instabilities. *Physics of Fluids* **18** (8), 085101.

Dimonte, G., Youngs, D. L., Dimits, A., Weber, S., Marinak, M., Wunsch, S., Garasi, C., Robinson, A., Andrews, M. J., Ramaprabhu, P., Calder, A. C., Fryxell, B., Biello, J., Dursi, L., MacNeice, P., Olson, K., Ricker, P., Rosner, R., Timmes, F., Tufo, H., Young, Y.-N. & Zingale, M. 2004 A comparative study of the turbulent Rayleigh–Taylor instability using high-resolution three-dimensional numerical simulations: The Alpha-Group collaboration. *Physics of Fluids* **16** (5), 1668–1693.

Dimotakis, P. E. 2000 The mixing transition in turbulent flows. *Journal of Fluid Mechanics* **409**, 69–98.

Dimotakis, P. E. & Samtaney, R. 2006 Planar shock cylindrical focusing by a perfect-gas lens. *Physics of Fluids* **18** (3), 031705.

Drake, R. P. 1999 Laboratory experiments to simulate the hydrodynamics of supernova remnants and supernovae. *Journal of Geophysical Research: Space Physics* **104** (A7), 14505–14515.

Drazin, P. G. & Reid, W. H. 2004 *Hydrodynamic Stability*, 2nd edn. Cambridge: Cambridge University Press.

Duff, R. E., Harlow, F. H. & Hirt, C. W. 1962 Effects of Diffusion on Interface Instability between Gases. *The Physics of Fluids* **5** (4), 417–425.

Durbin, P. A. & Zeman, O. 1992 Rapid distortion theory for homogeneous compressed turbulence with application to modelling. *Journal of Fluid Mechanics* **242**, 349–370.

Echekki, Tarek. & Mastorakos, Epaminodas. 2011 *Turbulent Combustion Modeling : Advances, New Trends and Perspectives*. Dordrecht: Springer.

El Rafei, M., Flaig, M., Youngs, D. L. & Thornber, B. 2019 Three-dimensional simulations of turbulent mixing in spherical implosions. *Physics of Fluids* **31** (11), 114101.

El Rafei, M. & Thornber, B. 2020 Numerical study and buoyancy–drag modeling of bubble and spike distances in three-dimensional spherical implosions. *Physics of Fluids* **32** (12), 124107.

El Rafei, M. & Thornber, B. 2024 Turbulence statistics and transport in compressible mixing driven by spherical implosions with narrowband and broadband initial perturbations. *Physical Review Fluids* **9** (3), 034501.

Elbaz, Y. & Shvarts, D. 2018 Modal model mean field self-similar solutions to the asymptotic evolution of Rayleigh-Taylor and Richtmyer-Meshkov instabilities and its dependence on the initial conditions. *Physics of Plasmas* **25** (6), 062126.

Epstein, R. 2004 On the Bell–Plesset effects: The effects of uniform compression and geometrical convergence on the classical Rayleigh–Taylor instability. *Physics of Plasmas* **11** (11), 5114–5124.

Farhat, C., Geuzaine, P. & Grandmont, C. 2001 The Discrete Geometric Conservation Law and the Nonlinear Stability of ALE Schemes for the Solution of Flow Problems on Moving Grids. *Journal of Computational Physics* **174** (2), 669–694.

Ferguson, K., Wang, K. M. & Morgan, B. E. 2023 Mass and momentum transport in the Tilted Rocket Rig experiment. *Physical Review Fluids* **8** (9), 094502.

Flaig, M., Clark, D., Weber, C., Youngs, D. L. & Thornber, B. 2018 Single-mode perturbation growth in an idealized spherical implosion. *Journal of Computational Physics* **371**, 801–819.

Fraley, G. 1986 Rayleigh–Taylor stability for a normal shock wave–density discontinuity interaction. *The Physics of Fluids* **29** (2), 376–386.

Fureby, C. & Grinstein, F. F. 2002 Large Eddy Simulation of High-Reynolds-Number Free and Wall-Bounded Flows. *Journal of Computational Physics* **181** (1), 68–97.

Garnier, E., Mossi, M., Sagaut, P., Comte, P. & Deville, M. 1999 On the use of shock-capturing schemes for large-eddy simulation. *Journal of Computational Physics* **153** (2), 273–311.

Gauthier, S. & Bonnet, M. 1990 A k-ε model for turbulent mixing in shock-tube flows induced by Rayleigh–Taylor instability. *Physics of Fluids A: Fluid Dynamics* **2** (9), 1685–1694.

Ge, J., Li, H., Zhang, X. & Tian, B. 2022 Evaluating the stretching/compression effect of Richtmyer–Meshkov instability in convergent geometries. *Journal of Fluid Mechanics* **946**, A18.

Ge, J., Zhang, X.-t., Li, H.-f. & Tian, B.-l. 2020 Late-time turbulent mixing induced by multimode Richtmyer–Meshkov instability in cylindrical geometry. *Physics of Fluids* **32** (12), 124116.

Godunov, S. K. & Bohachevsky, I. 1959 Finite difference method for numerical computation of discontinuous solutions of the equations of fluid dynamics. *Matematičeskij sbornik* **47(89)** (3), 271–306.

Godunov, S. K., Zabrodin, A. V., Ivanov, M. Ia., Kraiko, A. N. & Prokopov, G. P. 1976 *Numerical Solution of Multidimensional Problems of Gas Dynamics*. Nauka Press.

Goldstine, H. H. & Neumann, J. V. 1955 Blast wave calculation. *Communications on Pure and Applied Mathematics* **8** (2), 327–353.

Goncharov, V. N. 2002 Analytical Model of Nonlinear, Single-Mode, Classical Rayleigh-Taylor Instability at Arbitrary Atwood Numbers. *Physical Review Letters* **88** (13), 134502.

Gottlieb, S. & Shu, C. W. 1998 Total variation diminishing Runge-Kutta schemes. *Mathematics of Computation* **67**, 73–85.

Grégoire, O., Souffland, D. & Gauthier, S. 2005 A second-order turbulence model for gaseous mixtures induced by Richtmyer—Meshkov instability. *Journal of Turbulence* **6**, N29.

Grinstein, F. F., Chiravalle, V. P., Haines, B. M., Greene, R. K. & Pereira, F. S. 2024 Transition in ICF Capsule Implosions. *Flow, Turbulence and Combustion* .

Grinstein, F. F., Margolin, L. G. & Rider, William. 2007 *Implicit Large Eddy Simulation : Computing Turbulent Fluid Dynamics*. Cambridge ;: Cambridge University Press.

Groom, M. & Thornber, B. 2020 The influence of initial perturbation power spectra on the growth of a turbulent mixing layer induced by Richtmyer–Meshkov instability. *Physica D: Nonlinear Phenomena* **407**, 132463.

Hansom, J. C. V., Rosen, P. A., Goldack, T. J., Oades, K., Fieldhouse, P., Cowperthwaite, N., Youngs, D. L., Mawhinney, N. & Baxter, A. J. 1990 Radiation driven planar foil instability and mix experiments at the AWE HELEN laser*. *Laser and Particle Beams* **8** (1-2), 51–71.

Harten, A., Lax, P. D. & Van Leer, B. 1983 On Upstream Differencing and Godunov-Type Schemes for Hyperbolic Conservation Laws. *SIAM Review* **25** (1), 35–61, arXiv: 2030019.

Hawley, J. F. & Zabusky, N. J. 1989 Vortex paradigm for shock-accelerated density-stratified interfaces. *Physical Review Letters* **63** (12), 1241–1244.

Heidt, L., Flaig, M. & Thornber, B. 2021 The effect of initial amplitude and convergence ratio on instability development and deposited fluctuating kinetic energy in the single-mode Richtmyer–Meshkov instability in spherical implosions. *Computers & Fluids* **218**, 104842.

Hide, R. 1955 The character of the equilibrium of an incompressible heavy viscous fluid of variable density: An approximate theory. *Mathematical Proceedings of the Cambridge Philosophical Society* **51** (1), 179–201.

Hirschfelder, J. O., Curtiss, C. F. & Bird, R. B. 1969 *Molecular Theory of Gases and Liquids*, , vol. 8. New York: John Wiley & Sons.

Hosseini, S. H. R., Ogawa, T. & Takayama, K. 2000 Holographic interferometric visualization of the Richtmyer-Meshkov instability induced by cylindrical shock waves. *Journal of Visualization* **2** (3), 371–380.

Hunt, J. C. R. & Carruthers, D. J. 1990 Rapid distortion theory and the 'problems' of turbulence. *Journal of Fluid Mechanics* **212**, 497–532.

Hurricane, O. A. & Miller, P. L. 1998 Shock transmission and reflection from a material interface and subsequent reflection from a hard boundary. *Tech. Rep.* UCRL-ID-132586. Lawrence Livermore National Laboratory (LLNL), Livermore, CA (United States).

Hurricane, O. A., Smalyuk, V. A., Raman, K., Schilling, O., Hansen, J. F., Langstaff, G., Martinez, D., Park, H.-S., Remington, B. A., Robey, H. F., Greenough, J. A., Wallace, R., Di Stefano, C. A., Drake, R. P., Marion, D., Krauland, C. M. & Kuranz, C. C. 2012 Validation of a Turbulent Kelvin-Helmholtz Shear Layer Model Using a High-Energy-Density OMEGA Laser Experiment. *Physical Review Letters* **109** (15), 155004.

Israel, D. M. 2023 The myth of urans. *Journal of Turbulence* **24** (8), 367–392.

Jacobs, J. W. & Sheeley, J. M. 1996 Experimental study of incompressible Richtmyer–Meshkov instability. *Physics of Fluids* **8** (2), 405–415.

Jeans, J. H. 1997 The propagation of earthquake waves. *Proceedings of the Royal Society of London. Series A, Containing Papers of a Mathematical and Physical Character* **102** (718), 554–574.

Joggerst, C. C., Nelson, A., Woodward, P., Lovekin, C., Masser, T., Fryer, C. L., Ramaprabhu, P., Francois, M. & Rockefeller, G. 2014 Cross-code comparisons of mixing during the implosion of dense cylindrical and spherical shells. *Journal of Computational Physics* **275**, 154–173.

Jones, W. P. & Launder, B. E. 1972 The prediction of laminarization with a two-equation model of turbulence. *International Journal of Heat and Mass Transfer* **15** (2), 301–314.

Kida, S. & Orszag, S. A. 1990 Enstrophy budget in decaying compressible turbulence. *Journal of scientific computing* **5** (1), 1–34.

Kim, K. H. & Kim, C. 2005 Accurate, efficient and monotonic numerical methods for multi-dimensional compressible flows: Part II: Multi-dimensional limiting process. *Journal of Computational Physics* **208** (2), 570–615.

Kokkinakis, I. W., Drikakis, D. & Youngs, D. L. 2019 Modeling of Rayleigh-Taylor mixing using single-fluid models. *Physical Review E* **99** (1), 013104.

Kokkinakis, I. W., Drikakis, D. & Youngs, D. L. 2020 Two-equation and multi-fluid turbulence models for Richtmyer–Meshkov mixing. *Physics of Fluids* **32** (7), 074102.

Kokkinakis, I. W., Drikakis, D., Youngs, D. L. & Williams, R. J. R. 2015 Two-equation and multi-fluid turbulence models for Rayleigh–Taylor mixing. *International Journal of Heat and Fluid Flow* **56**, 233–250.

Kolmogorov, A. N. 1991 The Local Structure of Turbulence in Incompressible Viscous Fluid for Very Large Reynolds Numbers. *Proceedings: Mathematical and Physical Sciences* **434** (1890), 9–13, arXiv: 51980.

Kosović, B. 1997 Subgrid-scale modelling for the large-eddy simulation of high-Reynolds-number boundary layers. *Journal of Fluid Mechanics* **336**, 151–182.

Krivets, V. V., Ferguson, K. J. & Jacobs, J. W. 2017 Turbulent mixing induced by Richtmyer-Meshkov instability. *AIP Conference Proceedings* **1793** (1), 150003.

Launder, B. E. 1996 An Introduction to Single-Point Closure Methodology. In *Simulation and Modeling of Turbulent Flows* (ed. Thomas B Gatski, M Yousuff Hussaini & John L Lumley), p. 0. Oxford University Press.

Launder, B. E., Reece, G. J. & Rodi, W. 1975 Progress in the development of a Reynolds-stress turbulence closure. *Journal of Fluid Mechanics* **68** (3), 537–566.

Launder, B. E. & Spalding, D. B. 1974 The numerical computation of turbulent flows. *Computer Methods in Applied Mechanics and Engineering* **3** (2), 269–289.

Layzer, D. 1955 On the Instability of Superposed Fluids in a Gravitational Field. *The Astrophysical Journal* **122**, 1.

Lei, F., Ding, J., Si, T., Zhai, Z. & Luo, X. 2017 Experimental study on a sinusoidal air/SF interface accelerated by a cylindrically converging shock. *Journal of Fluid Mechanics* **826**, 819–829.

Li, H., He, Z., Zhang, Y. & Tian, B. 2019 On the role of rarefaction/compression waves in Richtmyer-Meshkov instability with reshock. *Physics of Fluids* **31** (5), 054102.

Li, H., Tian, B., He, Z. & Zhang, Y. 2021 Growth mechanism of interfacial fluid-mixing width induced by successive nonlinear wave interactions. *Physical Review E* **103** (5), 053109.

Li, M., Ding, J., Zhai, Z., Si, T., Liu, N., Huang, S. & Luo, X. 2020 On divergent Richtmyer–Meshkov instability of a light/heavy interface. *Journal of Fluid Mechanics* **901**, A38.

Li, Q.-x., Zhang, Y.-s. & Ruan, Y.-c. 2024 On the power-law exponent of multimode Richtmyer–Meshkov turbulent mixing width. *Physics of Fluids* **36** (5), 055155.

Li, X. L. & Zhang, Q. 1997 A comparative numerical study of the Richtmyer-Meshkov instability with nonlinear analysis in two and three dimensions. *Physics of Fluids* **9** (10), 3069–3077.

Likhachev, O. A. & Jacobs, J. W. 2005 A vortex model for Richtmyer–Meshkov instability accounting for finite Atwood number. *Physics of Fluids* **17** (3), 031704.

Linden, P. F., Redondo, J. M. & Youngs, D. L. 1994 Molecular mixing in Rayleigh–Taylor instability. *Journal of Fluid Mechanics* **265**, 97–124.

Lindl, J., Landen, O., Edwards, J., Moses, E. & NIC Team 2014 Review of the National Ignition Campaign 2009-2012. *Physics of Plasmas* **21** (2), 020501.

Lindl, J. D., Amendt, P., Berger, R. L., Glendinning, S. G., Glenzer, S. H., Haan, S. W., Kauffman, R. L., Landen, O. L. & Suter, L. J. 2004 The physics basis for ignition using indirect-drive targets on the National Ignition Facility. *Physics of Plasmas* **11** (2), 339–491.

Lombardini, M., Pullin, D. I. & Meiron, D. I. 2014 Turbulent mixing driven by spherical implosions. Part 1. Flow description and mixing-layer growth. *Journal of Fluid Mechanics* **748**, 85–112.

Luo, H., Baum, J. D. & Löhner, R. 2004 On the computation of multi-material flows using ALE formulation. *Journal of Computational Physics* **194** (1), 304–328.

Luo, X., Li, M., Ding, J., Zhai, Z. & Si, T. 2019 Nonlinear behaviour of convergent Richtmyer–Meshkov instability. *Journal of Fluid Mechanics* **877**, 130–141.

Luo, X., Zhang, F., Ding, J., Si, T., Yang, J., Zhai, Z. & Wen, C.-y. 2018 Long-term effect of Rayleigh–Taylor stabilization on converging Richtmyer–Meshkov instability. *Journal of Fluid Mechanics* **849**, 231–244.

Marinak, M. M., Kerbel, G. D., Gentile, N. A., Jones, O., Munro, D., Pollaine, S., Dittrich, T. R. & Haan, S. W. 2001 Three-dimensional HYDRA simulations of National Ignition Facility targets. *Physics of Plasmas* **8** (5), 2275–2280.

Marshall, J. S. & Grant, J. R. 1994 Evolution and breakup of vortex rings in straining and shearing flows. *Journal of Fluid Mechanics* **273**, 285–312.

Mason, P. J. 1994 Large-eddy simulation: A critical review of the technique. *Quarterly Journal of the Royal Meteorological Society* **120** (515), 1–26.

Massoni, J., Saurel, R., Nkonga, B. & Abgrall, R. 2002 Proposition de méthodes et modèles eulériens pour les problèmes à interfaces entre fluides compressibles en présence de transfert de chaleur: Some models and Eulerian methods for interface problems between compressible fluids with heat transfer. *International Journal of Heat and Mass Transfer* **45** (6), 1287–1307.

Mavriplis, D. J. & Yang, Z. 2006 Construction of the discrete geometric conservation law for high-order time-accurate simulations on dynamic meshes. *Journal of Computational Physics* **213** (2), 557–573.

Meyer, K. A. & Blewett, P. J. 1972 Numerical Investigation of the Stability of a Shock-Accelerated Interface between Two Fluids. *The Physics of Fluids* **15** (5), 753–759.

Meyers, J., Geurts, B. J. & Baelmans, M. 2003 Database analysis of errors in large-eddy simulation. *Physics of Fluids* **15** (9), 2740–2755.

Mikaelian, K. O. 1987 Comment on "Rayleigh-Taylor instability in spherical geometry". *Physical Review A* **36** (1), 411–412.

Mikaelian, K. O. 1993 Effect of viscosity on Rayleigh-Taylor and Richtmyer-Meshkov instabilities. *Physical Review E* **47** (1), 375–383.

Mikaelian, K. O. 1994 Freeze-out and the effect of compressibility in the Richtmyer–Meshkov instability. *Physics of Fluids* **6** (1), 356–368.

Mikaelian, K. O. & Olson, B. J. 2020 On modeling Richtmyer–Meshkov turbulent mixing widths. *Physica D: Nonlinear Phenomena* **402**, 132243.

Miles, A. R. 2004 Bubble merger model for the nonlinear Rayleigh–Taylor instability driven by a strong blast wave. *Physics of Plasmas* **11** (11), 5140–5155.

Miles, A. R. 2009 The Blast-Wave-Driven Instability as a Vehicle for Understanding Supernova Explosion Structure. *The Astrophysical Journal* **696**, 498–514.

Moin, P. & Mahesh, K. 1998 DIRECT NUMERICAL SIMULATION: A Tool in Turbulence Research. *Annual Review of Fluid Mechanics* **30** (Volume 30, 1998), 539–578.

Morán-López, J. T. & Schilling, O. 2013 Multicomponent Reynolds-averaged Navier–Stokes simulations of reshocked Richtmyer–Meshkov instability-induced mixing. *High Energy Density Physics* **9** (1), 112–121.

Morán-López, J. T. & Schilling, O. 2014 Multi-component Reynolds-averaged Navier–Stokes simulations of Richtmyer–Meshkov instability and mixing induced by reshock at different times. *Shock Waves* **24** (3), 325–343.

Morán-López, J. T., Schilling, O. & Holloway, J. P. 2015 Reynolds-Averaged Navier–Stokes Modeling of Reshocked Richtmyer–Meshkov Instability Experiments and Simulations. In *29th International Symposium on Shock Waves 2* (ed. Riccardo Bonazza & Devesh Ranjan), pp. 1047–1052. Cham: Springer International Publishing.

Morel, T. & Mansour, N. N. 1982 Modeling of Turbulence in Internal Combustion Engines. SAE Technical Paper 820040. SAE International, Warrendale, PA.

Morgan, B. E. 2021 Self-consistent, high-order spatial profiles in a model for two-fluid turbulent mixing. *Physical Review E* **104** (1), 015107.

Morgan, B. E. 2022 Simulation and Reynolds-averaged Navier-Stokes modeling of a three-component Rayleigh-Taylor mixing problem with thermonuclear burn. *Physical Review E* **105** (4), 045104.

Morgan, B. E., Ferguson, K. & Olson, B. J. 2023 Two self-similar Reynolds-stress transport models with anisotropic eddy viscosity. *Physical Review E* **108** (5), 055104.

Morgan, B. E. & Greenough, J. A. 2016 Large-eddy and unsteady RANS simulations of a shock-accelerated heavy gas cylinder. *Shock Waves* **26** (4), 355–383.

Morgan, B. E., Olson, B. J., Black, W. J. & McFarland, J. A. 2018*a* Large-eddy simulation and Reynolds-averaged Navier-Stokes modeling of a reacting Rayleigh-Taylor mixing layer in a spherical geometry. *Physical Review E* **98** (3), 033111.

Morgan, B. E., Schilling, O. & Hartland, T. A. 2018*b* Two-length-scale turbulence model for self-similar buoyancy-, shock-, and shear-driven mixing. *Physical Review E* **97** (1), 013104.

Morgan, B. E. & Wickett, M. E. 2015 Three-equation model for the self-similar growth of Rayleigh-Taylor and Richtmyer-Meskov instabilities. *Physical Review E* **91** (4), 043002.

Musci, B., Petter, S., Pathikonda, G., Ochs, B. & Ranjan, D. 2020 Supernova Hydrodynamics: A Lab-scale Study of the Blast-driven Instability Using High-speed Diagnostics. *The Astrophysical Journal* **896** (2), 92.

Naot, D., Shavit, A. & Wolfshtein, M. 1970 Interactions between components of the turbulent velocity tensor correlation due to pressure fluctuations. *Israel J. Technol* **8**, 259–269.

NASA, CXC, College, M. & Winkler, F. 2013 SN1006.

NASA, ESA, CSA, STScI & Temim, T. 2024 Crab Nebula.

Nocedal, J. & Wright, S. J. 2006 *Numerical Optimization*, 2nd edn. Springer New York.

Nuckolls, J., Wood, L., Thiessen, A. & Zimmerman, G. 1972 Laser Compression of Matter to Super-High Densities: Thermonuclear (CTR) Applications. *Nature* **239** (5368), 139–142.

Olson, R. E., Leeper, R. J., Kline, J. L., Zylstra, A. B., Yi, S. A., Biener, J., Braun, T., Kozioziemski, B. J., Sater, J. D., Bradley, P. A., Peterson, R. R., Haines, B. M., Yin, L., Berzak Hopkins, L. F., Meezan, N. B., Walters, C., Biener, M. M., Kong, C., Crippen, J. W., Kyrala, G. A., Shah, R. C., Herrmann, H. W., Wilson, D. C., Hamza, A. V., Nikroo, A. & Batha, S. H. 2016 First Liquid Layer Inertial Confinement Fusion Implosions at the National Ignition Facility. *Physical Review Letters* **117** (24), 245001.

Oron, D., Arazi, L., Kartoon, D., Rikanati, A., Alon, U. & Shvarts, D. 2001 Dimensionality dependence of the Rayleigh–Taylor and Richtmyer–Meshkov instability late-time scaling laws. *Physics of Plasmas* **8** (6), 2883–2889.

Orszag, S. A. & Patterson, G. S. 1972 Numerical Simulation of Three-Dimensional Homogeneous Isotropic Turbulence. *Physical Review Letters* **28** (2), 76–79.

Pascoe, B., Groom, M. & Thornber, B. 2025*a* Turbulence modeling of mixing layers under anisotropic strain. *Physical Review Fluids* **10** (6), 064609.

Pascoe, B., Groom, M., Youngs, D. & Thornber, B. 2025*b* The impact of transverse strain of linear, transitional, and self-similar turbulent mixing layers. *(Submitted)* .

Pascoe, B., Groom, M., Youngs, D. L. & Thornber, B. 2024 Impact of axial strain on linear, transitional and self-similar turbulent mixing layers. *Journal of Fluid Mechanics* **999**, A5.

Penney, W. & Price, A. 1942 On the changing form of a nearly spherical submarine bubble. *Underwater Explosion Research* **2**, 145–161.

Pfefferlé, D. & Abarzhi, S. I. 2020 Whittle maximum likelihood estimate of spectral properties of Rayleigh-Taylor interfacial mixing using hot-wire anemometry experimental data. *Physical Review E* **102** (5), 053107.

Plesset, M. S. 1954 On the Stability of Fluid Flows with Spherical Symmetry. *Journal of Applied Physics* **25** (1), 96–98.

Poinsot, T. & Veynante, D. 2012 *Theoretical and Numerical Combustion*, 3rd edn. Bordeaux, France: Aquaprint.

Pope, S. B. 1978 An explanation of the turbulent round-jet/plane-jet anomaly. *AIAA Journal* **16** (3), 279–281.

Pope, S. B. 2000 *Turbulent Flows*. Cambridge University Press.

Pope, S. B. 2004 Ten questions concerning the large-eddy simulation of turbulent flows. *New Journal of Physics* **6** (1), 35.

Porter, D. H., Jones, T. W. & Ryu, D. 2015 Vorticity, shocks, and magnetic fields in subsonic, ICM-like turbulence. *The Astrophysical Journal* **810** (2), 93.

Probyn, M., Thornber, B., Drikakis, D., Youngs, D. & Williams, R. 2014 An Investigation Into Nonlinear Growth Rate of Two-Dimensional and Three-Dimensional Single-Mode Richtmyer–Meshkov Instability Using an Arbitrary-Lagrangian–Eulerian Algorithm. *Journal of Fluids Engineering* **136** (9).

Probyn, M. G., Williams, R. J. R., Thornber, B., Drikakis, D. & Youngs, D. L. 2021 2D single-mode Richtmyer–Meshkov instability. *Physica D: Nonlinear Phenomena* **418**, 132827.

Ramshaw, J. D. 1998 Simple model for linear and nonlinear mixing at unstable fluid interfaces with variable acceleration. *Physical Review E* **58** (5), 5834–5840.

Rayleigh 1882 Investigation of the Character of the Equilibrium of an Incompressible Heavy Fluid of Variable Density. *Proceedings of the London Mathematical Society* **s1-14** (1), 170–177.

Read, K. I. 1984 Experimental investigation of turbulent mixing by Rayleigh-Taylor instability. *Physica D: Nonlinear Phenomena* **12** (1), 45–58.

Rejmanek, H. 2017 Weather: Understanding Kelvin-Helmholtz clouds. *Cross Country Magazine* **178**.

Reynolds, O. 1883 XXIX. An experimental investigation of the circumstances which determine whether the motion of water shall be direct or sinuous, and of the law of resistance in parallel channels. *Philosophical Transactions of the Royal Society of London* **174**, 935–982.

Reynolds, O. 1895 IV. On the dynamical theory of incompressible viscous fluids and the determination of the criterion. *Philosophical Transactions of the Royal Society of London. (A.)* **186**, 123–164.

Reynolds, W. 1987 Fundamentals of turbulence for turbulence modeling and simulation. *Tech. Rep.* Agard Report No. 755. Defense Technical Information Center.

Reynolds, W. C. 1980 Modeling of fluid motions in engines—an introductory overview. In *Symposium on Combustion Modeling in Reciprocatina Engine*, pp. 41–66. Plenum Press.

Reynolds, W. C. 1990 The potential and limitations of direct and large eddy simulations. In *Whither Turbulence? Turbulence at the Crossroads* (ed. J. L. Lumley), pp. 313–343. Berlin, Heidelberg: Springer.

Richtmyer, R. D. 1960 Taylor instability in shock acceleration of compressible fluids. *Communications on Pure and Applied Mathematics* **13** (2), 297–319.

Ristorcelli, J. R. & Clark, T. T. 2004 Rayleigh–Taylor turbulence: Self-similar analysis and direct numerical simulations. *Journal of Fluid Mechanics* **507**, 213–253.

Rogallo, R. S. 1981 Numerical experiments in homogeneous turbulence. *Tech. Rep.* NASA-TM-81315. NASA.

Rotta, J. 1951 Statistische Theorie nichthomogener Turbulenz. *Zeitschrift fur Physik* **129**, 547–572.

Saffman, P. G. & Meiron, D. I. 1989 Kinetic energy generated by the incompressible Richtmyer–Meshkov instability in a continuously stratified fluid. *Physics of Fluids A: Fluid Dynamics* **1** (11), 1767–1771.

Sandberg, R. D. & Zhao, Y. 2022 Machine-learning for turbulence and heat-flux model development: A review of challenges associated with distinct physical phenomena and progress to date. *International Journal of Heat and Fluid Flow* **95**, 108983.

Sarkar, S. 1992 The pressure–dilatation correlation in compressible flows. *Physics of Fluids A: Fluid Dynamics* **4** (12), 2674–2682.

Scannapieco, E. & Brüggen, M. 2008 Subgrid Modeling of AGN-driven Turbulence in Galaxy Clusters. *The Astrophysical Journal* **686** (2), 927.

Schilling, O. 2015 Comparative Study of the Predictions of Four Reynolds-Averaged Navier–Stokes Turbulence Models Applied to a Richtmyer–Meshkov Instability Experiment. In *29th International Symposium on Shock Waves 2* (ed. Riccardo Bonazza & Devesh Ranjan), pp. 1041–1046. Cham: Springer International Publishing.

Schilling, O. 2021 Self-similar Reynolds-averaged mechanical–scalar turbulence models for Rayleigh–Taylor, Richtmyer–Meshkov, and Kelvin–Helmholtz instability-induced mixing in the small Atwood number limit. *Physics of Fluids* **33** (8), 085129.

Schilling, O. 2024 Self-similar Reynolds-averaged mechanical–scalar turbulence models for Rayleigh–Taylor mixing induced by power-law accelerations in the small Atwood number limit. *Physics of Fluids* **36** (7), 075170.

Schwarzkopf, J. D., Livescu, D., Baltzer, J. R., Gore, R. A. & Ristorcelli, J. R. 2016 A Two-length Scale Turbulence Model for Single-phase Multi-fluid Mixing. *Flow, Turbulence and Combustion* **96** (1), 1–43.

Schwarzkopf, J. D., Livescu, D., Gore, R. A., Rauenzahn, R. M. & Ristorcelli, J. R. 2011 Application of a second-moment closure model to mixing processes involving multicomponent miscible fluids. *Journal of Turbulence* **12**, N49.

Sedov, L. I. 1946 Propagation of strong shock waves. *Journal of Applied Mathematics and Mechanics* **10**, 241–250.

Si, T., Long, T., Zhai, Z. & Luo, X. 2015 Experimental investigation of cylindrical converging shock waves interacting with a polygonal heavy gas cylinder. *Journal of Fluid Mechanics* **784**, 225–251.

Smalyuk, V. A., Tipton, R. E., Pino, J. E., Casey, D. T., Grim, G. P., Remington, B. A., Rowley, D. P., Weber, S. V., Barrios, M., Benedetti, L. R., Bleuel, D. L., Bradley, D. K., Caggiano, J. A., Callahan, D. A., Cerjan, C. J., Clark, D. S., Edgell, D. H., Edwards, M. J., Frenje, J. A., Gatu-Johnson, M., Glebov, V. Y., Glenn, S., Haan, S. W., Hamza, A., Hatarik, R., Hsing, W. W., Izumi, N., Khan, S., Kilkenny, J. D., Kline, J., Knauer, J., Landen, O. L., Ma, T., McNaney, J. M., Mintz, M., Moore, A., Nikroo, A., Pak, A., Parham, T., Petrasso, R., Sayre, D. B., Schneider, M. B., Tommasini, R., Town, R. P., Widmann, K., Wilson, D. C. & Yeamans, C. B. 2014 Measurements of an Ablator-Gas Atomic Mix in Indirectly Driven Implosions at the National Ignition Facility. *Physical Review Letters* **112** (2), 025002.

Smeeton, V. & Youngs, D. 1987 Experimental Investigation of Turbulent Mixing by Rayleigh-Taylor Instability III. *Tech. Rep.* O 35/87. AWE.

Sohn, S.-I. 2003 Simple potential-flow model of Rayleigh-Taylor and Richtmyer-Meshkov instabilities for all density ratios. *Physical Review E* **67** (2), 026301.

Soulard, O. & Griffond, J. 2022 Permanence of large eddies in Richtmyer–Meshkov turbulence for weak shocks and high Atwood numbers. *Physical Review Fluids* **7** (1), 014605.

Soulard, O., Guillois, F., Griffond, J., Sabelnikov, V. & Simoëns, S. 2018 Permanence of large eddies in Richtmyer-Meshkov turbulence with a small Atwood number. *Physical Review Fluids* **3** (10), 104603.

Speziale, C. & Sarkar, S. 1991 Second-order closure models for supersonic turbulent flows. In *29th Aerospace Sciences Meeting*, p. 217. American Institute of Aeronautics and Astronautics.

Speziale, C. G. 1987 On nonlinear K-l and K-ε models of turbulence. *Journal of Fluid Mechanics* **178**, 459–475.

Srebro, Y., Elbaz, Y., Sadot, O., Arazi, L. & Shvarts, D. 2003 A general buoyancy–drag model for the evolution of the Rayleigh–Taylor and Richtmyer–Meshkov instabilities. *Laser and Particle Beams* **21** (3), 347–353.

Taylor, G. I. 1950*a* The formation of a blast wave by a very intense explosion. - II. The atomic explosion of 1945. *Proceedings of the Royal Society of London. Series A. Mathematical and Physical Sciences* **201** (1065), 175–186.

Taylor, G. I. 1950*b* The formation of a blast wave by a very intense explosion I. Theoretical discussion. *Proceedings of the Royal Society of London. Series A. Mathematical and Physical Sciences* **201** (1065), 159–174.

Taylor, G. I. 1950*c* The instability of liquid surfaces when accelerated in a direction perpendicular to their planes. I. *Proceedings of the Royal Society of London. Series A. Mathematical and Physical Sciences* **201** (1065), 192–196.

Thomas, P. D. & Lombard, C. K. 1979 Geometric Conservation Law and Its Application to Flow Computations on Moving Grids. *AIAA Journal* **17** (10), 1030–1037.

Thomas, V. & Kares, R. 2012 Drive asymmetry and the origin of turbulence in an ICF implosion. *Physical review letters* .

Thornber, B., Drikakis, D., Williams, R. J. R. & Youngs, D. 2008*a* On entropy generation and dissipation of kinetic energy in high-resolution shock-capturing schemes. *Journal of Computational Physics* **227** (10), 4853–4872.

Thornber, B., Drikakis, D., Youngs, D. L. & Williams, R. J. R. 2010 The influence of initial conditions on turbulent mixing due to Richtmyer–Meshkov instability. *Journal of Fluid Mechanics* **654**, 99–139.

Thornber, B., Drikakis, D., Youngs, D. L. & Williams, R. J. R. 2011 Growth of a Richtmyer-Meshkov turbulent layer after reshock. *Physics of Fluids* **23** (9), 095107.

Thornber, B., Griffond, J., Bigdelou, P., Boureima, I., Ramaprabhu, P., Schilling, O. & Williams, R. J. R. 2019 Turbulent transport and mixing in the multimode narrowband Richtmyer-Meshkov instability. *Physics of Fluids* **31** (9), 096105.

Thornber, B., Griffond, J., Poujade, O., Attal, N., Varshochi, H., Bigdelou, P., Ramaprabhu, P., Olson, B., Greenough, J., Zhou, Y., Schilling, O., Garside, K. A., Williams, R. J. R., Batha, C. A., Kuchugov, P. A., Ladonkina, M. E., Tishkin, V. F., Zmitrenko, N. V., Rozanov, V. B. & Youngs, D. L. 2017 Late-time growth rate, mixing, and anisotropy in the multimode narrowband Richtmyer–Meshkov instability: The θ-group collaboration. *Physics of Fluids* **29** (10), 105107.

Thornber, B., Groom, M. & Youngs, D. 2018 A five-equation model for the simulation of miscible and viscous compressible fluids. *Journal of Computational Physics* **372**, 256–280.

Thornber, B., Mosedale, A., Drikakis, D., Youngs, D. & Williams, R. J. R. 2008*b* An improved reconstruction method for compressible flows with low Mach number features. *Journal of Computational Physics* **227** (10), 4873–4894.

Thornber, B. & Zhou, Y. 2012 Energy transfer in the Richtmyer-Meshkov instability. *Physical Review E* **86** (5), 056302.

Thornber, B. & Zhou, Y. 2015 Numerical simulations of the two-dimensional multimode Richtmyer-Meshkov instability. *Physics of Plasmas* **22** (3), 032309.

Toro, E. 2009 *Riemann Solvers and Numerical Methods for Fluid Dynamics: A Practical Introduction*. Springer Berlin Heidelberg.

Toro, E. F., Spruce, M. & Speares, W. 1994 Restoration of the contact surface in the HLL-Riemann solver. *Shock Waves* **4** (1), 25–34.

Trépanier, J. Y., Reggio, M., Zhang, H. & Camarero, R. 1991 A finite-volume method for the Euler equations on arbitrary lagrangian-eulerian grids. *Computers & Fluids* **20** (4), 399–409.

Van Leer, B. 1977 Towards the ultimate conservative difference scheme. iv. a new approach to numerical convection. *Journal of Computational Physics* **23** (3), 276–299.

van Leer, B. 1979 Towards the ultimate conservative difference scheme. V. A second-order sequel to Godunov's method. *Journal of Computational Physics* **32** (1), 101–136.

Vandenboomgaerde, M., Mügler, C. & Gauthier, S. 1998 Impulsive model for the Richtmyer-Meshkov instability. *Physical Review E* **58** (2), 1874–1882.

Vandenboomgaerde, M., Rouzier, P., Souffland, D., Biamino, L., Jourdan, G., Houas, L. & Mariani, C. 2018 Nonlinear growth of the converging Richtmyer-Meshkov instability in a conventional shock tube. *Physical Review Fluids* **3** (1), 014001.

Vetter, M. & Sturtevant, B. 1995 Experiments on the Richtmyer-Meshkov instability of an air/SF6 interface. *Shock Waves* **4** (5), 247–252.

Vreman, A. W., Geurts, B. J. & Kuerten, J. G. M. 1994 Subgrid-modelling in LES of Compressible Flow. In *Direct and Large-Eddy Simulation I: Selected Papers from the First ERCOFTAC Workshop on Direct and Large-Eddy Simulation* (ed. Peter R. Voke, Leonhard Kleiser & Jean-Pierre Chollet), pp. 133–144. Dordrecht: Springer Netherlands.

Vugrin, K. W., Swiler, L. P., Roberts, R. M., Stucky-Mack, N. J. & Sullivan, S. P. 2007 Confidence region estimation techniques for nonlinear regression in groundwater flow: Three case studies. *Water Resources Research* **43** (3).

Vuong, S. T. & Coakley, T. J. 1987 Modeling of Turbulence for Hypersonic Flows with and without Separation. In *25th AIAA Aerospace Sciences Meeting*, p. 287. Reno, Nevada USA: American Institute of Aeronautics and Astronautics.

Walchli, B. & Thornber, B. 2017 Reynolds number effects on the single-mode Richtmyer-Meshkov instability. *Physical Review E* **95** (1), 013104.

Wang, L. F., Wu, J. F., Guo, H. Y., Ye, W. H., Liu, J., Zhang, W. Y. & He, X. T. 2015 Weakly nonlinear Bell-Plesset effects for a uniformly converging cylinder. *Physics of Plasmas* **22** (8), 082702.

Wang, T., Zhong, M., Wang, B., Li, P. & Bai, J. 2023 Evolution of turbulent mixing driven by implosion in spherical geometry. *Journal of Turbulence* **24** (9-10), 419–444.

Weber, C. R., Clark, D. S., Casey, D. T., Hall, G. N., Jones, O., Landen, O., Pak, A. & Smalyuk, V. A. 2023 Reduced mixing in inertial confinement fusion with early-time interface acceleration. *Physical Review E* **108** (2), L023202.

Weber, C. R., Clark, D. S., Cook, A. W., Busby, L. E. & Robey, H. F. 2014 Inhibition of turbulence in inertial-confinement-fusion hot spots by viscous dissipation. *Physical Review E* **89** (5), 053106.

Wieczorek, M. A. & Meschede, M. 2018 SHTools: Tools for Working with Spherical Harmonics. *Geochemistry, Geophysics, Geosystems* **19** (8), 2574–2592.

Wilcox, D. C. 1998 Turbulence modeling for CFD. In *Turbulence Modeling for CFD*, 2nd edn., 2nd edn. La Cãnada, Calif: DCW Industries.

Wilcox, D. C. 2006 Turbulence modeling for CFD. In *Turbulence Modeling for CFD*, 3rd edn., 3rd edn. La Cãnada, Calif: DCW Industries.

Wilke, C. R. 1950 A Viscosity Equation for Gas Mixtures. *The Journal of Chemical Physics* **18** (4), 517–519.

Williams, F. A. 1985 *Combustion Theory*, 2nd edn. Boca Raton: CRC Press.

Williams, R. J. R. 2019 Fully-conservative contact-capturing schemes for multi-material advection. *Journal of Computational Physics* **398**, 108809.

Wong, M. L., Baltzer, J. R., Livescu, D. & Lele, S. K. 2022 Analysis of second moments and their budgets for Richtmyer-Meshkov instability and variable-density turbulence induced by reshock. *Physical Review Fluids* **7** (4), 044602.

Woodward, P. & Colella, P. 1984 The numerical simulation of two-dimensional fluid flow with strong shocks. *Journal of Computational Physics* **54** (1), 115–173.

Woodward, P. R., Jayayaraj, J., Lin, p.-H., Knox, M., Porter, D. H., Fryer, C. L., Dimonte, G., Joggerst, C. C., Rockefeller, G. M., Dai, W. W., Kares, R. J. & Thomas, V. A. 2013 Simulating Turbulent Mixing from Richtmyer-Meshkov and Rayleigh-Taylor Instabilities in Converging Geometries using Moving Cartesian Grids. *Tech. Rep.* LA-UR-13-20949. Los Alamos National Lab. (LANL), Los Alamos, NM (United States).

Woosley, S. E. & Weaver, T. A. 1986 The Physics of Supernova Explosions. *Annual Review of Astronomy and Astrophysics* **24** (Volume 24, 1986), 205–253.

Xiao, M., Zhang, Y. & Tian, B. 2020*a* Modeling of turbulent mixing with an improved K–L model. *Physics of Fluids* **32** (9), 092104.

Xiao, M., Zhang, Y. & Tian, B. 2020*b* Unified prediction of reshocked Richtmyer–Meshkov mixing with K-L model. *Physics of Fluids* **32** (3), 032107.

Xiao, M., Zhang, Y. & Tian, B. 2021 A K–L model with improved realizability for turbulent mixing. *Physics of Fluids* **33** (2), 022104.

Xie, H., Qi, H., Xiao, M., Zhang, Y. & Zhao, Y. 2025 An intermittency based Reynolds-averaged transition model for mixing flows induced by interfacial instabilities. *Journal of Fluid Mechanics* **1002**, A31.

Xie, H.-s., Xiao, M.-j. & Zhang, Y.-s. 2021 Predicting different turbulent mixing problems with the same k–ε model and model coefficients. *AIP Advances* **11** (7), 075213.

Yang, Y., Zhang, Q. & Sharp, D. H. 1994 Small amplitude theory of Richtmyer–Meshkov instability. *Physics of Fluids* **6** (5), 1856–1873.

Yeung, P. K., Ravikumar, K., Nichols, S. & Uma-Vaideswaran, R. 2025 GPU-enabled extreme-scale turbulence simulations: Fourier pseudo-spectral algorithms at the exascale using OpenMP offloading. *Computer Physics Communications* **306**, 109364.

Youngs, D. 1982 *Time-Dependent Multi-material Flow with Large Fluid Distortion*, p. 273–285. Academic Press.

Youngs, D. L. 1984 Numerical simulation of turbulent mixing by Rayleigh-Taylor instability. *Physica D: Nonlinear Phenomena* **12** (1), 32–44.

Youngs, D. L. 1989 Modelling turbulent mixing by Rayleigh-Taylor instability. *Physica D: Nonlinear Phenomena* **37** (1), 270–287.

Youngs, D. L. 1991 Three-dimensional numerical simulation of turbulent mixing by Rayleigh–Taylor instability. *Physics of Fluids A: Fluid Dynamics* **3** (5), 1312–1320.

Youngs, D. L. 1994 Numerical simulation of mixing by Rayleigh–Taylor and Richtmyer–Meshkov instabilities. *Laser and Particle Beams* **12** (4), 725–750.

Youngs, D. L. 2013 The density ratio dependence of self-similar Rayleigh–Taylor mixing. *Philosophical Transactions of the Royal Society A: Mathematical, Physical and Engineering Sciences* **371** (2003), 20120173.

Youngs, D. L. 2017 Rayleigh–Taylor mixing: Direct numerical simulation and implicit large eddy simulation. *Physica Scripta* **92** (7), 074006.

Youngs, D. L. & Thornber, B. 2020*a* Buoyancy–Drag modelling of bubble and spike distances for single-shock Richtmyer–Meshkov mixing. *Physica D: Nonlinear Phenomena* **410**, 132517.

Youngs, D. L. & Thornber, B. 2020*b* Early Time Modifications to the Buoyancy-Drag Model for Richtmyer–Meshkov Mixing. *Journal of Fluids Engineering* **142** (121107).

Youngs, D. L. & Williams, R. J. R. 2008 Turbulent mixing in spherical implosions. *International Journal for Numerical Methods in Fluids* **56** (8), 1597–1603.

Yu, H. & Girimaji, S. S. 2007 Extension of compressible ideal-gas rapid distortion theory to general mean velocity gradients. *Physics of Fluids* **19** (4), 041702.

Zhai, Z., Liu, C., Qin, F., Yang, J. & Luo, X. 2010 Generation of cylindrical converging shock waves based on shock dynamics theory. *Physics of Fluids* **22** (4), 041701.

Zhang, D., Ding, J., Si, T. & Luo, X. 2023 Divergent Richtmyer–Meshkov instability on a heavy gas layer. *Journal of Fluid Mechanics* **959**, A37.

Zhang, J., Wang, L. F., Ye, W. H., Wu, J. F., Guo, H. Y., Zhang, W. Y. & He, X. T. 2017 Weakly nonlinear incompressible Rayleigh-Taylor instability in spherical geometry. *Physics of Plasmas* **24** (6), 062703.

Zhang, Q. & Sohn, S.-I. 1996 An analytical nonlinear theory of Richtmyer-Meshkov instability. *Physics Letters A* **212** (3), 149–155.

Zhang, Q. & Sohn, S.-I. 1997 Nonlinear theory of unstable fluid mixing driven by shock wave. *Physics of Fluids* **9** (4), 1106–1124.

Zhang, Y.-s., He, Z.-w., Xie, H.-s., Xiao, M.-J. & Tian, B.-l. 2020 Methodology for determining coefficients of turbulent mixing model. *Journal of Fluid Mechanics* **905**, A26.

Zhou, Y. 2001 A scaling analysis of turbulent flows driven by Rayleigh–Taylor and Richtmyer–Meshkov instabilities. *Physics of Fluids* **13** (2), 538–543.

Zhou, Y. 2007 Unification and extension of the similarity scaling criteria and mixing transition for studying astrophysics using high energy density laboratory experiments or numerical simulations. *Physics of Plasmas* **14** (8), 082701.

Zhou, Y. 2017*a* Rayleigh–Taylor and Richtmyer–Meshkov instability induced flow, turbulence, and mixing. I. *Physics Reports* **720–722**, 1–136.

Zhou, Y. 2017*b* Rayleigh–Taylor and Richtmyer–Meshkov instability induced flow, turbulence, and mixing. II. *Physics Reports* **723–725**, 1–160.

Zhou, Y., Cabot, W. H. & Thornber, B. 2016 Asymptotic behavior of the mixed mass in Rayleigh–Taylor and Richtmyer–Meshkov instability induced flows. *Physics of Plasmas* **23** (5), 052712.

Zhou, Y., Groom, M. & Thornber, B. 2020 Dependence of Enstrophy Transport and Mixed Mass on Dimensionality and Initial Conditions in the Richtmyer–Meshkov Instability Induced Flows1. *Journal of Fluids Engineering* **142** (12).

Zhou, Y., Robey, H. F. & Buckingham, A. C. 2003 Onset of turbulence in accelerated high-Reynolds-number flow. *Physical Review. E, Statistical, Nonlinear, and Soft Matter Physics* **67** (5 Pt 2), 056305.

Zhou, Y., Williams, R. J. R., Ramaprabhu, P., Groom, M., Thornber, B., Hillier, A., Mostert, W., Rollin, B., Balachandar, S., Powell, P. D., Mahalov, A. & Attal, N. 2021

Rayleigh–Taylor and Richtmyer–Meshkov instabilities: A journey through scales. *Physica D: Nonlinear Phenomena* **423**, 132838.

APPENDIX A

K-L model verification and validation

The implementation of the K-L model in FLAMENCO was undertaken in order to perform the turbulence modelling of RMI-induced mixing layer in Chapter 6 for the investigation of the bulk compression closure. To ensure the K-L model was implemented correctly, the model was tested in two stages. Firstly, the implementation of the individual terms of the models was tested using specifically designed test cases to isolate the desired term, allowing for a comparison between the simulation results and an analytical solution. The second stage was to validate against published results on instability development with the K-L model. The work presented here focuses on the one-dimensional instability simulations provided in Xiao *et al.* (2020*a*). The full set of equations for the K-L model are listed in equation (3.33), and the coefficients used are the coefficients prescribed by Xiao *et al.* (2020*a*); Zhang *et al.* (2020) and are listed in table 6.2.

A.1 Verification

The K-L model introduces two additional transport equations for the turbulent kinetic energy $\tilde{K}$ and the turbulent length scale L. Additionally, additional terms are introduced into the other transport equations to model the higher-order correlations that are introduced by the averaging process. The additional terms and equations are separated into four categories for simplicity. The first category is the base inviscid transport equations for $\tilde{K}$ and L, which serve to advect the variables as passive scalars when none of the other terms are included. The second category is the diffusion fluxes, which take the form of $\frac{\partial}{\partial x_i}\frac{\mu_T}{N_\phi}\frac{\partial \phi}{\partial x_i}$. The third category is for the terms which depend upon the Reynolds stress $\bar{\tau}_{ij}$, and the final category is for the remaining sources terms for $\tilde{K}$ and L. Each term has a targeted case with a specified analytical solution to be compared to. For the cases which include spatial fluxes, a convergence study is also conducted by comparing the L_2 error norm under mesh refinement.

A.1.1 Advection

In FLAMENCO, the inviscid fluxes are evaluated using a Riemann solver. Neglecting the diffusion and source terms, the transport equations for $\tilde{K}$ and L are given by

$$\frac{\partial \bar{\rho} L}{\partial t} + \frac{\partial \bar{\rho} L \tilde{u}_i}{\partial x_i} = 0 \tag{A.1a}$$

$$\frac{\partial \bar{\rho} \tilde{K}}{\partial t} + \frac{\partial \bar{\rho} \tilde{K} \tilde{u}_i}{\partial x_i} = 0. \tag{A.1b}$$

In this form, $\tilde{K}$ and L are passive scalars that are advected with flow. The treatment of $\tilde{K}$ and L is no different from the treatment for species mass fraction, as they do not affect the solution of the Riemann problem (which depends on the ρ, $\tilde{u}_i$, and p), resulting in the flux being calculated using the up-winded cell's values. The one thing to take note of is the contribution of $\tilde{K}$ in the total energy contribution, $\tilde{E} = \tilde{e} + \tilde{u}_i \tilde{u}_i / 2 + \tilde{K}$. Inconsistencies in the advection of $\tilde{K}$ may cause fluctuations in the internal energy and pressure. A simple test of the ability of FLAMENCO to advect $\tilde{K}$ and L is the one-dimensional linear advection problem, with a constant velocity of $\tilde{u}_1 = 10\,\mathrm{m\,s^{-1}}$. The domain is initialised with pressure set to 10^4 Pa and a density of $2\,\mathrm{kg\,m^{-3}}$. The initial profiles of $\tilde{K}$ and L are cosine and sine waves with period of the domain length of 1 m. The waves are offset by an amount equal to the amplitude in order to remain positive. The amplitudes are $300\,\mathrm{m^2\,s^{-2}}$ and 5 m respectively. The simulation is run for one second, amounting to ten flow-through periods. The results are displayed in figure A.1 for the normalised profiles and the L_2 error norms. The results show second order convergence in space and time for the $\tilde{K}$ and L profiles. The pressure error appears to be increasing proportional to the number of time-steps, however this error is at machine precision relative to the total pressure.

A.1.2 Diffusion

The K-L model uses a turbulent viscosity for the diffusion of species, enthalpy, $\tilde{K}$, and L. The governing equations for the system that include only the diffusion aspect of the K-L model is described by

$$\bar{\rho} \frac{\mathrm{D} \bar{\rho} \tilde{Y}_a}{\mathrm{D}t} = \frac{\partial}{\partial x_i} \left(\frac{\mu_T}{N_Y} \frac{\partial \tilde{Y}_a}{\partial x_i} \right) \tag{A.2a}$$

$$\bar{\rho} \frac{\mathrm{D} E}{\mathrm{D}t} = \frac{\partial}{\partial x_i} \left(\frac{\mu_T}{N_h} \frac{\partial h}{\partial x_i} \right) + \frac{\partial}{\partial x_i} \left(\frac{\mu_T}{N_K} \frac{\partial \tilde{K}}{\partial x_i} \right) \tag{A.2b}$$

$$\bar{\rho} \frac{\mathrm{D} L}{\mathrm{D}t} = \frac{\partial}{\partial x_i} \left(\frac{\mu_T}{N_L} \frac{\partial L}{\partial x_i} \right) \tag{A.2c}$$

$$\bar{\rho} \frac{\mathrm{D} \tilde{K}}{\mathrm{D}t} = \frac{\partial}{\partial x_i} \left(\frac{\mu_T}{N_K} \frac{\partial \tilde{K}}{\partial x_i} \right) \tag{A.2d}$$

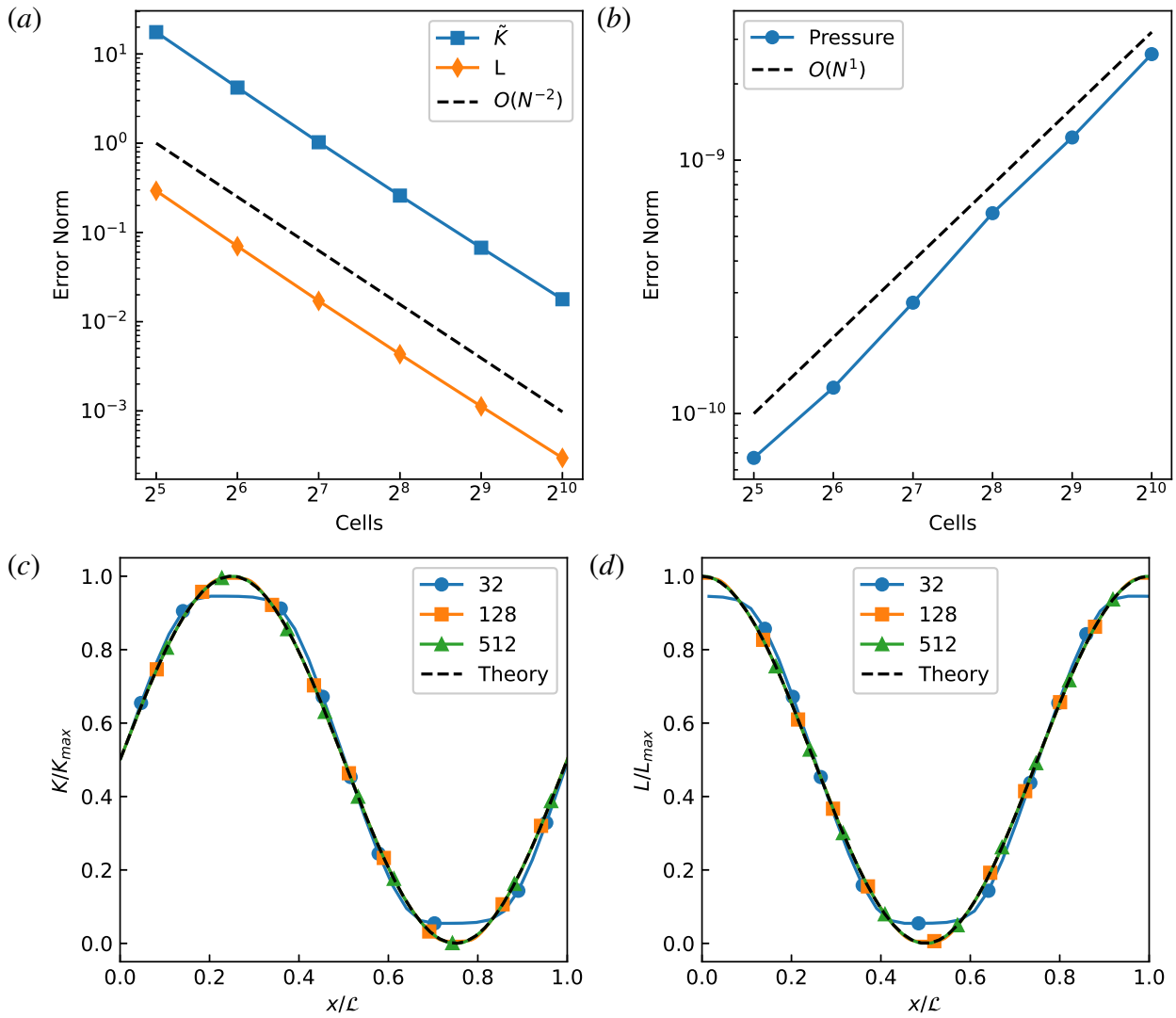

Figure A.1: Results for the linear advection of $\tilde{K}$ and L at the final time. (*a*) $\tilde{K}$ profile; (*b*) L profile; (*c*) Convergence of $\tilde{K}$ and L; (*d*) Pressure error.

In order to validate the implementation, two test cases are used. Both test cases use the analytical solution for an error function profile diffusing with a constant diffusivity. The solution to the profile is given by

$$\phi(x,t) = \frac{\phi_0}{2}\left[1 - \text{erf}\left(\frac{x - x_0}{\sqrt{4Dt + w_0^2}}\right)\right] \tag{A.3}$$

As the diffusivity depends on the turbulent viscosity, which in turn depends upon the $\tilde{K}$ and L, two different test cases are created. The first test case verifies the diffusion of $\tilde{K}$ and L by setting the turbulent viscosity to a constant. The second test case is initialised with uniform $\tilde{K}$ and $\tilde{L}$ to achieve the constant diffusivity to test the mixing of two different species at the same temperature. These test cases all use a domain of length $\mathcal{L} = 1$ m, a simulation time of 0.5 s, and inviscid wall boundary conditions in the x-direction.

Diffusion of K and L

As the evolution of the analytical profile requires a constant diffusivity, the turbulent viscosity is modified to achieve a constant diffusivity for each variable:

$$\mu_T = \rho D = 0.0005\rho. \tag{A.4}$$

The actual diffusivity of each variable will depend upon the factor N_ϕ. Using the coefficients of Xiao *et al.* (2020*a*); Zhang *et al.* (2020) where $N_L = 0.04$, the effective diffusivity of L will be $0.01\,\mathrm{m^2\,s^{-1}}$, whilst the diffusivity of $\tilde{K}$ will be smaller. For this simulation, $K_0 = 300\,\mathrm{m^2\,s^{-2}}$ and $L_0 = 5\,\mathrm{m}$ and the initial normalised error function profiles will be aligned. The final profile will be more diffuse for the turbulent length scale due to the higher diffusivity. The results of this simulation are shown in figure A.2, showing both variables are diffusing with second order accuracy, as expected from the discretisation scheme employed.

Enthalpy diffusion

To test the correct calculation of the diffusion and the diffusion of the species and enthalpy, the test case of two different species at the same temperature is used. The two fluids have initial densities of $20\,\mathrm{kg\,m^{-3}}$ and $1\,\mathrm{kg\,m^{-3}}$, with molecular weights of $200\,\mathrm{g\,mol^{-1}}$ and $10\,\mathrm{g\,mol^{-1}}$, respectively. With a uniform initial pressure of 10 kPa and an error function volume fraction profile, the initial temperature profile is also uniform and should be maintained through the diffusion process. To achieve the desired diffusivity of $D = 0.01\,\mathrm{m\,s^{-2}}$ for the enthalpy and mass fraction, the values of $\tilde{K}$ and L are uniformly set to achieve $\mu_T/N_Y = \rho D$. The difference in the densities requires a velocity offset in the simulation due to the misalignment between the density and volume weighted velocity. The velocity offset is calculated according to $\tilde{u}_i = -\frac{D}{\rho}\frac{\partial \rho}{\partial x}$. This velocity does not affect the uniformity of $\tilde{K}$ or L, but it does change the conserved quantities ($\bar{\rho}\tilde{K}$ and $\bar{\rho}L$) due to the changes in the density. The simulations are conducted for the case of equal specific heat ratios ($\gamma_1 = \gamma_2 = 1.4$), as well as for differing specific heat ratios ($\gamma_1 = 2$ and $\gamma_2 = 1.4$). The results for equal γ are shown in figure A.3, and for differing γ in figure A.4, showing the density profile, which follows an error function profile, and the convergence of the density and temperature.

It is important to note that the application of this test cases either focuses on just the error function profile (Thornber *et al.*, 2018), or used to show that the temperature fluctuation has been greatly reduced as compared to internal energy diffusion (Kokkinakis *et al.*, 2015). To this end, the temperature fluctuation, whilst not converging due to reverberating waves from the initial

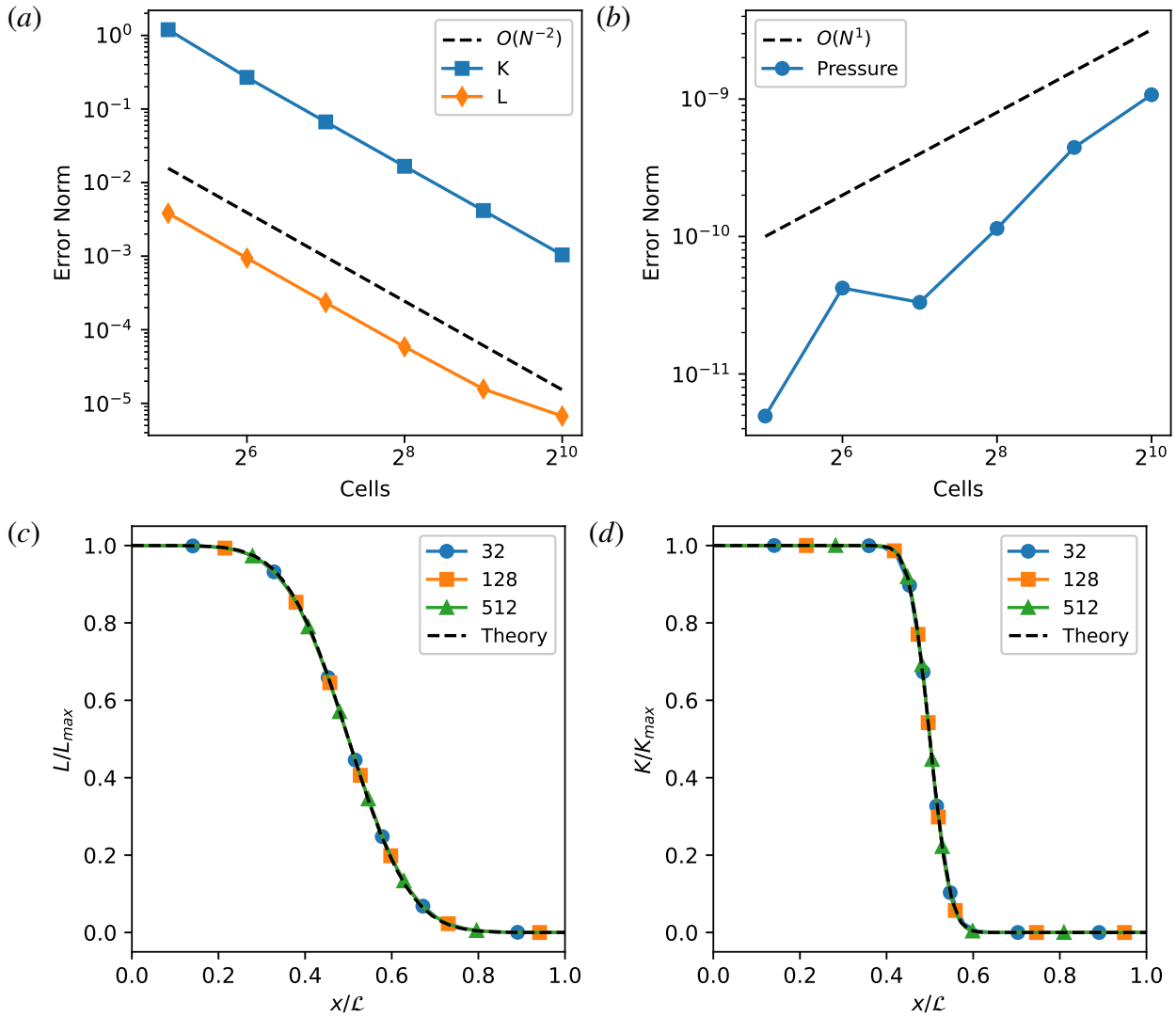

Figure A.2: Results for the diffusion of $\tilde{K}$ and L at the final time. (a) $\tilde{K}$ profile; (b) L profile; (c) Convergence of $\tilde{K}$ and L; (d) Pressure error.

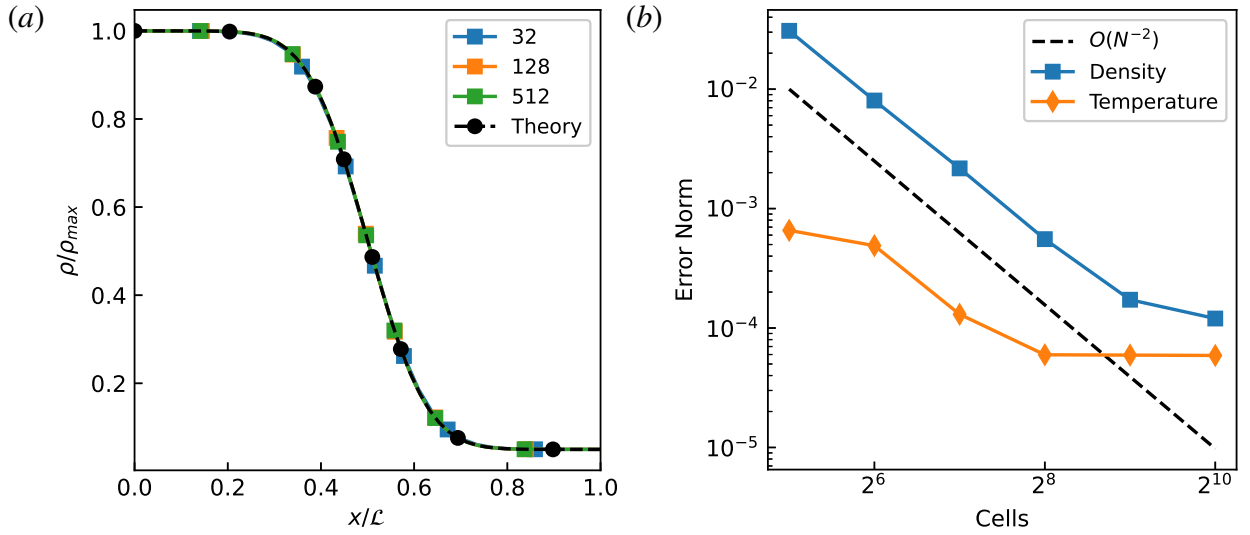

Figure A.3: Species and enthalpy diffusion for equal γ; (a) density profile; (b) density and temperature error.

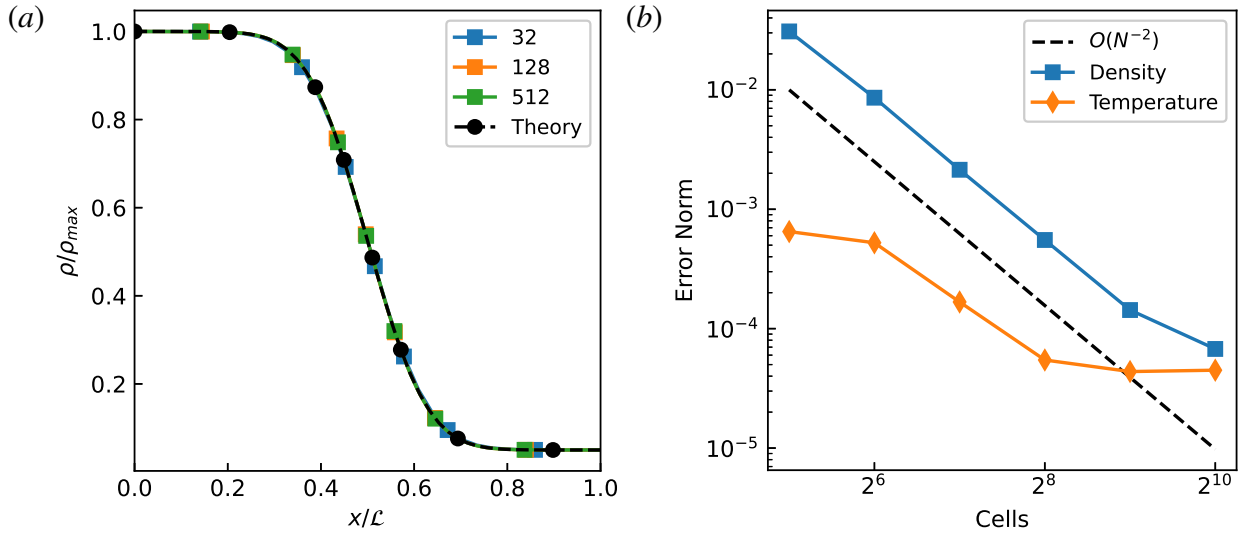

Figure A.4: Species and enthalpy diffusion for differing γ; (a) density profile; (b) density and temperature error.

conditions, is at a very small magnitude, and the diffusion profile converges with second order accuracy until the highest mesh resolution, which was also observed in Thornber *et al.* (2018).

A.1.3 Reynolds stress

Focusing on the Reynolds stress contribution, the inviscid governing equations are modified according to

$$\frac{\partial}{\partial t}\begin{pmatrix}\bar{\rho}\\ \bar{\rho}\tilde{u}_j\\ \bar{\rho}E\\ \bar{\rho}\tilde{Y}_a\\ \bar{\rho}K\\ \rho L\end{pmatrix}+\frac{\partial}{\partial x_i}\begin{pmatrix}\bar{\rho}\tilde{u}_i\\ \bar{\rho}\tilde{u}_j\tilde{u}_i+\bar{p}\delta_{ij}\\ (\bar{\rho}E+\bar{p})\tilde{u}_i\\ \bar{\rho}\tilde{Y}_a\tilde{u}_i\\ \bar{\rho}\tilde{K}\tilde{u}_i\\ \bar{\rho}L\tilde{u}_i\end{pmatrix}=\begin{pmatrix}0\\ \partial\bar{\tau}_{ij}/\partial x_i\\ \partial(\bar{\tau}_{ij}u_j)/\partial x_i\\ 0\\ \bar{\tau}_{ij}\,\partial u_j/\partial x_i\\ 0\end{pmatrix}. \tag{A.5}$$

The transport equation for $\tilde{K}$ includes the shear production source term, whilst the momentum and total energy equations include flux contributions based on the Reynolds stress.

Total pressure

In some numerical implementations, the Reynolds stress is separated into the deviatoric component $\bar{\tau}_{ij}^{(d)}$ and the isotropic component $\bar{\tau}_{ij}^{(i)} = -2/3\,\bar{\rho}\tilde{K}\delta_{ij}$. The isotropic component can

be treated as the turbulent pressure, and incorporated into the total pressure term, $\bar{p}_t = \bar{p} + 2/3\,\bar{\rho}\tilde{K}$. In this formulation the equations become

$$\frac{\partial}{\partial t}\begin{pmatrix} \bar{\rho} \\ \bar{\rho}\tilde{u}_j \\ \bar{\rho}E \\ \bar{\rho}\tilde{Y}_a \\ \bar{\rho}K \\ \rho L \end{pmatrix} + \frac{\partial}{\partial x_i}\begin{pmatrix} \bar{\rho}\tilde{u}_i \\ \bar{\rho}\tilde{u}_j\tilde{u}_i + \bar{p}_t\delta_{ij} \\ (\bar{\rho}E + \bar{p}_t)\tilde{u}_i \\ \bar{\rho}\tilde{Y}_a\tilde{u}_i \\ \bar{\rho}\tilde{K}\tilde{u}_i \\ \bar{\rho}L\tilde{u}_i \end{pmatrix} = \begin{pmatrix} 0 \\ \partial\bar{\tau}_{ij}^{(d)}/\partial x_i \\ \partial(\bar{\tau}_{ij}^{(d)}\tilde{u}_j)/\partial x_i \\ 0 \\ \bar{\tau}_{ij}^{(d)}\,\partial\tilde{u}_j/\partial x_i - \frac{2}{3}\bar{\rho}\tilde{K}\partial\tilde{u}_i/\partial x_i \\ 0 \end{pmatrix}. \tag{A.6}$$

In the absence of velocity gradients, the deviatoric Reynolds stress contributions and right-hand-side will go to zero. To test the implementation of the isotropic Reynolds stress contribution, a one-dimensional constant velocity test case is initialised with constant total pressure but varying pressure and turbulent kinetic energy. To achieve a constant total pressure the profiles used are

$$\bar{p}(x, t=0) = 10\,000 + \Delta P \sin(2\pi x), \tag{A.7}$$

$$\tilde{K}(x, t=0) = \frac{3}{2}\frac{\Delta P}{\rho}\left(1 - \sin(2\pi x)\right). \tag{A.8}$$

Without the turbulent pressure, the non-uniform pressure profile would cause the generation of acoustic waves, further changing the pressure and velocity profiles. However, the introduction of the turbulent pressure will counteract this behaviour, allowing the velocity and total pressure to remain uniform in the domain as the quantities advect through. The domain is initialised with the velocity $u = 10\,\mathrm{m\,s^{-1}}$ to achieve 10 cycles in the 0.1 s simulation time. The simulation uses periodic boundary conditions, and sets $\Delta P = 100\,\mathrm{Pa}$ and $\rho = 5\,\mathrm{kg\,m^{-3}}$. The results in figure A.5 shows the pressure and turbulent kinetic energy convect with second order accuracy, and maintain the initial profiles.

Shear production

To investigate the deviatoric component of the Reynolds stress, the domain is initialised with a uniform shear velocity gradient, $\partial\tilde{u}_2/\partial x_1 \neq 0$. For uniform pressure, density, turbulent kinetic energy, and turbulent length scale, the fluxes will cancel, and the resulting term will act as a source term for the turbulent kinetic energy:

$$\bar{\rho}\frac{\tilde{\mathrm{D}}\tilde{K}}{\tilde{\mathrm{D}}t} = \mu_T\left(\frac{\partial\tilde{u}_2}{\partial x_1}\right)^2. \tag{A.9}$$

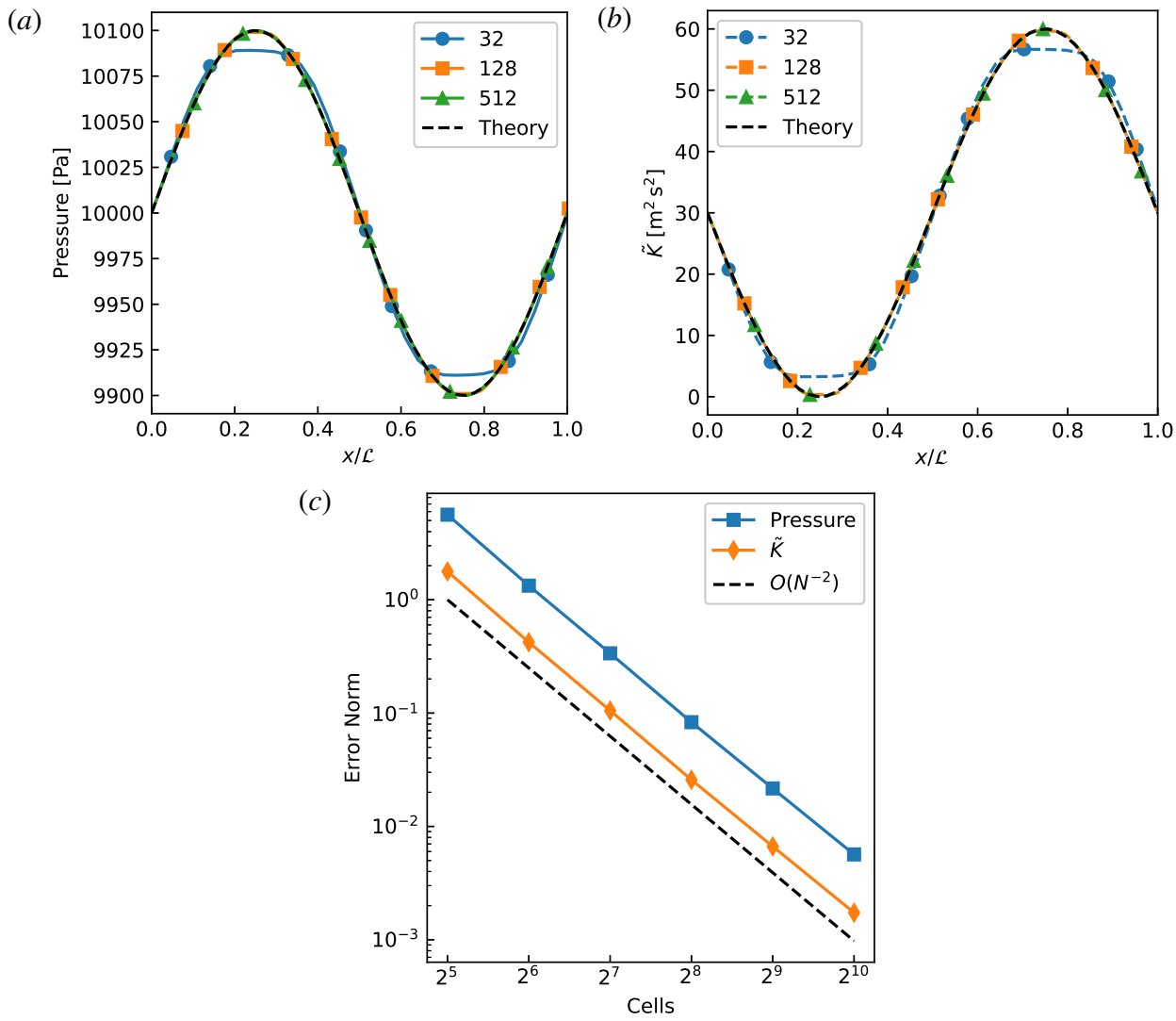

Figure A.5: Convergence of the test case with uniform total pressure: (*a*) evolution of the integral width and the maximum turbulent kinetic energy; (*b*) profiles of the volume fraction and turbulent kinetic energy at the final time.

As the turbulent viscosity if a function of the turbulent kinetic energy, the solution can be integrated to achieve the solution,

$$\tilde{K}(t) = \frac{1}{4}\left(\sqrt{2}C_\mu L\left(\frac{\partial \tilde{u}_2}{\partial x_1}\right)^2 t + 4\tilde{K}_0\right)^2. \tag{A.10}$$

The simulation is initialised with a uniform domain using the values $L = 3\,\mathrm{m}$ and $\tilde{K} = 0.001\,\mathrm{m^2\,s^{-2}}$. The results in figure A.6 show a growth that appears quadratic in time, agreeing with the analytical model.

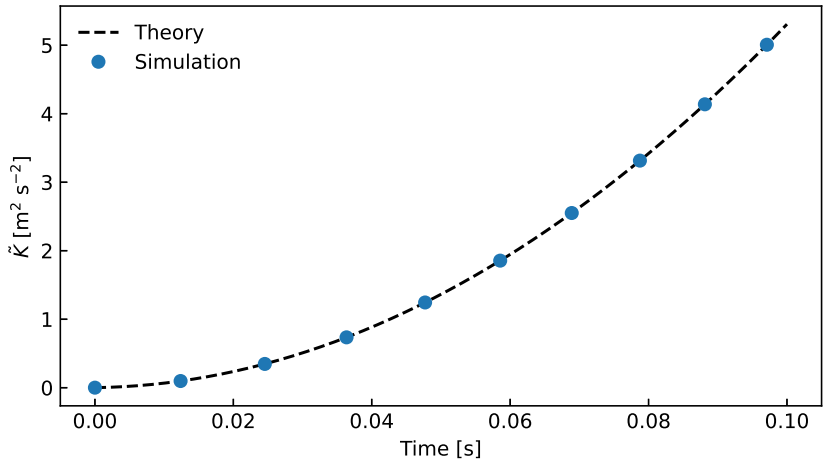

Figure A.6: Comparison of evolution of $\tilde{K}$ for the shear stress test.

A.1.4 Source terms

Isotropic decay

The isotropic decay test case is based upon the test case in Denissen *et al.* (2012) and serves to validate the L production term and the $\tilde{K}$ dissipation term. Spatially uniform profiles of $\tilde{K} = 3\,\mathrm{m^2\,s^{-2}}$ and $L = 2\,\mathrm{m}$ in a stationary flow with uniform density and pressure will evolve according to

$$\bar{\rho}\frac{\mathrm{d}\tilde{K}}{\mathrm{d}t} = -C_D\bar{\rho}\frac{(2\tilde{K})^{3/2}}{L}, \tag{A.11}$$

$$\bar{\rho}\frac{\mathrm{d}L}{\mathrm{d}t} = C_L\bar{\rho}\sqrt{2\tilde{K}}. \tag{A.12}$$

The solution to this model can be expressed as power law growth,

$$\tilde{K} = \tilde{K}_0\tau^{-a}, \tag{A.13}$$

$$L = \tilde{K}_0\tau^{-b}, \tag{A.14}$$

where $\tau = 1 + t/t_0$. For the specified source terms, the unknowns in the solution are given by

$$b = -\frac{C_L}{C_D + C_L}, \tag{A.15}$$

$$a = 2b + 2, \tag{A.16}$$

$$t_0 = \frac{aL_0}{2C_D\sqrt{2\tilde{K}_0}}. \tag{A.17}$$

The results for the simulation with t =2 s is shown in figure A.7 along with the theoretical trends, showing the results are aligned with each other.

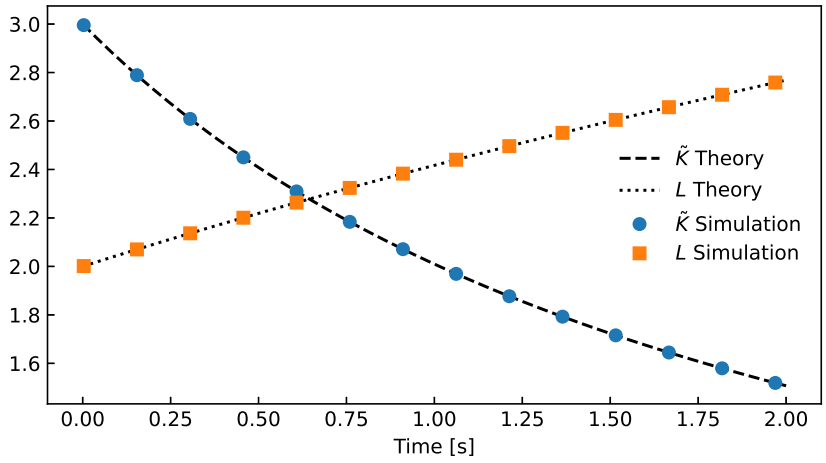

Figure A.7: Isotropic decay test case, showing the decay of the turbulent kinetic energy and growth of the turbulent length scale.

L bulk compression

The isolating the bulk compression closure of the turbulent length provides the ODE:

$$\frac{\mathrm{d}L}{\mathrm{d}t} = C_C L \frac{\partial \tilde{u}_i}{\partial x_j}. \tag{A.18}$$

A general solution for L with a time-varying $\partial \tilde{u}_i / \partial x_j$ can be written in terms of the expansion factor (see equation (3.102)),

$$L(t) = L_0 \Lambda^{C_C}. \tag{A.19}$$

In order to test this, two simulations are set up with a uniform strain rate in one direction but different strain rate profiles. The constant velocity case uses an initial strain rate of $\bar{S}_0 = -0.75\,\mathrm{s}^{-1}$, whilst the constant strain rate case uses a strain rate of $\bar{S} = -ln(4.0)\,\mathrm{s}^{-1}$, allowing both cases to achieve a final expansion factor of $\Lambda = 1/4$ at $t = 1\,\mathrm{s}$. The domain is s initially $\mathcal{L} = 1\,\mathrm{m}$ long, and uses moving inviscid walls. The initial value of L is 3 m, and the remaining properties of the domain are uniform except for the velocity, which is initialised with a linear profile as according to the strain rate. The simulation results are plotted in figure A.8, along with the theoretical trend lines. The different strain profiles follow different paths, however they achieve the same value at the final time when the expansion factor is the same.

A.2 Instability validation

The following section compares the implemented K-L model with the results provided in Xiao *et al.* (2020*a*). All the plotted reference data has been digitally extracted from the plots in the

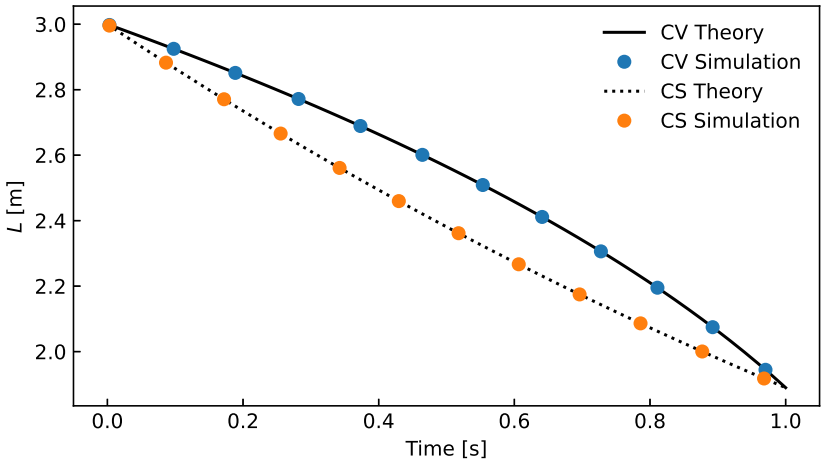

Figure A.8: Bulk compression of L test case, showing the reduction of L with bulk compression according to the constant velocity (CV) and constant strain rate (CS) profiles.

aforementioned paper. For brevity, the full details of the simulations will not be provided here unless there is a notable adjustment or correction to the details provided by Xiao *et al.* (2020*a*).

A.2.1 Rayleigh–Taylor

The Rayleigh-Taylor test case in Xiao *et al.* (2020*a*) is based upon the case in Kokkinakis *et al.* (2015). It uses a 3:1 density ratio and an isentropic pressure and density distribution. Both fluids use $\gamma = 1.4$, however to achieve the desired volume fraction profile it is necessary to adjust the singular specified molecular weight and use molecular weights for the light and heavy fluid which are in line with the density ratio i.e. $M_L = 28.8\,\mathrm{g\,mol^{-1}}$ and $M_H = 86.4\,\mathrm{g\,mol^{-1}}$. The results are shown in figure A.9, showing alignment between the evolution and final time profiles.

A.2.2 Richtmyer–Meshkov

The Richtmyer–Meshkov test case is a light-to-fluid case with a 1:3 density ratio. The interface is initially stationary and sharp, and the instability is initiated by a $Ma = 1.5$ shock wave. The results in figure A.10 shows that in the late-time, the simulation and reference data are aligned, observing a growth rate on the order of $t^{0.23}$. The values differ at the early time, likely due to different methods used to calculate the 1% and 99% volume-fraction cut-off width.

A.2.3 Kelvin–Helmholtz

The Kelvin-Helmholtz test case in Xiao *et al.* (2020*a*) is based upon the test case by Chiravalle (2006), conducted as a 2D or 1D simulation. Neither paper specifies the mesh size used, so a

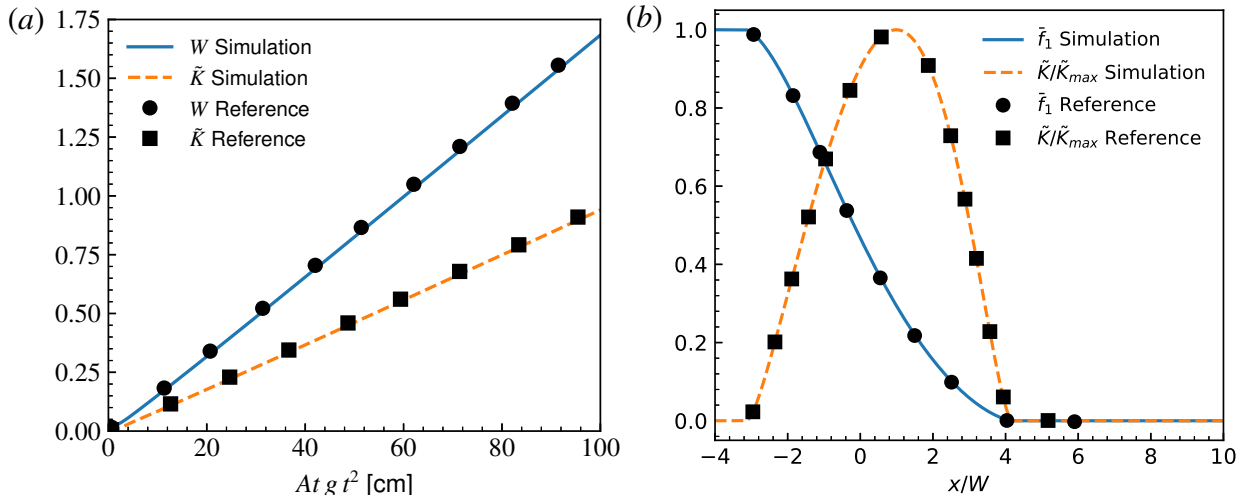

Figure A.9: One-dimensional Rayleigh-Taylor simulation: (*a*) evolution of the integral width and the maximum turbulent kinetic energy; (*b*) Profiles of the volume fraction and turbulent kinetic energy at the final time.

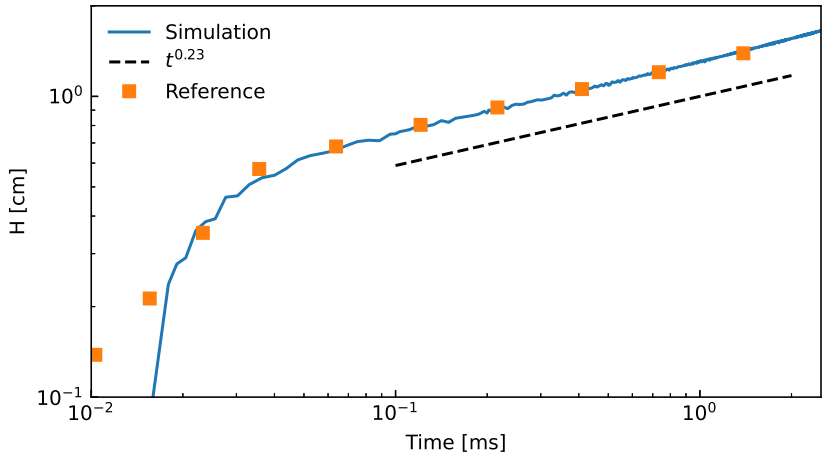

Figure A.10: Cut-off width of one-dimensional RMI case

computationally affordable choice of a one-dimensional simulation with 300 cells is performed. As a result, a slightly smaller initial value of $L_0 = 10^{-5}$ m is used in the cells adjacent to the interface, which is an order of magnitude lower than the value provided in Xiao *et al.* (2020*a*). The simulation results for $L_{\max}$ in figure A.11 appears well aligned with the reference results. The mixing layer width appears to grow slightly faster than the reference data and the desired linear trend of $0.18\Delta u$. The increased growth rate may be due to higher turbulent diffusion arising from the slightly higher asymptotic value of $\tilde{K}_{\max}$.

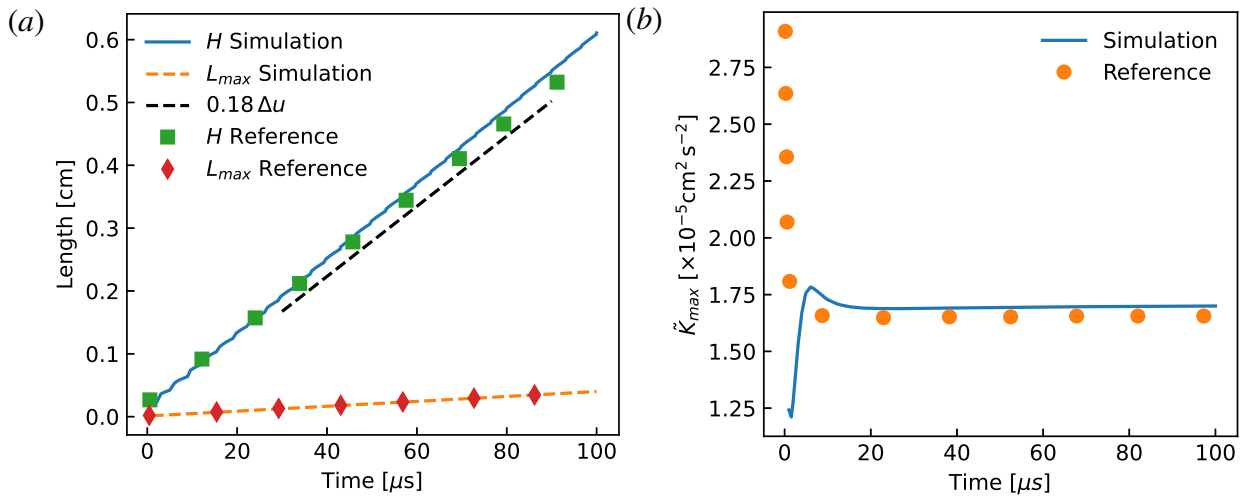

Figure A.11: Quasi-one- dimensional Kelvin–Helmholtz; (*a*) evolution of the mixing width and maximum integral length scale $L_{\max}$; (*b*) evolution of the maximum value of turbulent kinetic energy $\tilde{K}_{\max}$.

APPENDIX B

Strain rate verification

For the application of uniform strain rates in the domain, it is necessary for the simulation to preserve the specified linear velocity gradient. Additionally, a uniform pressure profile should be maintained throughout the domain. The following test cases serve to illustrate the capability of FLAMENCO to maintain the desired flow field under the applied strain rates.

Simulations are conducted with strain applied in one, two, and three directions. The magnitude of the strain rates are specified in table B.1. The specified strain rates are designed such that over a simulation time of 0.1 s, the length of the strained axis will change by a factor of two ($\Lambda_i = 2^{\pm 1}$). The initial domain is set to 1000 Pa, and is initialised with two fluids of density 3 kg m^{-3} and 1 kg m^{-3}, respectively. To ensure both fluids maintain pressure equilibrium, $\gamma = 5/3$ is used for both fluids. The initial cubic domain has sides of length 1 m. The unperturbed interface between the fluids is located at $x_0 = 0.5$ m.

Table B.1: Strain rates applied for the specified simulation test cases.

Label	Strain profile	Direction	Strain-rate $\bar{S}_0$ (s^{-1})
CV Compression	Constant velocity	Compression	-5.0
CV Expansion	Constant velocity	Expansion	10.0
CS Compression	Constant strain rate	Compression	$-10\ln(2)$
CS Expansion	Constant strain rate	Expansion	$10\ln(2)$

The main reported properties are for the velocity and pressure profiles. To allow for easy comparison between the simulation profiles, the error is quantified by the normalised root-mean-square deviation:

$$NRMSD_\phi = \frac{\sqrt{\sum_{i,j,k}\left[\phi_{i,j,k} - \hat{\phi}(x_i, y_j, z_k)\right]^2}}{\bar{\hat{\phi}}}. \tag{B.1}$$

The difference between the cell solution $\phi_{i,j,k}$ and the analytical solution at that point $\hat{\phi}_{i,j,k}$ is squared and summed over the whole domain. The resulting value is square rooted, and then normalised by the domain's theoretical average value, providing a normalised root-mean-square value. The absolute error value of the total volume of the domain and the total mass in the domain are also reported.

B.1 One-dimensional strain

The results for strain applied in one dimension are presented in figure B.1. For these cases, strain has been applied in the x-direction, representing the axial strain as done in §4. The mass and volume errors for all cases are on the order of machine precision, fluctuating around zero. The pressure error shows convergent behaviour with mesh refinement. For the constant velocity cases, the pressure converges at second order, whilst the constant strain rate cases have a 1.5 convergence rate. This is due to the approximation of the wall velocity as constant throughout the time step, which induces a small pressure fluctuation adjacent to the wall. The constant strain rate cases have the same convergence rate for velocity. In contrast, the constant velocity cases show an increasing error. The error starts out on the order of machine precision, and increase proportionally with the number of precisions. Despite this increase, the error is significantly lower than the constant strain error by many orders of magnitude.

B.2 Two-dimensional strain

For the two-dimensional strain, the strain rates are applied in the x- and y-directions, representing a normal and parallel direction to the interface respectively. The error magnitudes for all metrics behave the same as observed for the one-dimensional case, with some larger fluctuations in the mass and volume that are still negligible overall.

B.3 Three-dimensional strain

Strain rates are applied in all three directions for the three-dimensional strain cases. The simulation results in figure B.3 show that unlike the previous two cases, the mass error is no longer negligible. This is due to the second-order accurate scheme used for the time-stepping. Whilst the mesh is moving along the analytical profile and the total volume is calculated correctly, the flux through the outer boundaries will not be perfectly captured. The mass error converges at second-order, however using a third order time-stepping scheme will reduce this error to

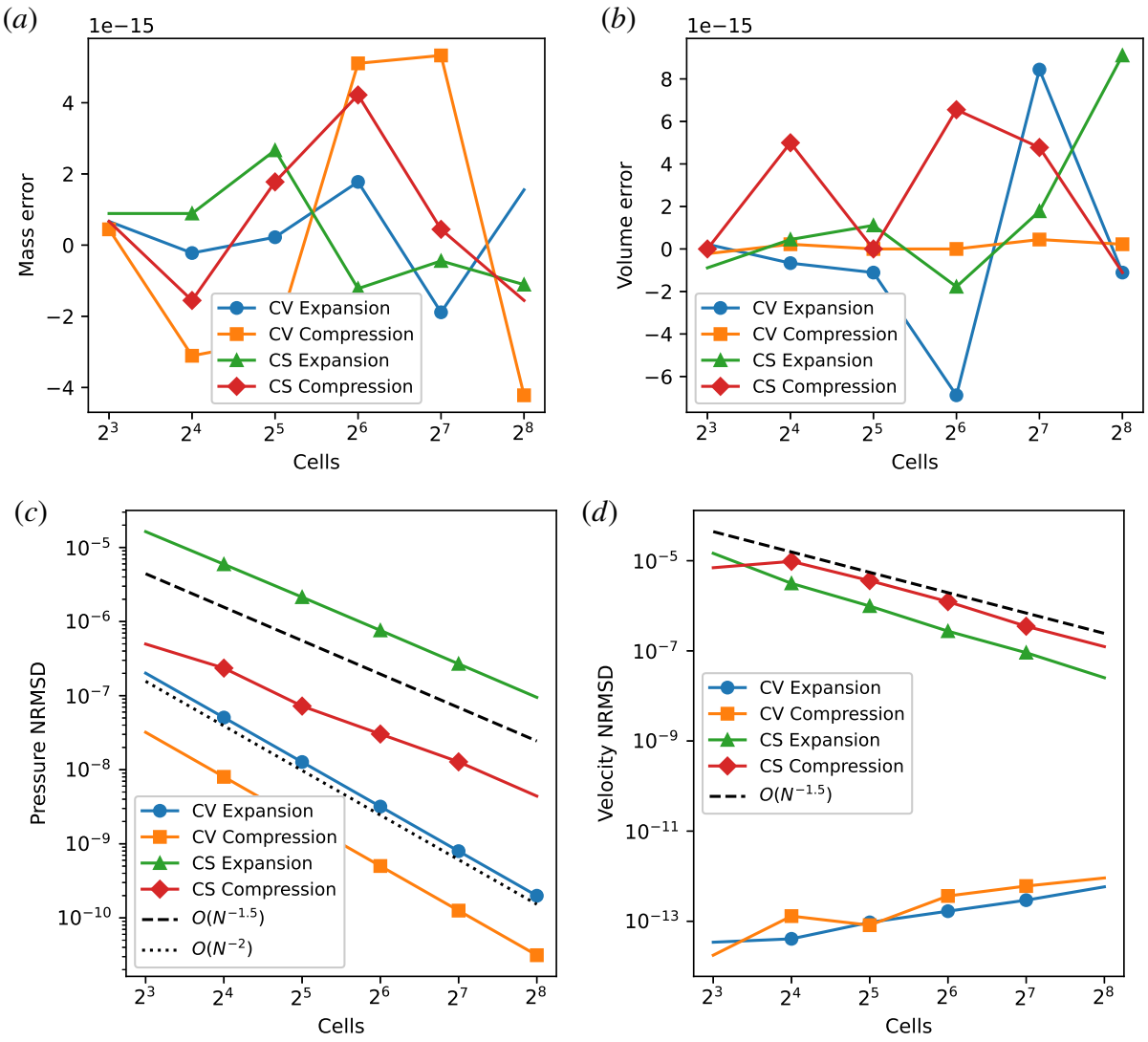

Figure B.1: Errors at the final time of $t = 0.1$s for applied strain in one direction; (a) absolute mass error; (b) absolute volume error; (c) pressure NRMSD; (d) velocity NRMSD.

negligible levels. The pressure and velocity errors converge at the same rates observed for the lower-dimensional strain cases.

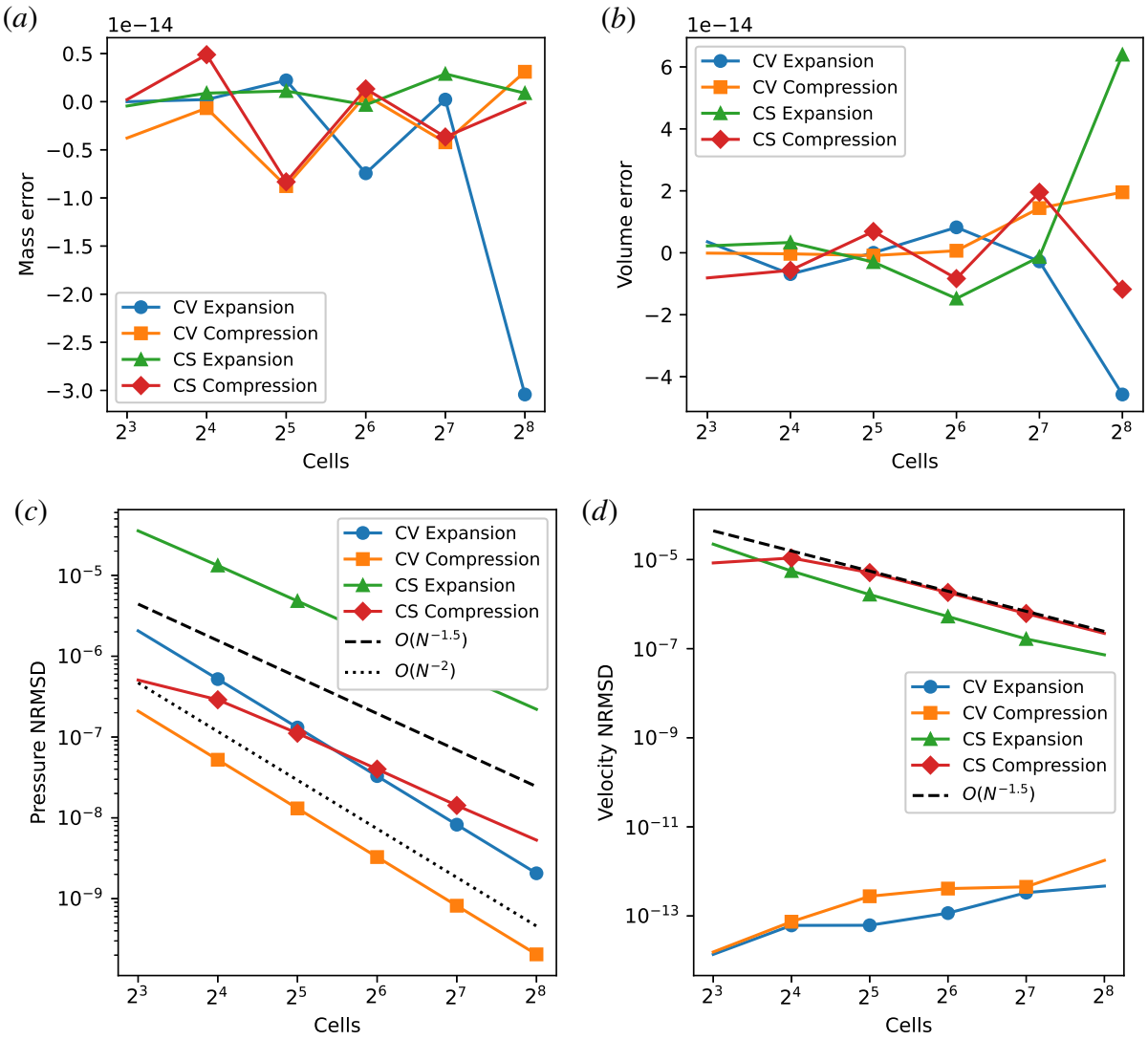

Figure B.2: Errors at the final time of $t = 0.1$s for applied strain in two directions; (a) absolute mass error; (b) absolute volume error; (c) pressure NRMSD; (d) velocity NRMSD.

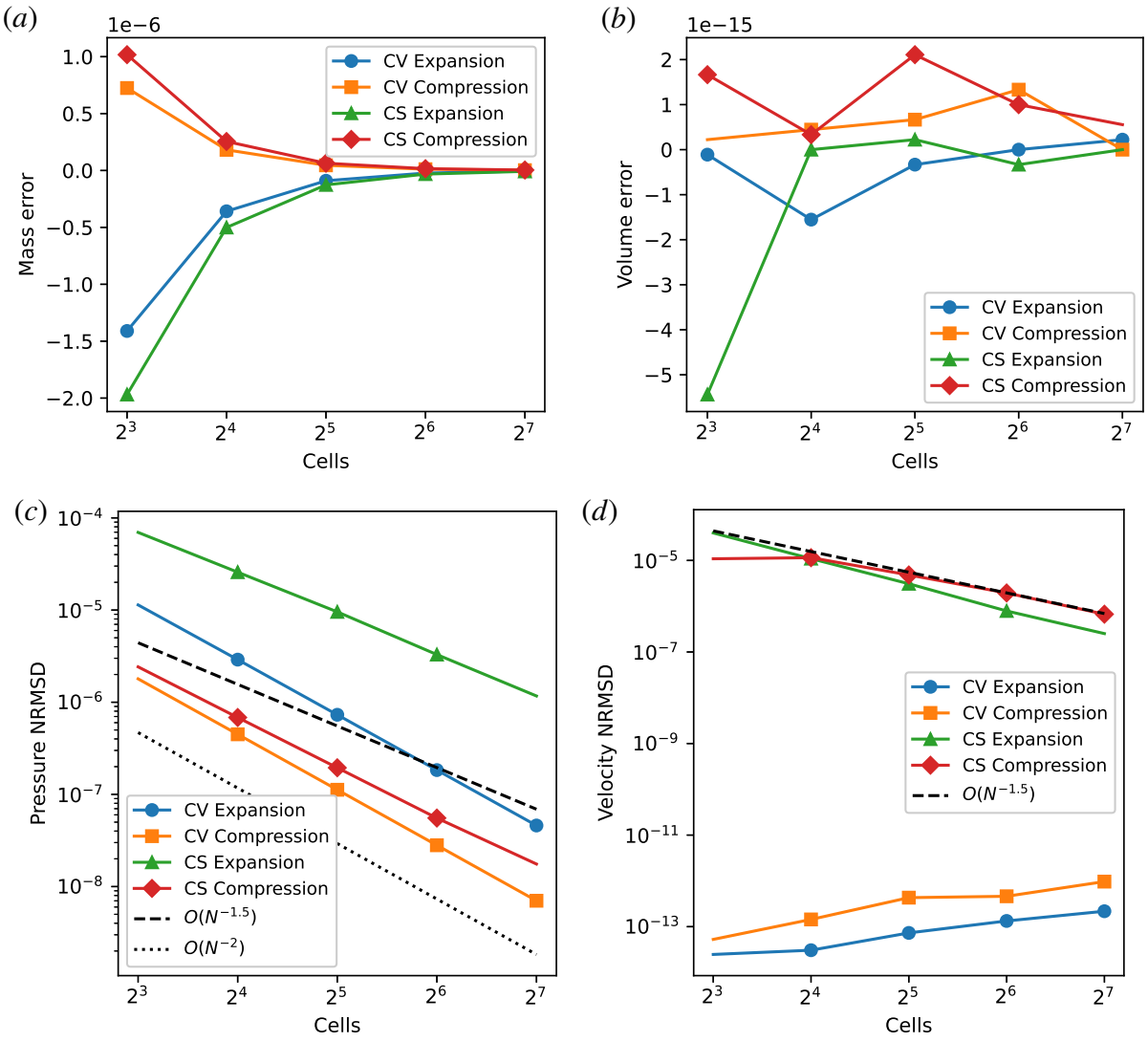

Figure B.3: Errors at the final time of $t = 0.1$s for applied strain in three directions; (a) absolute mass error; (b) absolute volume error; (c) pressure NRMSD; (d) velocity NRMSD.